Bases moleculars de la Leucoeocefalopatia Megalencefàllca amb Quists subcorlicals. Utilització de models animals i cel·lulars

Sònia Sirisi Dolcet

Bases moleculars de la Leucoencefalopatia Megalencefàlica amb Quists subcorticals. Utilització de models animals i cel·lulars.

Tesi doctoral: Sònia Sirisi Dolcet

Departament de Ciències Fisiològiques II, Unitat de Fisiologia

Universitat de Barcelona 2014

Directors:

Raúl Estévez Povedano i Virginia Nunes Martínez

Departament de Ciències Fisiològiques II, UB

Mutant GlialCAM Causes Megalencepahlic Leukoencephalopathy with Subcortical Cysts, Benign Familial Macrocephaly, and Macrocephaly with retardation and autism.

(The American Journal of Human Genetics, 2011)

Contribució:

- Purificació de l'anticós contra la proteïna GlialCAM
- Anàlisi de la mielina (Figura 3 G)

ARTICLE

Mutant GlialCAM Causes Megalencephalic Leukoencephalopathy with Subcortical Cysts, Benign Familial Macrocephaly, and Macrocephaly with Retardation and Autism

Tania López-Hernández,[1,9] Margreet C. Ridder,[3,9] Marisol Montolio,[1,4] Xavier Capdevila-Nortes,[1] Emiel Polder,[3] Sònia Sirisi,[1,6] Anna Duarri,[1,4] Uwe Schulte,[7] Bernd Fakler,[7] Virginia Nunes,[2,5,6] Gert C. Scheper,[3] Albert Martínez,[8] Raúl Estévez,[1,4,10,*] and Marjo S. van der Knaap[3,10,*]

Megalencephalic leukoencephalopathy with subcortical cysts (MLC) is a leukodystrophy characterized by early-onset macrocephaly and delayed-onset neurological deterioration. Recessive *MLC1* mutations are observed in 75% of patients with MLC. Genetic-linkage studies failed to identify another gene. We recently showed that some patients without *MLC1* mutations display the classical phenotype; others improve or become normal but retain macrocephaly. To find another MLC-related gene, we used quantitative proteomic analysis of affinity-purified MLC1 as an alternative approach and found that GlialCAM, an IgG-like cell adhesion molecule that is also called HepaCAM and is encoded by *HEPACAM*, is a direct MLC1-binding partner. Analysis of 40 MLC patients without *MLC1* mutations revealed multiple different *HEPACAM* mutations. Ten patients with the classical, deteriorating phenotype had two mutations, and 18 patients with the improving phenotype had one mutation. Most parents with a single mutation had macrocephaly, indicating dominant inheritance. In some families with dominant *HEPACAM* mutations, the clinical picture and magnetic resonance imaging normalized, indicating that *HEPACAM* mutations can cause benign familial macrocephaly. In other families with dominant *HEPACAM* mutations, patients had macrocephaly and mental retardation with or without autism. Further experiments demonstrated that GlialCAM and MLC1 both localize in axons and colocalize in junctions between astrocytes. GlialCAM is additionally located in myelin. Mutant GlialCAM disrupts the localization of MLC1-GlialCAM complexes in astrocytic junctions in a manner reflecting the mode of inheritance. In conclusion, GlialCAM is required for proper localization of MLC1. *HEPACAM* is the second gene found to be mutated in MLC. Dominant *HEPACAM* mutations can cause either macrocephaly and mental retardation with or without autism or benign familial macrocephaly.

Introduction

Megalencephalic leukoencephalopathy with subcortical cysts (MLC, MIM 604004) is a leukodystrophy with autosomal-recessive inheritance.[1] Patients develop macrocephaly during the first year of life. After several years, there is evidence of slow neurological deterioration, including cerebellar ataxia, spasticity, epilepsy, and mild cognitive decline. From early on, magnetic resonance imaging (MRI) reveals diffuse signal abnormality and swelling of the brain white matter and subcortical cysts (Figure S1, available online).[1] In follow-up exams, the white matter abnormalities remain and atrophy ensues.[1] A brain biopsy from an MLC patient showed extensive myelin vacuolation, mainly affecting the outer myelin layers, which causes the swollen appearance of the white matter.[2] In 2001, we demonstrated that mutations in *MLC1* (MIM 605908) cause MLC.[3] *MLC1* mutations are found in approximately 75% of the MLC patients.[4] MLC1 is an oligomeric membrane protein that is expressed almost exclusively in the brain. It has some degree of homology to ion channels.[5,6] Within the brain, MLC1 is mainly located in astrocyte-astrocyte junctions close to blood- and cerebrospinal fluid (CSF)-brain barriers, Bergmann glia, and main axonal tracts.[5–7] Thus far, the physiological role of MLC1 has remained unknown, and a suggested role in ion transport has not been confirmed.[3,5,8]

In some families, members with MLC do not have *MLC1* mutations, and these families do not show linkage to the *MLC1* locus, indicating that mutations in at least one other gene are involved in MLC,[9,10] but genetic-linkage studies failed to identify another disease gene. We recently described two distinct phenotypes among MLC patients without *MLC1* mutations.[11] The classical phenotype retains typical clinical and MRI features, as seen in patients with *MLC1* mutations.[1,11] The second, improving phenotype is initially the same as the classical phenotype but lacks clinical deterioration and shows major improvement or normalization of the MRI abnormalities (Figure S1).[11]

Because of the unsuccessful genetic-linkage studies and the possibility of further genetic heterogeneity, we decided to use alternative strategies to identify eligible candidate genes.

[1]Sección de Fisiología, [2]Sección de Genética, Departamento de Ciencias Fisiologicas II, University of Barcelona, 08907 Barcelona, Spain; [3]Department of Child Neurology, VU University Medical Center, De Boelelaan 1117, 1081 HV Amsterdam, The Netherlands; [4]Centro de Investigación en Red de Enfermedades Raras (CIBERER), U-750, [5]Centro de Investigación en Red de Enfermedades Raras (CIBERER), U-730, ISCIII, 08907 Barcelona, Spain; [6]Laboratorio de Genética Molecular-IDIBELL, 08907 Barcelona, Spain; [7]Logopharm GmbH, Engesserstrasse 4, 79108 Freiburg, Germany; [8]Department of Cell Biology, Faculty of Biology and Institute for Research in Biomedicine, University of Barcelona, 08907 Barcelona, Spain
[9]These authors contributed equally to this work
[10]These authors contributed equally to this work
*Correspondence: restevez@ub.edu (R.E.), ms.vanderknaap@vumc.nl (M.S.v.d.K.)
DOI 10.1016/j.ajhg.2011.02.009.

Material and Methods

The studies on human samples were performed with approval of the institutional review board, VU University Medical Center, Amsterdam, and informed consent from the families. The animal experimental protocols were approved by the Animal Care and Ethics Committee of the University of Barcelona. Protocols for the use and manipulation of the animals were approved by the Government of Catalonia.

Biochemistry

Preparation of Source Material

Plasma membrane-enriched protein fractions were prepared from pools of freshly isolated whole rat or mouse brains according to the procedure used in Zolles et al.[12] For solubilization, the prepared membrane vesicles were resuspended in ComplexioLyte buffer 47a (at 0.8 mg protein/ml, LOGOPHARM GmbH, Germany; with protease inhibitors added) and incubated for 30 min at 4°C; nonsoluble components were removed afterward by ultracentrifugation (10 min at 150.000 × g). Efficiency of solubilization was determined by immunoblot analysis of SDS-PAGE-resolved aliquots of solubilisate and pellet fractions. Polyvinylidene fluoride (PVDF) membranes were probed with rabbit polyclonal antibodies (α-N1 or α-NH, 1:10.000, see below), stained with goat anti-rabbit-HRP (Santa Cruz Biotechnologies, USA) and developed with ECL+ (GE Healthcare, USA).

Preparation of Antibodies

Immune sera against N-terminal mouse MLC1 peptides (α-N1 and α-N2) and the α-NH (anti-N-terminus of human MLC1) antibody were generated and characterized previously.[5,7,13] The α-NH also recognizes mouse/rat MLC1. Immune sera against a mouse GlialCAM synthetic peptide (QRIREQDESGQVEISA), corresponding to amino acids 403–418 of GlialCAM, were raised in rabbits with the help of the services provided by Eurogentec. The peptide was coupled to keyhole limpet hemocyanin via a cysteine residue that has been added to the N-terminal end of the peptide. After three boosts of immunization, the antisera were affinity purified with the peptide covalently coupled to Sulpholink (Pierce). The polyclonal antibody was tested by immunoblotting, immunofluorescence, and immunoprecipitation on HeLa cells expressing human GlialCAM and on mouse brain tissue.

Affinity Purification

For each experiment, 1.5 ml freshly prepared solubilisate (rat or mouse) was incubated for 2 hr at 4°C with 20 μg of the respective immobilized antibody[13] (*α-N1*, *α-N2* *α-NH*, *α-GlialCAM*, IgG = control rabbit IgG [Upstate, USA]). After a brief washing (twice for 5 min each time) with ComplexioLyte 47a, bound proteins were eluted with Laemmli buffer (dithiothreitol [DTT] was added after elution). Eluates were then briefly run on SDS-PAGE gels followed by silver staining and tryptic digestion. During these experiments, samples were taken for immunoblot analysis with the indicated MLC1 and GlialCAM antibodies.

Preparation of Myelin

Myelin was prepared as described previously.[14] Two brains from 6- to 8-week-old wild-type mice were homogenized in 20 volumes of homogenization buffer (0.32 M sucrose in 10 mM HEPES [pH 7.4]) with five strokes with a loose pestle and seven strokes with a tight pestle. The homogenate was layered over 0.85 M sucrose, centrifuged at 25,000 rpm for 30 min in a swinging bucket rotor. Proteins located in the interphase were removed, resuspended in 10 volumes of water, and centrifuged at 25,000 rpm for 15 min. The pellet was twice cleansed of sucrose by water suspension and centrifugation. Then, pellets were suspended again in homogenization buffer and layered over 0.85 M sucrose and centrifuged at 25,000 rpm for 30 min. The interphase layer was again suspended in water, centrifuged for 15 min, and resuspended in 10 mM HEPES buffer (pH 7.4) containing 1% Triton X-100. Protein was quantified by bicinchoninic acid, and 20 μg was used for SDS-PAGE and immunoblot analyses.

Mass Spectrometric Analysis

Liquid Chromatography-Mass Spectrometry/Mass Spectrometry Analysis

Stained gel lanes were excised in two parts (upper and lower), and proteins were digested with trypsin according to the procedure described previously.[15] Extracted peptides dissolved in 0.5% trifluoroacetic acid were loaded on a precolumn (C18 PepMap100, 5 μm; Dionex, Idstein, Germany) of an UltiMate 3000 HPLC (Dionex, Idstein, Germany). An aqueous organic gradient was then applied for elution and separation of peptides on a 75 μm column packed with C18 beads (ReproSil-Pur 120 ODS-3; Dr. A Maisch, Ammerbuch-Entringen, Germany) and directly electrosprayed into an LTQ-FT mass spectrometer (Thermo Scientific, Bremen, Germany; ion source: Proxeon, Odense, Denmark). Each scan cycle consisted of one FTMS full scan and up to five ITMS dependent MS/MS scans of the five most intense ions. Dynamic exclusion (30 s, mass width 20 ppm) and monoisotopic precursor selection were enabled. Using Mascot (Matrix Science, UK) we searched extracted MS/MS spectra against the Swiss-Prot database (*Mammalia*). We allowed common variable modifications and one missed tryptic cleavage; peptide tolerance was ± 10 ppm and MS/MS tolerance was ± 0.8 Da. Proteins that (1) were identified by only one specific MS/MS spectrum or (2) presented exogenous contaminations like keratins, trypsin, or immunoglobulins were not considered in further evaluations.

Protein Quantification

We used two previously detailed protein quantification methods[16] that are both based on liquid chromatography-mass spectrometry (LC-MS) peptide signal intensities extracted (as peak volumes [PVs]; m/z tolerance was 6 ppm) and aligned (between individual LC-MS runs by their retention times; tolerance was 8%) with MS Inspect (Computational Proteomics Laboratory, Fred Hutchinson Cancer Research Center, Seattle, WA, USA) and in-house written software. The *relative* quantity of a protein in affinity purification sample versus control was calculated as a median of consistent peak volume ratios of respective peptides (rPV). Ensuring the significance of rPVs, required that at least two peptide ratios had assigned PVs totaling 100,000 volume units. Proteins were regarded as specifically (co-) purified when their rPV values were higher than 10. The molar amounts of *different* proteins were compared by using $\text{abundance}_{\text{norm}}$ values (as in Figure 1), calculated as the sum of all assigned peak volumes (totalPV) divided by the number of MS-accessible amino acids (sequence of tryptic peptides with masses between 740 and 3000 Da under the MS settings used).

Genetic Analysis

The diagnosis of MLC was established by MRI criteria.[1] In those MLC patients in whom we found no mutations in *MLC1* by sequence analysis of genomic DNA, as well as analysis of *MLC1* cDNA and MLPA, we analyzed *HEPACAM* (hepatic and glial cell adhesion molecule, MIM 611642), the gene encoding GlialCAM. *HEPACAM* primers were designed with ExonPrimer (Table S1). Accession numbers of the reference sequences are NM_152722.4

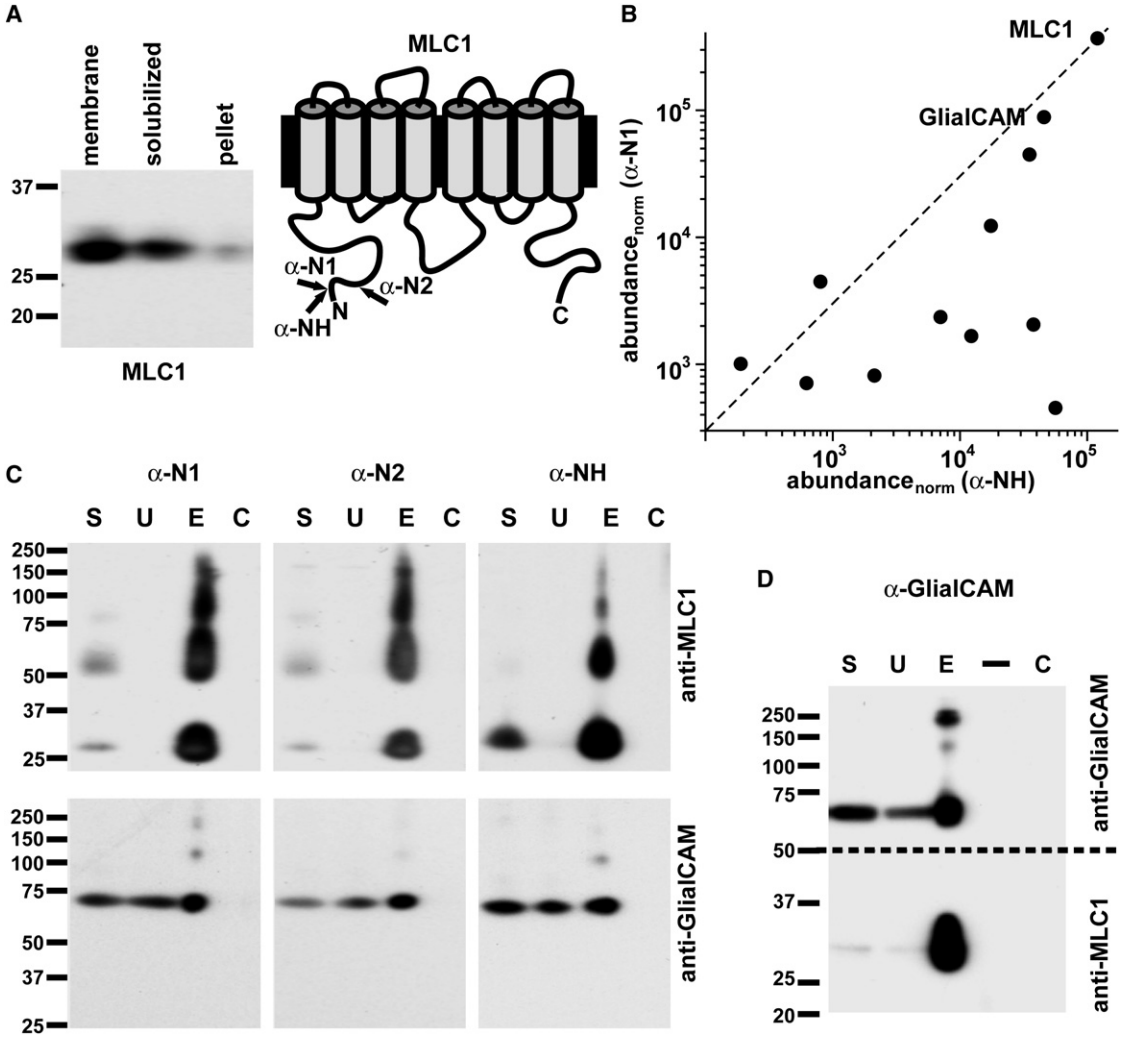

Figure 1. Proteomic Identification of GlialCAM as a Major Binding Partner of MLC1
(A) Affinity purification (AP) strategy based on efficient MLC1 solubilization (left) as visualized by immunoblot analysis of SDS-PAGE-resolved samples from rat brain membrane, solubilisate, and pellet (stained with anti-MLC1 (α-N1)) and three antibodies (right) directed against N-terminal epitopes of MLC1. Similar results were obtained when two different antibodies were applied or when the three antibodies were applied simultaneously, confirming the specificity of the proteomics data.
(B and C) Evaluation of MLC1 affinity purifications with the indicated antibodies. (B) 2D plot of protein abundances determined by mass spectrometry (for $abundance_{norm}$ values see Material and Methods) of AP with α-N1 (from rat brain) versus AP with α-NH (from mouse brain). Only proteins specifically enriched (more than 10-fold of the amount in the respective IgG control) and identified in both APs are shown (as dots). Note the distinct quantitative correlation of GlialCAM with MLC1. Pearson correlation of GlialCAM and MLC1 $abundance_{norm}$ values across all three APs and controls is $r = 0.96$. (C) Immunoblot analysis of APs with the indicated antibodies stained with anti-MLC1 (α-N1; upper) and anti-GlialCAM (lower); lanes resolve aliquots of solubilisate before (S) and after AP (U), of eluates from APs (E), and of corresponding IgG control APs (C).
(D) Immunoblots showing specific copurification of MLC1 in an AP with anti-GlialCAM (samples and antibodies labeled as before). "–" indicates no sample was loaded.

(mRNA) and NT_033899.8 (gDNA). PCR amplification of exons 1–6 of *HEPACAM* and their surrounding intronic regions was carried out with Platinum TAQ DNA Polymerase according to the manufacturer's instructions (Invitrogen). For exon 7, which has a very high-GC content, Platinum TAQ DNA-polymerase (Invitrogen) was used in combination with 5X AccuPrime™ GC-Rich Buffer A (Invitrogen). The PCR products were analyzed by cycle sequencing on an ABI3730 Genetic Analyzer (Applied Biosystems) with the same primers used for PCR amplification, with the exception of the forward primer of exon 1. The resulting chromatograms were analyzed with Sequence Pilot (JSI Medical Systems Gmbh) with ENSG00000165478 as reference sequence.

Immunofluorescent and Electron Microscopic Studies in Tissue
Tissue immunohistochemistry was performed as previously described.[5,7] For electron microscopic (EM) studies, small human cerebellum samples were obtained postmortem, fixed in 4% paraformaldehyde and 0.1% glutaraldehyde in 0.12 M phosphate buffer, and processed. They were cryoprotected gradually in sucrose and cryofixed by immersion in liquid propane. Freeze substitution was performed at −90°C during 3 days in an Automatic Freeze Substitution System (AFS, Leica); methanol containing 0.5% uranyl acetate was used as a substitution medium. Infiltration was carried out in Lowicryl HM20 at −50°C and then polymerized with UV lamps. Ultrathin sections were collected and processed for

postembedding immunostaining. For double immunostaining, grids were incubated with rabbit anti-N4-human MLC1 (1:10) and mouse anti-GlialCAM (1:10) antisera. The binding of primary antibodies was visualized by incubating with goat anti-rabbit or goat anti-mouse secondary antibodies conjugated to either 12 or 18 nm gold particles (British BioCell, International). In control experiments, the primary antibodies were omitted—no immunogold labeling occurred under these conditions.

Primary Culture and Adenoviral Transduction

Rat primary astrocytes were prepared as described previously[13] with some modifications. Cortex and hippocampus were removed from newborn (1 to 3 days old) Sprague Dawely rats (Charles River). Cerebral cortices were dissected and the meninges were carefully removed in cold sterile 0.3% BSA and 0.6% glucose in PBS. The tissue was trypsinized for 10 min at 37°C and mechanically dissociated in complete Dulbecco's modified Eagle's medium (DMEM; with 10% heat-inactivated fetal bovine serum [Biological Industries], 1% penicillin/streptomycin [Invitrogen] and 1% glutamine [Invitrogen] plus 40 U/ml DNase I [Sigma]) through a small bore fire-polished Pasteur pipette. The cell suspension was pelleted and resuspended in fresh complete DMEM, filtered through a 100-μm nylon membrane (BD Falcon) and plated into 75 cm^2 cell-culture flasks (TPP). When the mixed glial cells reached confluence, contaminating microglia, oligodendrocytes, and precursor cells were dislodged by mechanical agitation and removed as previously described.[17]

Astrocytes were plated in 6-well plates at a density of 4×10^5 cells per well or in poly-D-lysine-coated coverslips at 7.5×10^4 cells per 24-well plate. Medium was changed every 3 days. To increase the expression of MLC1 and GlialCAM detection at the plasma membrane (data not shown), we arrested astrocytic cultures in the cell cycle by addition of 2 μM cytosine β-D-arabinofuranoside (AraC, Sigma). Cultured astrocytes were identified by their positive GFAP staining (Dako).

Construction of adenovirus expressing wild-type HA-tagged human MLC1 has been described.[13] In a similar manner, we constructed and produced adenoviruses expressing three copies of the flag epitope fused to wild-type human GlialCAM or to human GlialCAM containing either the recessive mutations p.Arg92Gln, p.Arg98Cys, and p.Ser196Tyr or the dominant mutations p.Arg92Trp and p.Gly89Asp.

To infect astrocytes, we added adenoviruses at multiplicity of infection (MOI) 3 and kept them overnight at 37°C. Cells were washed, and then fresh medium was added. Astrocytes were incubated at 37°C until they were processed.

Results

MLC1-Interacting Proteins

We used a method of quantitative proteomic analysis of affinity-purified MLC1 to identify candidate genes for MLC. Independent affinity-purification experiments with MLC1 were performed with solubilized brain membranes and three different antibodies directed against peptides from the MLC1 N terminus (Figure 1A). Protein abundance determined by quantitative mass spectrometry identified HepaCAM, more correctly called GlialCAM,[18] as the protein with the second highest yield (after MLC1) in all purifications (Figure 1B and Figure S2A). Immunoblots with antibodies against GlialCAM (Figure S3) demonstrated that the protein was present in all purifications with all different MLC1 antibodies (Figure 1C). Not all GlialCAM coimmunoprecipitated with MLC1 (Figure 1C), possibly because not all GlialCAM is associated with MLC1 or because the coassembly dissolves during membrane protein solubilization. We confirmed the interaction between GlialCAM and MLC1 in reverse affinity purification experiments by using an antibody against GlialCAM that specifically coimmunoprecipitated GlialCAM and MLC1 from brain membranes. In the reverse purification, nearly all MLC1 was associated with GlialCAM (Figure 1D). Coimmunoprecipitation experiments with extracts from cells transfected with both genes also showed positive interaction (Figure S2B), indicating a direct interaction between the proteins. These findings made *HEPACAM* an excellent candidate gene for MLC patients without *MLC1* mutations.

HEPACAM Mutations in MLC Patients without *MLC1* Mutations

We analyzed the exons and surrounding intronic regions of *HEPACAM* in 40 patients from 34 families from around the world. In ten patients from eight families, we found two *HEPACAM* mutations (Table 1). Sequence analysis of *HEPACAM* in the parents showed autosomal-recessive inheritance of the two mutations in all cases except for one family with a de novo mutation. None of the patients had two mutations that abrogate expression of GlialCAM. In 18 patients from 16 families, we found one *HEPACAM* mutation, which was either inherited from a parent or arose de novo (Table 1). In 12 patients from ten families, we did not find *HEPACAM* mutations.

The observed nucleotide changes in *HEPACAM* are most likely pathogenic. They were not observed in 400 control chromosomes. All missense mutations affect amino acids that are conserved across a wide range of species (Figure 2B). Nine missense mutations affect amino acids in the predicted immunoglobulin domains in the extracellular part of GlialCAM (Figures 2A and 2C). p.Pro148Ser affects a residue between the two immunoglobulin domains. All these amino acid substitutions are predicted to affect protein function (SIFT). The substitution of residue Leu23 by His is predicted to affect the signal peptide, which spans the first 33 amino acids (SignalP 3.0 Server). Patient EL775 had two missense mutations, both inherited from the father. p.Asp128Asn is probably the pathogenic mutation because it is also observed in patients EL158 and EL708.

In 12 patients from ten families, neither *MLC1* nor *HEPACAM* mutations were found. In these families, we could not exclude linkage with both the *MLC1* and *HEPACAM* loci with certainty (data not shown). The possibility of hidden *MLC1* or *HEPACAM* mutations cannot, therefore, be excluded, and it is not certain that there must be a third gene mutated in MLC.

Table 1. *HEPACAM* Mutations

Patient	Exon	DNA	Protein	P/M/de novo[a]
Two Mutations				
EL84/85	3	c.587C>A	p.Ser196Tyr	P[b]
	4	c.789G>A	p.Trp263X	M
EL106	3	c.580 delC, 582C>T (hom)	p.Leu194PhefsX60	P + M
EL125	3	c.442C>T (hom)	p.Pro148Ser	***P*** + M
EL726	2	c.275G>A	p.Arg92Gln	P
	3	p.631G>A	p.Asp211Asn	M
EL774	2	c.292C>T (hom)	p.Arg98Cys	–[c]
EL785	1	c.68T>A	p.Leu23His	de novo
		c.461_462 del	p.Ser154TyrfsX16	***P***[d]
	4	c.742G>T	p.Gly248X	***P***[d]
EL816	3	c.442C>T (hom)	p.Pro148Ser	P+M
EL889/890	2	c.292C>T (hom)	p.Arg98Cys	P+M
One Mutation				
EL128	2	c.265G>A	p.Gly89Ser	de novo
EL158	2	c.382G>A	p.Asp128Asn	***P***[e]
EL604	2	c.265G>A	p.Gly89Ser	***P***
EL611	2	c.274C>T	p.Arg92Trp	***M***
EL624/625	2	c.274C>T	p.Arg92Trp	***M***
EL683/684	2	c.265G>A	p.Gly89Ser	***P***
EL686	2	c.266G>A	p.Gly89Asp	***P***
EL700	2	c.274C>T	p.Arg92Trp	–
EL708	2	c.382G>A	p.Asp128Asn	–
EL743	2	c.274C>T	p.Arg92Trp	M
EL775	2	c.382G>A	p.Asp128Asn	P[d]
	5	c.862C>T	p.Arg288Cys	P[d]
EL847	2	c.404_406 del	p.Lys135 del	***P***
EL862	2	c.265G>A	p.Gly89Ser	***M***
EL882	2	c.265G>A	p.Gly89Ser	de novo
EL903	2	c.265G>A	p.Gly89Ser	***M***[e]
EL944	2	c.274C>T	p.Arg92Trp	de novo

[a] P, paternal; M, maternal; bold and italic indicates macrocephaly.
[b] Probably from father but no DNA available.
[c] No DNA of the parents available.
[d] Both changes from same parental allele.
[e] Transient macrocephaly.

Inheritance, Phenotypes, and Mutations

All ten patients with two *HEPACAM* mutations inherited in an autosomal-recessive fashion had the classical phenotype (Table S2). They had infantile-onset macrocephaly and delayed-onset motor deterioration, epilepsy, and cognitive decline of variable severity. The MRI showed typical white matter abnormalities in all stages of the disease (Figure S1). The parents were normal, but two of the 16 had macrocephaly (Table 1).

All 18 patients with one *HEPACAM* mutation had the improving phenotype (Table S3). They developed macrocephaly within the first year. In two of the 18, the head circumference subsequently normalized. The motor capabilities became normal or almost normal. Some patients had normal intelligence, and others, with intelligence quoficients (IQs) between 50 and 75, had a stable mental retardation. Three of the mentally retarded patients also had autism or pervasive developmental disorder not otherwise specified according to DSM IV criteria. In summary, 11 of the 18 patients became clinically normal, apart from macrocephaly. MRI initially showed typical abnormalities but, on follow up, major improvement or normalization (Figure S1). For 13 patients from 11 families, eight of the 11 parents with the mutated allele had macrocephaly, one had transient macrocephaly as a child, and two never had macrocephaly as far as they could remember. Regarding the five remaining patients, the *HEPACAM* mutation arose de novo in three, and their parents had normal head circumference; DNA of the parents was not available in two. Only one of the parents without the mutated allele had macrocephaly. The family data suggest autosomal-dominant inheritance for the single *HEPACAM* mutations with variable penetrance. An analysis of microsatellite markers near *HEPACAM* in the families with the two most common dominant mutations (p.Gly89Ser and p.Arg92Trp) revealed no shared haplotype, excluding the possibility of founder effects for these two mutations (data not shown).

The *HEPACAM* mutations were either recessive or dominant. The recessive mutations were spread over the extracellular region of GlialCAM, whereas the dominant mutations were clustered in one of the predicted immunoglobulin-like domains (Figure 2C). Molecular modeling of the extracellular domain of GlialCAM showed that dominant mutations are located in a putative interface of the first immunoglobulin domain (Figure 2D).

GlialCAM-MLC1 Interaction

Immunohistochemistry of human brain tissue demonstrated GlialCAM expression mainly around blood vessels (Figure 3 and Figure S3). Double immunostaining with a monoclonal antibody against GlialCAM and a polyclonal antibody against human MLC1[13] showed that MLC1 and GlialCAM colocalize at astrocytic end-feet (Figure 3A). Immunogold EM confirmed this colocalization in astrocyte-astrocyte junctions (Figure 3B).

GlialCAM mRNA and protein have been detected in oligodendrocytes, astrocytes,[18] and neurons[19] (Figure S3), whereas MLC1 has not been detected in oligodendrocytes.[5–7,20] In MLC, vacuolation mainly affects the outer layers of myelin sheaths.[2] We investigated whether GlialCAM is localized in myelin. EM immunogold revealed

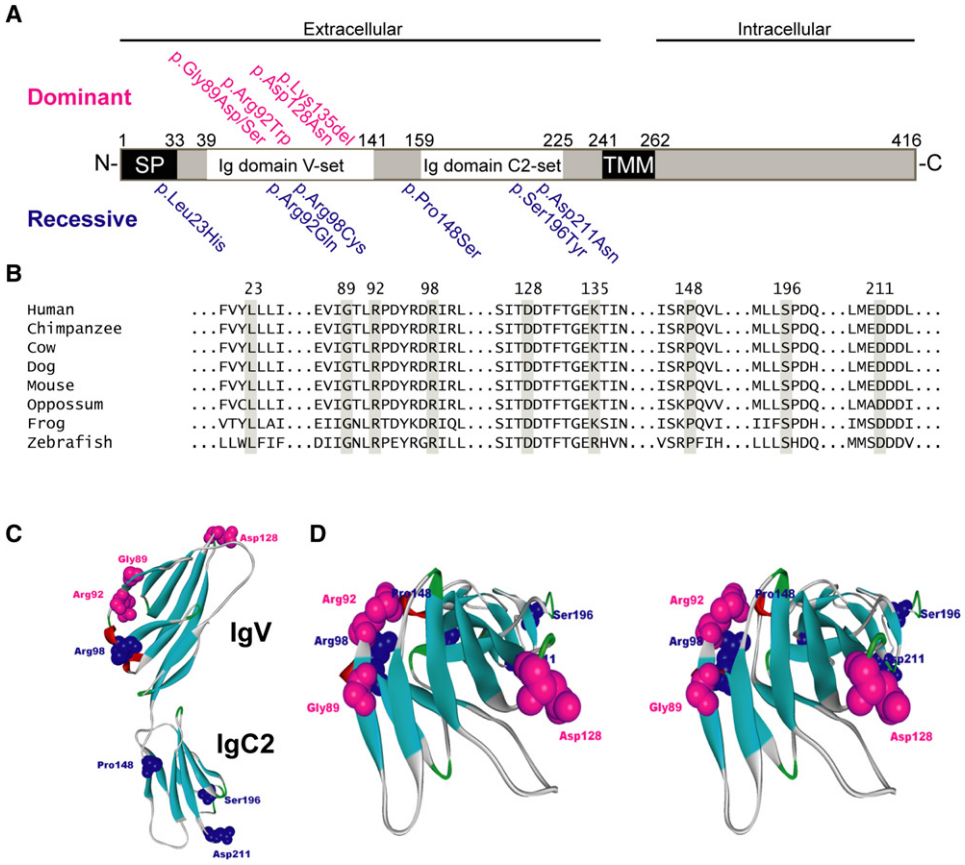

Figure 2. Genetic Studies in MLC Patients

(A) Schematic representation of domains in GlialCAM and position of missense mutations. The positions of several domains in human GlialCAM were predicted with PFAM, SOSUI, and SignalP 3.0. The following abbreviations are used: SP, signal peptide; TMM, transmembrane domain; Ig, Immunoglobulin. The missense mutations found in MLC patients are indicated above (dominant, in pink) and below (recessive, in blue) the figure.

(B) Conservation of affected amino acids. GlialCAM protein sequences were aligned with ClustalW software. The amino acids affected by missense mutations are indicated by a gray bar. The position of the affected residues in the human sequence is given above the sequences. NCBI accession numbers: *Homo sapiens*, NP_689935.2; Pan troglodytes, XP_522240.2; Bos taurus, NP_001026929.1; Canis familiaris, XP_852267.1; Mus musculus, NP_780398.2; Monodelphis domestica, XP_001371494.1; Danio rerio, NP_001018526.1. Ensembl protein ID: *Xenopus tropicalis*, ENSXETP00000008539.

(C) Schematic model of the protein GlialCAM. The structural model of the extracellular domain was accomplished with the automated homology-modeling server of the ExPASy server. Mutated residues are depicted with the same color-code as in (A).

(D) Stereo view of a ribbon representation viewed from the top of a structural model of the extracellular domain of GlialCAM. Pink highlights the residues mutated in dominant MLC, and blue highlights the residues in recessive MLC. Dominantly mutated residues are located in the putative extracellular-binding pocket, suggesting that it might mediate protein-ligand interactions.

particles inside axons, in contact regions between myelin and axons, and surrounding myelin (arrows in Figure 3C). In human medulla oblongata sections, where axons and myelin can be observed easily, immunostainings combining antibodies against GlialCAM with antibodies against neurofilament heavy chain (NF-H) or myelin basic protein (MBP) demonstrated that GlialCAM and NF-H staining coincide in axons (Figures 3D and 3E) and that not only is GlialCAM observed on the outside of myelin sheaths (inset in Figure 3E), but there is also a weak colocalization with MBP in myelin (Figure 3F). Classical biochemical fractionation protocols to purify myelin[14] and immunoblotting to detect specific proteins revealed GlialCAM but not MLC1 in the myelin fraction (Figure 3G).

The effect of mutations located in the extracellular domain of GlialCAM was studied in cultures of primary astrocytes, the cell type with the highest natural abundance of both MLC1 and GlialCAM. After adenoviral-mediated expression, lysates of astrocytes were analyzed by immunoblot and immunofluorescence. Expression levels of all types of mutant GlialCAM were not statistically different from wild-type GlialCAM (Figure S4). Immunofluorescence revealed that MLC1 and GlialCAM are located in cell-cell junctions between astrocytes (Figure 4A). Coexpression of wild-type MLC1 and GlialCAM containing the recessive mutations p.Arg92Gln or p.Arg98Cys resulted in diffuse intracellular MLC1 and GlialCAM localization with partial enrichment in cell membranes but not specifically in cell junctions (Figure 4B and Figure S5A). No defect

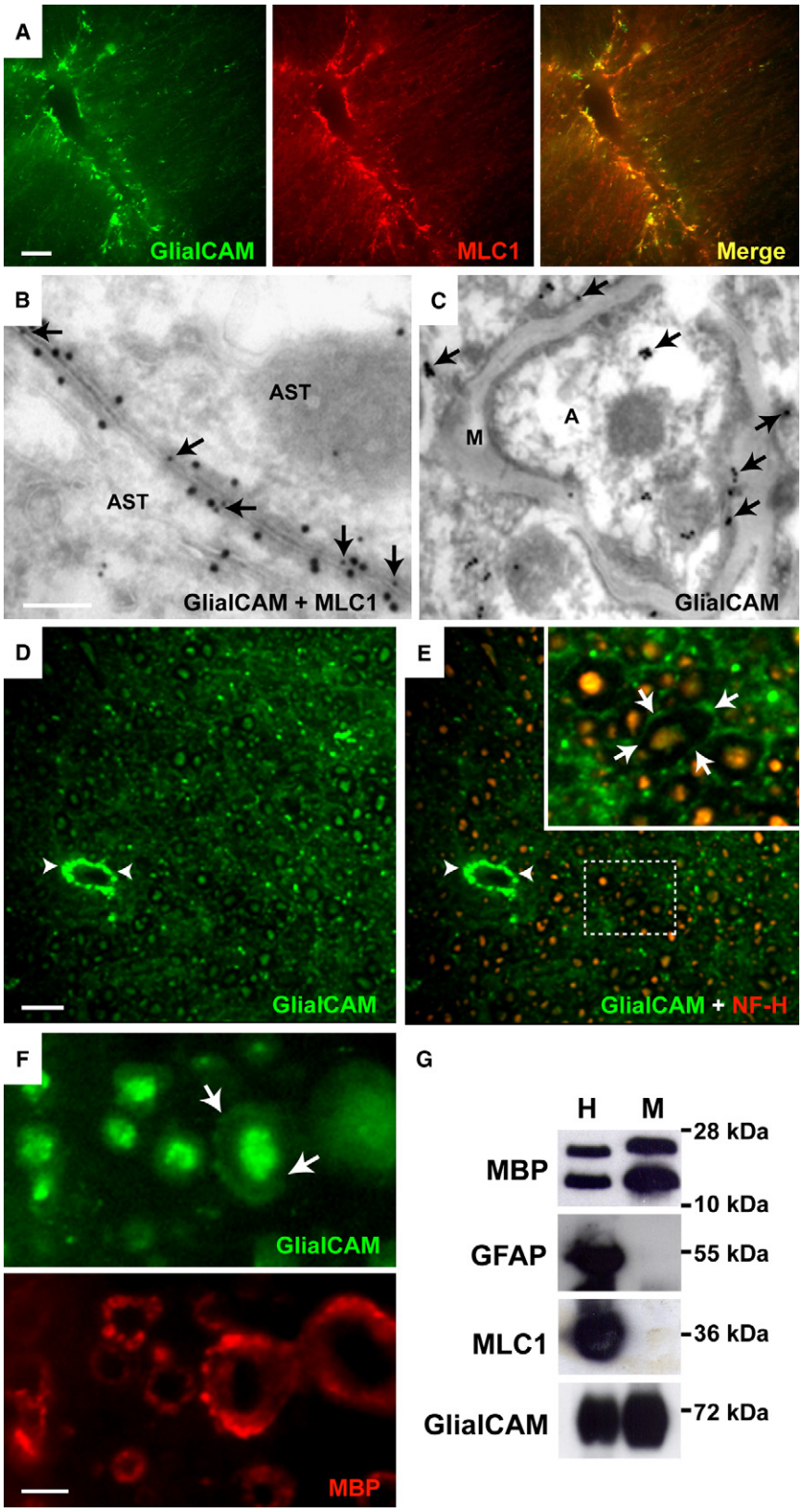

Figure 3. Colocalization of MLC1 and GlialCAM in Brain Tissue

(A) Double-immunolabeling experiments in human cerebellum, combining GlialCAM (in green) with MLC1 (in red), shows nearly complete colocalization (Merge, in yellow) in astrocytic processes surrounding a blood vessel.

(B) Double-immunolabeling EM shows colocalization of MLC1 (18 nm gold particles) and GlialCAM (with a commercially available monoclonal antibody; 12 nm gold particles, arrows) in astrocyte-astrocyte junctions in human tissue.

(C) Postembedding staining of GlialCAM in human cerebellum also shows immunoreactivity (arrows) inside axons, in contact regions between myelin and axons, and in cells that surround myelin.

(D–F) Localization of GlialCAM in human medulla oblongata. Using the polyclonal rabbit antibody, we detected GlialCAM in astrocytes surrounding blood vessels (arrowheads in D and E), in axons, and in myelin (arrows in inset in E and in F). Double immunolabeling of GlialCAM and NF-H, which stains axons, confirmed colocalization of GlialCAM and NF-H (yellow staining in E). The dashed line in E indicates the area amplified in the inset. Double immunolabeling of GlialCAM and MBP, which stains myelin, demonstrated a weak labeling of GlialCAM in myelin.

(G) Myelin was purified from brains of 6- to 8-month-old mice as described in the Material and Methods. Twenty microgram of the initial homogenate (H) and of myelin (M) were analyzed by SDS-PAGE and immunoblotting. Blots were probed with antibodies against MBP, GFAP, MLC1, and GlialCAM. The amount of GFAP detected in the myelin fraction was low as compared to the homogenate, indicating that the contamination of the myelin fraction with nonmyelin proteins was low. The following abbreviations are used: AST, astrocyte; MBP, myelin basic protein; GFAP, glial fibrillary acid protein; NF-H, neurofilament heavy chain; M, myelin; A, axon.

The scale bars indicate 50 μm (A and D), 500 nm (B and C), and 10 μm (F).

was found for the mutation p.Ser196Tyr (Figure S5C). Similar mislocalization of MLC1 and GlialCAM was observed after coexpression of wild-type MLC1 and GlialCAM containing the dominant mutations p.Arg92Trp and p.Gly89Asp (Figures 4D and Figure S5D).

To address the mode of inheritance of the mutations biochemically, we performed experiments with equal levels of wild-type GlialCAM and GlialCAM containing a dominant or recessive mutation together with MLC1. The localization of MLC1 and GlialCAM was analyzed by immunofluorescence. Coexpression of wild-type GlialCAM rescued the MLC1-trafficking defect caused

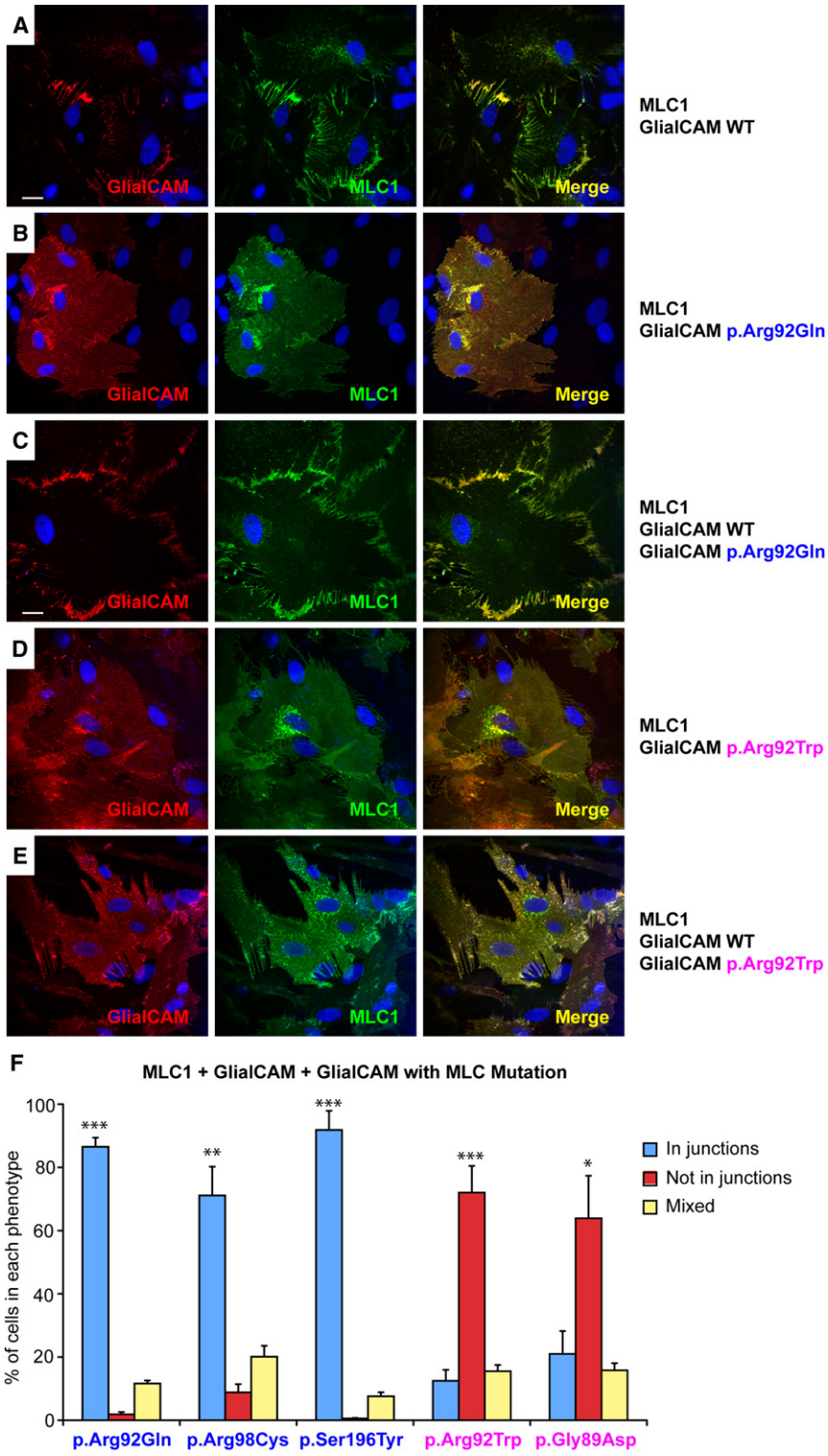

Figure 4. MLC1 and GlialCAM Subcellular Localization Changes Caused by Recessive and Dominant GlialCAM Mutations in Primary Cultures of Astrocytes

(A–F) Astrocytes were coinfected with adenoviruses expressing MLC1 and wild-type GlialCAM (A) or GlialCAM containing a recessive (B, p.Arg92Gln) or a dominant (D, p.Arg92Trp) MLC-related mutation at MOI 3. In (C) and (E), cells were coinfected with MLC1, wild-type GlialCAM, and GlialCAM containing the indicated mutation at a MOI ratio of 3:2:2. Cells were fixed, and permeabilized and then immunofluorescence was performed with a rabbit polyclonal antibody against human MLC1 (green) and a monoclonal antibody detecting GlialCAM protein (red). Nuclei were stained with DAPI (blue). Colocalization between the green and the red channel is shown in yellow. Images correspond to representative cells from four independent experiments. The scale bars represent 20 μm. (F) Random pictures from different experiments were taken. Quantification of the percentage of cells located in junctions (blue), not in junctions (red), or with a mixed phenotype (yellow, located partially in junctions and not in junctions) was performed manually. Data are mean ± standard error of the mean of four independent experiments. Bonferroni's multiple comparison test versus in junctions and not in junctions was used. *$p < 0,05$; **$p < 0,01$; ***$p < 0,001$. Representative images for the other mutations shown in the quantification are depicted in Figure S5.

by GlialCAM with recessive mutations (Figures 4C and 4F and Figure S5B) but did not rescue the trafficking defect caused by GlialCAM with dominant mutations (Figures 4E and 4F and Figure S5E). No difference in protein levels was observed between the mutants and the wild-type (Figure S4), making it unlikely that the trafficking defect is due to gene-dosage effects.

Discussion

The leukodystrophy MLC is characterized by infantile-onset macrocephaly and delayed neurological deterioration. The diagnosis is based on MRI criteria.[1] In 2001, causative mutations of MLC were identified in *MLC1*, accounting for approximately 75% of the patients. The fact that genetic-linkage studies failed to identify a second gene was ascribed to further genetic heterogeneity.[9,10] We recently identified two presumably autosomal recessive, phenotypes among MLC patients without *MLC1* mutations,[11] corroborating the notion of genetic heterogeneity. We now show that the genetic heterogeneity does not involve the gene but the mode of inheritance. We circumvented the problem of genetic heterogeneity by using a proteomic approach. This method is validated by the discovery of *HEPACAM* (hepatic and glial cell adhesion molecule, MIM 611642) as a gene disrupted in MLC and

can be considered in the future to identify disease genes for other rare or genetically heterogeneous disorders.

We prefer the name GlialCAM above HepaCAM for the related protein. Although the protein was first isolated from liver and called HepaCAM,[21] it was subsequently found to be predominantly expressed in the central nervous system and was renamed GlialCAM.[18] In the present paper, we show that mutations in *HEPACAM* lead to a neurological phenotype without any sign of liver involvement.

That mutations in one gene cause both autosomal-recessive and -dominant disease is rare but not unique. It has been described for a few other genes, including *LMNA* (MIM 150330), *SOX18* (MIM 601618), *ANK1* (MIM 612641), *COL6A1* (MIM 120220), *PMP22* (MIM 601097), and *MPZ* (MIM 159440).[22–27] However, patients with the dominant mutations in these genes do not display an improving phenotype, as seen in our MLC patients with dominant *HEPACAM* mutations. In MLC, the macrocephaly and cerebral white-matter disease on MRI arise in the first year of life, the period of most rapid myelin deposition in the brain. Apparently, MLC1 and GlialCAM exert their most important function during this process. The functions of both MLC1 and GlialCAM are unknown. We, therefore, do not understand the mechanism of the improving phenotype for the dominant *HEPACAM* mutations. A hypothetical gene-dose effect is not supported by the finding that normal GlialCAM does not partially rescue the localization of the GlialCAM-MLC1 complex in astrocytes expressing a dominant *HEPACAM* mutation. The dominant mutations are located in a putative pocket of the immunoglobulin domain and might disrupt interactions with GlialCAM itself and other unknown molecules.

GlialCAM acts as a MLC1 beta subunit needed for its correct trafficking to cell-cell junctions. Probably, *cis*- or *trans*-interactions mediated by GlialCAM are necessary for its correct localization. The function of GlialCAM as an adhesion molecule suggests that both GlialCAM and MLC1 have a role in the maintenance of correctly sealed cell-cell contacts. Interestingly, GlialCAM and not MLC1 is detected in myelin, the place where most vacuoles are found in MLC.[2] GlialCAM is not obligatorily associated with MLC1, indicating that it might have other functions by itself or in association with other molecules. Recently, it has been suggested that MLC1 interacts with the β1 subunit of the Na,K-ATPase pump.[28] We did not detect this protein in our affinity purifications. Further studies on MLC1-interacting proteins might provide better insights into the pathophysiology of MLC.

GlialCAM is an interesting protein. In 60% of the families with dominant *HEPACAM* mutations, the affected persons in fact display benign familial macrocephaly (MIM 153470). They have macrocephaly, but they are otherwise normal. MRI shows large but normal brains. The parents did not undergo MRI as children, and a transient leukoencephalopathy was not documented in any of them. Benign familial macrocephaly is most likely genetically heterogeneous, and *HEPACAM* is likely to be one of the related genes. Another interesting finding is that in 40% of the patients with a dominant *HEPACAM* mutation, macrocephaly, and mental retardation with or without autism, which are known to be associated features, persist.[29] This clinical syndrome is probably genetically heterogeneous, and specific *HEPACAM* mutations could cause it. The fact that single *HEPACAM* mutations might be associated with different phenotypes requires the geneticist to be cautious when counseling an affected family. From the age of approximately 2–3 years, the combination of clinical picture and MRI findings allows an accurate prediction of the phenotype.

In conclusion, we have found that *HEPACAM* is mutated in MLC. Recessive mutations cause a progressive leukodystrophy that is indistinguishable clinically and by MRI from the disease caused by recessive *MLC1* mutations. Dominant mutations can cause transient clinical and MRI features of MLC, benign familial macrocephaly, and the clinical syndrome of macrocephaly and mental retardation with or without autism.

Supplemental Data

Supplemental Data include five figures and three tables and can be found with this article online at http://www.cell.com/AJHG/.

Acknowledgments

Research in our laboratories was supported by Ministerio de Ciencia y Tecnología (SAF) 2009-07014 (R.E.), Fundación Ramon Areces project (R.E.), European Leukodystrophy Association Foundation 2007-017C4 project (R.E. and M.S.v.d.K.), PS09/02672-ERARE (R.E.), ERARE grant 11-330-1024 (G.C.S. and M.S.v.d.K.), 2009 Grups de Recerca de Catalunya 719 (R.E.), SAF 2009-12606-C02-02 (V.N.), CIBERER INTRA08/750 (R.E. and V.N.), and 2009 SGR01490 (V.N.). M.S.v.d.K., G.C.S., and M.C.R. are supported by the Dutch Organization for Scientific Research ZonMw (TOP Grant 9120.6002), the Hersenstichting (Grants 13F05.04, 15F07.30 and 2009[2]-14), and the Optimix Foundation for Scientific Research. R.E. is a recipient of an ICREA Academia prize. We thank all colleagues who contributed MRI, clinical information, and blood samples. We thank Alejandro Barrallo, Michael Pusch, and Jim M. Powers for critical review of the manuscript.

Received: December 7, 2010
Revised: January 12, 2011
Accepted: February 21, 2011
Published online: March 17, 2011

Web Resources

The URLs for data presented herein are as follows:

ExonPrimer, http://ihg.gsf.de/ihg/ExonPrimer.html
Online Mendelian Inheritance in Man, http://www.ncbi.nlm.nih.gov/Omim/
SIFT, http://sift.jcvi.org/

Signal P, http://www.cbs.dtu.dk/services/SignalP/
Swissmodel, http://swissmodel.expasy.org/

References

1. van der Knaap, M.S., Barth, P.G., Stroink, H., van Nieuwenhuizen, O., Arts, W.F., Hoogenraad, F., and Valk, J. (1995). Leukoencephalopathy with swelling and a discrepantly mild clinical course in eight children. Ann. Neurol. *37*, 324–334.
2. van der Knaap, M.S., Barth, P.G., Vrensen, G.F., and Valk, J. (1996). Histopathology of an infantile-onset spongiform leukoencephalopathy with a discrepantly mild clinical course. Acta Neuropathol. *92*, 206–212.
3. Leegwater, P.A., Yuan, B.Q., van der Steen, J., Mulders, J., Könst, A.A., Boor, P.K., Mejaski-Bosnjak, V., van der Maarel, S.M., Frants, R.R., Oudejans, C.B., et al. (2001). Mutations of MLC1 (KIAA0027), encoding a putative membrane protein, cause megalencephalic leukoencephalopathy with subcortical cysts. Am. J. Hum. Genet. *68*, 831–838.
4. Ilja Boor, P.K., de Groot, K., Mejaski-Bosnjak, V., Brenner, C., van der Knaap, M.S., Scheper, G.C., and Pronk, J.C. (2006). Megalencephalic leukoencephalopathy with subcortical cysts: An update and extended mutation analysis of MLC1. Hum. Mutat. *27*, 505–512.
5. Teijido, O., Martínez, A., Pusch, M., Zorzano, A., Soriano, E., Del Río, J.A., Palacín, M., and Estévez, R. (2004). Localization and functional analyses of the MLC1 protein involved in megalencephalic leukoencephalopathy with subcortical cysts. Hum. Mol. Genet. *13*, 2581–2594.
6. Boor, P.K.I., de Groot, K., Waisfisz, Q., Kamphorst, W., Oudejans, C.B., Powers, J.M., Pronk, J.C., Scheper, G.C., and van der Knaap, M.S. (2005). MLC1: A novel protein in distal astroglial processes. J. Neuropathol. Exp. Neurol. *64*, 412–419.
7. Teijido, O., Casaroli-Marano, R., Kharkovets, T., Aguado, F., Zorzano, A., Palacín, M., Soriano, E., Martínez, A., and Estévez, R. (2007). Expression patterns of MLC1 protein in the central and peripheral nervous systems. Neurobiol. Dis. *26*, 532–545.
8. Kaganovich, M., Peretz, A., Ritsner, M., Bening Abu-Shach, U., Attali, B., and Navon, R. (2004). Is the WKL1 gene associated with schizophrenia? Am. J. Med. Genet. B. Neuropsychiatr. Genet. *125B*, 31–37.
9. Blattner, R., Von Moers, A., Leegwater, P.A., Hanefeld, F.A., Van Der Knaap, M.S., and Köhler, W. (2003). Clinical and genetic heterogeneity in megalencephalic leukoencephalopathy with subcortical cysts (MLC). Neuropediatrics *34*, 215–218.
10. Patrono, C., Di Giacinto, G., Eymard-Pierre, E., Santorelli, F.M., Rodriguez, D., De Stefano, N., Federico, A., Gatti, R., Benigno, V., Megarbané, A., et al. (2003). Genetic heterogeneity of megalencephalic leukoencephalopathy and subcortical cysts. Neurology *61*, 534–537.
11. van der Knaap, M.S., Lai, V., Köhler, W., Salih, M.A., Fonseca, M.J., Benke, T.A., Wilson, C., Jayakar, P., Aine, M.R., Dom, L., et al. (2010). Megalencephalic leukoencephalopathy with cysts without MLC1 defect. Ann. Neurol. *67*, 834–837.
12. Zolles, G., Wenzel, D., Bildl, W., Schulte, U., Hofmann, A., Müller, C.S., Thumfart, J.O., Vlachos, A., Deller, T., Pfeifer, A., et al. (2009). Association with the auxiliary subunit PEX5R/Trip8b controls responsiveness of HCN channels to cAMP and adrenergic stimulation. Neuron *62*, 814–825.
13. Duarri, A., Teijido, O., López-Hernández, T., Scheper, G.C., Barriere, H., Boor, I., Aguado, F., Zorzano, A., Palacín, M., Martínez, A., et al. (2008). Molecular pathogenesis of megalencephalic leukoencephalopathy with subcortical cysts: Mutations in MLC1 cause folding defects. Hum. Mol. Genet. *17*, 3728–3739.
14. Norton, W.T., and Poduslo, S.E. (1973). Myelination in rat brain: Method of myelin isolation. J. Neurochem. *21*, 749–757.
15. Pandey, A., Andersen, J.S., and Mann, M. (2000). Use of mass spectrometry to study signaling pathways. Sci. STKE *2000*, pl1.
16. Schwenk, J., Metz, M., Zolles, G., Turecek, R., Fritzius, T., Bildl, W., Tarusawa, E., Kulik, A., Unger, A., Ivankova, K., et al. (2010). Native GABA(B) receptors are heteromultimers with a family of auxiliary subunits. Nature *465*, 231–235.
17. McCarthy, K.D., and de Vellis, J. (1980). Preparation of separate astroglial and oligodendroglial cell cultures from rat cerebral tissue. J. Cell Biol. *85*, 890–902.
18. Favre-Kontula, L., Rolland, A., Bernasconi, L., Karmirantzou, M., Power, C., Antonsson, B., and Boschert, U. (2008). GlialCAM, an immunoglobulin-like cell adhesion molecule is expressed in glial cells of the central nervous system. Glia *56*, 633–645.
19. Spiegel, I., Adamsky, K., Eisenbach, M., Eshed, Y., Spiegel, A., Mirsky, R., Scherer, S.S., and Peles, E. (2006). Identification of novel cell-adhesion molecules in peripheral nerves using a signal-sequence trap. Neuron Glia Biol. *2*, 27–38.
20. Schmitt, A., Gofferje, V., Weber, M., Meyer, J., Mössner, R., and Lesch, K.P. (2003). The brain-specific protein MLC1 implicated in megalencephalic leukoencephalopathy with subcortical cysts is expressed in glial cells in the murine brain. Glia *44*, 283–295.
21. Chung Moh, M., Hoon Lee, L., and Shen, S. (2005). Cloning and characterization of hepaCAM, a novel Ig-like cell adhesion molecule suppressed in human hepatocellular carcinoma. J. Hepatol. *42*, 833–841.
22. Raffaele Di Barletta, M., Ricci, E., Galluzzi, G., Tonali, P., Mora, M., Morandi, L., Romorini, A., Voit, T., Orstavik, K.H., Merlini, L., et al. (2000). Different mutations in the LMNA gene cause autosomal dominant and autosomal recessive Emery-Dreifuss muscular dystrophy. Am. J. Hum. Genet. *66*, 1407–1412.
23. Irrthum, A., Devriendt, K., Chitayat, D., Matthijs, G., Glade, C., Steijlen, P.M., Fryns, J.P., Van Steensel, M.A., and Vikkula, M. (2003). Mutations in the transcription factor gene SOX18 underlie recessive and dominant forms of hypotrichosis-lymphedema-telangiectasia. Am. J. Hum. Genet. *72*, 1470–1478.
24. Eber, S.W., Gonzalez, J.M., Lux, M.L., Scarpa, A.L., Tse, W.T., Dornwell, M., Herbers, J., Kugler, W., Ozcan, R., Pekrun, A., et al. (1996). Ankyrin-1 mutations are a major cause of dominant and recessive hereditary spherocytosis. Nat. Genet. *13*, 214–218.
25. Lampe, A.K., and Bushby, K.M. (2005). Collagen VI related muscle disorders. J. Med. Genet. *42*, 673–685.
26. Roa, B.B., Garcia, C.A., Pentao, L., Killian, J.M., Trask, B.J., Suter, U., Snipes, G.J., Ortiz-Lopez, R., Shooter, E.M., Patel, P.I., and Lupski, J.R. (1993). Evidence for a recessive PMP22 point mutation in Charcot-Marie-Tooth disease type 1A. Nat. Genet. *5*, 189–194.
27. Nicolaou, P., Zamba-Papanicolaou, E., Koutsou, P., Kleopa, K.A., Georghiou, A., Hadjigeorgiou, G., Papadimitriou, A.,

Kyriakides, T., and Christodoulou, K. (2010). Charcot-Marie-Tooth disease in Cyprus: Epidemiological, clinical and genetic characteristics. Neuroepidemiology *35*, 171–177.

28. Brignone, M.S., Lanciotti, A., Macioce, P., Macchia, G., Gaetani, M., Aloisi, F., Petrucci, T.C., and Ambrosini, E. (2011). The beta1 subunit of the Na,K-ATPase pump interacts with megalencephalic leucoencephalopathy with subcortical cysts protein 1 (MLC1) in brain astrocytes: New insights into MLC pathogenesis. Hum. Mol. Genet. *20*, 90–103.
29. White, S., O'Reilly, H., and Frith, U. (2009). Big heads, small details and autism. Neuropsychologia *47*, 1274–1281.

Molecular mechanisms of MLC1 and GLIALCAM mutations in Megalencephalic Leukoencephalopathy with subcortical cysts

(Human Molecular Genetics, 2011)

Contribució:

- Construcció de la mutació de MLC1 S69L
- Estudis bioquímics *in vitro* de la mutació de MLC1 S69L (Figura 2)
- Anàlisis de MLC1 i GlialCAM en el teixit de la pacient (Figura 3)

HMG Advance Access published June 7, 2011

Human Molecular Genetics, 2011 **1–12**
doi:10.1093/hmg/ddr238

Molecular mechanisms of *MLC1* and *GLIALCAM* mutations in megalencephalic leukoencephalopathy with subcortical cysts

Tania López-Hernández[1,†], Sònia Sirisi[1,5,†], Xavier Capdevila-Nortes[1], Marisol Montolio[1,6], Victor Fernández-Dueñas[3], Gert C. Scheper[8], Marjo S. van der Knaap[8], Pilar Casquero[9], Francisco Ciruela[3], Isidre Ferrer[4,10], Virginia Nunes[2,5,7] and Raúl Estévez[1,6,*]

[1]Sección de Fisiología, [2]Sección de Genética, Departamento de Ciencias Fisiologicas II, [3]Unitat de Farmacologia, Departament Patologia i Terapèutica Experimental, Facultat de Medicina and [4]Institut Neuropatologia, Servei Anatomia Patològica, Idibell-Hospital Universitari de Bellvitge, Hospitalet de LLobregat, Universitat de Barcelona, Barcelona, Spain, [5]Laboratorio de Genética Molecular-IDIBELL, Centro de Investigación en Red de Enfermedades rara (CIBERER), Barcelona, Spain, [6]U-750 and [7]U-730: ISCIII, Valencia, Spain, [8]Department of Child Neurology, VU University Medical Center, Amsterdam, The Netherlands, [9]Sección de Neurología, Hospital Mateu Orfila, Maó, Menorca, Spain and [10]CIBERNED (Centro de Investigación Biomédica en Red de Enfermedades Neurodegenerativas), ISCIII, Barcelona, Spain

Received April 12, 2011; Revised and Accepted May 22, 2011

Megalencephalic leukoencephalopathy with subcortical cysts (MLC) is a rare leukodystrophy caused by mutations in *MLC1* or *GLIALCAM*. The *GLIALCAM* gene product functions as an MLC1 beta-subunit. We aim to further clarify the molecular mechanisms of MLC caused by mutations in *MLC1* or *GLIALCAM*. For this purpose, we analyzed a human post-mortem brain obtained from an MLC patient, who was homozygous for a missense mutation (S69L) in *MLC1*. We showed that this mutation affects the stability of MLC1 *in vitro* and reduces MLC1 protein levels in the brain to almost undetectable. However, the amount of GlialCAM and its localization were nearly unaffected, indicating that MLC1 is not necessary for GlialCAM expression or targeting. These findings were supported by experiments in primary astrocytes and in heterologous cells. In addition, we demonstrated that MLC1 and GlialCAM form homo- and hetero-complexes and that MLC-causing mutations in *GLIALCAM* mainly reduce the formation of GlialCAM homo-complexes, leading to a defect in the trafficking of GlialCAM alone to cell junctions. *GLIALCAM* mutations also affect the trafficking of its associated molecule MLC1, explaining why *GLIALCAM* and *MLC1* mutations lead to the same disease: MLC.

INTRODUCTION

Megalencephalic leukoencephalopathy with subcortical cysts (MLC, OMIM 604004) is a rare type of leukodystrophy (1), characterized by macrocephaly which appears during the first year of life. After several years, slow neurological deterioration with cerebellar ataxia and spasticity occurs. MRI reveals diffuse signal abnormality and swelling of the cerebral white matter and the presence of subcortical cysts, mainly in the anterior temporal regions. Initial studies of a brain biopsy from an MLC patient showed that myelin is vacuolated (2). The first disease gene, named *MLC1*, was identified in 2001 (3). Mutations in *MLC1* have been identified in ~75% of the MLC patients (4).

MLC1 is an oligomeric membrane protein that is expressed mainly in the brain and in white blood cells (WBCs) (3,5). Within the brain, MLC1 is predominantly located in astrocyte–astrocyte junctions close to blood– and CSF–

*To whom correspondence should be addressed at: Faculty of Medicine, Department of Physiological Sciences II, Campus de Bellvitge, Pavelló de Govern, C/Feixa Llarga s/n. 08907, L'Hospitalet de Llobregat, Barcelona, Spain. Tel: +34 934039781; Fax: +34 934024268; Email: restevez@ub.edu
†The authors wish it to be known that, in their opinion, the first two authors should be regarded as joint First Authors.

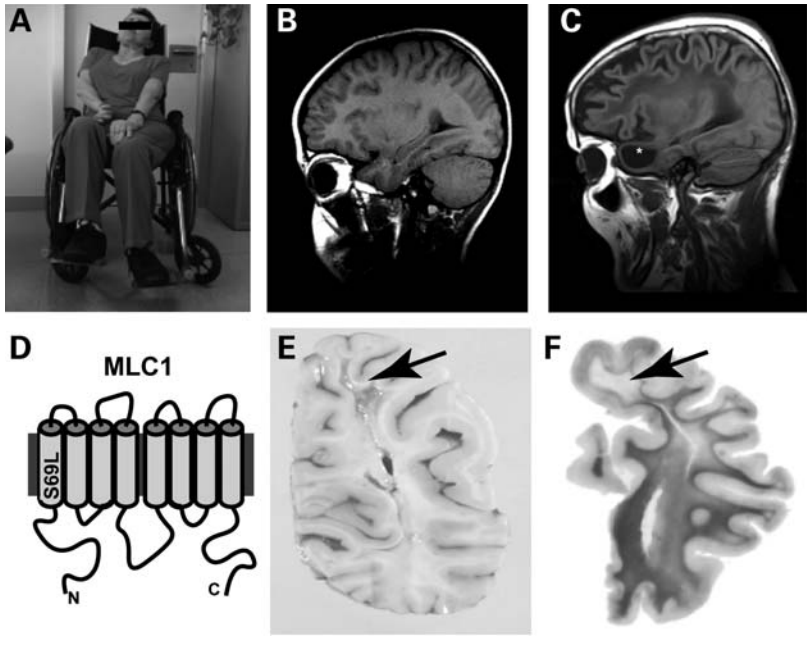

Figure 1. Characterization of an MLC patient. (**A**) Picture of the MLC-affected patient studied, which showed macrocephaly, motor clumsiness and ataxia. (**B** and **C**) Sagittal T1-weighted images of a control subject (B) and of the patient (C) showing subcortical cysts on frontal and temporal regions (asterisk) (**D**) A predicted 2D model of the MLC1 protein, showing the localization of the mutation (S69L) identified in this patient. (**E**) Gross coronal sections of the brain showing atrophy of the cerebral white matter with cavitation of the centrum semiovale and preservation of the cortico-cortical U-fibers, corpus callosum, anterior commissure, fornix and optic nerves. (**F**) Klüver–Barrera stain showed demyelination of the central white matter of the brain with preservation of the cortico-cortical U-fibers. Arrow points to an area with lack of myelin.

brain barriers, Bergmann glia and main axonal tracts (6–8). Knockdown of MLC1 in astrocyte cultures causes vacuolation (9). In a similar manner, re-examination of the brain biopsy from an MLC patient (2) revealed that vacuoles are also consistently present in astrocytic endfeet (9). A role of MLC1 in volume regulation of astrocytes has been suggested based on changes in its localization in hypo-osmotic conditions (10). However, functional data indicating the role of MLC1 are lacking.

Genetic information suggested that at least one other gene is involved in MLC (11,12), but genetic linkage studies and studies of candidate genes were negative (13). Recently, two different phenotypes were described among MLC patients without *MLC1* mutations: a classical phenotype which retains the typical clinical and MRI features, as seen in patients with *MLC1* mutations, and an improving phenotype which shows transient MLC features and lacks clinical deterioration (14).

Quantitative proteomic analysis of affinity-purified MLC1 revealed that GlialCAM (15) interacts directly with MLC1. GlialCAM is an Ig-like protein of unknown function (15,16). It was shown that *GLIALCAM*, also called *HEPACAM*, is the second MLC gene (17). Interestingly, MLC-causing *GLIALCAM* mutations are inherited in a recessive manner in patients with the classical phenotype, and in a dominant manner in patients with the improving phenotype (17).

Missense mutations in *MLC1* reduce MLC1 protein expression *in vitro* (5,18,19) and *in vivo*, as shown in WBCs (19), although no data are available from brain tissue of MLC patients with missense mutations. Studies in primary astrocytes indicate that most *GLIALCAM* mutations disrupt the normal localization of MLC1 and GlialCAM in astrocyte–astrocyte junctions (17), suggesting that their localization is crucial for physiological function.

In the present work, we present a more detailed characterization of the effect of mutations found in *MLC1* and *GLIALCAM*. The availability of a brain obtained at autopsy from an MLC patient homozygous for an *MLC1* missense mutation greatly facilitated our studies.

RESULTS

Studies on brain samples of an MLC patient

The patient studied was a female who developed a macrocephaly within the first few months of life and after several years experienced a slow motor deterioration, epilepsy and cognitive decline (Fig. 1A). MRI imaging at the age of 40 years [control (Fig. 1B) versus patient (Fig. 1C)] showed diffuse signal abnormalities in the cerebral white matter, with global atrophy and presence of subcortical cysts in the anterior temporal region, indicative of MLC. Analysis of the *MLC1* gene showed that the patient is homozygous for the mutation c.206C>T. The mutation leads to an amino acid change (S69L) in the predicted first transmembrane domain (Fig. 1D). DNA of the parents was not available to confirm that they both carry the same mutation. The amino acid change affects a residue that is highly conserved among different species. It has not been observed in 400 control chromosomes and it was detected in other patients with MLC (4), indicating that the mutation is most likely pathogenic. The patient died at the age of 57 years following a

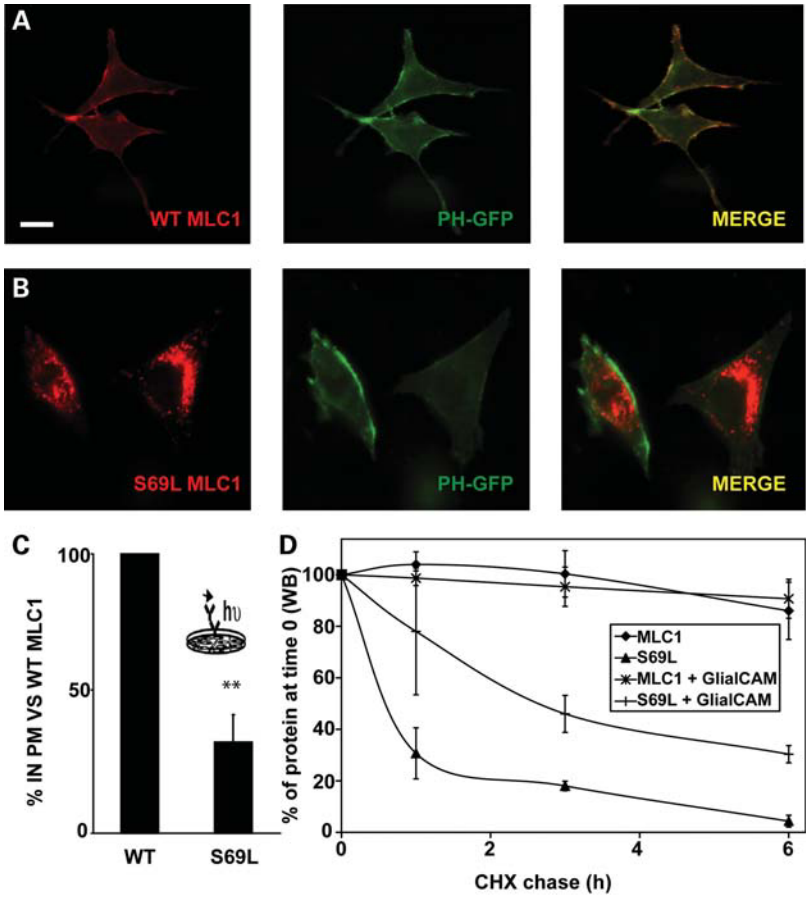

Figure 2. *In vitro* studies of the defective protein S69L MLC1 with or without GlialCAM. (**A** and **B**) HeLa cells were co-transfected with PH-GFP, as a marker of plasma membrane, together with wild-type MLC1 (A) or the S69L-defective protein (B) containing two HA epitope tags. Two days after the transfection, cells were fixed and permeabilized, and immunofluorescence was performed using 3F10 (against the HA epitope tags) as a primary antibody. The bar line corresponds to 20 μm. (**C**) HeLa cells were transfected with wild-type MLC1 or the S69L-defective protein with HA tags. Plasma membrane levels were measured using a luminescence-based method, as described in Materials and Methods. Data correspond to the average of three experiments, expressed as a percentage of the wild-type MLC1 protein. $^{**}P < 0.01$. The inset shows an overview of the method. (**D**) Twenty-four hours after transfection, cells were incubated with the protein synthesis inhibitor CHX (100 μg/ml) for the times indicated (0, 1, 3 and 6 h). Cells were harvested, solubilized and processed by western blot against human MLC1. The signal was quantified using the Multigauge software (Fujifilm), and the values were normalized to the value at time 0 for each of the groups (wild-type MLC1, wild-type MLC1+GlialCAM, S69L, S69L+GlialCAM). The result corresponds to the average of three independent experiments. Values depicted are mean ± SEM.

cranial trauma. With the consent of the family, brain autopsy was performed.

Gross examination of the brain revealed reduced cerebral white matter with cavitation in the frontal and parietal lobes (Fig. 1E). Subcortical U-fibers, internal capsule, corpus callosum, anterior commissure and optic nerves and tracts were better preserved. The cerebellar peduncles and cerebellar white matter appeared normal. Myelin stains confirmed the predominant involvement of the deep cerebral white matter with better preservation of the other white matter structures (Fig. 1F).

Microscopic examination (Supplementary Material, Fig. S1) revealed preservation of the cerebral cortex and alterations limited to the white matter. These alterations consisted of lack of myelin of the deep white matter with cavitation in the most affected areas, reduction in the number of astrocytes and oligodendrocytes and accompanying loss of axons. Many astrocytes in the white matter lacking myelin and in the vicinity of cavities contained αB-crystallin, a stress protein. Rosenthal fibers were absent. Large numbers of corpora amylacea were found in the damaged white matter. Small and focal perivascular lymphocytes and macrophages were indicative of white matter damage (Supplementary Material, Fig. S1). We conclude that the degeneration and the infiltration of immune system cells observed in the MLC brain from the patient are mild.

In vitro studies of the mutation identified in the patient

We introduced the mutation S69L in human MLC1 containing two HA epitope tags, as already described (5). The first tag at the N-terminus allows detection by western blot and the second tag, which is located in an extracellular loop, allows detection of surface-expressed protein. Localization was assayed in HeLa cells after co-transfection with the GFP-tagged pleckstrin homology (PH) domain of the phospholipase C δ1 (PH-GFP), a fluorescent protein probe that specifically labels the plasma membrane. Wild-type MLC1 was mainly detected at the plasma membrane (Fig. 2A), co-localizing with

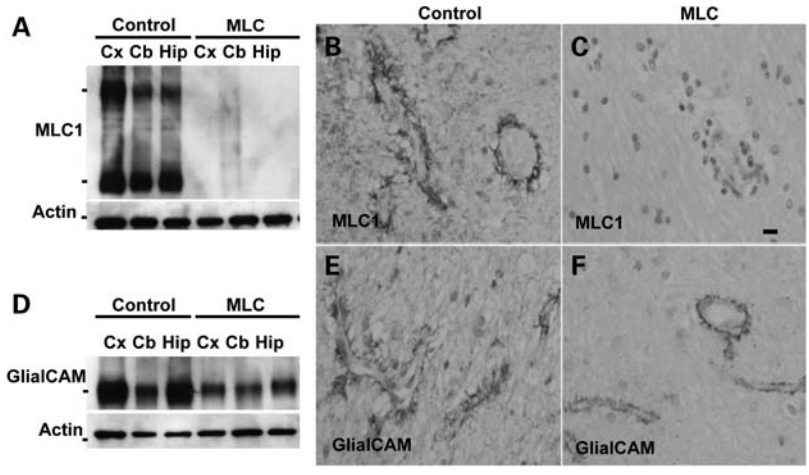

Figure 3. MLC1 and GlialCAM expression in brain tissue. (**A**) MLC1 expression is detected in solubilized extracts from the control brain, but it is nearly undetectable in extracts from the MLC patient. Actin was used as a loading control. Cx, cortex; Cb, cerebellum; Hip, hippocampus. The positions of the MLC1 monomer and dimer (36 and 72 kDa) and actin (53 kDa) are indicated on the left. (**B** and **C**) MLC1 immunoreactivity is found in astrocytic processes surrounding blood vessels in the normal brain. No MLC1 immunoreactivity is found in the brain from the MLC patient. (**D**) GlialCAM expression is detected in solubilized extracts from the control brain and from the MLC patient. Actin was used as a loading control. Cx, cortex; Cb, cerebellum; Hip, hippocampus. The positions of GlialCAM (72 kDa) and actin (53 kDa) are indicated on the left. (**E**) GlialCAM immunoreactivity is found in astrocytic processes surrounding blood vessels in control and MLC (**F**) brains. Paraffin sections were slightly counterstained with hematoxylin to stain nuclei. Magnification: ×200. Scale bar: 40 μm.

PH-GFP. In contrast, the S69L-MLC1-defective protein was almost exclusively detected in intracellular compartments (Fig. 2B). Surface expression levels of the defective protein were quantified using a luminescence-based method, which indicated that the defective protein had a reduced surface expression (Fig. 2C). In other MLC1 proteins containing MLC-causing mutations, it was shown that increased endoplasmatic reticulum-associated degradation (ERAD) and endo-lysosomal-associated degradation (ELAD) contributed to the cell surface expression defect (19).

In these MLC1 pathogenic variants, reduced surface expression was a consequence of reduced stability (19). We therefore studied the protein stability of this variant in comparison with the wild-type protein, by measuring the remaining protein after incubation with the protein synthesis inhibitor cycloheximide (CHX) (Fig. 2D). Similarly, a reduced stability was detected for the defective S69L MLC1 protein. We also tested whether the stability of the wild-type and the defective protein S69L-MLC1 was altered by the co-expression of GlialCAM (Fig. 2D). The results showed that the S69L protein was stabilized by the presence of the GlialCAM molecule, but the defective protein still remained less stable than the wild-type (Fig. 2D).

Expression studies of MLC1 and GlialCAM in the patient brain

With brain tissue from the MLC patient, we validated the *in vitro* results in native tissue. No apparent MLC1 protein signal was detected by western blot in cell lysates from different brain regions from the patient, whereas MLC1 was clearly detected in a control case (Fig. 3A). In the control brain, MLC1 immunoreactivity was found in astrocytic processes surrounding blood vessels (Fig. 3B). In contrast, no MLC1 immunostaining was detected in the brain from the MLC patient (Fig. 3C).

Similar experiments were performed for GlialCAM (17). Western blot experiments detected expression in the MLC patient (Fig. 3D). Quantification of GlialCAM levels in three independent experiments revealed a 40% decrease versus the control brain. However, it cannot be concluded that its expression was changed compared with the control case, as the post-mortem time differs. Immunohistochemistry detected GlialCAM in astrocytic processes surrounding blood vessels, and subventricular and subpial astrocytes in the control case [Fig. 3E and (17)] and in the brain of the MLC patient.

Expression of GlialCAM in primary astrocytes depleted of MLC1 by RNA interference

We investigated the expression and localization of GlialCAM in primary cultures of astrocytes, which have been depleted of MLC1 by RNA interference (Fig. 4). Although knockdown of MLC1 was nearly complete, as confirmed by western blot, no changes in endogenous GlialCAM protein expression was found compared with control scrambled-shRNA (SCR)-infected astrocytes (Fig. 4A). GlialCAM was detected in astrocyte–astrocyte processes in both SCR-transduced (Fig. 4B) and MLC1-depleted astrocytes (shRNA 905) (Fig. 4C). Infection with adenovirus-expressing GlialCAM-flag in MLC1-depleted astrocytes also resulted in GlialCAM localization in astrocyte processes (data not shown). Overall, this result, together with the localization studies in the patient, suggests that the GlialCAM subcellular localization is independent of MLC1 expression.

In vitro characterization of GlialCAM–MLC1 interaction

To further increase our understanding of the relationship between MLC1 and GlialCAM, several studies were done expressing both proteins in heterologous systems. Split-TEV (tobacco etch virus protease) interaction assays (20)

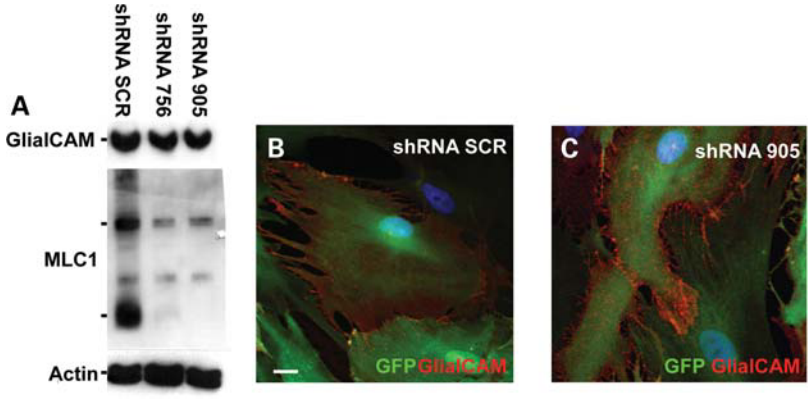

Figure 4. Expression and localization of GlialCAM in primary astrocytes depleted of MLC1 by RNA interference. (**A**) Seven days after shRNA (SCR: Scrambled or 756 and 905: against MLC1) adenovector-mediated expression, cell extracts were analyzed in western blot studies using antibodies against GlialCAM and MLC1. Actin was used as a loading control. The result is a representative experiment of three independent experiments. The positions of the MLC1 monomer and dimer (36 and 72 kDa), GlialCAM (72 kDa) and actin (53 kDa) are indicated on the left. (**B** and **C**) At the same time after transduction, astrocytes were fixed and processed for immunofluorescence using antibodies against GlialCAM. Transduced cells were visualized by the positive GFP signal. Scale bar: 20 μm.

demonstrated that MLC1 homo-oligomerizes, but also hetero-oligomerizes, with GlialCAM (Fig. 5A). As controls, no interaction was detected with the unrelated proteins 4F2hc [a single transmembrane protein as GlialCAM (21)] and with the adenosine A_{2A} receptor [$A_{2A}R$, a polytopic membrane protein as MLC1 (22)]. In the reverse experiment, GlialCAM homo-oligomerizes, as described earlier (23), and hetero-oligomerizes with MLC1, but does not interact with the control unrelated proteins 4F2hc and $A_{2A}R$ (Fig. 5A).

Additionally, we assessed the formation of MLC1 and GlialCAM hetero-complexes by means of fluorescence resonance energy transfer (FRET) experiments. HEK-293T cells were transiently transfected with MLC1 and GlialCAM tagged with a FlAsH epitope and cyan fluorescent protein (CFP), respectively ($MLC1^{FlAsH}$ and $GlialCAM^{CFP}$). The $GlialCAM^{CFP}/MLC1^{FlAsH}$ hetero-oligomer formation caused FRET between the fluorescent proteins (Fig. 5B, left panel). Significant FRET was not observed in cells expressing only $glialCAM^{CFP}$ or co-expressing $glialCAM^{CFP}$ with the negative controls YFP and $A_{2A}R^{YFP}$ (Fig. 5B, right panel). Thus, both methods (split-TEV and FRET), together with previously reported co-immunoprecipitation experiments (17), indicate that GlialCAM and MLC1 interact directly, although every method has different sensitivity.

Next, we addressed whether GlialCAM expression modified the surface levels of the MLC1 protein. Using a luminescence-based assay, the levels of MLC1 at the plasma membrane were investigated in transfected cells expressing MLC1 with an extracellular HA epitope, in the presence or absence of GlialCAM. These studies revealed that expression of GlialCAM did not modify MLC1 surface levels (Fig. 5C).

Both MLC1 and GlialCAM were reported to be located in tissue in astrocyte–astrocyte junctions (6,17). In HeLa cells, MLC1 was detected at the plasma membrane [Fig. 5D and (5)], but not particularly enriched in cell junctions, as illustrated by the intensity profile of the associated fluorescence (Fig. 5D, inset). In contrast, GlialCAM expressed alone was clearly detected in most cells in junctions (Fig. 5E, inset), as reported previously (16,23). Interestingly, after co-expression of MLC1 with GlialCAM, both molecules were clearly enriched at cell junctions (Fig. 5F and G). Quantification of intensity profile calculations revealed that both GlialCAM and MLC1 are enriched at cell junctions in the presence of the other, but GlialCAM does not need MLC1 to be located in cell junctions (Fig. 5).

GlialCAM-defective proteins showed a reduced tendency to homo-oligomerize

Next, we aimed to analyze the molecular consequences of MLC-causing *GLIALCAM* mutations in its oligomerization abilities. Using the split-TEV interaction assay, it was shown that all defective proteins except S196Y had a lower tendency to homo-oligomerize than with the wild-type protein (Fig. 6A).

We subsequently studied whether GlialCAM-defective proteins affected the direct protein–protein interaction with MLC1 (Fig. 6B). Although the recessive pathogenic variants R92Q and R98C showed a reduction in their ability to hetero-oligomerize, the proteins containing the recessive mutation S196Y or the dominant mutations R92W and G89D still retained the capacity to oligomerize with MLC1 at similar levels as the wild-type protein.

GlialCAM-defective proteins show a trafficking defect independent of MLC1

As the mutations mainly affect the ability of GlialCAM to homo-oligomerize, then the question was whether the MLC-causing *GLIALCAM* mutations would affect the localization of GlialCAM *per se*.

In HeLa cells, wild-type GlialCAM mainly shows two localization patterns: at the plasma membrane (Fig. 7A) and in junctions (Figs 5E and 7B). Typical examples for different proteins containing recessive and dominant mutations expressed in HeLa cells are shown in Figure 7C–G. Multiple pictures from different experiments were taken and the percentage of cells in which GlialCAM was located either in junctions or not in junctions or intracellularly was quantified for

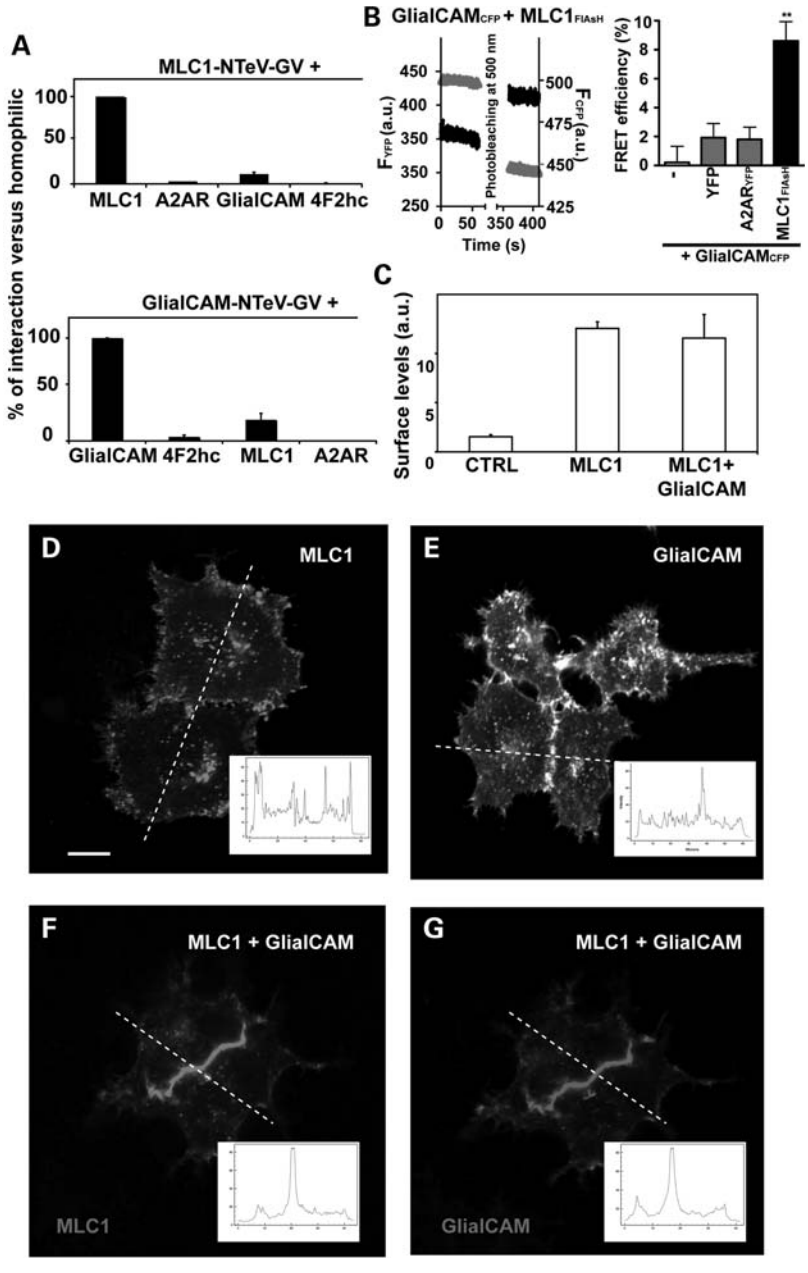

Figure 5. *In vitro* characterization of the interaction between MLC1 and GlialCAM. (**A**) HeLa cells were co-transfected with the indicated constructs, and interaction was monitored by split-TEV assays as described in Materials and Methods. The signal that was obtained for homo-oligomerization of MLC1 (upper panel) or GlialCAM (lower panel) was set to 100%. The result is the summary of five independent experiments. (**B**) Determination of the MLC1 and GlialCAM association by FRET experiments in living cells. Effect of photobleaching (left panel). Emission intensities of FlAsH (535 nm, green) and CFP (480 nm, blue) recorded from single cells co-expressing $MLC1^{FlAsH}$ and $GlialCAM^{CFP}$ using fluorescence microscopy. Emission intensities were recorded before and after FlAsH (the acceptor fluorophore) was photobleached by 5 min exposure to light at 500 nm. FRET efficiency (right panel) from cells expressing: $GlialCAM^{CFP}$ ($n = 6$), $GlialCAM^{CFP}$ and YFP ($n = 6$), $GlialCAM^{CFP}$ and $A_{2A}R^{YFP}$ ($n = 6$), and $GlialCAM^{CFP}$ and $MLC1^{FlAsH}$ ($n = 10$); data indicate mean $\pm$ SEM and the double-asterisk indicates statistically significant differences ($P < 0.01$; Student's *t*-test). (**C**) HeLa cells were transfected with wild-type MLC1 with HA tags or wild-type MLC1 together with GlialCAM. Plasma membrane levels were measured using a luminescence-based method, as described in Materials and Methods. Data correspond to the average of three experiments. (**D**–**G**) HeLa cells were transfected with plasmids expressing wild-type MLC1 (D), wild-type GlialCAM flag-tagged (E) or wild-type MLC1 plus wild-type GlialCAM flag-tagged (F and G). Cells were fixed and permeabilized and then immunofluorescence was performed using rabbit polyclonal antibodies against human MLC1 and flag monoclonal antibodies detecting GlialCAM protein. Scale bar: 20 μm. Pairs of cells were analyzed performing an intensity profile through the indicated white dashed line. The result of this profile is shown as an inset in every case. The analysis revealed that MLC1 alone had an *R*-value (see Materials and Methods) of 1.08 $\pm$ 0.06 ($n = 45$), and MLC1 in the presence of GlialCAM had a value of 3.95 $\pm$ 0.06 ($n = 42$). On the other hand, GlialCAM alone had a value of 2.43 $\pm$ 0.15 ($n = 44$), and GlialCAM in the presence of MLC1 had a value of 3.99 $\pm$ 0.23 ($n = 42$).

each of the variants. As depicted in Figure 7H, GlialCAM-defective proteins showed an altered trafficking compared with wild-type GlialCAM, being located preferentially at the plasma membrane but not in cell junctions. Similar results were found in primary cultures of astrocytes (Supplementary Material, Fig. S2). No defect was observed for the GlialCAM

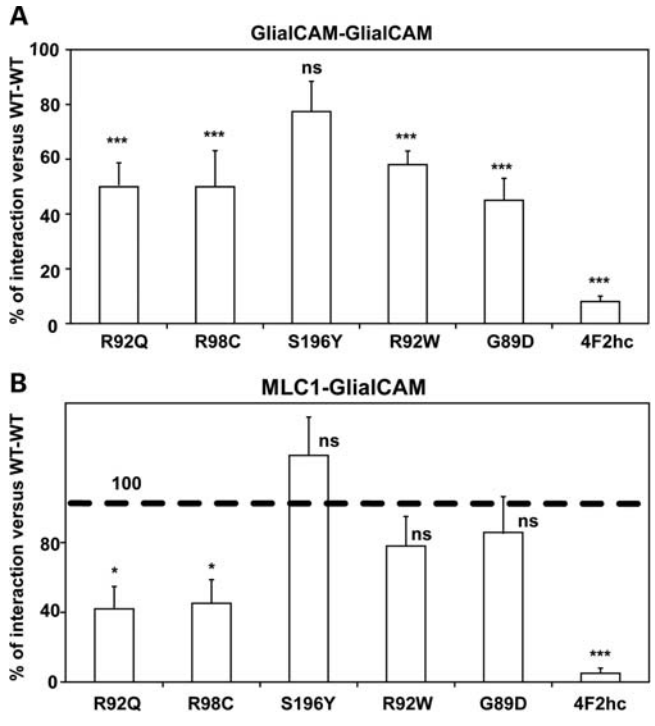

Figure 6. MLC-causing *GLIALCAM* mutations affect the interaction mainly between GlialCAM molecules. HeLa cells were co-transfected with the indicated constructs, and interaction was monitored by split-TEV assays as described in Materials and Methods. The signal that was obtained for homo-oligomerization of wild-type GlialCAM (upper panel) or the hetero-oligomerization of MLC1 and wild-type GlialCAM (lower panel) was set to 100%. Bars indicate the percentage of interaction compared with the interaction between the corresponding wild-type proteins ± SEM. The result is the summary of five independent experiments. Bonferroni's multiple comparison test was used. $^{*}P < 0.05$; $^{**}P < 0.01$; $^{***}P < 0.001$. ns, no significant difference. Statistical significance was probably minor in the heteromeric interaction (MLC1–GlialCAM) compared with the homomeric interaction (GlialCAM–GlialCAM), as the fold signal induction in the split-TEV assays was higher in the homomeric studies.

protein containing the mutation S196Y in HeLa cells (Fig. 7) and in astrocytes (Supplementary Material, Fig. S2).

We investigated whether the localization of MLC1 in junctions when co-expressed in HeLa cells with GlialCAM was altered by the mutations in *GLIALCAM*. We found that MLC1 was also mislocalized (Fig. 8) in all studied GlialCAM-defective proteins, except the S196Y variant.

DISCUSSION

Studies on *MLC1* missense mutations indicate that a deficiency of cell-surface MLC1 protein expression is the molecular basis of MLC disease (19). This hypothesis has been reconfirmed by the present studies on brain tissue from an MLC patient.

Interestingly, the MLC patient studied here was the oldest MLC patient to our knowledge. However, MLC1 protein was undetectable in the brain of the patient. The lack of detailed clinical data for all the MLC patients limits possible correlations between protein expression and the phenotype of each patient. Possible genotype–phenotype correlations are also difficult to estimate due to the high intrafamilial phenotypic variability (24), the slow progression of the disease and the fact that the disease phenotype may worsen abruptly after trauma or infections. We conclude that, in MLC disease, no correlation can be established between the cellular or clinical phenotype and the genotype. Probably, unknown modifier factors could influence the phenotype.

GlialCAM was identified as a beta-subunit of MLC1 (17). The present work defines the role of GlialCAM as an escort molecule, necessary to bring MLC1 to cell–cell junctions.

In the MLC patient and in astrocytes depleted of MLC1 by RNA interference, the expression and localization of GlialCAM are independent of MLC1. GlialCAM molecules may form complex structures involving homo-*cis*, hetero-*cis* and *trans*-interactions with itself and with other molecules (25,26). Here, we show that recessive and dominant *GLIALCAM* mutations affect mainly the formation of homo-oligomeric structures, leading to a trafficking defect. An exception is the S196Y protein variant, for which we have not found any defect. Collectively, the results presented here indicate a direct correlation between the GlialCAM homo-oligomerization and the subcellular localization of this protein in cellular junctions, suggesting that GlialCAM homo-oligomerization is a prerequisite for correct targeting. Defective GlialCAM-MLC1 hetero-oligomerization is differentially affected by several *GLIALCAM* mutations, but it could also contribute to the trafficking defect of MLC1, as MLC1 alone is not able to reach cell–cell junctions.

At present, we do not understand why some mutations behave as recessive and others as dominant. As all dominant mutations identified so far are located in a putative pocket of the immunoglobulin variable domain (17), we could speculate that these mutations may affect *trans*-interactions between GlialCAM molecules or other unknown proteins, although experimental evidence is lacking.

GlialCAM protein has been also identified as a molecule with a role in cell growth, differentiation, motility and adhesion in various cell types (15,16,23,27–30). It could be suggested that these functions of GlialCAM are affected in MLC patients. Whether MLC1 cooperates with GlialCAM in these functions needs to be explored. The biology of the GlialCAM protein could facilitate the understanding of other discoveries that have been obtained about the cell biology of MLC1. For instance, MLC1 was reported to be associated with caveolae (31), and GlialCAM was shown to be associated with caveolin 1 (32). Furthermore, localization of MLC1 in astrocytes was found to be dependent on the actin cytoskeleton (9), whereas GlialCAM was also shown to have a direct interaction with actin (28). Whether the oligomerization state of GlialCAM molecules is necessary for interaction with intracellular complexes which may be important for its localization in cell junctions is an interesting hypothesis that should be tested. In this sense, affinity purification studies revealed co-immunoprecipitation between MLC1 and the junction-associated protein ZO-1 (9).

In summary, this work offers new interesting clues about the pathogenic mechanism of *MLC1* and *GLIALCAM* mutations. We have shown that the MLC1 protein containing the S69L mutation can be stabilized by the presence of GlialCAM. Probably, GlialCAM increase the stability of the defective protein by protecting from the ERAD or the ELAD mechanisms. These data suggest that a therapeutical strategy aimed

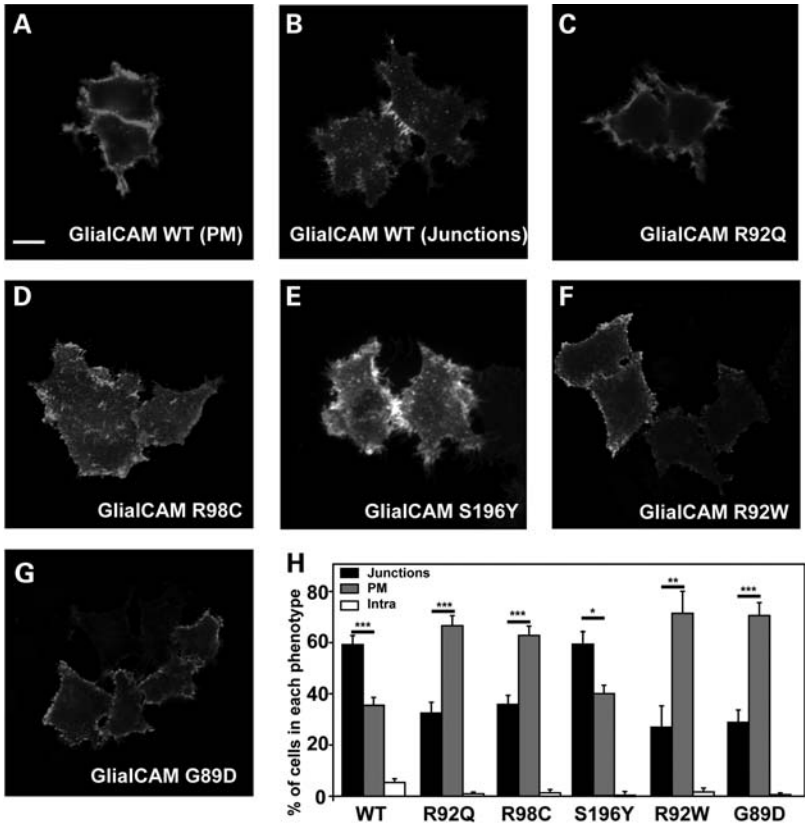

Figure 7. Trafficking defect of GlialCAM-defective proteins expressed in HeLa cells. HeLa cells were transfected with plasmids expressing flag-tagged wild-type GlialCAM (**A** and **B**) or containing recessive [R92Q (**C**), R98C (**D**), S196Y (**E**)] or dominant [R92W (**F**), G89D (**G**)] MLC-causing mutations. Cells were fixed and permeabilized and then immunofluorescence was performed using flag monoclonal antibodies detecting GlialCAM protein. Scale bar: 20 μm. (**H**) Pairs of cells were analyzed manually and quantified as being in junctions, around the plasma membrane or intracellularly. Intensity profile analysis was used to discern between junctional and plasma membrane localization. Data represent the mean of 4–11 independent experiments, corresponding to 954 cells (GlialCAM, $n = 11$), 744 cells (R92Q, $n = 5$), 644 cells (R98C, $n = 5$), 718 cells (S196Y, $n = 5$), 460 cells (R92W, $n = 4$) and 433 cells (G89D, $n = 4$). Bonferroni's multiple comparison test versus 'in junctions' and not 'in junctions' was used. $^{**}P < 0.01$; $^{***}P < 0.001$.

at the over-expression of GlialCAM may be beneficial to improve the surface expression of MLC1 protein variants containing MLC-causing mutations, which could be envisaged as new therapies to MLC patients.

MATERIALS AND METHODS

Animal experimentation and human samples

All the experimental protocols have been approved by the Animal Care and Ethics Committee of the University of Barcelona and conformed to the rules set by the Government of Catalunya.

Neuropathological study in a patient's brain sample

The post-mortem delay was 34 h. At autopsy, one hemisphere was cut in coronal sections, 1 cm thick, frozen on dry ice and stored at −80°C until use. The other hemisphere was fixed by immersion in 4% buffered formalin for 3 weeks. Selected samples were embedded in paraffin. De-waxed sections were stained with hematoxylin and eosin and Klüver–Barrera, or processed for immunohistochemistry. After incubation with methanol and normal serum, the sections were incubated with one of the primary antibodies overnight at 4°C. Antibodies to glial fibrillary acidic protein (Dako, Barcelona, Spain), β-amyloid (Boehringer-Ingelheim, Barcelona, Spain) and ubiquitin (Dako) were used at dilutions of 1:250, 1:50 and 1:200, respectively. CD68 (Dako), used as a marker of microglia, was diluted at 1:100. AT8 antibody (Innogenetics, Barcelona, Spain) was used at a dilution of 1:50. Anti-phosphorylated neurofilament antibody RT97 (Boehringer-Ingelheim) was used at a dilution of 1:100. Rabbit polyclonal anti-α-synuclein antibody (Chemicon, Barcelona, Spain) was used at a dilution of 1:3000. TDP-43 was examined using a mouse monoclonal antibody (Abnova, Tebu-Bio, Barcelona, Spain) raised against a full-length recombinant human TARDBP at a dilution of 1:1000. Monoclonal anti-αB-crystallin (Novocastra) was utilized at 1:50 (Stressgen, Bionova, Madrid, Spain). Antibodies to MLC1 (19) and GlialCAM (17) were used, both diluted 1:100. Following incubation with the primary antibody, the sections were incubated with EnVision+ system peroxidase (Dako) for 15 min at room temperature (RT). The peroxidase reaction was visualized with diaminobenzidine and H_2O_2. Control of the immunostaining included omission of the primary antibody; no signal was obtained following incubation with only the secondary antibody. Sections were slightly counterstained with hematoxylin.

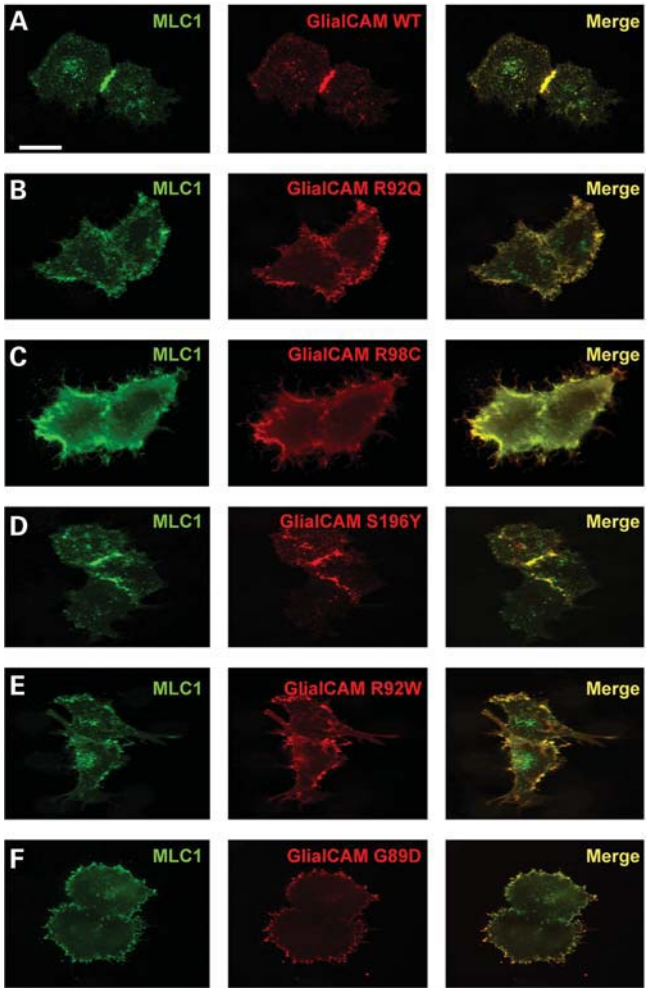

Figure 8. MLC1 follows GlialCAM localization in transfected HeLa cells. HeLa cells were transfected with plasmids expressing wild-type MLC1 and flag-tagged wild-type GlialCAM (**A**) or containing recessive [R92Q (**B**), R98C (**C**), S196Y (**D**)] or dominant [R92W (**E**), G89D (**F**)] MLC-causing mutations. Cells were fixed and permeabilized and immunofluorescence was performed using rabbit polyclonal antibodies against human MLC1 (green) and flag monoclonal antibodies detecting GlialCAM protein (red). Co-localization is shown in yellow (Merge). The images represent typical examples of these experiments. Using different images from four to eight independent experiments, the localization of MLC1 was studied. MLC1 (with GlialCAM) was detected in 71.5 $\pm$ 3.6% in junctions versus 25.3 $\pm$ 3.6% at the plasma membrane (646 cells), MLC1 (with GlialCAM R92Q) was detected in 41.9 $\pm$ 4.4% in junctions versus 54 $\pm$ 6% at the plasma membrane (697 cells), MLC1 (with GlialCAM R98C) was detected in 48.4 $\pm$ 4.8% in junctions versus 51.4 $\pm$ 4.8% at the plasma membrane (688 cells), MLC1 (with GlialCAM S196Y) was detected in 62.5 $\pm$ 4% in junctions versus 37.5 $\pm$ 4% at the plasma membrane (281 cells), MLC1 (with GlialCAM R92W) was detected in 35.6 $\pm$ 4.5% in junctions versus 63.8 $\pm$ 4.8% at the plasma membrane (455 cells), MLC1 (with GlialCAM G89D) was detected in 43.8 $\pm$ 2.8% in junctions versus 56.2 $\pm$ 2.8% at the plasma membrane (444 cells). Scale bar: 20 μm.

Genetic analyses of *MLC1* mutations

Sequence analysis of *MLC1* exons and their surrounding intronic regions was carried out on genomic DNA extracted from blood, as described (4).

Molecular biology

A tetracysteine epitope, compatible with the fluorescein arsenical helix binder (FlAsH) staining method, was introduced at the N-terminus of human MLC1, thus resulting in the following sequence: MAFLN**CCPGCC**MEPF (tetracysteine epitope is in boldface). This epitope tag did not affect the subcellular localization and the surface expression levels of the tagged protein (data not shown). Plasmids presented herein were made using standard molecular biology techniques employing recombinant PCR and the MultiSite Gateway System (Invitrogen). The integrity of all cloned constructs was confirmed by DNA sequencing.

Cell culture and transfection

HEK-293T or HeLa cells were grown at 37°C in an atmosphere of 5% CO_2 in Dulbecco's modified Eagle's medium (Sigma-Aldrich, St Louis, MO, USA) supplemented with 1 mM sodium pyruvate, 2 mM L-glutamine, 100 U/ml streptomycin, 100 mg/ml penicillin and 5% (v/v) fetal bovine serum. The cells were seeded into plates containing or not poly-D-lysine-coated cover slips. Cells were transiently transfected with the corresponding cDNA constructs using Transfectin (Bio-Rad, Hercules, CA, USA) and following the manufacturer's instructions.

Measurement of surface expression in cells by luminescence

Surface expression in transfected mammalian cells was performed as previously described (5). Briefly, 48 h after transfection, cells were cleaned with PBS and fixed with 3% paraformaldehyde. After PBS washing, cells were then blocked with 1% BSA in PBS for 30 min, and incubated with 1 ml of 3F10 anti-HA antibody at 0.2 μg/ml in blocking solution for 1 h at RT. Cells were washed six times with blocking solution, and incubated for 20 min with 1 ml of a 1:1000 dilution horseradish peroxidase-coupled secondary antibody (donkey anti-rat IgG, Jackson, Suffolk, UK) in blocking solution. Cells were washed four times with blocking solution and eight times with PBS. Luminescence was measured of one dish at a time with 500 μl of Power Signal ELISA solution (Pierce) in a Turner TD-20/20 luminometer (Turner Biosystems, Madison, WI, USA).

Split-TEV method

Split-TEV assay was performed as described (20,33) but with some modifications. To this end, a mutant form of the TEV protease (S219V) was used, which prevents its self-digestion but does not affect its catalytic efficiency. The oligopeptide substrate used as the TEV protease-recognition site was ENLYFQS, and the chimeric transcription factor used was GV (obtained from the pM3-VP16 vector; Clontech, Nucliber, Madrid, Spain), which contains the yeast Gal4DNA-binding domain and the herpes simplex VP16 transactivation domain. After TEV protease cleavage, GV translocates into the nucleus and induces the reporter Gaussia luciferase gene

expression (pNEBr-X1Gluc) (New England BioLabs, IZASA, Barcelona, Spain), which is secreted into the cell culture medium.

TEV protease was divided in two fragments: the TEV-N (residues 1–118) and the TEV-C (residues 119–242). We fused the TEV-N fragment, the TEV protease-recognition site and the chimeric transcription factor GV to the C-terminal of MLC1 and GlialCAM in a pCDNA3 vector containing a CMV promoter. In addition, we fused the TEV-C fragment to the C-terminal of MLC1, GlialCAM wild-type, GlialCAM containing the mutations R92Q, R98C, S196Y, R92W and G89D, and the adenosine 2A receptor (A2AR). The fusion of the TEV-C fragment to 4F2hc was done at the N-terminus. All the proteins with the TEV-C fragments were cloned in a pCDNA6.2/V5-pL Dest, containing the herpes simplex virus thymidine kinase promoter, to provide low-to-moderate levels of expression.

All the expression plasmids were constructed by PCR using a polymerase with proofreading (KOD Hot Start polymerase, Calbiochem, Darnstadt, Germany), adding the attB1, attB2, attB5R or attB5 recombination sites compatible with the MultiSite Gateway System (Invitrogen). All protocols were performed according to the manufacturer's instructions (Invitrogen).

HeLa cells were transiently transfected with the corresponding cDNA constructs. The total DNA transfected was 2 μg, with the following ratios: 0.75 μg of each protein containing the TEV-N and the TEV-C fragments, 0.3 μg of the reporter vector pNEBr-X1GLuc and 0.2 μg of the pCMV-βGal vector, which was used to monitor the transfection efficiency. After 48 h, 20 μl of liquid were removed from the supernatant of the cells and Gaussia luciferase activity was measured in a TD-20/20 luminometer (Turner BioSystems), after the addition of 20 μM native colenterazine. To normalize the data, cells were solubilized and 30 μl of the cell lysates were used to measure the β-galactosidase enzyme activity, using the Luminiscent β-Galactosidase Detection Kit II (Clontech) in the same luminometer.

FlAsH labeling

FlAsH labeling was performed as described (34). In brief, transfected cells growing on poly-D-lysine-coated cover slips were washed three times with phenol red-free Hank's balanced salt solution (HBSS) with glucose containing (in mM): 137 NaCl, 0.34 Na_2HPO_4, 5 KCl, 0.44 KH_2PO_4, 0.5 $MgCl_2$, 0.4 Mg_2SO_4, 1.26 $CaCl_2$, 10 HEPES, 2 D-glucose and 1 ascorbic acid (pH 7.4 with NaOH), and then incubated at 37°C for 1 h with an HBSS solution containing 500 nM FlAsH/EDT_2. FlAsH was purchased from Invitrogen and 1,2-ethanedithiol (EDT) from Sigma-Aldrich. Subsequently, to reduce non-specific labeling, cells were washed once with HBSS containing 250 μM EDT for 10 min at 37°C, and thereafter rinsed three times with HBSS to reduce remnants of EDT.

FRET experiments

FRET between CFP and FlAsH in cells expressing the corresponding constructs was determined by donor recovery after acceptor photobleaching, in which FRET is revealed as a significant increase in the fluorescence of the donor (i.e. CFP) after photobleaching of the acceptor (i.e. FlAsH) (35). FlAsH-labeled cells were mounted in an Attofluor holder and placed on an inverted Axio Observer microscope (Zeiss Microimaging, Oberkochen, Germany) equipped with a 63× oil immersion objective and a dual-emission photometry system (TILL Photonics, Gräfelfing, Germany). A Polychrome V (TILL Photonics) was used as the light source and signals detected by photodiodes were digitized using a Digidata 1440A analog/digital converter (Molecular Devices, Sunnyvale, CA, USA). pCLAMP (Molecular Devices) and GraphPad Prism (GraphPad Prism, San Diego, CA, USA) software were used for data collection and analysis. Therefore, upon excitation at 436 ± 10 nm [beam splitter dichroic long-pass (DCLP) 460 nm] and an illumination time set to 10 ms at 10 Hz, the emission light intensities were determined at 535 ± 15 nm (FlAsH) and 480 ± 20 nm (CFP_{pre}) with a beam splitter DCLP of 505 nm. No corrections for spillover between channels or direct YFP excitation were made. Subsequently, acceptor photobleaching was performed by direct illumination of FlAsH at 500 nm for 5 min. Finally, the emission intensities of FlAsH and CFP (CFP_{post}) were recorded again. FRET efficiency was calculated according to the equation: $FRET_{efficiency} = 1 - (CFP_{pre}/CFP_{post})$.

Primary culture and adenoviral transduction

Rat primary astrocyte cultures were prepared as described previously (17). Construction of adenovirus-expressing wild-type HA-tagged human MLC1 has been described (19). Adenoviruses expressing human GlialCAM fused to three copies of the flag epitope, either wild-type or containing the recessive mutations R92Q, R98C and S196Y, or the dominant mutations R92W and G89D have been described recently (17). Transduction of astrocytes was performed as already described (19).

Immunofluorescence and immunohistochemical studies

Immune sera against N-terminal mouse MLC1 and the N4 anti-N-terminus of human MLC1 antibody were generated and characterized previously (5,6,19). Immune sera against a GlialCAM synthetic peptide have also been described recently (17).

Tissue immunohistochemistry was performed as previously described (5,6). For immunofluorescent staining of cells, these were fixed with PBS containing 3% paraformaldehyde for 15 min, blocked and permeabilized with 10% FBS and 0.1% Triton X-100 in PBS for 2 h at RT. Primary antibodies were diluted in the same solution and incubated overnight at 4°C. Cells were washed and incubated for 2 h at RT with secondary antibodies: Alexa-568 goat anti-mouse and Alexa-488 goat anti-rabbit (1:500 dilution; Invitrogen). Cover slips were mounted in Vectashield medium (Vector Laboratories, ATOM, Barcelona, Spain) with 1.5 μg/ml DAPI (Sigma) and visualized using an Olympus DSU spinning disk confocal microscope (Barcelona, Spain). Co-localization and intensity profile experiments were analyzed using ImageJ (http://rsbweb.nih.gov/ij/). After intensity profile calculations, we defined a ratio (R) considering the signal at the plasma membrane of two cells (cell 1 and cell 2) and the signal in junctions [$R = I_{junctions}/((I_{membrane1} + I_{membrane2})/2)$]. Then, if the

R-value is >1, the signal will be more concentrated at junctions.

Western blot analysis

For western blot studies, lysates were prepared by homogenization of cells in PBS containing 1% Triton X-100 and protease inhibitors: 1 μM pepstatin and leupeptin, 1 mM aprotinin and 1 mM PMSF, incubated for 1 h at 4°C and centrifugated. Proteins in supernatants were quantified using the BCA Kit (Pierce, Thermo Scientific, Rockford, IL, USA) and mixed with SDS loading sample buffer. Western blot analysis was performed as described (5). Membranes were incubated with primary antibodies: anti-MLC1 (1:100), anti-GlialCAM (1:100) and anti-β-actin (1:10 000, Sigma) and secondary antibodies: HRP-conjugated anti-rabbit and anti-mouse (1:10 000; Jackson). Quantification of western blots was performed using Multigauge (Fujifilm, Barcelona, Spain) or ImageJ.

RNA interference

Conditions for knockdown of MLC1 in rat primary astrocytes have been described recently (9).

SUPPLEMENTARY MATERIAL

Supplementary Material is available at *HMG* Online.

ACKNOWLEDGEMENTS

We thank Thomas J. Jentsch for advice in the intensity-profiling analysis and Alejandro Barrallo, Michael Pusch and Gergely Luckacs for critical reading of the manuscript.

Conflict of Interest statement. None declared.

FUNDING

This study was supported in part by SAF 2009-07014 (R.E.), PS09/02672-ERARE (R.E.), ELA Foundation 2009-017C4 project (R.E. and V.N.), 2009 SGR 719 (R.E.), SAF 2009-12606-C02-02 (V.N.), 2009 SGR01490 (V.N.), SAF2008-01462 (F.C.) and CSD2008-00005 (F.C.). R.E. and F.C. are recipients of an ICREA Academia prize. M.S. van der Knaap and G.C.S. are supported by the Dutch Organization for Scientific Research ZonMw (TOP grant 9120.6002), the Hersenstichting (grants 10F02(2).02, 13F05.04 and 15F07.30), ERARE grant 11-330-1024 and the Optimix Foundation for Scientific Research.

REFERENCES

1. van der Knaap, M.S., Barth, P.G., Stroink, H., van Nieuwenhuizen, O., Arts, W.F., Hoogenraad, F. and Valk, J. (1995) Leukoencephalopathy with swelling and a discrepantly mild clinical course in eight children. *Ann. Neurol.*, **37**, 324–334.
2. van der Knaap, M.S., Barth, P.G., Vrensen, G.F. and Valk, J. (1996) Histopathology of an infantile-onset spongiform leukoencephalopathy with a discrepantly mild clinical course. *Acta Neuropathol.*, **92**, 206–212.
3. Leegwater, P.A., Yuan, B.Q., van der Steen, J., Mulders, J., Konst, A.A., Boor, P.K., Mejaski-Bosnjak, V., van der Maarel, S.M., Frants, R.R., Oudejans, C.B. *et al.* (2001) Mutations of MLC1 (KIAA0027), encoding a putative membrane protein, cause megalencephalic leukoencephalopathy with subcortical cysts. *Am. J. Hum. Genet.*, **68**, 831–838.
4. Ilja Boor, P.K., de Groot, K., Mejaski-Bosnjak, V., Brenner, C., van der Knaap, M.S., Scheper, G.C. and Pronk, J.C. (2006) Megalencephalic leukoencephalopathy with subcortical cysts: an update and extended mutation analysis of MLC1. *Hum. Mutat.*, **27**, 505–512.
5. Teijido, O., Martinez, A., Pusch, M., Zorzano, A., Soriano, E., Del Rio, J.A., Palacin, M. and Estevez, R. (2004) Localization and functional analyses of the MLC1 protein involved in megalencephalic leukoencephalopathy with subcortical cysts. *Hum. Mol. Genet.*, **13**, 2581–2594.
6. Teijido, O., Casaroli-Marano, R., Kharkovets, T., Aguado, F., Zorzano, A., Palacin, M., Soriano, E., Martinez, A. and Estevez, R. (2007) Expression patterns of MLC1 protein in the central and peripheral nervous systems. *Neurobiol. Dis.*, **26**, 532–545.
7. Ambrosini, E., Serafini, B., Lanciotti, A., Tosini, F., Scialpi, F., Psaila, R., Raggi, C., Di Girolamo, F., Petrucci, T.C. and Aloisi, F. (2008) Biochemical characterization of MLC1 protein in astrocytes and its association with the dystrophin–glycoprotein complex. *Mol. Cell. Neurosci.*, **37**, 480–493.
8. Boor, P.K., de Groot, K., Waisfisz, Q., Kamphorst, W., Oudejans, C.B., Powers, J.M., Pronk, J.C., Scheper, G.C. and van der Knaap, M.S. (2005) MLC1: a novel protein in distal astroglial processes. *J. Neuropathol. Exp. Neurol.*, **64**, 412–419.
9. Duarri, A., de Heredia, M.L., Capdevila-Nortes, X., Ridder, M.C., Montolio, M., Lopez-Hernandez, T., Boor, I., Lien, C.F., Hagemann, T., Messing, A. *et al.* (2011) Knockdown of MLC1 in primary astrocytes causes cell vacuolation: a MLC disease cell model. *Neurobiol. Dis.*, **43**, 228–238.
10. Brignone, M.S., Lanciotti, A., Macioce, P., Macchia, G., Gaetani, M., Aloisi, F., Petrucci, T.C. and Ambrosini, E. (2011) The beta1 subunit of the Na,K-ATPase pump interacts with megalencephalic leucoencephalopathy with subcortical cysts protein 1 (MLC1) in brain astrocytes: new insights into MLC pathogenesis. *Hum. Mol. Genet.*, **20**, 90–103.
11. Patrono, C., Di Giacinto, G., Eymard-Pierre, E., Santorelli, F.M., Rodriguez, D., De Stefano, N., Federico, A., Gatti, R., Benigno, V., Megarbane, A. *et al.* (2003) Genetic heterogeneity of megalencephalic leukoencephalopathy and subcortical cysts. *Neurology*, **61**, 534–537.
12. Blattner, R., Von Moers, A., Leegwater, P.A., Hanefeld, F.A., van der Knaap, M.S. and Kohler, W. (2003) Clinical and genetic heterogeneity in megalencephalic leukoencephalopathy with subcortical cysts (MLC). *Neuropediatrics*, **34**, 215–218.
13. Scheper, G.C., van Berkel, C.G., Leisle, L., de Groot, K.E., Errami, A., Jentsch, T.J. and van der Knaap, M.S. (2010) Analysis of CLCN2 as candidate gene for megalencephalic leukoencephalopathy with subcortical cysts. *Genet. Test. Mol. Biomarkers*, **14**, 255–257.
14. van der Knaap, M.S., Lai, V., Kohler, W., Salih, M.A., Fonseca, M.J., Benke, T.A., Wilson, C., Jayakar, P., Aine, M.R., Dom, L. *et al.* (2010) Megalencephalic leukoencephalopathy with cysts without MLC1 defect. *Ann. Neurol.*, **67**, 834–837.
15. Favre-Kontula, L., Rolland, A., Bernasconi, L., Karmirantzou, M., Power, C., Antonsson, B. and Boschert, U. (2008) GlialCAM, an immunoglobulin-like cell adhesion molecule is expressed in glial cells of the central nervous system. *Glia*, **56**, 633–645.
16. Lee, L.H., Moh, M.C., Zhang, T. and Shen, S. (2009) The immunoglobulin-like cell adhesion molecule hepaCAM induces differentiation of human glioblastoma U373-MG cells. *J. Cell. Biochem.*, **107**, 1129–1138.
17. Lopez-Hernandez, T., Ridder, M.C., Montolio, M., Capdevila-Nortes, X., Polder, E., Sirisi, S., Duarri, A., Schulte, U., Fakler, B., Nunes, V. *et al.* (2011) Mutant GlialCAM causes megalencephalic leukoencephalopathy with subcortical cysts, benign familial macrocephaly, and macrocephaly with retardation and autism. *Am. J. Hum. Genet.*, **88**, 422–432.
18. Montagna, G., Teijido, O., Eymard-Pierre, E., Muraki, K., Cohen, B., Loizzo, A., Grosso, P., Tedeschi, G., Palacin, M., Boespflug-Tanguy, O. *et al.*. (2006) Vacuolating megalencephalic leukoencephalopathy with subcortical cysts: functional studies of novel variants in MLC1. *Hum. Mutat.*, **27**, 292.

19. Duarri, A., Teijido, O., Lopez-Hernandez, T., Scheper, G.C., Barriere, H., Boor, I., Aguado, F., Zorzano, A., Palacin, M., Martinez, A. *et al.* (2008) Molecular pathogenesis of megalencephalic leukoencephalopathy with subcortical cysts: mutations in MLC1 cause folding defects. *Hum. Mol. Genet.*, **17**, 3728–3739.
20. Wehr, M.C., Laage, R., Bolz, U., Fischer, T.M., Grunewald, S., Scheek, S., Bach, A., Nave, K.A. and Rossner, M.J. (2006) Monitoring regulated protein–protein interactions using split TEV. *Nat. Methods*, **3**, 985–993.
21. Estevez, R., Camps, M., Rojas, A.M., Testar, X., Deves, R., Hediger, M.A., Zorzano, A. and Palacin, M. (1998) The amino acid transport system y+L/4F2hc is a heteromultimeric complex. *FASEB J.*, **12**, 1319–1329.
22. Ferre, S., Karcz-Kubicha, M., Hope, B.T., Popoli, P., Burgueno, J., Gutierrez, M.A., Casado, V., Fuxe, K., Goldberg, S.R., Lluis, C. *et al.* (2002) Synergistic interaction between adenosine A2A and glutamate mGlu5 receptors: implications for striatal neuronal function. *Proc. Natl Acad. Sci. USA*, **99**, 11940–11945.
23. Moh, M.C., Zhang, C., Luo, C., Lee, L.H. and Shen, S. (2005) Structural and functional analyses of a novel Ig-like cell adhesion molecule, hepaCAM, in the human breast carcinoma MCF7 cells. *J. Biol. Chem.*, **280**, 27366–27374.
24. Pascual-Castroviejo, I., van der Knaap, M.S., Pronk, J.C., Garcia-Segura, J.M., Gutierrez-Molina, M. and Pascual-Pascual, S.I. (2005) Vacuolating megalencephalic leukoencephalopathy: 24 year follow-up of two siblings. *Neurologia*, **20**, 33–40.
25. Gaudry, J.P., Arod, C., Sauvage, C., Busso, S., Dupraz, P., Pankiewicz, R. and Antonsson, B. (2008) Purification of the extracellular domain of the membrane protein GlialCAM expressed in HEK and CHO cells and comparison of the glycosylation. *Protein Expr. Purif.*, **58**, 94–102.
26. Favre-Kontula, L., Sattonnet-Roche, P., Magnenat, E., Proudfoot, A.E., Boschert, U., Xenarios, I., Vilbois, F. and Antonsson, B. (2008) Detection and identification of plasma proteins that bind GlialCAM using ProteinChip arrays, SELDI-TOF MS, and nano-LC MS/MS. *Proteomics*, **8**, 378–388.
27. Chung Moh, M., Hoon Lee, L. and Shen, S. (2005) Cloning and characterization of hepaCAM, a novel Ig-like cell adhesion molecule suppressed in human hepatocellular carcinoma. *J. Hepatol.*, **42**, 833–841.
28. Moh, M.C., Tian, Q., Zhang, T., Lee, L.H. and Shen, S. (2009) The immunoglobulin-like cell adhesion molecule hepaCAM modulates cell adhesion and motility through direct interaction with the actin cytoskeleton. *J. Cell. Physiol.*, **219**, 382–391.
29. Xun, C., Luo, C., Wu, X., Zhang, Q., Yan, L. and Shen, S. (2010) Expression of hepaCAM and its effect on proliferation of tumor cells in renal cell carcinoma. *Urology*, **75**, 828–834.
30. Zhang, T., Moh, M.C., Lee, L.H. and Shen, S. (2010) The immunoglobulin-like cell adhesion molecule hepaCAM is cleaved in the human breast carcinoma MCF7 cells. *Int. J. Oncol.*, **37**, 155–165.
31. Lanciotti, A., Brignone, M.S., Camerini, S., Serafini, B., Macchia, G., Raggi, C., Molinari, P., Crescenzi, M., Musumeci, M., Sargiacomo, M. *et al.* (2010) MLC1 trafficking and membrane expression in astrocytes: role of caveolin-1 and phosphorylation. *Neurobiol. Dis.*, **37**, 581–595.
32. Moh, M.C., Lee, L.H., Zhang, T. and Shen, S. (2009) Interaction of the immunoglobulin-like cell adhesion molecule hepaCAM with caveolin-1. *Biochem. Biophys. Res. Commun.*, **378**, 755–760.
33. Wehr, M.C., Reinecke, L., Botvinnik, A. and Rossner, M.J. (2008) Analysis of transient phosphorylation-dependent protein–protein interactions in living mammalian cells using split-TEV. *BMC Biotechnol.*, **8**, 55.
34. Hoffmann, C., Gaietta, G., Zurn, A., Adams, S.R., Terrillon, S., Ellisman, M.H., Tsien, R.Y. and Lohse, M.J. (2010) Fluorescent labeling of tetracysteine-tagged proteins in intact cells. *Nat. Protoc.*, **5**, 1666–1677.
35. Vilardaga, J.P., Nikolaev, V.O., Lorenz, K., Ferrandon, S., Zhuang, Z. and Lohse, M.J. (2008) Conformational cross-talk between alpha2A-adrenergic and mu-opioid receptors controls cell signaling. *Nat. Chem. Biol.*, **4**, 126–131.

GlialCAM, a Protein Defective in a Leukodystrophy, Serves as a ClC-2 Cl^- Channel Auxiliary subunit

(Neuron, 2012)

Contribució:

- Purificació de l'anticós generat contra la proteïna ClC-2
- Estudis de localització de GlialCAM i ClC-2 en teixit (Figura 2 B,E,F)
- Estudis de localització de GlialCAM i ClC-2 en cèl·lules progenitores d'oligodendròcits (material generat per als referees).

Neuron
Article

GlialCAM, a Protein Defective in a Leukodystrophy, Serves as a ClC-2 Cl^- Channel Auxiliary Subunit

Elena Jeworutzki,[1,11] Tania López-Hernández,[2,11] Xavier Capdevila-Nortes,[2] Sònia Sirisi,[2,5] Luiza Bengtsson,[4] Marisol Montolio,[2,6] Giovanni Zifarelli,[1] Tanit Arnedo,[2] Catrin S. Müller,[8] Uwe Schulte,[8] Virginia Nunes,[3,5,7] Albert Martínez,[9] Thomas J. Jentsch,[4] Xavier Gasull,[10] Michael Pusch,[1,11] and Raúl Estévez[2,6,11,*]
[1]Istituto di Biofisica, Consiglio Nazionale delle Ricerche, 16149 Genoa, Italy
[2]Physiology section
[3]Genetic section
Department Physiological Sciences II, School of Medicine, University of Barcelona, 08907 Barcelona, Spain
[4]Leibniz-Institut für Molekulare Pharmakologie (FMP) and Max-Delbrück-Centrum für Molekulare Medizin (MDC), D-13125 Berlin, Germany
[5]Laboratorio de Genética Molecular-IDIBELL
[6]U-750, Centro de Investigación en Red de Enfermedades Raras (CIBERER), ISCIII
[7]U-730, Centro de Investigación en Red de Enfermedades Raras (CIBERER), ISCIII
[8]Logopharm GmbH, D-79232 March-Buchheim, Germany
[9]Department of Cell Biology, Faculty of Biology, University of Barcelona, 08028 Barcelona, Spain
[10]Laboratory Neurophysiology, Department Physiological Sciences I, School of Medicine, University of Barcelona-IDIBAPS, 08007, Spain
[11]These authors contributed equally to this work
*Correspondence: restevez@ub.edu
DOI 10.1016/j.neuron.2011.12.039

SUMMARY

Ion fluxes mediated by glial cells are required for several physiological processes such as fluid homeostasis or the maintenance of low extracellular potassium during high neuronal activity. In mice, the disruption of the Cl^- channel ClC-2 causes fluid accumulation leading to myelin vacuolation. A similar vacuolation phenotype is detected in humans affected with megalencephalic leukoencephalopathy with subcortical cysts (MLC), a leukodystrophy which is caused by mutations in *MLC1* or *GLIALCAM*. We here identify GlialCAM as a ClC-2 binding partner. GlialCAM and ClC-2 colocalize in Bergmann glia, in astrocyte-astrocyte junctions at astrocytic endfeet around blood vessels, and in myelinated fiber tracts. GlialCAM targets ClC-2 to cell junctions, increases ClC-2 mediated currents, and changes its functional properties. Disease-causing *GLIALCAM* mutations abolish the targeting of the channel to cell junctions. This work describes the first auxiliary subunit of ClC-2 and suggests that ClC-2 may play a role in the pathology of MLC disease.

INTRODUCTION

Megalencephalic leukoencephalopathy with subcortical cysts (MLC) is a rare type of leukodystrophy (van der Knaap et al., 1995a) characterized by macrocephaly that appears in the first years of life. MRI of patients shows swelling of the cerebral white matter and the presence of subcortical cysts, mainly in the anterior temporal regions. In MLC patients, diffusion studies indicate increased water content of the brain (van der Knaap et al., 1995b). A brain biopsy from an MLC patient revealed myelin (van der Knaap et al., 1996) and astrocyte vacuolation (Duarri et al., 2011). It was suggested that MLC may be caused by impaired ion transport across cellular membranes, thereby leading to an osmotic imbalance and disturbed fluid homeostasis (Brignone et al., 2011; Duarri et al., 2011). Indeed, *MLC1*, the first disease gene discovered to underlie MLC in most patients (Leegwater et al., 2001), encodes an integral membrane protein with 8 putative transmembrane domains with low and questionable homology to ion channels (Teijido et al., 2004). Recently, MLC1 has been proposed to be related to the activation of the volume-regulated anion channel (Ridder et al., 2011). However, the precise role of MLC1 in volume-regulated chloride transport is not clear (Ridder et al., 2011).

Among the ion channels that are expressed in glia, the hyperpolarization-activated and osmosensitive ClC-2 Cl^- channel (Gründer et al., 1992; Thiemann et al., 1992) has been proposed to be an important player in extracellular ion homeostasis (Blanz et al., 2007; Fava et al., 2001; Makara et al., 2003). Mice lacking ClC-2 (*Clcn2*$^{-/-}$ mice) exhibit vacuolation of the white matter that resembles the pathology of MLC patients (Blanz et al., 2007). *MLC1* mutations account for only 75% of patients with MLC, but none of the patients without mutations in *MLC1* carried bona fide disease-causing mutations in *CLCN2* (Blanz et al., 2007; Scheper et al., 2010). Tests for a crosstalk between ClC-2 and MLC1 also gave negative results. The proteins could not be coprecipitated, and reduction of MLC1 levels by RNA interference did not change ClC-2 protein levels (Duarri et al., 2011). Hence, no role of ClC-2 in human MLC could be established.

GLIALCAM was recently identified as a second MLC gene (López-Hernández et al., 2011a). GlialCAM is an Ig-like cell-adhesion molecule of poorly characterized function (Favre-Kontula

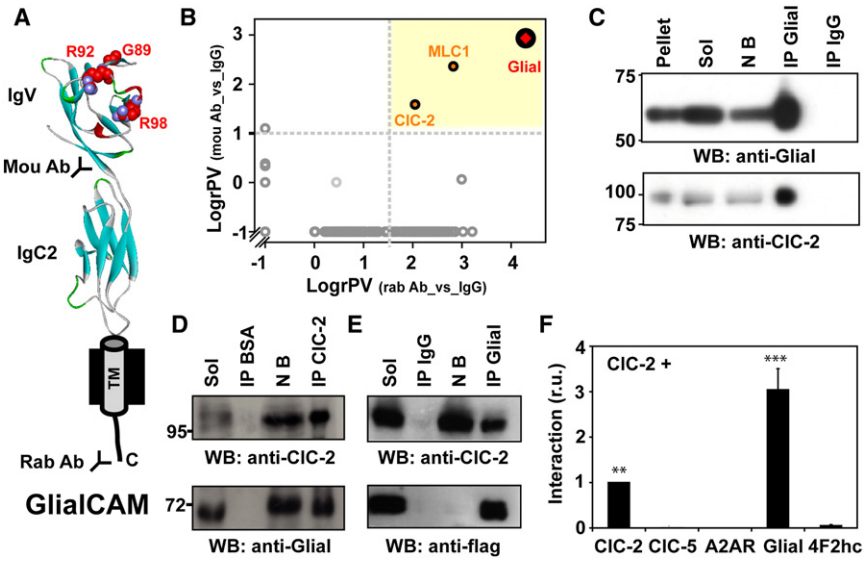

Figure 1. Identification of ClC-2 as a GlialCAM-Interacting Protein

(A) Scheme of the GlialCAM molecule. Mutated residues studied in this work are depicted. Antibodies used for purification (mou: mouse; rab: rabbit) are shown.

(B) Evaluation of GlialCAM affinity purification from mouse brain. The scheme shows a 2D plot of relative protein enrichment in affinity purifications versus IgG controls. Proteins specifically copurified are shown in the yellow area; dashed lines indicate the specificity thresholds as suggested by the distribution of all protein ratios (gray circles).

(C), Immunoblot analysis of a sample of the affinity purification with the anti-GlialCAM rabbit polyclonal antibody stained with the same antibody (upper) and with anti-ClC-2 C1 antibody (lower); lanes resolve aliquots of pellet after solubilization, solubilizate (Sol), not bound (NB), or eluates from the purification (IP Glial). IP IgG: eluate from an IgG control.

(D) Copurification of GlialCAM with anti-ClC-2 C2 antibody. Lanes were labeled as before.

(E) Coimmunoprecipitation from HeLa cells transiently transfected with ClC-2 and Flag-tagged GlialCAM. Lanes were labeled as before.

(F) Quantification of interaction using the split-TEV assay. ClC-2 was tested for interaction with the proteins indicated below the graph. $^{**}p < 0.01$; $^{***}p < 0.001$ versus 4F2hc.

See also Figure S1.

et al., 2008). A role of GlialCAM in MLC was first suggested by biochemical assays that demonstrated that both proteins bind each other and colocalize in astrocyte-astrocyte junctions at astrocytic endfeet (López-Hernández et al., 2011a). GlialCAM targets MLC1 to cell-cell junctions (López-Hernández et al., 2011b) and *GLIALCAM* mutations identified in MLC patients impair the correct trafficking of GlialCAM and MLC1 to astrocyte-astrocyte junctions (López-Hernández et al., 2011a, 2011b).

Unlike MLC1, GlialCAM is also detected in myelin (López-Hernández et al., 2011a), mainly in oligodendroglial extensions (Favre-Kontula et al., 2008). In the present work, we show that GlialCAM interacts with ClC-2 in several glial cell types including oligodendrocytes, targeting it to cell junctions and dramatically increasing its conductance. We thus identified GlialCAM as an auxiliary subunit of ClC-2, potentially implicating the channel in the pathogenesis of MLC.

RESULTS

Identification of ClC-2 as GlialCAM Binding Partner

We used two different antibodies directed against GlialCAM (Figure 1A) to identify proteins from solubilized mouse brain membranes that copurify with GlialCAM. In addition to peptides from GlialCAM and MLC1, quantitative mass spectroscopy identified peptides corresponding to the ClC-2 chloride channel (Figure 1B and see Figure S1 available online) as the only other consistently and specifically copurified protein in the eluate. Western blot analysis confirmed that ClC-2 was copurified with at least a fraction of GlialCAM (Figure 1C), which may result from a partial dissociation of the complex or may indicate that not all GlialCAM is associated with ClC-2. Coimmunoprecipitation experiments using an antibody against ClC-2 confirmed the interaction between GlialCAM and ClC-2 (Figure 1D). Similar experiments using extracts from cells transfected with ClC-2 and C terminally tagged GlialCAM (Figure 1E), as well as split-TEV interaction experiments (Figure 1F), suggested that ClC-2 and GlialCAM directly interact. The interaction appeared specific since no association was observed between ClC-2 and the related $2Cl^-/H^+$ antiporter ClC-5, the unrelated polytopic adenosine 2A receptor (A2AR), or the unrelated single transmembrane span protein 4F2hc (Figure 1F).

Colocalization of ClC-2 and GlialCAM in Tissue

For the interaction of GlialCAM and ClC-2 to be physiologically relevant, both proteins must colocalize in native tissue. GlialCAM is found exclusively in brain, where it localizes to astrocyte-astrocyte junctions at endfeet, Bergmann glia, some pyramidal neurons and to myelin (López-Hernández et al., 2011a). In addition to neurons, ClC-2 is expressed on astrocytes and oligodendrocytes and was found in myelin-enriched fractions (Blanz et al., 2007; Fava et al., 2001; Földy et al., 2010; Makara et al., 2003; Rinke et al., 2010; Sík et al., 2000). GlialCAM colocalized in mouse brain with ClC-2 in cerebellar Bergmann glia which was counterstained for GFAP (Figure 2A). Both proteins were present at astrocytic endfeet surrounding blood vessels (Figure 2B; Blanz et al., 2007; López-Hernández et al., 2011a; Sík et al., 2000) in the cortex and in the cerebellum. In human cerebellum, immunogold electron microscopy detected ClC-2 at astrocyte-astrocyte contacts in the endfeet (Figures 2C and 2D), a location where also GlialCAM and MLC1 are present (López-Hernández et al., 2011a). GlialCAM and ClC-2 were also found to colocalize in myelinated fiber tracts along the circumference of oligodendrocytic cell bodies in mouse cerebellum (Figure 2E), where GlialCAM, ClC-2, and the oligodendrocyte-expressed gap junction protein Cx47 were present in the same cell membrane (Figure 2F; Blanz et al., 2007). In vitro cell culture

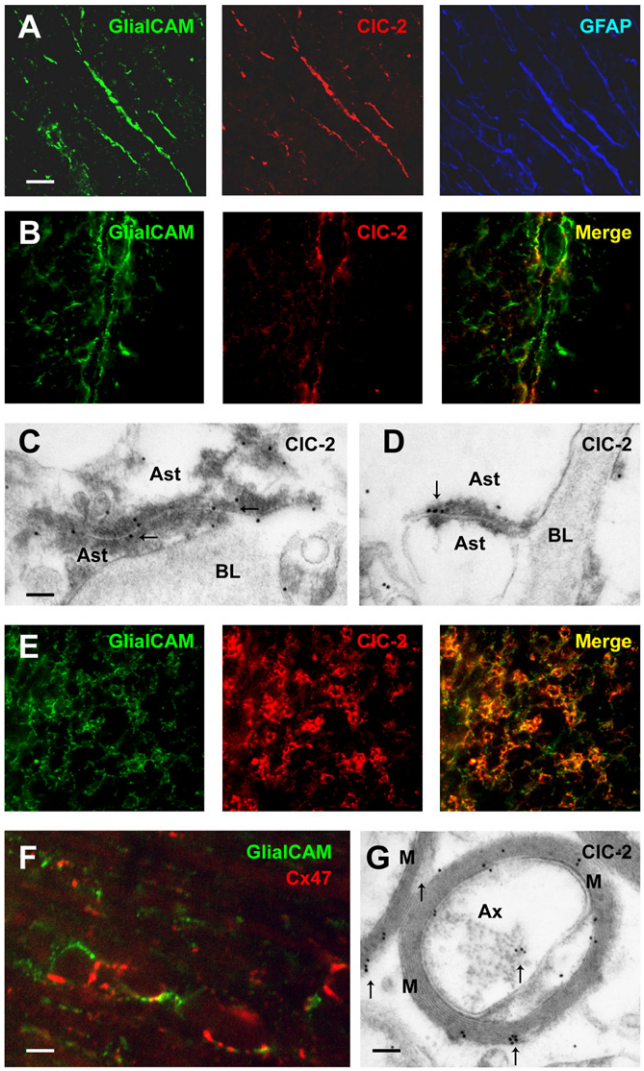

Figure 2. Localization of ClC-2 and GlialCAM in the Brain

Mouse brain sections labeled with antibodies against GlialCAM, ClC-2, or GFAP antibodies. (A) cerebellar Bergmann glia; (B) astrocytic endfeet surrounding blood vessels in cortex; (C and D) EM immunolabeling of human cerebellum shows localization of ClC-2 (arrows) in astrocyte-astrocyte junctions near basal lamina; (E) oligodendrocytic cell bodies in myelinated fibers of cerebellar white matter tracts.

(F) Coexpression of GlialCAM and the oligodendrocyte marker Cx47 in membranes of oligodendrocytic bodies in the cerebellum.

(G) EM immunolabeling detects ClC-2 in myelin (arrows).

Scale bars for (A), (B), and (E) 20 μm; (F) 5 μm; for panels (C) and (D) 200 nm; (G) 500 nm. M: myelin; Ax: axon; Ast: astrocyte; BL: basal lamina. ClC-2 antibodies used: C1 (A); C2 (B–F). See also Figure S2.

studies have shown that GlialCAM is expressed in different stages of oligodendrocytic differentiation, including the bipotential O2-A progenitor NG2 positive cells (OPC cells) (Favre-Kontula et al., 2008). Immunogold EM confirmed the presence of ClC-2 in human myelin (Figure 2G).

Localization and expression of GlialCAM is independent of MLC1 (López-Hernández et al., 2011b). We similarly asked whether the expression of GlialCAM or MLC1 depends on ClC-2. Western blots revealed that the total amount of GlialCAM and MLC1 proteins were unchanged in the brain of *Clcn2*$^{-/-}$ mice (Figure S2A). Likewise, there was no change in the subcellular localization of GlialCAM and MLC1 in Bergmann glia, nor in the astrocytic endfeet around blood vessels in *Clcn2*$^{-/-}$ mice (Figures S2B and S2C).

GlialCAM Changes the Subcellular Distribution of ClC-2

We then studied whether GlialCAM changes the abundance or localization of ClC-2 in heterologous expression systems. We could not detect that GlialCAM changes ClC-2 protein levels (data not shown) and ClC-2 surface expression after transfection of HeLa cells or transduction of primary astrocytes, as ascertained in a chemiluminescence assay (Figure S3).

Since GlialCAM has been described to target MLC1 to cell-cell junctions (López-Hernández et al., 2011b), we assayed if GlialCAM could also modify ClC-2 localization in the same manner. In HeLa cells, ClC-2 transfected alone was detected at the plasma membrane and intracellularly (Figure 3A). Coexpression with GlialCAM directed the ClC-2 channel to cell-cell contacts (Figures 3B–3D), where both proteins colocalized (data not shown). Localization of ClC-2 together with GlialCAM was observed in long (Figure 3B) or short (Figure 3C) cell-cell contact processes and in extensive contact areas between opposite cells (Figure 3D). Such a clustering was never observed in contacting cells expressing only ClC-2 (Figure 3A). Similar results were observed in HEK293 cells (data not shown). We performed analogous experiments in primary cultures of astrocytes, where both proteins are endogenously expressed. In these cultures, adenoviral-mediated expression of ClC-2 with or without GlialCAM showed that the latter protein was necessary to target ClC-2 to astrocyte-astrocyte processes (compare Figures 3E and 3F). In these junctions, ClC-2 and GlialCAM displayed colocalization (Figures 3F–3H).

GlialCAM Modifies ClC-2 Currents

We next asked whether GlialCAM could modify ClC-2 function. Coexpression of GlialCAM and ClC-2 in *Xenopus* oocytes dramatically increased ClC-2-mediated currents and changed their characteristics (Figure 4A). Initial currents measured at +60 mV were more than 15-fold larger in cells coexpressing ClC-2 and GlialCAM compared to ClC-2 alone. Whereas ClC-2 currents are strongly inwardly rectifying and activate slowly upon hyperpolarization, ClC-2/GlialCAM currents were almost ohmic and displayed time-independent, instantaneously active currents (Figure 4B). Of note, the apparent inactivation observed sometimes at very negative voltages is an artifact caused by chloride depletion inside the oocytes.

Similar effects of GlialCAM on ClC-2 currents were seen in transfected HEK293 cells, although a residual time-dependent component was present (Figure 4C). Importantly, GlialCAM alone does not induce any significant current in HEK cells or *Xenopus* oocytes (Figure S4). Similarly, in transfected cells, ClC-2 steady state currents at +60 mV were dramatically increased by GlialCAM (Figure 4D). Specificity of the currents was demonstrated by the characteristic block by extracellular

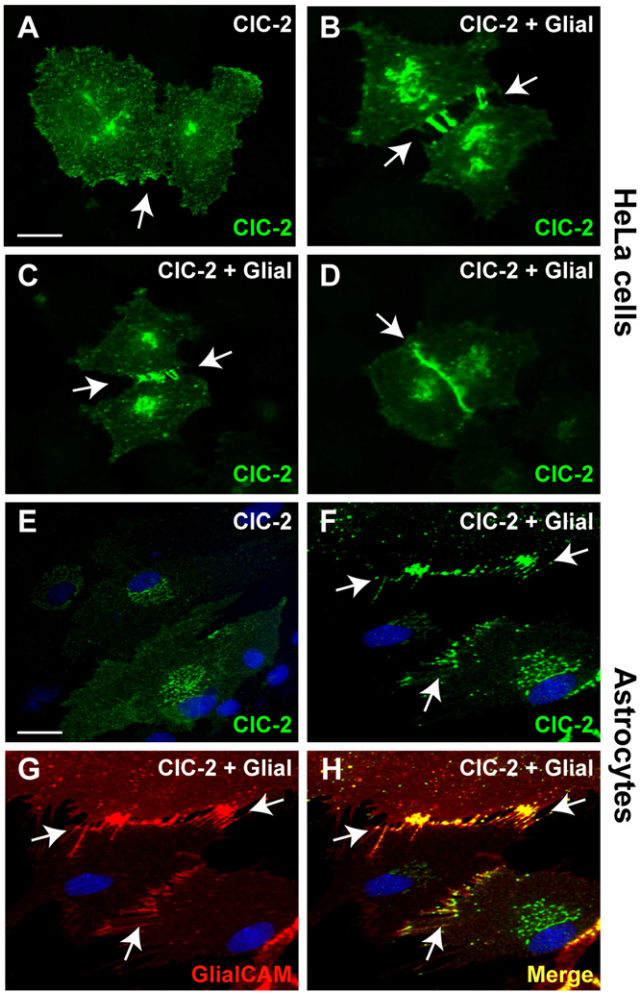

Figure 3. GlialCAM Changes the Subcellular Distribution of ClC-2 in HeLa Cells and in Primary Cultures of Astrocytes

(A–D) GlialCAM changed the subcellular distribution of ClC-2 in transiently transfected HeLa cells from being at the plasma membrane when transfected alone (A) versus being at long cell-cell contact processes (B), at short cell-cell contact processes (C), or in extensive contact regions (D) when cotransfected with GlialCAM (arrows label cell-cell contacts). Scale bar: 10 μm.

(E–H) Astrocytes were transduced with adenoviruses expressing ClC-2 alone or together with C terminally tagged GlialCAM at MOI 3. GlialCAM similarly brought ClC-2 to cell-cell contacts. Arrows point to astrocyte-astrocyte contacts. Immunofluorescence used a flag monoclonal antibody detecting GlialCAM protein (red) or a rabbit polyclonal antibody (C1) detecting ClC-2 (green). Colocalization between the red and the green fluorescence results in a yellow coloring (Merge). Nuclei of astrocytes were stained using DAPI (blue). Scale bar: 20 μm.

See also Figure S3.

iodide (Gründer et al., 1992; Thiemann et al., 1992; Figure 4B) and cadmium (Clark et al., 1998) (data not shown).

To test if GlialCAM may alter native ClC-2 currents we performed whole-cell patch-clamp experiments in differentiated rat astrocytes. These cells exhibit typical hyperpolarization-activated ClC-2-like currents that were blocked by iodide (Ferroni et al., 1997; Makara et al., 2003; Figure 4E). After GlialCAM overexpression, currents were increased and showed a large instantaneous component and less rectification (Figure 4F), qualitatively similar to the effect on ClC-2 in the heterologous systems. These currents were also blocked by iodide to similar degree (Figure 4E).

Even if GlialCAM and connexins do not overlap significantly (Figures 2F and S4D), it may be hypothesized that GlialCAM expression increases ionic currents by stimulating currents through gap junction proteins. However, overexpression of GlialCAM did not modify expression and localization of connexin 43, the major connexin of astrocytes (Figures S4C and S4E). Furthermore, blocking gap junctions with glycyrrhetinic acid did not influence GlialCAM-induced currents in coupled astrocytes (Figure S4F), which were, however, blocked by iodide which is known to block ClC-2 (Gründer et al., 1992; Thiemann et al., 1992; Figure 4F).

We next addressed whether the effect of GlialCAM was specific to ClC-2. GlialCAM did not change currents of ClC-5 at positive or negative voltages (Figure 5A). We studied if human GlialCAM could interact with the ClC-2 ortholog from *Drosophila melanogaster* (DmClC-2) (Flores et al., 2006), whose genome lacks a GlialCAM ortholog. GlialCAM interacted biochemically and increased currents of DmClC-2 (Figures 5B and 5C), suggesting that GlialCAM evolved to interact with the channel at an interface that is evolutionary conserved among ClC-2 like channels. Additionally, we addressed interaction with the closest homolog of GlialCAM named HepaCAM2. No biochemical and functional interaction was observed between HepaCAM2 and ClC-2 (Figures 5D and 5E). Finally, we asked whether wild-type MLC1 or MLC1 containing MLC-causing mutations could influence ClC-2 or ClC-2/GlialCAM induced current in *Xenopus* oocytes. We did not find any effect on ClC-2 mediated currents (Figure 5F).

Insights into the Molecular Mechanism of ClC-2 Activation by GlialCAM

Currents of *Xenopus* oocytes expressing GlialCAM/ClC-2 resemble those of an N-terminal deletion of ClC-2 (ΔN), in which the osmosensitivity and the voltage-dependence is drastically altered (Gründer et al., 1992). This might suggest that GlialCAM activates ClC-2 by interacting with its N terminus. However, we found that GlialCAM still interacted biochemically with (Figure S5A) and targeted the ΔN mutant to cell-cell contacts (Figure S5B) just like wild-type ClC-2. Moreover, GlialCAM potentiated ΔN currents in transfected HEK293 cells (Figure S5C).

We then compared the functional properties of ClC-2, ΔN and GlialCAM/ClC-2. Hypo-osmolarity increased currents of GlialCAM/ClC-2 and ClC-2, but had no effect on ΔN (Gründer et al., 1992; Figure 6A). All of them have the same anion permeability sequence (Figure 6B), strongly suggesting that GlialCAM has no effect on the open-pore properties of the channel. We also addressed whether GlialCAM could increase the single channel conductance of the channel by performing nonstationary noise analysis of currents induced by ClC-2 or by ClC-2/GlialCAM at −100 mV in transfected HEK cells. The conductance of ClC-2 was estimated at 2.9 ± 0.4 pS (n = 8), a value very similar to what has been previously reported (Weinreich and Jentsch,

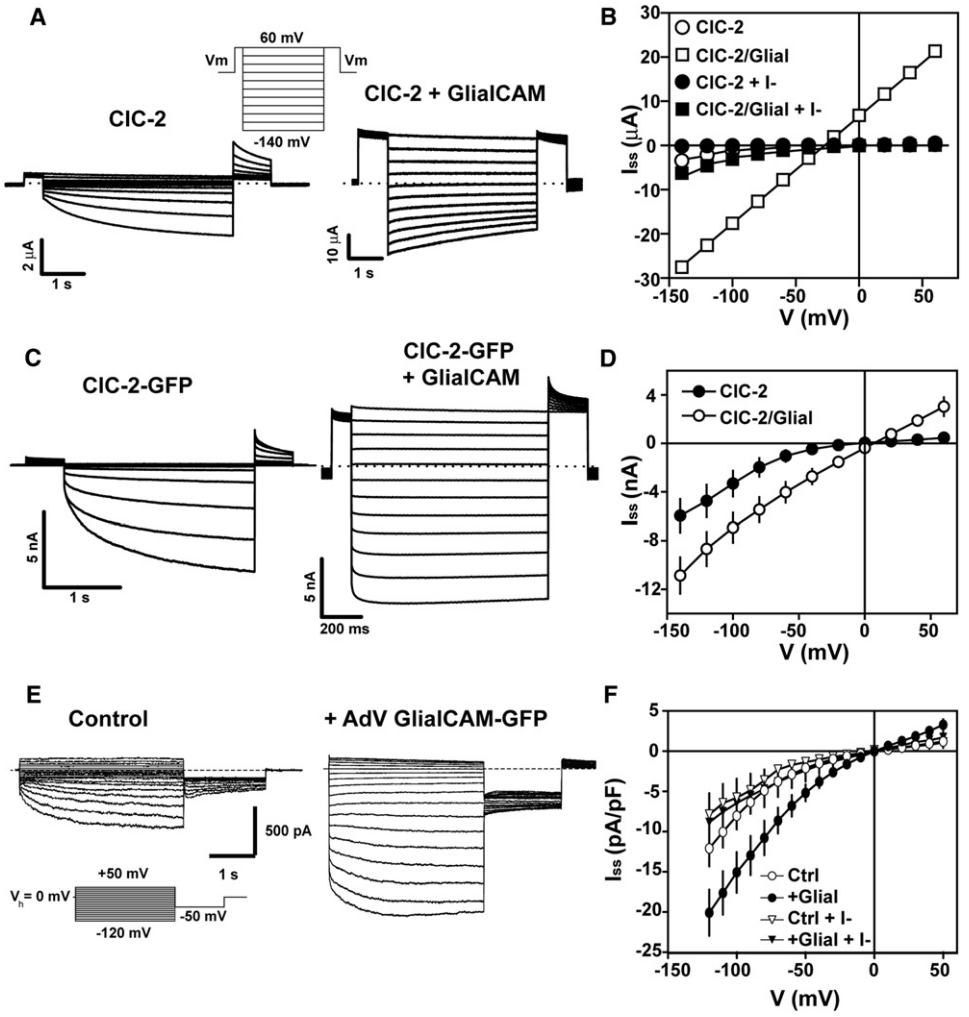

Figure 4. GlialCAM Modifies ClC-2 Currents in *Xenopus* Oocytes, HEK Cells, and Primary Rat Astrocytes

(A) Currents mediated by ClC-2 (left) expressed in oocytes and after coexpression of ClC-2 with GlialCAM (right).

(B) Representative steady-state current-voltage relationship of ClC-2 (circles) and ClC-2 coexpressed with GlialCAM (squares) in chloride (open symbols) or iodide (filled symbols). Average initial currents measured at +60 mV were 0.96 ± 0.17 μA (n = 14) for ClC-2 and 17.2 ± 2.2 μA (n = 10) for ClC-2/GlialCAM.

(C) Typical whole-cell currents from transfected HEK293 cells with ClC-2-GFP alone (left) or together with GlialCAM (right). The GFP tag does not affect ClC-2 current properties.

(D) Average steady-state current voltage from ClC-2-GFP (filled circles) or ClC-2-GFP/GlialCAM (circles) transfected HEK293 cells.

(E) Left: representative trace of whole-cell inwardly rectifying chloride currents in dbcAMP-treated cultured neocortical rat astrocytes. These currents, as described (Ferroni et al., 1997), were blocked when chloride was replaced by iodide (F) and were not blocked by tamoxifen (data not shown). Right: representative trace of chloride currents of dbcAMP-treated astrocytes transduced with adenoviruses expressing GlialCAM fused to GFP. The inset shows the voltage protocol used.

(F) Average steady-state current-voltage relationship of dbcAMP-treated astrocytes (circles, n = 14) or transduced with adenoviruses expressing GlialCAM-GFP (filled circles, n = 14) in chloride medium. Recordings were performed in symmetrical chloride concentrations. In some recordings chloride was exchanged by iodide (triangles or filled triangles). At hyperpolarizing voltages iodide block was by 32.7% ± 3.2% for control astrocytes (n = 6) and by 56.8% ± 2.9% for astrocytes transduced with adenoviruses expressing GlialCAM-GFP (n = 8).

See also Figure S4.

2001). For ClC-2/GlialCAM we obtained a value of 2.6 ± 0.2 pS (n = 8), not statistically significantly different from the value for ClC-2 alone ($p > 0.5$). We conclude that GlialCAM does not modify single-channel properties of ClC-2. Interestingly, GlialCAM similarly diminished the inhibition by acidic pH of both ClC-2 and ΔN (Figure 6C). This result suggested that GlialCAM may activate ClC-2 by opening the common gate that acts on both pores of the homodimeric channel, as this gate is sensitive to acidic pH (Niemeyer et al., 2009).

GlialCAM displays a long cytoplasmatic C terminus comprising about 30% of the protein (Favre-Kontula et al., 2008). However, consistent with its poor sequence conservation between species, the deletion of the entire C terminus did not abolish the interaction with ClC-2, its targeting to cell junctions, and the

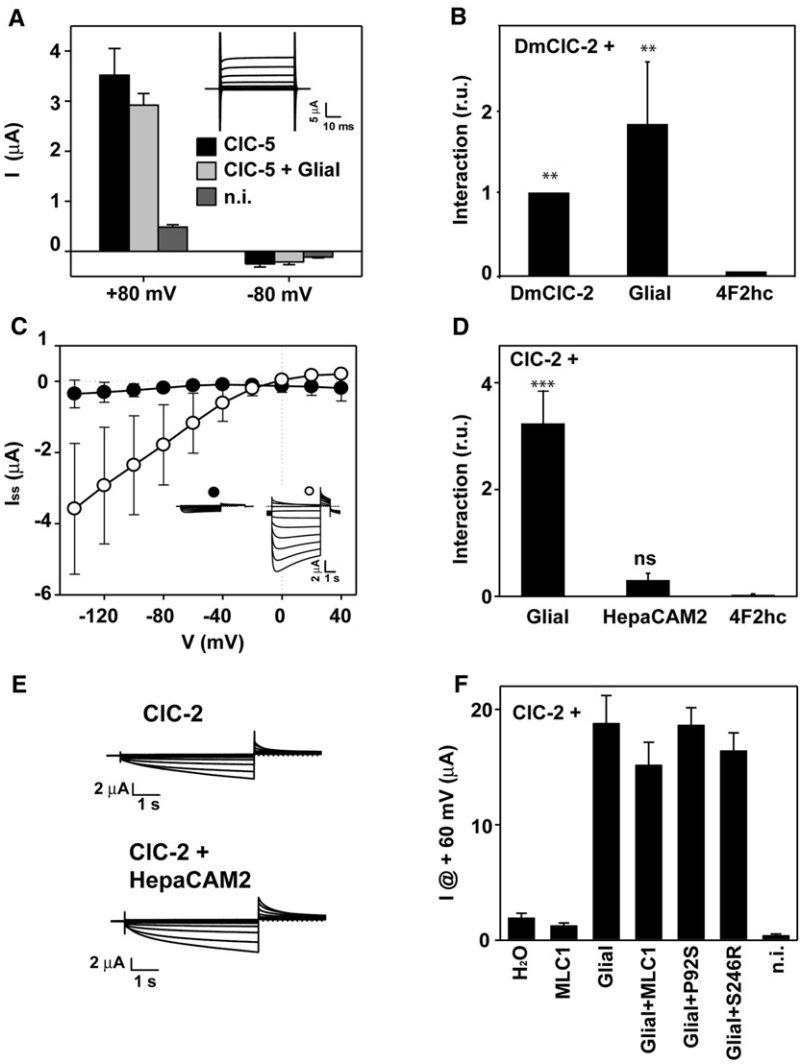

Figure 5. Specificity of the ClC-2 GlialCAM Interaction

(A) Human ClC-5 was expressed in oocytes with and without GlialCAM. Currents were quantified at positive (+80 mV) and negative (−80 mV) voltages 3 days after injection. The inset shows representative ClC-5 + GlialCAM traces using a voltage-clamp protocol with pulses ranging from +120 mV to −120 mV in 20 mV steps.

(B) Interaction between DmClC-2 and DmClC-2 or GlialCAM was monitored using split-TEV assays. 4F2hc was used as a negative control. The result is an average of 5 independent experiments. **$p < 0.01$ versus 4F2hc.

(C) DmClC-2 was expressed in *Xenopus* oocytes by itself or together with GlialCAM. Two days after injection in oocytes DmClC-2 ± GlialCAM currents were determined. Steady state currents are plotted against voltage (n = 5 ± SEM). The inset shows representative current traces of DmClC-2 (filled circle) and DmClC-2 / GlialCAM (open circle).

(D) Interaction between ClC-2 and GlialCAM or HepaCAM2 by split-TEV assays. 4F2hc was used as a negative control. The result is an average of 13 independent experiments. ***$p < 0.001$; "ns" indicates no significant difference versus 4F2hc.

(E) Typical ClC-2 currents in *Xenopus* oocytes expressed by itself (left) or coexpressed with HepaCAM2 (right). HepaCAM2 positive protein expression was assessed by Western blot (data not shown).

(F) Currents measured in *Xenopus* oocytes at + 60 mV after the expression of ClC-2 alone (3 ng), ClC-2 (3 ng) + GlialCAM (5 ng), or ClC-2 (3 ng) + GlialCAM (5 ng) + wild-type MLC1 (3 ng) or containing the MLC-causing mutations P92S and S246R (3 ng). The result is a representative experiment of two experiments with at least 5 oocytes measured for each condition.

activation of ClC-2 currents in transfected cells (Figures S5D–S5F). Hence the interaction between both proteins may depend on the transmembrane and/or the N-terminal part of GlialCAM. Deletion of the N-terminal part of GlialCAM, while keeping the cleavable signal peptide, resulted in a lack of surface expression (data not shown), precluding proper biochemical studies.

Impact of MLC-Related Mutations Identified in *GLIALCAM* on ClC-2

Several *GLIALCAM* mutations found in patients with MLC truncate the protein before the transmembrane domain or result in amino-acid changes in the N-terminal, extracellular part of GlialCAM (López-Hernández et al., 2011a). We studied four of these missense mutations located within the IgV domain (Figure 1A). All GlialCAM proteins containing MLC-causing missense mutations retained their physical interaction with ClC-2 (Figures 7A and S6A) and increased ClC-2 activity similar to wild-type GlialCAM in *Xenopus* oocytes (Figures 7B and S6B) and in transfected cells (data not shown). In contrast, all of them abolished the targeting of ClC-2 to cell junctions in HeLa or HEK293 cells (Figures 7C and 7D).

We also analyzed the effect of the MLC-causing mutations in GlialCAM on the localization of ClC-2 in primary cultures of rat astrocytes through adenoviral-mediated transduction (Figure 8). Coexpression of ClC-2 with GlialCAM mutant variants resulted in intracellular and cell membrane staining of ClC-2 (Figures 8B–8E), but not the typical wild-type GlialCAM induced localization in cell junctions (Figure 8A).

DISCUSSION

In this work, we have identified GlialCAM as an interaction partner of the ClC-2 chloride channel. As ClC-2 is functional in the absence of GlialCAM, albeit displays different biophysical properties, and since GlialCAM shows a much more restricted expression pattern than ClC-2 (Thiemann et al., 1992), it is clear that GlialCAM is not an obligate β-subunit of ClC-2, but an auxiliary subunit that associates with ClC-2 only in some cell types. MLC1 wild-type or containing MLC-causing mutations, by contrast, does not modify ClC-2 currents neither in the presence nor in the absence of GlialCAM, and biochemical studies indicate that ClC-2 and MLC1 do not interact directly (Duarri

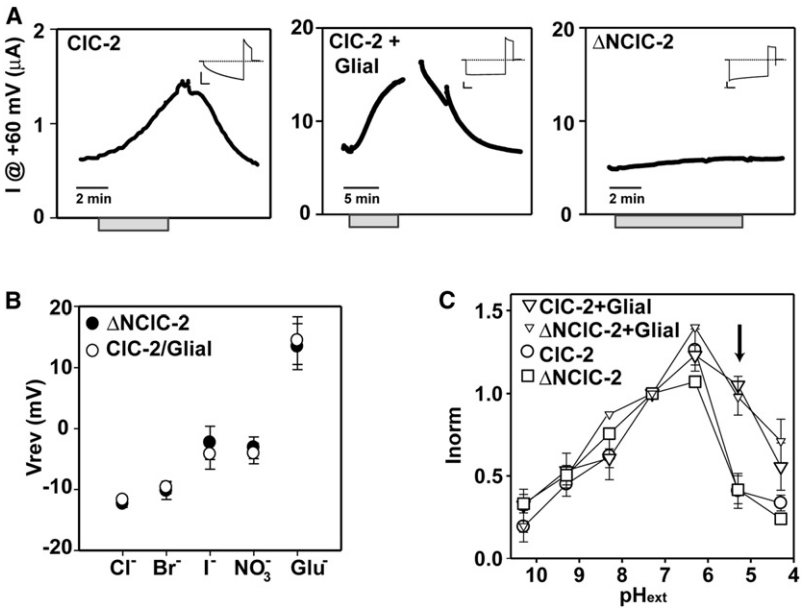

Figure 6. Electrophysiological Characterization of the GlialCAM/ClC-2 Complex

(A) Dependence on the extracellular osmolarity of ClC-2, ClC-2 + GlialCAM, or ΔNClC-2 currents. Gray bars indicate application of the hypotonic solution. Insets show typical responses of the same oocytes to a pulse to −140 mV before swelling.

(B) Reversal potential of ΔNClC-2 (n = 5 ± SEM) and ClC-2/GlialCAM (n = 5 ± SEM) currents under different anionic conditions.

(C) pH dependence of ClC-2 and ΔNClC-2, each without and with GlialCAM. Currents were normalized to the value at pH 7.3. Arrow points to the pH value with the largest difference between the groups that express or not GlialCAM.

See also Figure S5.

et al., 2011). Furthermore, MLC1 expression and localization is unaltered in *Clcn2*$^{-/-}$ mice. These data suggest that GlialCAM/MLC1 and GlialCAM/ClC-2 may form distinct complexes. Recently, the lack of MLC1 has been correlated with a variable impairment in cell volume regulation that may be mediated by the volume regulated anion channel (VRAC) (Ridder et al., 2011). However, VRAC is distinct from ClC-2 as evident from very different biophysical characteristics (Jordt and Jentsch, 1997). Furthermore, the mechanism of modulation of VRAC by MLC1 is unclear. As MLC1 and ClC-2 share GlialCAM as a subunit, we cannot exclude that MLC1 could regulate ClC-2 function in an indirect/unknown manner. Therefore, an interesting hypothesis that should be tested in the next future is whether ClC-2 function is altered in cells lacking MLC1.

GlialCAM by itself localizes to cell-cell junctions (López-Hernández et al., 2011b), probably being retained there by homophilic or heterophilic interactions with membrane proteins of the apposing cell. In other GlialCAM homolog proteins such as the members of the SLAM family (Engel et al., 2003), localization at the immunological synapse of SLAM proteins is achieved by trans-homophilic interactions between the IgV domains of opposite molecules. Furthermore, GlialCAM is also able to localize ClC-2 and MLC1 (López-Hernández et al., 2011b) to cell-cell junctions in heterologous expression systems and in primary cultures of astrocytes. The role of GlialCAM as a ClC-2 subunit appears to be specific within its protein family, as its closest homolog, HepaCAM2, did not interact with ClC-2. GlialCAM carrying MLC-related mutations (López-Hernández et al., 2011a) fails to arrive at cell-cell junctions (López-Hernández et al., 2011b). As a consequence, also their associated subunits, MLC1 and ClC-2, are not properly targeted to cell-cell junctions. Thus, GlialCAM function may be needed to cluster ClC-2 and MLC1 in particular to astrocyte-astrocyte junctions at astrocytic endfeet. Here, the ClC-2 chloride channel may be needed to support a transcellular chloride flux or to compensate large electrochemical ion gradients that may occur at these junctions during ion-driven changes in osmolarity. However, the chloride flux mediated by ClC-2/GlialCAM in cell junctions most likely fulfills a different role compared to the one mediated by gap junctions as these proteins do not colocalize completely. Our experiments also exclude that GlialCAM activates astrocyte gap junctions, since their blockade did not influence currents induced by GlialCAM overexpression, and GlialCAM overexpression had no influence on connexin 43 protein levels or its subcellular localization.

Recent reports indicated that the ClC-2 channel in neurons constitutes a part of the background conductance regulating input resistance and providing an efflux pathway for chloride (Földy et al., 2010; Rinke et al., 2010), which may be a safeguard mechanism to prevent chloride accumulation in active GABAergic synapses. In contrast, the role of ClC-2 in glial cells is unknown. Recordings from mouse slices demonstrated that ClC-2-mediated current was reduced in reactive astrocytes within a lesion (Makara et al., 2003). Strong evidence in favor of an important physiological role of ClC-2 in glial cells is provided by the phenotype of *Clcn2*$^{-/-}$ mice, which display an MLC-like vacuolization in the brain (Blanz et al., 2007). Vacuolization in the brain has been also observed in mice disrupted for the potassium channel Kir4.1 (Neusch et al., 2001) or double-disrupted for connexins 32 *and* 47 (Menichella et al., 2006). These proteins are thought to be crucial for potassium siphoning by glial cells, a process that is needed to avoid neuronal depolarization by extracellular K^+ during repetitive action potential firing (Rash, 2010). In agreement with this role in ion siphoning, in Kir4.1 knockout mice there was no vacuolation in the optic nerve after blocking action potential generation with tetrodotoxin (Neusch et al., 2001). It was neither observed in the *Clcn2*$^{-/-}$ mice possibly because they are blind due to retinal degeneration (Blanz et al., 2007). Hence degeneration in both mouse models depend on nerve activity, in accord with the siphoning process that is required after neuronal repolarization. It has been suggested that ClC-2 may play a role in charge compensation during potassium influx or efflux in glial cells (Blanz et al., 2007).

ClC-2-mediated currents were increased upon GlialCAM expression and showed less inward rectification. However,

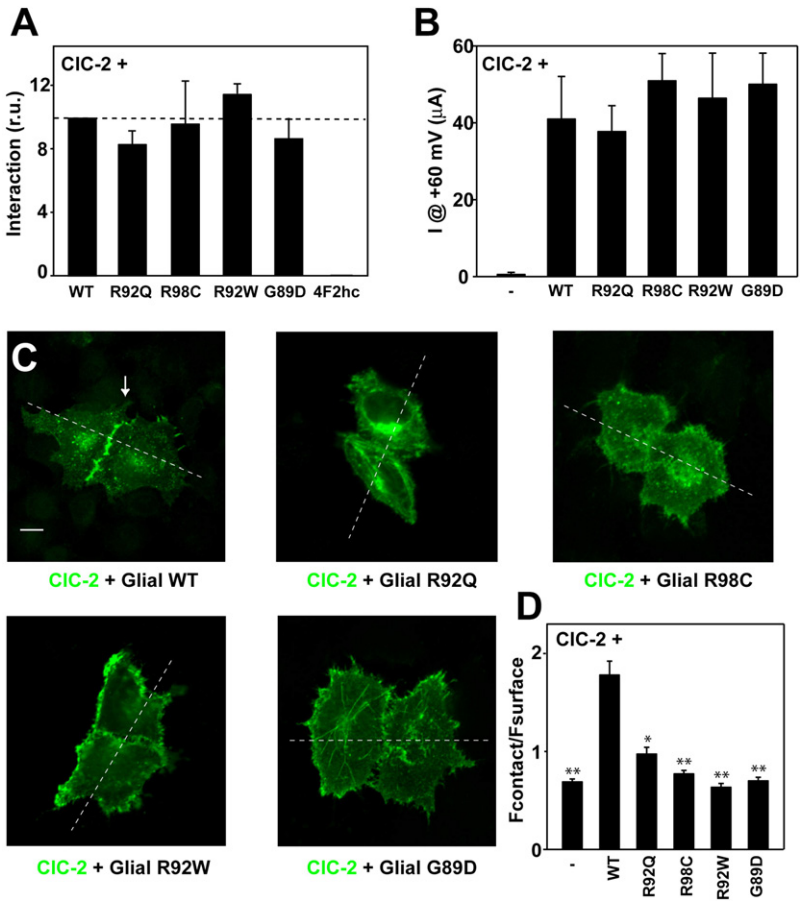

Figure 7. Biochemical and Functional Consequences of *GLIALCAM* Mutations on ClC-2

(A) Interaction between ClC-2 and GlialCAM or GlialCAM containing MLC-related mutations revealed by split-TEV interaction assays (n = 5).

(B) Average instantaneous currents at +60 mV from ClC-2 expressing oocytes coinjected with saturating concentrations of GlialCAM or the indicated GlialCAM variants. The result is an average of n = 5 in each experiment from three independent experiments.

(C) Immunofluorescence of HeLa cells expressing ClC-2 plus wild-type GlialCAM or GlialCAM containing the MLC-related mutations R92Q, R98C, R92W, and G89D. Scale bar: 10 μm. Expression at contact sites and non-contact surface membrane was determined by the analysis of the intensity profile along the dashed line.

(D) Relative fluorescence intensity at cell contacts. Intensity profile analysis revealed that ClC-2 alone had a ratio R of fluorescence $F_{contact}/F_{surface}$ (see Experimental Procedures) of 0.7 ± 0.03 (n = 58), ClC-2 + GlialCAM a value of 1.8 ± 0.14 (n = 55), and the GlialCAM variants studied (with at least 24 pair of cells analyzed) had R values less than 1 (see Experimental Procedures), indicating that the variants containing MLC-related mutations were not able to cluster ClC-2 to cell junctions. *p < 0.05, **p < 0.01 versus wild-type GlialCAM plus ClC-2. Similar results were observed in HEK cells (not shown).

See also Figure S6.

ClC-2 activity recorded in cultured astrocytes (Ferroni et al., 1997) or in astrocytes in brain slices (Makara et al., 2003) resembles that of ClC-2 alone. This may be due to different recording conditions, or, alternatively, it may be that GlialCAM interacts with ClC-2 only under special circumstances, such as those occurring during high neuronal activity.

A polarized distribution of the Kir4.1 channel in astrocyte membranes in contact with endothelial cells, mediated by interaction with proteins of the DGC (dystrophin-glycoprotein complex) (Nagelhus et al., 2004), is required for potassium siphoning. In an analogous way, the polarized localization of ClC-2 mediated by GlialCAM in astrocyte-astrocyte or oligodendrocyte-astrocyte contacts may be also needed to support a directional flux of potassium from neurons to blood vessels. As a cell-adhesion molecule, GlialCAM could influence the expression of other molecules expressed in cell junctions such as connexins. Similar to DGC proteins, the localization in cell-cell contacts of GlialCAM itself and of associated molecules may be achieved by transmediated interactions or by interactions with intracellular scaffolds in each cell. It seems possible that GlialCAM may organize a more extensive cluster of proteins at the astrocytic junctions in the endfeet.

We propose that the lack of the stimulatory effect of GlialCAM on ClC-2 currents, or a mislocalization of this Cl^- channel, or both, will impair glial chloride transport. This may impair not only chloride homeostasis, but also potassium siphoning and cell volume regulation that is particularly important during neuronal activity. This in turn may entail accumulation of osmotically driven water, lead to the vacuolization observed in MLC patients with mutations in *GLIALCAM* or in *Clcn2*$^{-/-}$ mice. Vacuolization observed in MLC patients with *GLIALCAM* mutations could also be due to defects in GlialCAM by itself, or to a mislocalization of MLC1, an established causal player in MLC. Additionally, the adhesive properties of GlialCAM, and their importance for the anatomy of the brain and the pathogenesis of MLC remain to be studied.

The fact that so far no disease-causing *CLCN2* mutation has been found in patients with MLC (Blanz et al., 2007; Scheper et al., 2010) might be explained by the presence of additional symptoms (e.g., blindness, male infertility, as expected from the phenotype of *Clcn2*$^{-/-}$ mice [Bösl et al., 2001]) that could result in improper disease classification. The male infertility could also lead to an underrepresentation of *CLCN2* mutations in the human population. Thus, proof of the involvement of ClC-2 in MLC disease will require, for example, immunolocalization studies in brain biopsies of MLC patients with *GLIALCAM* mutations.

In summary, the discovery of GlialCAM as the first auxiliary subunit of ClC-2 increases the complexity of regulation of the CLC chloride transporter/channel family for which so far only two β-subunits have been described (Estévez et al., 2001; Lange et al., 2006). Our work provides new clues to uncover the physiological role of the ClC-2 channel in glial cells, and suggests that

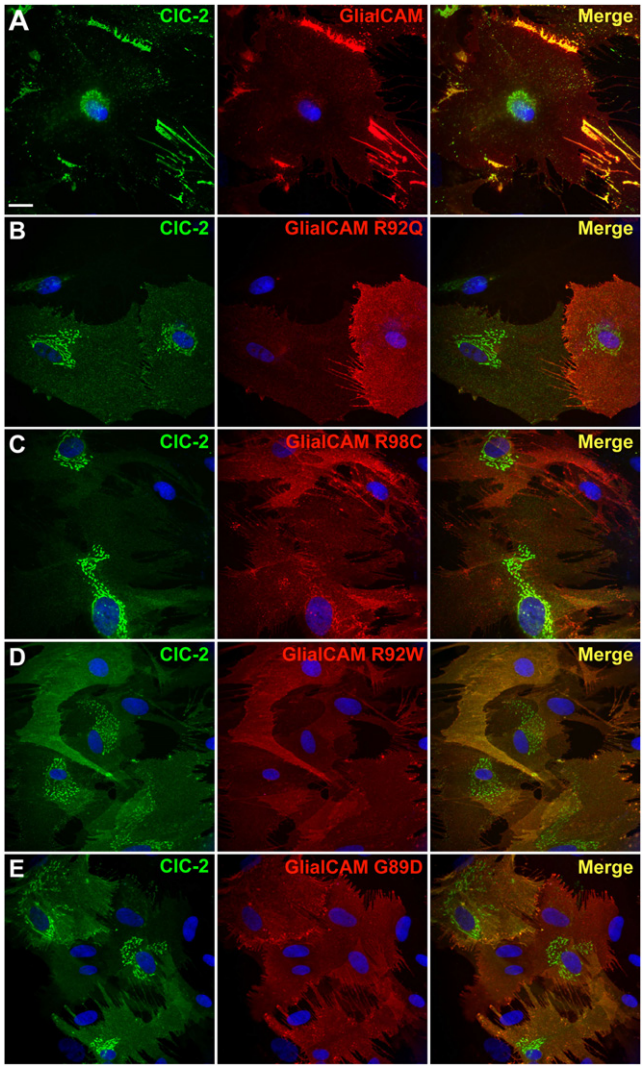

Figure 8. ClC-2 and GlialCAM Subcellular Localization Changes Caused by *GLIALCAM* Mutations in Primary Cultures of Astrocytes

(A–E) Astrocytes were cotransduced with adenoviruses expressing ClC-2 together with wild-type GlialCAM (A) or containing the MLC-related mutations R92Q (B), R98C (C), R92W (D), and G89D (E). Cells were fixed, permeabilized, and then immunofluorescence was performed with a rabbit polyclonal antibody against ClC-2 (green) and a monoclonal antibody detecting GlialCAM protein (red). Nuclei were stained with DAPI (blue). Colocalization between the green and the red channel is shown in yellow. Images correspond to representative cells from three independent experiments. Scale bar: 20 μm.

the ClC-2 channel may be involved in the physiopathology of MLC disease.

EXPERIMENTAL PROCEDURES

Biochemistry

Proteomic analysis: for solubilization, membrane vesicles (1 mg) were resuspended in ComplexioLyte buffer 47a (at 0.8 mg protein/ml, LOGOPHARM GmbH, Germany; with protease inhibitors), incubated for 30 min at 4°C and cleared by ultracentrifugation (10 min at 150,000 × g). 0.8 ml solubilizates were incubated for 2 hr at 4°C with 10 μg of immobilized anti-rabbit GlialCAM (López-Hernández et al., 2011a), anti-mouse GlialCAM (Vitro, Spain) and control IgG (Upstate, USA), respectively. After brief washing (2 × 5 min) with ComplexioLyte 47a, bound proteins were eluted with Laemmli buffer (DTT added after elution). Eluates were shortly run on SDS-PAGE gels and silver-stained prior to tryptic digestion for MS analysis. LC-MS/MS analysis was performed as described (López-Hernández et al., 2011a). Immunoprecipitation and western blot studies of HeLa cells transiently transfected or solubilized rat brain to confirm protein-protein interactions with ClC-2 and GlialCAM antibodies was performed as described (López-Hernández et al., 2011a). Relative MS sequence coverage of ClC-2 protein (Figure S1) was calculated as $SC = N_i/(N_i + N_{an})$, where N_i is the number of amino acid residues of the identified peptides (with Mascot score $\geq$ 20) and N_{an} is the number of MS-accessible but not identified amino acids (peptides with mass of 740–3,000 u) of the respective Swiss-Prot sequence.

Molecular Biology

Rat ClC-2 and the N-terminal deletion (Δ16–61) mutant ΔN (Gründer et al., 1992) constructs for expression in oocytes were in the pTLN vector (Lorenz et al., 1996). For localization studies in HEK293 or HeLa cells, rClC-2 and ΔN were C-terminally fused to GFP or to flag. DmClC-2 and ClC-2 with an HA extracellular tag was provided by LP Cid (Centro de Estudios Científicos, Chile). GlialCAM-ΔC was constructed eliminating residues from 289 until the stop codon.

Voltage-Clamp Experiments

Xenopus oocytes were injected and maintained as described (Estévez et al., 2003). For ClC-2, 5 ng cRNA and for ΔN 0.25 ng cRNA/oocyte were injected. When coexpressing, 1.25 ng cRNA of GlialCAM were coinjected with ClC-2. Oocytes were perfused with (in mM): 100 NaCl, 5 $MgSO_4$, and 10 HEPES/NaOH (pH 7.3). To estimate the specific ClC-2-mediated chloride currents, iodide (100 mM NaI replacing the NaCl), which blocks ClC-2-mediated outward currents (Gründer et al., 1992; Thiemann et al., 1992), was applied in every experiment. Oocytes which did not exhibit a significant block were discarded. For selectivity experiments (Figure 6B), 100 mM Cl^- was exchanged by 100 mM of the tested anion. For pH experiments, 10 mM buffer was used (pH 10–9: CAPS [*N*-cyclohexyl-3-aminopropanesulfonic acid]; pH 8–7: HEPES; pH 6–5: MES; and pH 4: Glutamic acid). Hypotonicity effects were studied as described (Gründer et al., 1992). For ClC-2, an initial 1 s voltage pulse at +60 mV was applied, followed by 5 s voltage steps from −140 mV to +60 mV in 20 mV increments and a tail pulse of 1 s to 60 mV. To quantify expression levels, the initial tail current (at +60 mV) after the −140 mV test pulse was estimated by back extrapolation of a single exponential fit to the decaying tail current. To estimate the number of constitutively active channels, instantaneous currents were measured during a short test pulse to +60 mV without prior activation by hyperpolarization.

Patch-Clamp Experiments

Fluorescent HEK293 cells, expressing CLC-2-GFP or ΔN-GFP with or without GlialCAM, were measured with an extracellular solution containing (in mM): 140 NaCl, 2 $MgSO_4$, 2 $CaCl_2$, and 10 HEPES/NaOH (pH 7.3) using standard patch-clamp technique. Intracellular solution was (in mM) 130 NaCl, 2 $MgSO_4$, 2 EGTA, and 10 HEPES/NaOH (pH 7.3). Only cells for which currents were reversibly blocked by iodide were used for analysis. Patch-clamp of astrocytes was performed as described (Ferroni et al., 1997).

Surface Expression by Chemiluminescence

Surface expression in transfected mammalian cells or astrocytes was performed similarly as previously described (Duarri et al., 2008; Teijido et al., 2004). Briefly, 48 hr after transfection, cells were cleaned with PBS and fixed with 3% paraformaldehyde. After PBS washing, cells were blocked with 1% BSA in PBS for 30 min, and incubated with 1 ml of 3F10 anti-HA antibody at 0.2 μg/ml in blocking solution for 1 hr at RT. Cells were washed six times with blocking solution, and incubated for 20 min with 1 ml of a 1:1,000 dilution horseradish peroxidase-coupled secondary antibody (donkey anti-rat IgG, Jackson, Suffolk, UK) in blocking solution. Cells were washed four times with blocking solution and eight times with PBS. Luminescence was measured

of one dish at a time with 500 μl of Power Signal ELISA solution (Pierce) in a Turner TD-20/20 luminometer (Turner Biosystems, Madison, WI, USA).

Immunological Procedures

Two immune sera against ClC-2 were generated against overlapping sequences of the C terminus. In the first antibody (C1 Ab), the peptide used for immunization was (C)HGLPREGTPSDSDDKSQ. The native protein sequence contains a cysteine residue instead of the highlighted serine in order to avoid coupling this residue to the carrier protein. In the second antibody (C2 Ab), the peptide used for immunization was (C)RSRHGLPREGTPSDSDD. (C) is the cysteine that was used for coupling. Affinity purification of the antibodies was used as described (López-Hernández et al., 2011a). Mostly, the C1 antibody was used in western blot studies, and the C2 antibody was used in immunoprecipitation, immunocytochemistry, and EM immunogold. Both antibodies gave no staining in the *Clcn2*$^{-/-}$ mice.

Primary Culture and Adenoviral Transduction

Rat primary quiescent astrocyte cultures were prepared as described previously (Duarri et al., 2008). Dibutyryl-cAMP differentiated rat astrocytes were obtained as described (Ferroni et al., 1997). Adenoviruses expressing three copies of the flag epitope fused to human GlialCAM, either wild-type or containing mutations have been described (López-Hernández et al., 2011a). Adenoviruses expressing GlialCAM fused to EmGFP or ClC-2 fused to three copies of the Flag epitope or containing an extracellular HA epitope were constructed in a similar manner. Transduction of astrocytes was performed as already described (López-Hernández et al., 2011a).

Immunofluorescence and Electron Microscopic Studies

Tissue immunohistochemistry and immunofluorescence were performed as previously described (Blanz et al., 2007; Teijido et al., 2004). For electron microscopic studies, human cerebellum samples were processed as previously described (López-Hernández et al., 2011a).

Quantification of Localization in Cell Contacts

Image J (http://rsbweb.nih.gov/ij/) was used to quantify fluorescence at cell contacts and in the plasma membrane at cell contact free sites by performing intensity profile experiments. We defined a ratio (R) considering the fluorescence signal at the plasma membrane of two cells (cell 1 and cell 2) and the signal in junctions. [$R = F_{junction}/(F_{membrane1}+F_{membrane2})$]. Thus, if the R value is > 1, the signal will be concentrated at junctions.

Split-TEV Method

Split-TEV (Tobacco etch virus protease) assays were performed as described (López-Hernández et al., 2011b). We used a mutant form of the TEV protease (S219V) which prevents its self-digestion but does not affect its catalytic efficiency. The oligopeptide substrate used as the TEV protease-recognition site was ENLYFQS, and the chimeric transcription factor used was GV (obtained from the pM3-VP16 vector) (Clontech, Nucliber, Madrid, Spain), which contains the yeast Gal4DNA binding domain and the herpes simples VP16 transactivaction domain. After TEV protease cleavage, GV translocates into the nucleus and induces the reporter Gaussia Luciferase gene expression (pNEBr-X1Gluc) (New England BioLabs, IZASA, Barcelona, Spain), which is secreted into the cell culture medium.

TEV protease was divided in two fragments: the TEV-N (residues 1–118) and the TEV-C (residues 119–242). We fused the TEV-N fragment, the TEV protease recognition site and the chimeric transcription factor GV to the C-terminal of ClC-2, the mutant ΔNClC-2, or DmClC-2 in a pCDNA3 vector containing a CMV promoter. In addition, we fused the TEV-C fragment to the C-terminal of ClC-2, ClC-5, ΔNClC-2, GlialCAM wild-type, HepaCAM2, GlialCAMΔC, GlialCAM containing the mutations R92Q, R98C, R92W, and G89D, and the adenosine 2A receptor. The fusion of the TEV-C fragment to 4F2hc was done N-terminal. All the proteins with the TEV-C fragments were cloned in a pCDNA6.2/V5-pL Dest, containing the herpes simplex virus thymidine kinase (HSV-TK) promoter, to provide low to moderate levels of expression.

All the expression plasmids were constructed by PCR using a polymerase with proofreading (KOD Hot Start polymerase, Calbiochem, Darnstadt, Germany), adding the attB1, attB2, attB5R, or attB5 recombination sites compatible with the Multisite Gateway System (Invitrogen, Carlsbad, CA, USA). All protocols were performed according to the manufacturer's instructions (Invitrogen).

HeLa cells were transiently transfected with the corresponding cDNA constructs. The total DNA transfected was 2 μg, with the following ratios: 0.75 μg of each protein containing the TEV-N and the TEV-C fragments, 0.3 μg of the reporter gene pNEBr-X1GLuc, and 0.2 μg of the pCMV-βGal vector, which was used to monitor the transfection efficiency. After 48 hr, 20 μl were removed from the supernatant of the cells and Gaussia luciferase activity was measured in a TD-20/20 luminometer (Turner BioSystems, Madison, USA), after the addition of 20 μM of native colenterazine. To normalize the data, cells were solubilized and 30 μl of the cell lysates were used to measure the β-Galactosidase enzyme activity using the Luminiscent β-Galactosidase Detection Kit II (Clontech) in the same luminometer.

Statistical Analyses

For determination of the statistical significance between groups, either the Student's t test or the Bonferroni's comparison test were used. p values are annotated in each figure. Values depicted are means ± SEM.

SUPPLEMENTAL INFORMATION

Supplemental Information includes six figures and can be found with this article online at doi:10.1016/j.neuron.2011.12.039.

ACKNOWLEDGMENTS

We thank Pablo Cid for the gift of DmClC-2 and human ClC-2 with an HA extracellular tag, Muriel Auberson for the generation of the ClC-2 C1 antibody and Soledad Alcántara for the NG2 antibody. We thank Alejandro Barrallo and Manuel Palacín for comments on the manuscript. This study was supported in part by SAF 2009-07014 (R.E.), PS09/02672-ERARE to R.E., ELA Foundation 2009-017C4 project (R.E. and V.N.), 2009 SGR 719 to R.E., SAF 2009-12606-C02-02 (V.N.), 2009 SGR01490 to V.N., FIS08/0014 (X.G.), FIS PI11/01601 (X.G.), and 2009 SGR869 (X.G.). R.E. is a recipient of an ICREA Academia prize. M.P. and E.J. are supported by the Compagnia San Paolo (Torino, Italy), Telethon Italy (GGP08064), and the Italian Institute of Technology (progetto SEED). This work is dedicated to the memory of Günter Jeworutzki.

Accepted: December 23, 2011
Published: March 7, 2012

REFERENCES

Blanz, J., Schweizer, M., Auberson, M., Maier, H., Muenscher, A., Hübner, C.A., and Jentsch, T.J. (2007). Leukoencephalopathy upon disruption of the chloride channel ClC-2. J. Neurosci. *27*, 6581–6589.

Bösl, M.R., Stein, V., Hübner, C., Zdebik, A.A., Jordt, S.E., Mukhopadhyay, A.K., Davidoff, M.S., Holstein, A.F., and Jentsch, T.J. (2001). Male germ cells and photoreceptors, both dependent on close cell-cell interactions, degenerate upon ClC-2 Cl^- channel disruption. EMBO J. *20*, 1289–1299.

Brignone, M.S., Lanciotti, A., Macioce, P., Macchia, G., Gaetani, M., Aloisi, F., Petrucci, T.C., and Ambrosini, E. (2011). The beta1 subunit of the Na,K-ATPase pump interacts with megalencephalic leucoencephalopathy with subcortical cysts protein 1 (MLC1) in brain astrocytes: new insights into MLC pathogenesis. Hum. Mol. Genet. *20*, 90–103.

Clark, S., Jordt, S.E., Jentsch, T.J., and Mathie, A. (1998). Characterization of the hyperpolarization-activated chloride current in dissociated rat sympathetic neurons. J. Physiol. *506*, 665–678.

Duarri, A., Teijido, O., López-Hernández, T., Scheper, G.C., Barriere, H., Boor, I., Aguado, F., Zorzano, A., Palacín, M., Martínez, A., et al. (2008). Molecular pathogenesis of megalencephalic leukoencephalopathy with subcortical cysts: mutations in MLC1 cause folding defects. Hum. Mol. Genet. *17*, 3728–3739.

Duarri, A., Lopez de Heredia, M., Capdevila-Nortes, X., Ridder, M.C., Montolio, M., López-Hernández, T., Boor, I., Lien, C.F., Hagemann, T., Messing, A., et al. (2011). Knockdown of MLC1 in primary astrocytes causes cell vacuolation: a MLC disease cell model. Neurobiol. Dis. *43*, 228–238.

Engel, P., Eck, M.J., and Terhorst, C. (2003). The SAP and SLAM families in immune responses and X-linked lymphoproliferative disease. Nat. Rev. Immunol. *3*, 813–821.

Estévez, R., Boettger, T., Stein, V., Birkenhäger, R., Otto, E., Hildebrandt, F., and Jentsch, T.J. (2001). Barttin is a Cl^- channel beta-subunit crucial for renal Cl^- reabsorption and inner ear K^+ secretion. Nature *414*, 558–561.

Estévez, R., Schroeder, B.C., Accardi, A., Jentsch, T.J., and Pusch, M. (2003). Conservation of chloride channel structure revealed by an inhibitor binding site in ClC-1. Neuron *38*, 47–59.

Fava, M., Ferroni, S., and Nobile, M. (2001). Osmosensitivity of an inwardly rectifying chloride current revealed by whole-cell and perforated-patch recordings in cultured rat cortical astrocytes. FEBS Lett. *492*, 78–83.

Favre-Kontula, L., Rolland, A., Bernasconi, L., Karmirantzou, M., Power, C., Antonsson, B., and Boschert, U. (2008). GlialCAM, an immunoglobulin-like cell adhesion molecule is expressed in glial cells of the central nervous system. Glia *56*, 633–645.

Ferroni, S., Marchini, C., Nobile, M., and Rapisarda, C. (1997). Characterization of an inwardly rectifying chloride conductance expressed by cultured rat cortical astrocytes. Glia *21*, 217–227.

Flores, C.A., Niemeyer, M.I., Sepúlveda, F.V., and Cid, L.P. (2006). Two splice variants derived from a Drosophila melanogaster candidate ClC gene generate ClC-2-type Cl^- channels. Mol. Membr. Biol. *23*, 149–156.

Földy, C., Lee, S.H., Morgan, R.J., and Soltesz, I. (2010). Regulation of fast-spiking basket cell synapses by the chloride channel ClC-2. Nat. Neurosci. *13*, 1047–1049.

Gründer, S., Thiemann, A., Pusch, M., and Jentsch, T.J. (1992). Regions involved in the opening of CIC-2 chloride channel by voltage and cell volume. Nature *360*, 759–762.

Jordt, S.E., and Jentsch, T.J. (1997). Molecular dissection of gating in the ClC-2 chloride channel. EMBO J. *16*, 1582–1592.

Lange, P.F., Wartosch, L., Jentsch, T.J., and Fuhrmann, J.C. (2006). ClC-7 requires Ostm1 as a beta-subunit to support bone resorption and lysosomal function. Nature *440*, 220–223.

Leegwater, P.A., Yuan, B.Q., van der Steen, J., Mulders, J., Könst, A.A., Boor, P.K., Mejaski-Bosnjak, V., van der Maarel, S.M., Frants, R.R., Oudejans, C.B., et al. (2001). Mutations of MLC1 (KIAA0027), encoding a putative membrane protein, cause megalencephalic leukoencephalopathy with subcortical cysts. Am. J. Hum. Genet. *68*, 831–838.

López-Hernández, T., Ridder, M.C., Montolio, M., Capdevila-Nortes, X., Polder, E., Sirisi, S., Duarri, A., Schulte, U., Fakler, B., Nunes, V., et al. (2011a). Mutant GlialCAM causes megalencephalic leukoencephalopathy with subcortical cysts, benign familial macrocephaly, and macrocephaly with retardation and autism. Am. J. Hum. Genet. *88*, 422–432.

López-Hernández, T., Sirisi, S., Capdevila-Nortes, X., Montolio, M., Fernández-Dueñas, V., Scheper, G.C., van der Knaap, M.S., Casquero, P., Ciruela, F., Ferrer, I., et al. (2011b). Molecular mechanisms of MLC1 and GLIALCAM mutations in megalencephalic leukoencephalopathy with subcortical cysts. Hum. Mol. Genet. *20*, 3266–3277.

Lorenz, C., Pusch, M., and Jentsch, T.J. (1996). Heteromultimeric CLC chloride channels with novel properties. Proc. Natl. Acad. Sci. USA *93*, 13362–13366.

Makara, J.K., Rappert, A., Matthias, K., Steinhäuser, C., Spät, A., and Kettenmann, H. (2003). Astrocytes from mouse brain slices express ClC-2-mediated Cl^- currents regulated during development and after injury. Mol. Cell. Neurosci. *23*, 521–530.

Menichella, D.M., Majdan, M., Awatramani, R., Goodenough, D.A., Sirkowski, E., Scherer, S.S., and Paul, D.L. (2006). Genetic and physiological evidence that oligodendrocyte gap junctions contribute to spatial buffering of potassium released during neuronal activity. J. Neurosci. *26*, 10984–10991.

Nagelhus, E.A., Mathiisen, T.M., and Ottersen, O.P. (2004). Aquaporin-4 in the central nervous system: cellular and subcellular distribution and coexpression with KIR4.1. Neuroscience *129*, 905–913.

Neusch, C., Rozengurt, N., Jacobs, R.E., Lester, H.A., and Kofuji, P. (2001). Kir4.1 potassium channel subunit is crucial for oligodendrocyte development and in vivo myelination. J. Neurosci. *21*, 5429–5438.

Niemeyer, M.I., Cid, L.P., Yusef, Y.R., Briones, R., and Sepúlveda, F.V. (2009). Voltage-dependent and -independent titration of specific residues accounts for complex gating of a ClC chloride channel by extracellular protons. J. Physiol. *587*, 1387–1400.

Rash, J.E. (2010). Molecular disruptions of the panglial syncytium block potassium siphoning and axonal saltatory conduction: pertinence to neuromyelitis optica and other demyelinating diseases of the central nervous system. Neuroscience *168*, 982–1008.

Ridder, M.C., Boor, I., Lodder, J.C., Postma, N.L., Capdevila-Nortes, X., Duarri, A., Brussaard, A.B., Estevez, R., Scheper, G.C., Mansvelder, H.D., and van der Knaap, M.S. (2011). Megalencephalic leucoencephalopathy with cysts: defect in chloride currents and cell volume regulation. Brain *134*, 3342–3354.

Rinke, I., Artmann, J., and Stein, V. (2010). ClC-2 voltage-gated channels constitute part of the background conductance and assist chloride extrusion. J. Neurosci. *30*, 4776–4786.

Scheper, G.C., van Berkel, C.G., Leisle, L., de Groot, K.E., Errami, A., Jentsch, T.J., and Van der Knaap, M.S. (2010). Analysis of *CLCN2* as candidate gene for megalencephalic leukoencephalopathy with subcortical cysts. Genet. Test. Mol. Biomarkers *14*, 255–257.

Sík, A., Smith, R.L., and Freund, T.F. (2000). Distribution of chloride channel-2-immunoreactive neuronal and astrocytic processes in the hippocampus. Neuroscience *101*, 51–65.

Teijido, O., Martínez, A., Pusch, M., Zorzano, A., Soriano, E., Del Río, J.A., Palacín, M., and Estévez, R. (2004). Localization and functional analyses of the MLC1 protein involved in megalencephalic leukoencephalopathy with subcortical cysts. Hum. Mol. Genet. *13*, 2581–2594.

Thiemann, A., Gründer, S., Pusch, M., and Jentsch, T.J. (1992). A chloride channel widely expressed in epithelial and non-epithelial cells. Nature *356*, 57–60.

van der Knaap, M.S., Barth, P.G., Stroink, H., van Nieuwenhuizen, O., Arts, W.F., Hoogenraad, F., and Valk, J. (1995a). Leukoencephalopathy with swelling and a discrepantly mild clinical course in eight children. Ann. Neurol. *37*, 324–334.

van der Knaap, M.S., Valk, J., Barth, P.G., Smit, L.M., van Engelen, B.G., and Tortori Donati, P. (1995b). Leukoencephalopathy with swelling in children and adolescents: MRI patterns and differential diagnosis. Neuroradiology *37*, 679–686.

van der Knaap, M.S., Barth, P.G., Vrensen, G.F., and Valk, J. (1996). Histopathology of an infantile-onset spongiform leukoencephalopathy with a discrepantly mild clinical course. Acta Neuropathol. *92*, 206–212.

Weinreich, F., and Jentsch, T.J. (2001). Pores formed by single subunits in mixed dimers of different CLC chloride channels. J. Biol. Chem. *276*, 2347–2353.

Insights into MLC pathogenesis: GlialCAM is an MLC chaperone required for proper activation of volume-regulated anion currents

(Human Molecular Genetics, 2013)

Contribució:

- Estudi de la localització de mutacions de MLC1 en presència de GlialCAM (Figura Suplementària 3)

Human Molecular Genetics, 2013, Vol. 22, No. 21 **4405–4416**
doi:10.1093/hmg/ddt290
Advance Access published on June 20, 2013

Insights into MLC pathogenesis: GlialCAM is an MLC1 chaperone required for proper activation of volume-regulated anion currents

Xavier Capdevila-Nortes[1], Tania López-Hernández[1,7], Pirjo M. Apaja[3,4], Miguel López de Heredia[5,6], Sònia Sirisi[1,5], Gerard Callejo[8,9], Tanit Arnedo[1,7], Virginia Nunes[2,5,6], Gergely L. Lukacs[3,4], Xavier Gasull[8,9] and Raúl Estévez[1,7,*]

[1]Sección de Fisiología, Departamento de Ciencias Fisiológicas II and [2]Sección de Genética, Departamento de Ciencias Fisiológicas II, University of Barcelona, Barcelona, Spain, [3]Department of Physiology and [4]Research Group Focused on Protein Structure, McGill University, Montréal, Quebec, Canada H3E 1Y6, [5]Laboratorio de Genética Molecular, IDIBELL, Barcelona, Spain, [6]U-730 and [7]U-750, Centro de Investigación en red de enfermedades raras (CIBERER), ISCIII, Barcelona, Spain, [8]Neurophysiology Lab, Department Physiological Sciences I, Medical School, University of Barcelona, Barcelona, Spain and [9]Institut d'Investigacions Biomèdiques August Pi i Sunyer (IDIBAPS), Barcelona, Spain

Received May 11, 2013; Revised and Accepted June 18, 2013

Megalencephalic leukoencephalopathy with subcortical cysts (MLC) is a rare type of leukodystrophy caused by mutations in either *MLC1* or *GLIALCAM* genes and is associated with myelin and astrocyte vacuolation. It has been suggested that MLC is caused by impaired cell volume regulation as a result of defective activation of astrocytic volume-regulated anion currents (VRAC). GlialCAM brings MLC1 and the ClC-2 Cl^- channel to cell–cell junctions, even though the role of ClC-2 in MLC disease remains incompletely understood. To gain insights into the biological role of GlialCAM in the pathogenesis of MLC disease, here we analyzed the gain- and loss-of-function phenotypes of GlialCAM in Hela cells and primary astrocytes, focusing on its interaction with the MLC1 protein. Unexpectedly, GlialCAM ablation provoked intracellular accumulation and reduced expression of MLC1 at the plasma membrane. Conversely, over-expression of GlialCAM increased the cellular stability of mutant MLC1 variants. Reduction in GlialCAM expression resulted in defective activation of VRAC and augmented vacuolation, phenocopying MLC1 mutations. Importantly, over-expression of GlialCAM together with MLC1 containing MLC-related mutations was able to reactivate VRAC currents and to reverse the vacuolation caused in the presence of mutant MLC1. These results indicate a previously unrecognized role of GlialCAM in facilitating the biosynthetic maturation and cell surface expression of MLC1, and suggest that pharmacological strategies aimed to increase surface expression of MLC1 and/or VRAC activity may be beneficial for MLC patients.

INTRODUCTION

Megalencephalic leukoencephalopathy with subcortical cysts (MLC) is a rare type of leukodystrophy (genetic alteration of the white matter) that affects brain chloride and fluid homeostasis (1). MRI of patients shows diffuse signal abnormality, swelling of the cerebral white matter and the presence of subcortical cysts, mainly in the anterior temporal regions (2,3). Studies from an MLC patient brain biopsy revealed that the major phenotype of the disease was myelin vacuolation (4). These results, together with proton magnetic spectroscopic resonance data (5,6), suggested that MLC is caused by disturbed fluid homeostasis.

MLC1 was the first gene to be identified in MLC patients (7) and accounts for MLC in most patients. In mouse and human tissue, high MLC1 levels were present in astroglial–astroglial junctions and ependymal cells in blood–brain and CSF–brain barriers, apart from astrocytic junctions of Bergmann glia in the cerebellum (8–11). Thus, it has been proposed that MLC

*To whom correspondence should be addressed at: Facultat de Medicina, Departament de Ciències Fisiològiques II, Universitat de Barcelona, C/Feixa Llarga s/n 08907 L'Hospitalet de Llobregat, Barcelona, Spain. Tel: +34 934039781; Fax: +34 934024268; Email: restevez@ub.edu

has an astrocytic origin (12), based on the fact that MLC1 is mostly expressed in astrocytes. In agreement with this hypothesis, depletion of MLC1 in astrocytes causes vacuolation, a phenotype that was also observed after re-examination of a MLC patient's brain biopsy (13), which showed previously only myelin vacuoles. Interestingly, reduction in MLC1 in astrocytes and in lymphoblast cell lines from MLC patients was found to be associated with a reduced activity of volume-regulated anion currents (VRAC) by an unknown mechanism (14). In parallel, the rate of regulatory volume decrease after cell swelling was reduced in MLC1-depleted cells (14). It has also been suggested that MLC1 could interact functionally with the β-subunit of the Na^+/K^+ ATPase (15) and with the TRPV4 ion channel (16). However, the role of MLC1 is still completely unknown, and whether these interactions are related to the effects of MLC1 depletion on VRAC activity is unknown.

GLIALCAM was recently identified as a second gene mutated in MLC (17). It was demonstrated that GlialCAM functions as an escort molecule necessary to target MLC1 to cell–cell junctions (18). Moreover, the changed localization of the MLC1/GlialCAM complexes seems to play an important role in the development of the disease, as most *GLIALCAM* mutations impair the correct trafficking of GlialCAM and MLC1 to astrocyte–astrocyte junctions (17,18).

Histological studies in tissue indicated that GlialCAM is mostly localized in astrocyte–astrocyte junctions where it co-localizes with MLC1 (17), but also in oligodendrocyte processes (19,20). Proteomic studies searching for additional GlialCAM protein partners revealed that GlialCAM also acts as an auxiliary subunit of the ClC-2 chloride channel, targeting it to astrocytic cell junctions and modifying its functional properties (20). Similar to its effect on MLC1 targeting, *GLIALCAM* MLC-related mutations also impair the trafficking of ClC-2 to cell junctions. Strikingly, *Clcn2* KO mice also displayed similar vacuolation to what is seen in MLC patients (21), suggesting its involvement in the pathogenesis of MLC. However, no *CLCN2* mutations were detected in MLC patients (22) and no direct protein interaction was found between MLC1 and ClC-2 (13,20). Thus, the involvement of ClC-2 in MLC disease is unclear. However, very recently, it has been shown that CLCN2 mutations may cause certain forms of a human leukodystrophy characterized by white matter oedema (23).

Dominant mutations in *GLIALCAM* cause other type of disease called MLC2B characterized by transient features of MLC (24). Similar to the recessive *GLIALCAM* mutations, also dominant mutations cause MLC1 and ClC-2 trafficking defects (17,18,20). It is still unknown why dominant mutations and not recessive mutations show a trafficking dominant behavior. Furthermore, dominant mutations are also associated with different clinical phenotypes than MLC1 mutations, while the clinical and MRI phenotypes related to recessive *MLC1* and *GLIALCAM* mutations are the same.

In the present work, we have analyzed biochemically and functionally what the consequences of a reduced GlialCAM expression are, and compared them with the effects of a reduced MLC1 expression. The effect of *GLIALCAM* and *MLC1* mutations was also addressed. The results obtained indicate that GlialCAM is necessary for MLC1 protein expression, and its reduction affects the activity of VRAC, which may cause astrocyte vacuolation. Thus, this work extends the role of GlialCAM as a chaperone of MLC1 needed for proper VRAC activation. In addition, based on functional data obtained, we suggest that a therapeutic strategy aimed to recover the surface expression of MLC1 and/or the activation of VRAC currents can be envisaged as beneficial for all MLC patients.

RESULTS

Experimental approach to create an astrocyte cell model with reduced GlialCAM expression

To study the cellular effects of GlialCAM ablation, adenoviral vectors expressing two distinct shRNA (1 or 2) against rat GlialCAM with the fluorescent protein EmGFP, allowing visualization of transduced cells, were produced. An adenoviral vector expressing non-targeted or scrambled shRNA (SCR) was used as a control. RT-qPCR experiments performed 7 days after GlialCAM shRNA infection of astrocytes demonstrated that endogenous GlialCAM mRNA levels were profoundly depleted (Fig. 1A). Accordingly, western blot (WB) analysis indicated that the GlialCAM protein level was reduced by 80% when compared with the control SCR (Fig. 1B and Supplementary Material, Fig. S1). Immunofluorescence experiments confirmed no detectable GlialCAM protein in shRNA-treated cells (Fig. 1C). Both types of experiments (WB and immunofluorescence) also demonstrated the specificity of the GlialCAM antibodies used (17). As an additional control, to exclude side effects of shRNAs, we also complemented with an adenovector expressing human C-terminally flag-tagged GlialCAM, which was resistant to the rat-specific GlialCAM shRNAs (Fig. 1B and C).

Reduction in GlialCAM expression led to intracellular retention and reduced expression of MLC1 in rat astrocytes

We studied the consequences of reduced GlialCAM expression at the mRNA, protein and subcellular localization of MLC1 (Fig. 2). As a specificity control, we monitored the expression and subcellular localization of a subset of proteins associated with tight, adherent and gap junctions. Knockdown of GlialCAM led to a reduction (about 30%) of the *MLC1* mRNA levels (not significant) (Fig. 2A). However, the MLC1 protein abundance was reduced to 60% of wild-type values (Fig. 2B and Supplementary Material, Fig. S1), which cannot be explained by the reduction in the mRNA levels. Protein levels of some junction proteins were not altered, excluding non-specific effects (Fig. 2B and data not shown).

Importantly, while MLC1 was predominantly confined to an intracellular perinuclear compartment (Fig. 2D, arrowheads) in astrocyted depleted of GlialCAM, MLC1 remained associated with cell–cell junctions in astrocytes transduced with control shRNA (Fig. 2C). Furthermore, the junctional localization of MLC1 was recovered after complementation of the astrocytes with flag-tagged human GlialCAM cDNA (Fig. 2E), which was resistant to this shRNA (Fig. 1 and Supplementary Material, Fig. S1). Therefore, altered processing and decreased stability of the MLC1 may account for the cellular phenotype of MLC1 rather than non-specific effects of the shRNA. Additional control experiments also showed that localization of some junction proteins was not changed in GlialCAM-depleted astrocytes (Supplementary Material, Fig. S2 and data not shown).

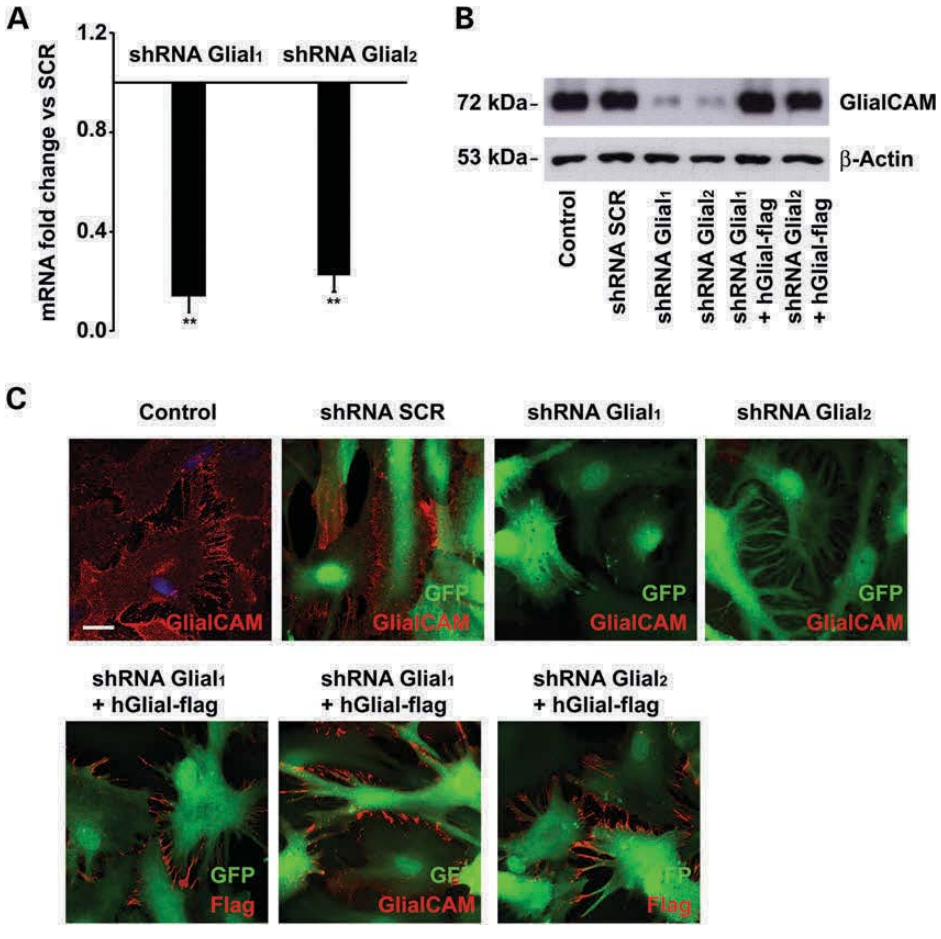

Figure 1. Adenovector-mediated knockdown of GlialCAM in primary astrocytes. (**A**) RT-qPCR experiments using specific primers to detect rat *GLIALCAM* mRNA. Data represent the ratio of mRNA fold change versus the SCR control (mean ± SEM) of at least four different astrocyte preparations either treated at MOI 10 with SCR (scrambled) or with 2 different shRNAs against *GLIALCAM*. Both shRNA Glial1 and Glial2 (see Materials and Methods) caused almost complete inhibition of mRNA expression. $^{**}P < 0.01$ (**B**) Astrocytes (untreated or transduced at MOI 10 with the shRNA indicated during 7 days, or complemented with adenovirus expressing flag-tagged human GlialCAM at MOI 2 during 2 days) were analyzed by WB using antibodies against GlialCAM. The GlialCAM antibodies used were able to detect the rat and human GlialCAM proteins. β-Actin was used as a loading control. Other different experiments gave similar results ($n = 5$). (**C**) Control or astrocytes transduced with the adenovirus indicated were fixed and processed for immunofluorescence using antibodies against GlialCAM. Transduced cells were visualized by the positive GFP signal. GlialCAM signal in astrocyte–astrocyte processes was detected in control cells and in cells transduced with the SCR shRNA but not in cells transduced with the shRNA1 against GlialCAM. In the panels below, cells were co-transduced with an shRNA against GlialCAM and flag-tagged human GlialCAM (resistant to shRNA) and immunofluorescence was performed using antibodies against the flag epitope or GlialCAM. Scale bar: 20 μm.

GlialCAM improves the protein stability and surface expression of MLC1 variants containing MLC-related mutations

The above results suggest that GlialCAM may function as a chaperone needed for correct MLC1 folding and expression. If this is the case, GlialCAM over-expression may correct the localization of MLC1 variants containing MLC-related mutations, which primarily affect MLC1 protein folding (25). To test this hypothesis, we constructed adenoviruses expressing a HA-tagged human MLC1 variant containing the MLC-related mutations Pro92Ser (P92S) or Ser246Arg (S246R), and they were used to transduce rat astrocytes with or without GlialCAM. The immunostaining of the mutant MLC1-P92S showed a perinuclear intracellular distribution in astrocytes (Fig. 3A), similar to the endoplasmatic reticulum (ER) (25). However, co-expression with GlialCAM led to a re-distribution of the P92S variant to astrocyte–astrocyte junctions (Fig. 3B left, arrowheads), co-localizing with GlialCAM (Fig. 3B, right, arrowheads). Similar results were obtained with the MLC1-S246R mutant (Supplementary Material, Fig. S3A). We next asked whether MLC1 intracellular retention could be attenuated in HeLa cells expressed heterologously. GlialCAM was indeed able to rescue the intracellular accumulation of all MLC1 mutants studied (G59E, C85W, L311Ins and N141K) and re-locate them to the cell junction [Supplementary Material, Fig. S3B–E and (18)].

Using a chemiluminescence-based cell surface ELISA assay, the MLC1 cell surface density was determined as a function of GlialCAM expression, taking advantage of the extracellular HA epitope. The MLC1-P92S has an 80% reduced cell surface expression relative to its wild-type counterpart (Fig. 3C). GlialCAM over-expression increased the relative surface-expression levels of the MLC1-P92S in rat astrocytes (Fig. 3D). The

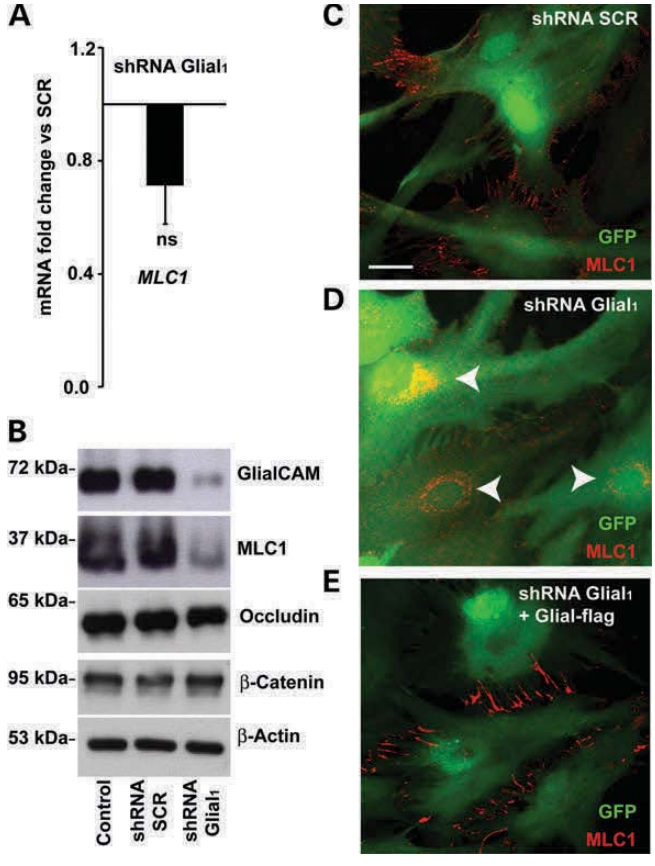

Figure 2. Expression of MLC1 in GlialCAM-depleted astrocytes. (**A**) RT-qPCR experiments using specific primers to detect rat *MLC1* mRNA. Data represent the mean ± SEM of four different astrocyte preparations either treated at MOI 10 with SCR (scrambled) or with a shRNAs against GlialCAM. Both shRNA Glial1 and Glial2 gave similar results. Ns, not significative; $^{*}P < 0.01$. (**B**) Astrocytes (untreated or transduced at MOI 10 with the shRNA indicated during 7 days) were analyzed by WB using antibodies against the indicated proteins. β-Actin was used as a loading control. Different experiments gave similar results ($n = 3–5$). (**C**) Localization of MLC1 in astrocyte–astrocyte junction in cells transduced with the adenovirus expressing a control shRNA, which were visualized by the positive GFP signal. (**D**) Localization of MLC1 in astrocytes with reduced expression of GlialCAM was detected mostly intracellular around the nucleus (arrowheads). (**E**) Astrocytes were co-transduced with a shRNA against GlialCAM and flag-tagged human GlialCAM (resistant to shRNA) and processed by immunofluorescence. Localization of endogenous MLC1 was detected in astrocyte–astrocyte junctions. Scale bar: 20 μm.

increase in surface levels detected by this method was moderate but significant. It may be that the surface levels of MLC1 quantified by this assay in astrocytes were underestimated, due to a possible masking of the extracellular HA epitope present in MLC1 by GlialCAM in astrocyte–astrocyte junctions, as happened in other membrane proteins with accessory subunits (26).

To assess whether GlialCAM can influence MLC1 stability, the disappearance kinetics of the cellular pool was monitored by WB during a cycloheximide chase (CHX). The MLC1-P92S variant showed significantly reduced stability as demonstrated by the accelerated removal of the mutant upon translation termination with CHX (Fig. 3E and F). Co-expression with GlialCAM considerably improved the protein stability of the mutated P92S variant and also of the wild-type MLC1 protein.

Knockdown of GlialCAM affects MLC1 protein expression also in HeLa cells

The above results indicate that GlialCAM has two important functions. On the one hand, as reported previously, it is necessary to target MLC1 to cell–cell junctions (18,20). On the other hand, GlialCAM is necessary to stabilize MLC1 and this stabilization is important for translocation to the plasma membrane. This second role was unexpected, as MLC1 localization at the plasma membrane was detected without GlialCAM expression in HeLa cells. To explain this controversy, we hypothesized that GlialCAM is endogenously expressed in HeLa cells at low levels. Importantly, GlialCAM protein could be detected at the plasma membrane, using a monoclonal antibody directed against extracellular GlialCAM by a chemiluminescence-based ELISA assay (Fig. 4A). Transfection of two independent shRNAs against GlialCAM reduced the antibody signal, confirming that the plasma membrane signal detected by the antibody was due to GlialCAM (Fig. 4A).

To address whether the stabilization effect of GlialCAM in MLC1 could be also observed in HeLa cells, we transfected HeLa cells with wild-type MLC1 or MLC-related mutant variants P92S (PS) or C326R (CR) together with and unrelated shRNA as a control or shRNAs against GlialCAM, and assayed the cellular and surface MLC1 expression by immunoblotting and cell surface ELISA, respectively. Knockdown of GlialCAM reduced total (Fig. 4B) and cell surface (Fig. 4C) expression of all MLC1 variants, including the wild-type MLC1, as observed in rat astrocytes. Considering that GlialCAM and MLC1 physically interact [revealed by split-TEV or FRET studies (18)], these data strongly suggest that GlialCAM exerts a stabilizing effect on MLC1, which is independent of the cell system studied.

Effect of GlialCAM MLC-related variants on MLC1 expression

GlialCAM variants containing MLC-related mutations affect GlialCAM and MLC1 trafficking to cell junctions, without substantially interfering with GlialCAM expression or the biochemical interaction between GlialCAM/MLC1 (17,18,20). We thus addressed whether *GLIALCAM* mutations can compromise MLC1 stabilization in astrocytes. To this aim, we first depleted endogenous GlialCAM in astrocytes by adenovirus-mediated RNA interference, and then complemented with wild-type GlialCAM wild-type or two mutant variants, Arg92Gln (R92Q), found in MLC2A patients, or Arg92Trp (R92W), found in MLC2B patients. As a control for protein expression, we complemented with MLC1. Astrocytes were analyzed by WB or immunofluorescence (Fig. 5 and Supplementary Material, Fig. S1). Knockdown of GlialCAM reduced both GlialCAM and MLC1 expression (Fig. 5A and Supplementary Material, Fig. S1), and led to a mislocalization of MLC1 to an intracellular compartment (Fig. 5B). After knockdown of endogenous GlialCAM, complementation with human GlialCAM rescued MLC1 protein expression (Fig. 5A and Supplementary Material, Fig. S1) and junctional localization (Fig. 5C).

Complementation with GlialCAM variants containing the mutations R92Q or R92W also rescued MLC1 protein expression (Fig. 5A and Supplementary Material, Fig. S1). However,

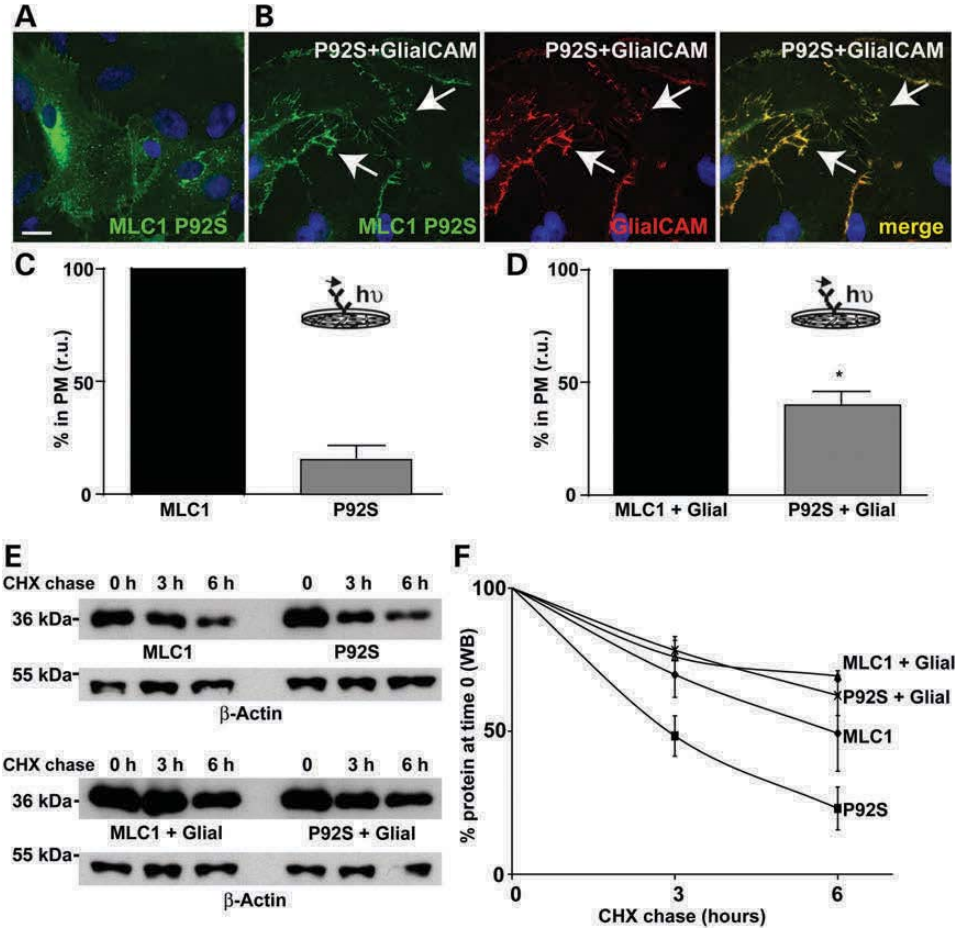

Figure 3. GlialCAM increases surface expression and protein stability of MLC1 containing MLC-related mutations in primary astrocytes. (**A** and **B**) Astrocytes were transduced with adenoviruses expressing *HA*-tagged MLC1 containing the MLC-related mutation P92S alone (A) or in combination with GlialCAM (B). After 48 h, cells were fixed and processed by immunofluorescence using antibodies against HA tag (3F10) or GlialCAM. The yellow merge channel indicates co-localization. Arrowheads point to contacts between astrocytes, where MLC1 P92S and GlialCAM co-localized. Scale bar: 20 μm. (**C** and **D**) Astrocytes were transduced with adenoviruses expressing MLC1 wild-type or MLC1 containing the MLC-related mutation P92S alone (C) or in combination with GlialCAM (D). MLC1 constructs have an extracellular *HA* epitope. Plasma membrane levels were measured using a luminescence-based method, as described in Materials and Methods, and they were normalized to the level of the wild-type MLC1 in each condition. The inset shows an overview of the method. Data correspond to the average of three independent experiments. $^{*}P < 0.05$, comparing the levels of the mutant at the plasma membrane with or without GlialCAM. (**E** and **F**) Astrocytes were transduced with adenoviruses expressing MLC1 wild-type or MLC1 containing the MLC-related mutation P92S alone or in combination with GlialCAM. 48 h after transduction, cells were treated or not with cycloheximide (CHX, 100 μg/ml) at the times indicated. Cells extracts were obtained, and the remaining protein was analyzed by western-blot against the *HA* epitope. β-Actin detection was used as a loading control. The result is a representative experiment of four with similar results. In (F), a summary of the quantification of all experiments using ImageJ software is shown. To quantify signals by WB, we performed at least three expositions of all WBs, to ensure linearity. The signal is normalized to the value at time 0 for each of the experimental groups. The stability of the mutant P92S increased significantly when co-expressed with GlialCAM ($P < 0.01$).

the junctional localization of endogenous MLC1 was not corrected by the different mutated variants (Fig. 5D for R92Q and Fig. 5E for R92W).

Volume-regulated chloride currents are affected in MLC1- and GlialCAM-depleted astrocytes

Lack of MLC1 in rat astrocytes or in lymphoblast cell lines obtained from MLC patients have been related with a defective activation of VRAC (14), whose molecular identity is still unknown (27). We next addressed whether lack of GlialCAM may also affect VRAC currents.

Previous electrophysiological studies addressing VRAC currents were performed in mild trypsin-treated astrocytes (14). As this assays needed an enzymatic treatment to round astrocytes potentially leading to other effects related with the trypsin treatment (28), we switched to dB-cAMP-treated astrocytes that are already rounded due to the elongation of processes (29). We focused only in changes in VRAC activity, taking advantage of the fact that not all astrocytes express ClC-2 mRNA in isotonic conditions (30), but most express VRAC currents in hypotonic conditions. In both cases, reduction in MLC1 or GlialCAM led to a dramatic decrease of VRAC activity of 80%, although it was still detectable (Fig. 6).

Lack of GlialCAM and MLC1 causes astrocyte vacuolation

Lack of MLC1 in astrocytes and in MLC patients caused the appearance of vacuoles in the cytoplasm of astrocytes [(13) and compare Fig. 7A with Fig. 7B]. Similarly, knockdown of

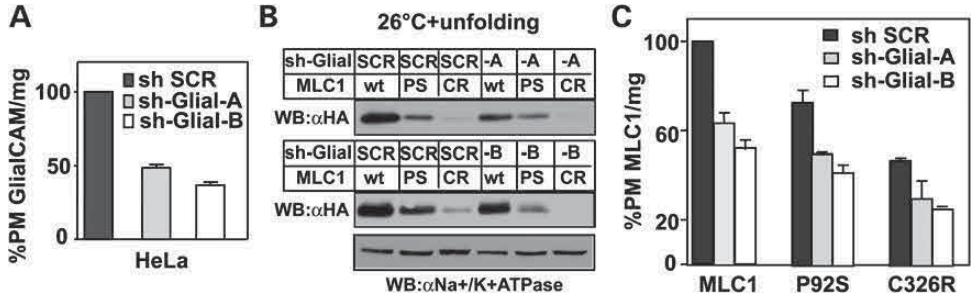

Figure 4. Effect of GlialCAM expression levels on MLC1 expression levels and trafficking in HeLa cells. Hela cells transduced with two lentivirus expressing shRNAs against GlialCAM (sh-Glial-A, sh-Glial-B) or shRNA Scrambled (sh SCR) were analyzed with anti-HepaCAM antibody for GlialCAM cell surface expression using ELISA as described in Materials and Methods. (**B**) The shGlialCAM cells (A or B) were transfected with indicated MLC1 cDNAs (wt, wild-type; PS, P92S; CR, C326R). Cells were seeded on 24-well plates 20 h after transfection and incubated at 37°C for 24 h. Cells were temperature rescued at 26°C for 24 h, and unfolding was performed at 37°C for 1 h prior of experiment. They were analyzed by immunoblotting against the *HA* epitope present in MLC1. Na^+-K^+-ATPase was used as a loading control. (**C**) Cell surface density of MLC1 in shGlialCAM cells was done as in (A), but using anti-HA antibody. The expression was normalized for MLC1 wt expression in shSCR cells.

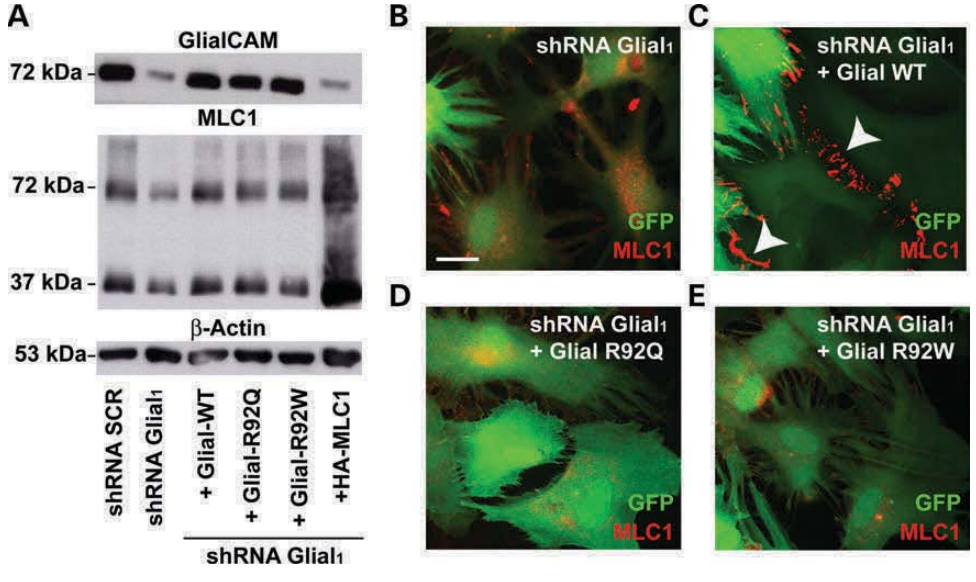

Figure 5. GlialCAM with MLC-related mutations increase MLC1 expression but show a trafficking defect. (**A**) Astrocytes transduced with the shRNA indicated during 7 days and complemented or not with the indicated constructs were analyzed by WB using antibodies against the indicated proteins GlialCAM and MLC1. β-Actin was used as a loading control. Four different experiments gave similar results. A quantification of several experiments is shown in Supplementary Material, Figure S1. (**B**–**E**) Similarly, for the different experimental groups showed here, astrocytes were fixed and processed by immunofluorescence using antibodies against MLC1. Green signal indicates the GFP which is co-expressed with the shRNA. Arrows label contacts between astrocytes. Scale bar: 20 μm.

GlialCAM also led to astrocyte vacuolation (Fig. 7C). Vacuoles appearing in MLC1 or GlialCAM-depleted astrocytes were also of endosomal origin, as revealed by staining with the endodomal protein marker EEA1 (early-endosomal antigen 1) (Fig. 7B and C).

We next aimed to correlate if vacuolation was directly linked to an increase in intracellular water. Treatment of astrocytes for 24 h with a hypoosmotic medium induced the appearance of water vacuoles of endosomal origin [(15) and Fig. 7D]. To test if a defective VRAC activity causally can contribute to the vacuolation phenotype, we inhibited VRAC activity, indirectly by attenuating the chloride gradient or directly. This was accomplished by incubating astrocytes with Bumetanide (Fig. 7E), which blocks sodium/potassium/chloride co-transporters (31–34), or by DCPIB (Fig. 7F), the most specific VRAC inhibitor known (35). Both treatments led to the appearance of vacuoles of endosomal origin. In order to correlate the biochemical and electrophysiological data with the vacuolation phenotype, we quantified the number of cells containing vacuoles for all experimental groups (see Materials and Methods). Quantification of the vacuolation phenotype in cells treated with Bumetanide or DCPIB revealed a similar degree of defect as cells treated with the shRNAs against MLC1 or GlialCAM (Fig. 8 and Supplementary Material, Fig. S4) [Bumetanide, $15.4 \pm 2.3\%$ (4 independent exp, 1033 cells); DCPIB, $18.8 \pm 2.9\%$ (4 independent exp, 1226 cells)].

Recovery of MLC1 in junctions rescued the vacuolation defect and VRAC activation

The astrocyte vacuolation caused by the lack of GlialCAM was rescued with complementation with human GlialCAM (Fig. 8A and Supplementary Material, Fig. S4). However,

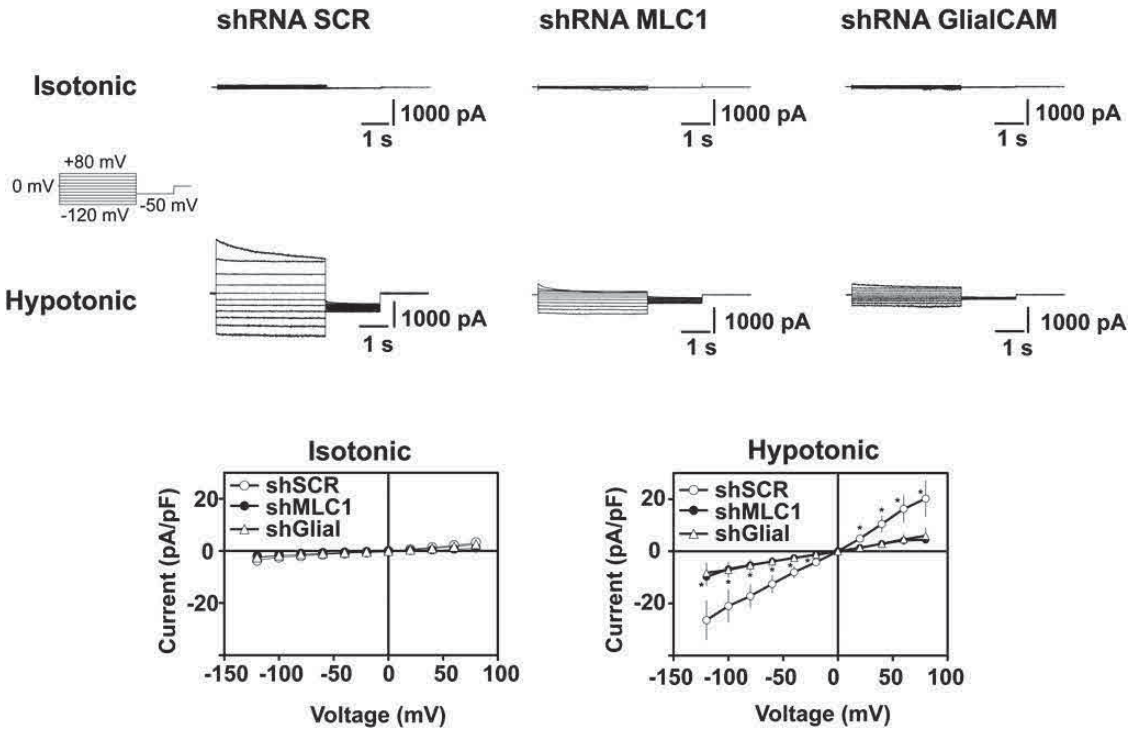

Figure 6. VRAC activity is reduced in astrocytes with reduced expression of MLC1 and GlialCAM. Representative family of whole-cell chloride currents in dbcAMP-treated cultured neocortical astrocytes transduced with shRNA scrambled or shRNA against MLC1 or GlialCAM, elicited by the pulse protocol shown in the inset. Astrocytes that did not show ClC-2-like currents in isotonic conditions were selected. They correspond to about 60% of recorded cells. In about 85% of these cells do not having ClC-2 current in isotonic conditions, application of a hypotonic solution activated VRAC current. As expected, these currents were blocked by DCPIB, but not with iodide replacement (data not shown). The plot shows average steady-state current–voltage relationship of dbcAMP-treated astrocytes transduced with shRNA SCR (circles), shRNA MLC1 (filled circles) or shRNA GlialCAM (triangles) in isotonic and hypotonic conditions. Results corresponds to $n = 15$ for shRNA SCR, $n = 14$ for shRNA MLC1 and $n = 14$ for shRNA GlialCAM. $^{*}P < 0.05$ *t*-test versus scramble for both MLC1 and GlialCAM groups.

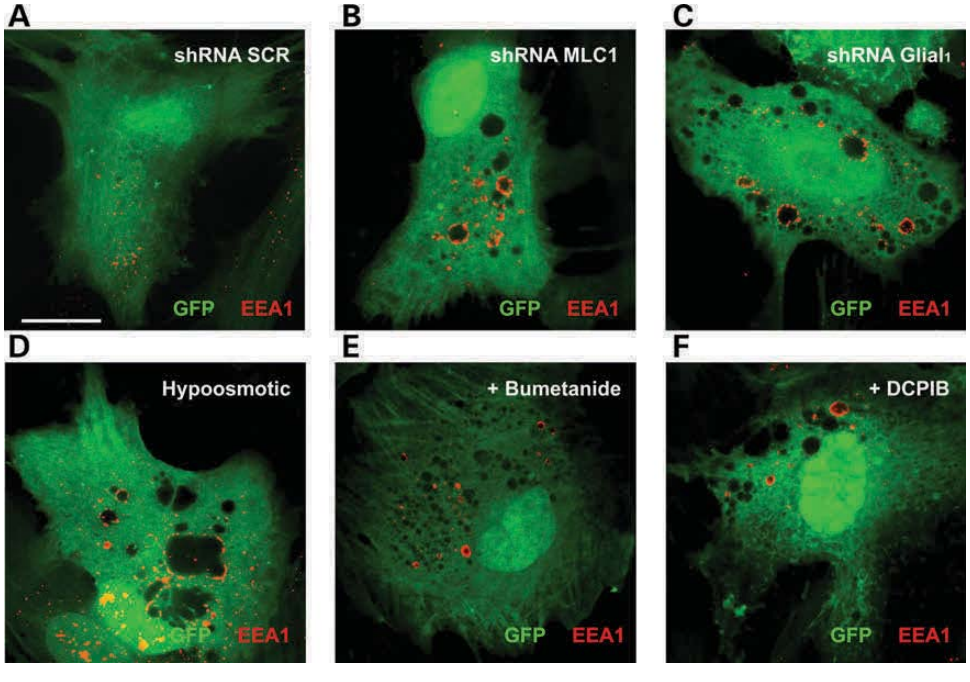

Figure 7. Similarities between the vacuolation induced by the lack of GlialCAM and the inhibition of VRAC activity. (**A**–**C**) Primary cultures of astrocytes were transduced with adenovectors expressing shRNA SCR, shRNA against MLC1 or shRNA against GlialCAM. After 7 days, cells were fixed and immunostained using antibodies against early-endosomal antigen 1 (EEA1). In (**D**–**F**), cells were transduced with adenovector expressing shRNA SCR and incubated with 50 μM bumetanide during 7 days (D) or 10 μM DCPIB during 7 days (E) or with a hypo-osmotic medium during 24 h (F). Cells were then fixed and immunostained using antibodies against EEA1. Green signal corresponds to GFP which is expressed together with the shRNA. Scale bar: 20 μm.

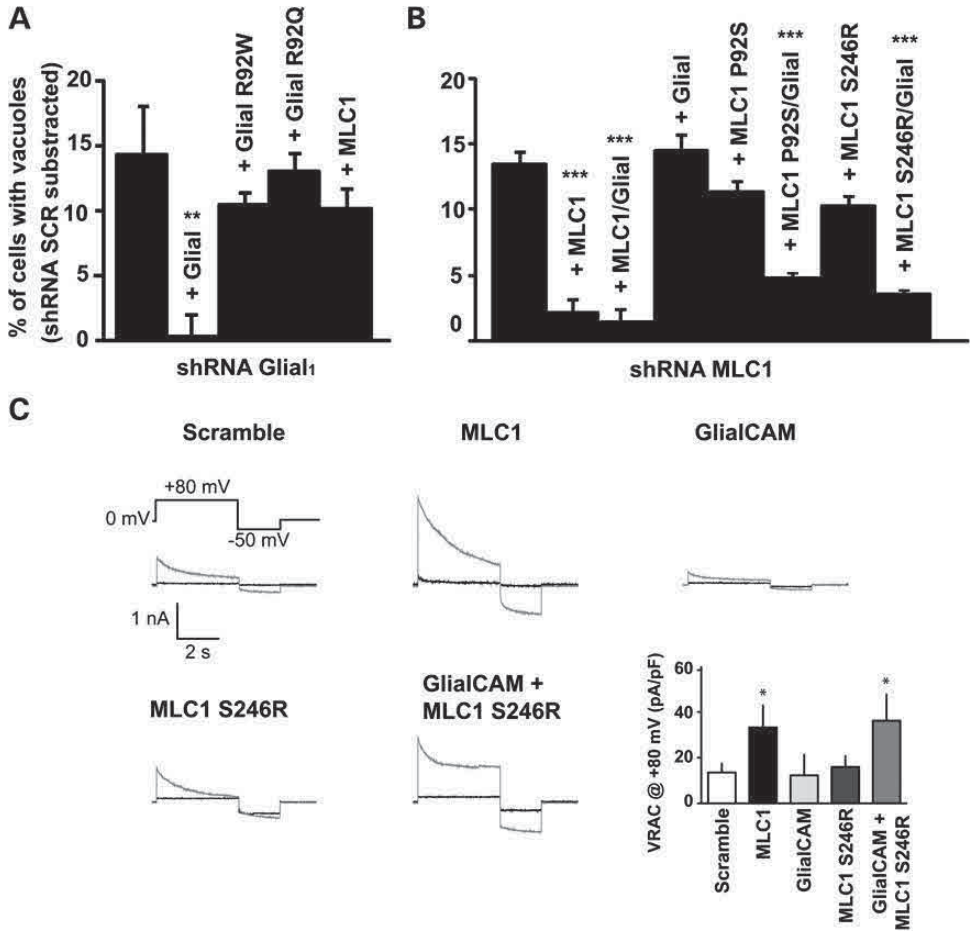

Figure 8. Correlation between VRAC activity and the vacuolation phenotype of astrocytes. (**A** and **B**) Quantification of the number of cells showing vacuolation after transduction with the shRNA-indicated and complemented or not with adenoviruses expressing the indicated constructs. In (A), data correspond to four to five independent experiments with the number of cells analyzed for each group as follows: shRNA SCR ($n = 1483$), shRNA Glial1 ($n = 1646$), shRNA Glial1 + Glial ($n = 1502$), shRNA Glial1 + Glial R92W ($n = 1776$), shRNA Glial1 + Glial R92Q ($n = 1917$), i shRNA Glial1 + MLC1 ($n = 1606$). $^{**}P < 0.01$ compared with shRNA Glial1. The background of cells with vacuoles of shRNA SCR (MOI 10) is 13.81 ± 1.98%. In (B), data correspond to four to five independent experiments with the number of cells analyzed for each group as follows: shRNA SCR ($n = 1009$), shRNA MLC1 ($n = 1064$), shRNA MLC1 + MLC1 ($n = 1094$), shRNA MLC1 + Glial ($n = 1164$), shRNA MLC1 + MLC1 P92S ($n = 1585$), shRNA MLC1 + MLC1 P92S + Glial ($n = 1379$), shRNA MLC1 + MLC1 S246R ($n = 1248$), shRNA MLC1 + MLC1 S246R + Glial ($n = 1203$). $^{***}P < 0.001$ compared with shRNA MLC1. The background of cells with vacuoles of shRNA SCR (MOI 5) is 5.38 ± 1.23%. (**C**) Representative traces at +80 mV of whole-cell chloride currents in isotonic (black) or hypotonic conditions (grey) elicited by the pulse protocol showed in the inset, in dbcAMP-treated cultured neocortical astrocytes transduced with shRNA scrambled or adenoviruses over-expressing MLC1, GlialCAM, MLC1 S246R or GlialCAM + MLC1 S246R. Astrocytes that did not show ClC-2 currents in isotonic conditions were selected. The plot shows average conductance values at +80 mV in hypotonic conditions. Results correspond to $n = 9$ for shRNA SCR, $n = 8$ for MLC1, $n = 5$ for GlialCAM, $n = 9$ for MLC1 S246R and $n = 9$ for GlialCAM + MLC1 S246R. $^{*}P < 0.05$ *t*-test versus. Scramble for all groups. Differences in the kinetics of inactivation were observed between groups in an unrelated manner, even in the same experimental group, and probably are related with differences in ionic strength between cells.

complementation with GlialCAM containing the MLC-related mutations R92Q or R92W, or further expression of MLC1 did not rescue the vacuolation defect (Fig. 8A). In agreement with these cellular defects, localization of over-expressed human MLC1 in GlialCAM-depleted astrocytes was detected mostly intracellularly (Supplementary Material, Fig. S5).

Similarly, vacuolation caused by the lack of MLC1 was rescued by expressing MLC1 or GlialCAM together with MLC1 (Fig. 8B). However, further expression of GlialCAM did not rescue the vacuolation phenotype. Rescue of MLC1 expression by MLC1 containing MLC-related mutations also failed to counteract the vacuolation phenotype (Fig. 8B), probably due to its intracellular localization (Fig. 3). However, restoring the localization of these proteins in junctions (Fig. 3) after co-expressing with GlialCAM successfully suppressed the vacuolation (Fig. 8B).

We next addressed whether the vacuolation could be correlated with changes in VRAC activity. Over-expression of MLC1 in dB-cAMP-treated astrocytes increased VRAC activity [Fig. 8C and (14)]. However, over-expression of GlialCAM alone or MLC1 containing the MLC-related mutation S246R did not increase VRAC activity [Fig. 8C and (14)]. In agreement with the rescue of the vacuolation defect, over-expression of MLC1 S246R together with GlialCAM also increased VRAC activity (Fig. 8C). Therefore, we suggest that defective VRAC activity may be directly linked to astrocyte vacuolation.

DISCUSSION

In this work, we have studied the effects of reducing GlialCAM expression in astrocytes, a recently identified MLC1 and ClC-2 subunit (18,20). Taking into account these new results presented here, we conclude that whereas GlialCAM is necessary for the targeting to astrocyte–astrocyte junctions of both MLC1 and ClC-2 (18,20), it has an additional role as an MLC1-chaperone. Based on the fact that the stabilization is observed in HeLa cells, that GlialCAM interacts directly with MLC1 (18) and that GlialCAM stabilizes also ER retained folding mutant variants of MLC1 (18), we propose that GlialCAM may protect MLC1 from ER-associated degradation. We hypothesize that this ER-protective effect of GlialCAM was not previously recognized due to the presence of endogenous GlialCAM expression in all the cell lines studied. Thus, it can be seen how expression of MLC1 in astrocytes without GlialCAM resulted in no plasma membrane staining of MLC1. As expression of MLC1 in astrocytes alone is able to arrive to the plasma membrane, it suggests that astrocytes should have an excess of endogenous GlialCAM compared with MLC1.

It has been shown that MLC-related mutations in GlialCAM do not substantially affect the interaction with MLC1 (18). Here, we also show that MLC-related GlialCAM variants are able to stabilize MLC1 protein, although they are not able to direct MLC1 to astrocyte junctions.

Reduction in both GlialCAM and MLC1 led to astrocyte vacuolation and a decreased VRAC activity (14). The function of VRAC currents which are heterogeneous is related with the efflux of water during the regulatory volume response (36). A decreased VRAC activity may cause an increase of intracellular water. We suggest that astrocyte vacuolation could be a consequence of increased water content, as blocking VRAC or the presence of a hypoosmotic medium (15) led to a similar type of vacuolation of endosomal origin. However, it is not clear how increased water content causes the appearance of vacuoles. It could be that astrocytes, which are cells evolutionary adapted to live in changing osmotic conditions, have gained the ability to keep the excess of intracellular water in the form of a vacuole, as happens in other organisms that form contractive vacuoles, and then they can survive in extracellular changing conditions (37–41).

How MLC1 and GlialCAM are related to VRAC activity? At this moment, it is very difficult to provide a clear answer to this question, as the function of MLC1 is unknown and the protein(s) responsible for VRAC activity still have to be discovered (27). Identification of the VRAC channel is a major and difficult task, as revealed by the reports of many potential candidates that later turned out to be wrong, such as ICln, p-Glycoprotein or the ClC-3 transporter (27,36). GlialCAM may affect VRAC activity due to the lack of MLC1, as GlialCAM over-expression by itself cannot compensate the vacuolation caused by the lack of MLC1. However, we believe that it is unlikely that MLC1 is directly responsible of VRAC, as VRAC activity is present in all the cells of the body (36), whereas MLC1 is mostly restricted to the brain and no other MLC1-homologous genes exists in mammals (7). In addition, VRAC activity is still present in astrocytes depleted of MLC1. MLC1 may affect VRAC activity indirectly, for instance, by modifying the adhesion strength of astrocytes or by affecting water or chloride handling in the brain. In this sense, aquaporin 4 depletion has also been shown to affect VRAC activity (42). It is worth to mention that MLC1 protein has also been found surrounding the endosomal membranes of astrocytes treated with a hypoosmotic solution (15) or with blockers such as DCPIB or Bumetanide (this work, data not shown). In these endosomal vesicles, MLC1 could contribute to the formation of water vacuoles by regulating water and/or chloride fluxes.

Interestingly, although GlialCAM proteins containing MLC-related mutations re-establish MLC1 protein expression, they do not direct MLC1 to junctions and are not able to rescue the vacuolation defect caused by the lack of MLC1. Therefore, we suggest that the correct localization of MLC1 is critical to perform its physiological function. In relation with putative roles suggested for MLC1 in ion transport or adhesion (10,14), its localization in junctions may be needed to allow transcellular fluxes of solutes or to detect easily changes in adhesion strength.

No treatment exists yet for MLC disease (1). Although the role of MLC1 is unknown, over-expression of GlialCAM rescues the vacuolation and the VRAC activity defect caused by some MLC1 mutants. Thus, the present data suggest that therapeutic strategies aimed at improving the surface expression of MLC1 or increasing the activity of VRAC may be envisaged as beneficial for MLC patients. This could be done by isolating pharmacological chaperones based on increased MLC1 plasma membrane expression (43) or molecules aimed to increase VRAC activity, as has been done for other chloride channels (44).

MATERIALS AND METHODS

Primary culture, adenoviral transduction and vacuolation analysis

Rat primary quiescent astrocyte cultures were prepared as described previously from P0–P2 pups (13). Dibutyryl-cAMP differentiated rat astrocytes, which were used for electrophysiological measurements, were obtained as described (29). Adenoviruses expressing three copies of the flag epitope fused to human GlialCAM, either wild-type or containing the MLC-related mutations R92Q or R92W have been described (17). Similarly, adenoviruses expressing HA-tagged wild-type MLC1 or containing the MLC-related mutations S246R or P92S were also constructed. Transduction of astrocytes was performed as already described (25).

To study the vacuolation of astrocytes, we counted the cells with showed clear vacuoles. A cell was positive for vacuolation if have at least three vacuoles of a size bigger than 0.5 μm. The minor vacuolation observed in astrocytes transduced with the corresponding group expressing SCR shRNA instead of the specific shRNA was subtracted from all the experimental groups. This was done to compare directly MLC1 and GlialCAM depleted astrocytes, as the multiplicity of infection was different between both groups (MOI 5 for shRNA MLC1 and MOI 10 for shRNA GlialCAM) and the day of processing after the infection (5 days for shRNA MLC1 and 7 days for shRNA GlialCAM).

RNA interference and RT-qPCR

RNAi entry-clone (Gateway, Invitrogen) vectors were prepared using the Block-it PolII miR RNAi EmGFP expression vector kit following manufacturer's instructions. Entry clones were

recombinated using LR clonase into the vector pAdVD EST-CMV/V5. Adenoviruses were produced and titrated using fluorescence microscopy detecting EmGFP which is expressed together with the shRNA. The adenoviruses expressing a negative control shRNA (shRNA SCR, scrambled) or expressing an shRNA directed against rat MLC1 (shRNA 905) were described previously (13). The sequence of the oligos used to knockdown rat GlialCAM expression was: shRNA Glial1 (shRNA 1392): 5′aagatcagcgctccacccattgttttggccactgactgacaatgggtggcgctgatctt3′ and shRNA Glial2 (shRNA 908): 5′tatagagcgccattggattctgtttt ggccactgactgacagaatccaggcgctctata3′.

Total RNA was prepared from a 10 cm culture plate using NucleoSpin RNA/Prot (Macherey–Nagel) as indicated by the manufacturer. RNA concentration was determined in a Nanodrop spectrophotometer. All samples had an A260/A280 ratio >1.8. RNA was stored at −80°C until further use. Eight hundred to 1000 ng of total RNA were reverse-transcribed with Transcriptor First Strand cDNA synthesis kit (Roche) following manufacturer's instructions at 25°C for 10 min followed by 50°C for 60 min, using random hexamers as primers. cDNA was stored at −80°C. qPCR was performed with Lightcycler 480 probes master kit (Roche) following manufacturer's instructions in a final volume of 10 μl, with cDNA at 1:10 dilution. The primers and UPL probes used were designed with the ProbeFinder version 2.45 (Roche) by the on-line application (https://www.roche-applied-science.com/sis/rtpcr/upl/index.jsp?Id=UP030000) considering exon spanning and covering all splicing species and have been previously indicated (13). qPCR was run in a LightCycler 480 II on 384 well plates with the settings previously indicated. Efficiency curves were used for each of the analyzed genes and relative gene expression for each sample was calculated using ACTB (actin) as reference after testing its suitability for the experimental setup. All amplifications were inside the linear range. Data came from six different astrocyte preparations. Means of triplicates were used for each analysis. The standard deviation of the triplicates was 0.2 or lower. Data analysis was made with LightCycler 480 SW 1.5 software (Roche) and MS-Excel and MS-Access 2007. Significance was calculated using a Bootstrap method (45), BootstRatio (http://regstattools.net/br), using the 'with control sample' condition and following tool instructions. Scrambled was used as a control sample.

For HeLa cells knockdown, constitutive (pGIPZ) lentivirus vectors, encoding shRNAmir-adapted short hairpin RNA specific for GlialCAM (GIPZ, V2LMM_69402 and V3LHS_413353), non-targeted variant (NT, ATCTCGCTTGGGCGAGAGTAAG), were obtained from Thermo Scientific, OpenBiosystems (USA). Lentivirus was produced and HeLa cells were transduced as described (46).

Immunofluorescence, western and surface expression studies in cells

For immunofluorescence staining, cells were fixed and processed as previously described (25). Antibodies used were the following: anti-GlialCAM [1:100, (17)], anti-MLC1 [1:100, (10)], anti-Occludin (1:100, Zymed), anti-β-Catenin (1:250, BD Transduction Lab), anti-Connexin 43 (1:100, Zymed) and anti-EEA1 (early endosomal antigen 1) (1:100, AbCAM). For WB studies, astrocyte lysates were prepared and processed as previously described (25). β-Actin protein levels were used as a loading control. To quantify signals by WB, we performed at least three expositions of all WBs, to ensure linearity. Scanned images were quantified using Multigauge software (Fujifilm) or the freely available Image J program (http://rsbweb.nih.gov/ij/) with similar results. Surface expression in transfected mammalian cells or astrocytes was performed as previously described (25).

In HeLa cells, the PM density of MLC1 and GlialCAM knockdown efficiency were determined by ELISA-based assay. HeLa cells expressing shGlialCAM or shSCR were trasfected with MLC1 cDNA constructs with Lipofectamine 2000 (Invitrogen, USA) 72 h prior to analysis. Cells were seeded on 24 well plates 20 h after transfection and incubated at 37°C for 24 h. Cells were temperature rescued at 26°C for 24 h, and unfolding was performed at 37°C for 1 h prior of experiment. Primary and secondary Abs were bound on ice in DMEM containing 5% bovine serum (Gibco, USA). The extracellular epitope was detected with mouse anti-human HepaCAM (1:1000, R&D Systems, USA) and mouse anti-HA (1:1000 cl11, Covance, Canada) antibodies. Excess antibody was washed away and specific binding was determined by HRP-conjugated secondary Ab (Amersham Biosciences, Canada) with Amplex® Red (Invitrogen) as a substrate. The fluorescence intensity was measured from quadruplicate samples using a Infinite 1000 m PRO (Tecan Group Ltd, USA) fluorescence plate-reader at 544 nm excitation and 590 nm emission wavelengths. Total Ab binding was corrected with non-specific Ab binding, determined in mock transfected cells.

For immunoblotting, the cells were lysed in RIPA buffer containing 10 μM MG132, 10 μg/ml pepstatin + leupeptin, 1 mM phenylmethylsulfonyl fluoride and 5 mM *N*-ethylmaleimide. Polypeptides were separated by SDS–PAGE and probed by immunoblotting using Supersignal Western Pico (Pierce, USA). Na^+–K^+-Atpase (1:500, Santa Cruz, USA) was used as a loading control.

Patch-clamp experiments of astrocytes

Three days before the experiment, dB-cAMP differentiated astrocytes were trypsinized and replated at a density of 1- to 3×10^4 onto 24-well plates containing a glass cover slip with DMEM supplemented medium and 250 μM dB-cAMP. For electrophysiological recordings, the glass cover slip was mounted on the stage of an inverted microscopy equipped with phase-contrast optics and fluorescence illumination. Patch pipettes were pulled from borosilicate glass capillaries (Clark Electromedical, UK) and used after fire polishing (Narishige, Japan). Electrophysiological recordings were performed with a patch-clamp amplifier (Axopatch 200B, Molecular Devices, Union City, CA, USA) Patch electrodes were fabricated in a Flaming/Brown micropipettepuller P-97 (Sutter instruments). Electrodes had a resistance between 4 and 5 MΩ when filled with intracellular solution (in mM): 144 NMDG-Cl, 2 $MgCl_2$, 5 EGTA, 5 HEPES at pH 7.3 and 308 ± 2 mOsm/kg. Extracellular solution contained (in mM): 144 NMDG-Cl, 2 $CaCl_2$, 2 $MgCl_2$, 5 HEPES, 5 glucose at pH 7.4 and 310 ± 3 mOsm/kg. Hypotonic extracellular solution (−25%) was prepared by decreasing NMDG-Cl concentration to 105 mM (229 ± 2 mOsm/kg). All solution osmolarities were adjusted with sorbitol. An Ag/AgCl ground electrode

mounted in a 3 M KCl agar bridge was used. Membrane currents were recorded in the whole-cell patch clamp configuration, filtered at 2 kHz, digitized at 10 kHz and acquired with pClamp 9 software (Molecular Devices). Data were analyzed with Clampfit 9 (Molecular Devices) and Prism 4 (GraphPad Software, Inc., La Jolla, CA, USA). Whole-cell capacitance and series resistance were compensated with the amplifier circuitry. Series resistance was always kept below 10 MΩ and compensated at 70–80%. All recordings were performed at room temperature (22–23°C). Currents were evoked with 4 s pulses from +80 to −120 mV from a holding potential of 0 mV.

SUPPLEMENTARY MATERIAL

Supplementary Material is available at *HMG* online.

ACKNOWLEDGEMENTS

We thank Michael Pusch, Thomas Jentsch and Herbert Schwarz for helpful comments about the manuscript.

Conflict of Interest statement. None declared.

FUNDING

This study was supported in part by SAF 2009-07014 (R.E.) and SAF2012-31486 (R.E.), PS09/02672-ERARE to R.E., ELA Foundation 2009-017C4 project (R.E. and V.N.), 2009 SGR 719 (R.E.), FISPI11/01601 (X.G.), 2009 SGR869 (X.G.), RD12/0034/0003 (X.G.), SAF 2009-12606-C02-02 (V.N.), 2009 SGR01490 (V.N.) and Canadian Institute of Health Research and Canada Foundation of Innovation (G.L.L.). G.L.L. is a Canada Research Chair and RE is a recipient of an ICREA Academia prize.

REFERENCES

1. van der Knaap, M.S., Boor, I. and Estevez, R. (2012) Megalencephalic leukoencephalopathy with subcortical cysts: chronic white matter oedema due to a defect in brain ion and water homoeostasis. *Lancet Neurol.*, **11**, 973–985.
2. van der Knaap, M.S., Barth, P.G., Stroink, H., van Nieuwenhuizen, O., Arts, W.F., Hoogenraad, F. and Valk, J. (1995) Leukoencephalopathy with swelling and a discrepantly mild clinical course in eight children. *Ann. Neurol.*, **37**, 324–334.
3. van der Knaap, M.S., Valk, J., Barth, P.G., Smit, L.M., van Engelen, B.G. and Tortori Donati, P. (1995) Leukoencephalopathy with swelling in children and adolescents: MRI patterns and differential diagnosis. *Neuroradiology*, **37**, 679–686.
4. van der Knaap, M.S., Barth, P.G., Vrensen, G.F. and Valk, J. (1996) Histopathology of an infantile-onset spongiform leukoencephalopathy with a discrepantly mild clinical course. *Acta Neuropathol.*, **92**, 206–212.
5. Gelal, F., Calli, C., Apaydin, M. and Erdem, G. (2002) Van der knaap's leukoencephalopathy: report of five new cases with emphasis on diffusion-weighted MRI findings. *Neuroradiology*, **44**, 625–630.
6. De Stefano, N., Balestri, P., Dotti, M.T., Grosso, S., Mortilla, M., Morgese, G. and Federico, A. (2001) Severe metabolic abnormalities in the white matter of patients with vacuolating megalencephalic leukoencephalopathy with subcortical cysts. A proton MR spectroscopic imaging study. *J. Neurol.*, **248**, 403–409.
7. Leegwater, P.A., Yuan, B.Q., van der Steen, J., Mulders, J., Konst, A.A., Boor, P.K., Mejaski-Bosnjak, V., van der Maarel, S.M., Frants, R.R., Oudejans, C.B. *et al.* (2001) Mutations of MLC1 (KIAA0027), encoding a putative membrane protein, cause megalencephalic leukoencephalopathy with subcortical cysts. *Am. J. Hum. Genet.*, **68**, 831–838.
8. Boor, P.K., de Groot, K., Waisfisz, Q., Kamphorst, W., Oudejans, C.B., Powers, J.M., Pronk, J.C., Scheper, G.C. and van der Knaap, M.S. (2005) MLC1: a novel protein in distal astroglial processes. *J. Neuropathol. Exp. Neurol.*, **64**, 412–419.
9. Schmitt, A., Gofferje, V., Weber, M., Meyer, J., Mossner, R. and Lesch, K.P. (2003) The brain-specific protein MLC1 implicated in megalencephalic leukoencephalopathy with subcortical cysts is expressed in glial cells in the murine brain. *Glia*, **44**, 283–295.
10. Teijido, O., Martinez, A., Pusch, M., Zorzano, A., Soriano, E., Del Rio, J.A., Palacin, M. and Estevez, R. (2004) Localization and functional analyses of the MLC1 protein involved in megalencephalic leukoencephalopathy with subcortical cysts. *Hum. Mol. Genet.*, **13**, 2581–2594.
11. Teijido, O., Casaroli-Marano, R., Kharkovets, T., Aguado, F., Zorzano, A., Palacin, M., Soriano, E., Martinez, A. and Estevez, R. (2007) Expression patterns of MLC1 protein in the central and peripheral nervous systems. *Neurobiol. Dis.*, **26**, 532–545.
12. Gorospe, J.R. and Maletkovic, J. (2006) Alexander disease and megalencephalic leukoencephalopathy with subcortical cysts: leukodystrophies arising from astrocyte dysfunction. *Ment. Retard. Dev. Disabil. Res. Rev.*, **12**, 113–122.
13. Duarri, A., Lopez de Heredia, M., Capdevila-Nortes, X., Ridder, M.C., Montolio, M., Lopez-Hernandez, T., Boor, I., Lien, C.F., Hagemann, T., Messing, A. *et al.* (2011) Knockdown of MLC1 in primary astrocytes causes cell vacuolation: a MLC disease cell model. *Neurobiol. Dis.*, **43**, 228–238.
14. Ridder, M.C., Boor, I., Lodder, J.C., Postma, N.L., Capdevila-Nortes, X., Duarri, A., Brussaard, A.B., Estevez, R., Scheper, G.C., Mansvelder, H.D. *et al.* (2011) Megalencephalic leucoencephalopathy with cysts: Defect in chloride currents and cell volume regulation. *Brain*, **134**, 3342–3354.
15. Brignone, M.S., Lanciotti, A., Macioce, P., Macchia, G., Gaetani, M., Aloisi, F., Petrucci, T.C. and Ambrosini, E. (2011) The beta1 subunit of the na,K-ATPase pump interacts with megalencephalic leucoencephalopathy with subcortical cysts protein 1 (MLC1) in brain astrocytes: New insights into MLC pathogenesis. *Hum. Mol. Genet.*, **20**, 90–103.
16. Lanciotti, A., Brignone, M.S., Molinari, P., Visentin, S., De Nuccio, C., Macchia, G., Aiello, C., Bertini, E., Aloisi, F., Petrucci, T.C. *et al.* (2012) Megalencephalic leukoencephalopathy with subcortical cysts protein 1 functionally cooperates with the TRPV4 cation channel to activate the response of astrocytes to osmotic stress: dysregulation by pathological mutations. *Hum. Mol. Genet.*, **21**, 2166–2180.
17. Lopez-Hernandez, T., Ridder, M.C., Montolio, M., Capdevila-Nortes, X., Polder, E., Sirisi, S., Duarri, A., Schulte, U., Fakler, B., Nunes, V. *et al.* (2011) Mutant GlialCAM causes megalencephalic leukoencephalopathy with subcortical cysts, benign familial macrocephaly, and macrocephaly with retardation and autism. *Am. J. Hum. Genet.*, **88**, 422–432.
18. Lopez-Hernandez, T., Sirisi, S., Capdevila-Nortes, X., Montolio, M., Fernandez-Duenas, V., Scheper, G.C., van der Knaap, M.S., Casquero, P., Ciruela, F., Ferrer, I. *et al.* (2011) Molecular mechanisms of MLC1 and GLIALCAM mutations in megalencephalic leukoencephalopathy with subcortical cysts. *Hum. Mol. Genet.*, **20**, 3266–3277.
19. Favre-Kontula, L., Rolland, A., Bernasconi, L., Karmirantzou, M., Power, C., Antonsson, B. and Boschert, U. (2008) GlialCAM, an immunoglobulin-like cell adhesion molecule is expressed in glial cells of the central nervous system. *Glia*, **56**, 633–645.
20. Jeworutzki, E., Lopez-Hernandez, T., Capdevila-Nortes, X., Sirisi, S., Bengtsson, L., Montolio, M., Zifarelli, G., Arnedo, T., Muller, C.S., Schulte, U. *et al.* (2012) GlialCAM, a protein defective in a leukodystrophy, serves as a ClC-2 cl(-) channel auxiliary subunit. *Neuron*, **73**, 951–961.
21. Blanz, J., Schweizer, M., Auberson, M., Maier, H., Muenscher, A., Hubner, C.A. and Jentsch, T.J. (2007) Leukoencephalopathy upon disruption of the chloride channel ClC-2. *J. Neurosci.*, **27**, 6581–6589.
22. Scheper, G.C., van Berkel, C.G., Leisle, L., de Groot, K.E., Errami, A., Jentsch, T.J. and Van der Knaap, M.S. (2010) Analysis of CLCN2 as candidate gene for megalencephalic leukoencephalopathy with subcortical cysts. *Genet. Test. Mol. Biomarkers*, **14**, 255–257.
23. Depienne, C., Bugiani, M., Dupuits, C., Galanaud, D., Touitou, V., Postma, N., van Berkel, C., Polder, E., Tollard, E., Darios, F. *et al.* (2013) Brain white matter oedema due to ClC-2 chloride channel deficiency: An observational analytical study. *Lancet Neurol.*, **12**, 659–668.
24. van der Knaap, M.S., Lai, V., Kohler, W., Salih, M.A., Fonseca, M.J., Benke, T.A., Wilson, C., Jayakar, P., Aine, M.R., Dom, L. *et al.* (2010)

Megalencephalic leukoencephalopathy with cysts without MLC1 defect. *Ann. Neurol.*, **67**, 834–837.
25. Duarri, A., Teijido, O., Lopez-Hernandez, T., Scheper, G.C., Barriere, H., Boor, I., Aguado, F., Zorzano, A., Palacin, M., Martinez, A. *et al.* (2008) Molecular pathogenesis of megalencephalic leukoencephalopathy with subcortical cysts: mutations in MLC1 cause folding defects. *Hum. Mol. Genet.*, **17**, 3728–3739.
26. Leisle, L., Ludwig, C.F., Wagner, F.A., Jentsch, T.J. and Stauber, T. (2011) ClC-7 is a slowly voltage-gated 2Cl(-)/1H(+)-exchanger and requires Ostm1 for transport activity. *EMBO J.*, **30**, 2140–2152.
27. Jentsch, T.J., Stein, V., Weinreich, F. and Zdebik, A.A. (2002) Molecular structure and physiological function of chloride channels. *Physiol. Rev.*, **82**, 503–568.
28. Parkerson, K.A. and Sontheimer, H. (2004) Biophysical and pharmacological characterization of hypotonically activated chloride currents in cortical astrocytes. *Glia*, **46**, 419–436.
29. Ferroni, S., Marchini, C., Nobile, M. and Rapisarda, C. (1997) Characterization of an inwardly rectifying chloride conductance expressed by cultured rat cortical astrocytes. *Glia*, **21**, 217–227.
30. Benesova, J., Rusnakova, V., Honsa, P., Pivonkova, H., Dzamba, D., Kubista, M. and Anderova, M. (2012) Distinct expression/function of potassium and chloride channels contributes to the diverse volume regulation in cortical astrocytes of GFAP/EGFP mice. *PLoS ONE*, **7**, e29725.
31. Gagnon, K.B., Adragna, N.C., Fyffe, R.E. and Lauf, P.K. (2007) Characterization of glial cell K-cl cotransport. *Cell. Physiol. Biochem.*, **20**, 121–130.
32. Jayakumar, A.R., Panickar, K.S., Curtis, K.M., Tong, X.Y., Moriyama, M. and Norenberg, M.D. (2011) Na-K-cl cotransporter-1 in the mechanism of cell swelling in cultured astrocytes after fluid percussion injury. *J. Neurochem.*, **117**, 437–448.
33. Su, G., Kintner, D.B., Flagella, M., Shull, G.E. and Sun, D. (2002) Astrocytes from na(+)-K(+)-cl(-) cotransporter-null mice exhibit absence of swelling and decrease in EAA release. *Am. J. Physiol. Cell. Physiol.*, **282**, C1147–C1160.
34. Su, G., Kintner, D.B. and Sun, D. (2002) Contribution of na(+)-K(+)-cl(-) cotransporter to high-[K(+)](o)- induced swelling and EAA release in astrocytes. *Am. J. Physiol. Cell. Physiol.*, **282**, C1136–C1146.
35. Zhang, Y., Zhang, H., Feustel, P.J. and Kimelberg, H.K. (2008) DCPIB, a specific inhibitor of volume regulated anion channels (VRACs), reduces infarct size in MCAo and the release of glutamate in the ischemic cortical penumbra. *Exp. Neurol.*, **210**, 514–520.
36. Nilius, B. and Droogmans, G. (2003) Amazing chloride channels: An overview. *Acta Physiol. Scand.*, **177**, 119–147.
37. Komsic-Buchmann, K., Stephan, L.M. and Becker, B. (2012) The SEC6 protein is required for contractile vacuole function in chlamydomonas reinhardtii. *J. Cell. Sci.*, **125**, 2885–2895.
38. Schonemann, B., Bledowski, A., Sehring, I.M. and Plattner, H. (2012) A set of SNARE proteins in the contractile vacuole complex of paramecium regulates cellular calcium tolerance and also contributes to organelle biogenesis. *Cell Calcium*, **53**, 204–216.
39. Sivaramakrishnan, V. and Fountain, S.J. (2012) Intracellular P2X receptors as novel calcium release channels and modulators of osmoregulation in dictyostelium: a comparison of two common laboratory strains. *Channels (Austin)*, **7**, 43–46.
40. Ulrich, P.N., Jimenez, V., Park, M., Martins, V.P., Atwood, J. 3rd, Moles, K., Collins, D., Rohloff, P., Tarleton, R., Moreno, S.N. *et al.* (2011) Identification of contractile vacuole proteins in trypanosoma cruzi. *PLoS ONE*, **6**, e18013.
41. Essid, M., Gopaldass, N., Yoshida, K., Merrifield, C. and Soldati, T. (2012) Rab8a regulates the exocyst-mediated kiss-and-run discharge of the dictyostelium contractile vacuole. *Mol. Biol. Cell*, **23**, 1267–1282.
42. Benfenati, V., Nicchia, G.P., Svelto, M., Rapisarda, C., Frigeri, A. and Ferroni, S. (2007) Functional down-regulation of volume-regulated anion channels in AQP4 knockdown cultured rat cortical astrocytes. *J. Neurochem.*, **100**, 87–104.
43. Okiyoneda, T., Veit, G., Dekkers, J.F., Bagdany, M., Soya, N., Xu, H., Roldan, A., Verkman, A.S., Kurth, M., Simon, A. *et al.* (2013) Mechanism-based corrector combination restores DeltaF508-CFTR folding and function. *Nat. Chem. Biol.*, **9**, 444–454.
44. Verkman, A.S. and Galietta, L.J. (2009) Chloride channels as drug targets. *Nat. Rev. Drug Discov.*, **8**, 153–171.
45. Cleries, R., Galvez, J., Espino, M., Ribes, J., Nunes, V. and de Heredia, M.L. (2012) BootstRatio: a web-based statistical analysis of fold-change in qPCR and RT-qPCR data using resampling methods. *Comput. Biol. Med.*, **42**, 438–445.
46. Apaja, P.M., Xu, H. and Lukacs, G.L. (2010) Quality control for unfolded proteins at the plasma membrane. *J. Cell Biol.*, **191**, 553–570.

Disrupting MLC1 and GlialCAM and ClC-2 interactions in leukodistrophy entails glial chloride channel disfunction

(Nature Communications, 2014)

Contribució:

- Estudi de l'expressió de MLC1, GlialCAM i ClC-2 en el model *knock-out* per *Mlc1* (Figura 1)
- Estudi de la localització de MLC1, GlialCAM i ClC-2 en el model *knock-out* per *Mlc1* (Figura 2).
- Estudi del fenotip vacuolitzant mitjançant ME en el model *knock-out* per *Mlc1* (Figura 8, Figura Suplementària 9)

nature COMMUNICATIONS

ARTICLE

Received 10 Oct 2013 | Accepted 18 Feb 2014 | Published 19 Mar 2014

Disrupting MLC1 and GlialCAM and ClC-2 interactions in leukodystrophy entails glial chloride channel dysfunction

Maja B. Hoegg-Beiler[1,2,*], Sònia Sirisi[3,4,*], Ian J. Orozco[1,2,*], Isidre Ferrer[5], Svea Hohensee[1], Muriel Auberson[1,2,†], Kathrin Gödde[1,2], Clara Vilches[4], Miguel López de Heredia[4,6], Virginia Nunes[4,6,7], Raúl Estévez[3,8] & Thomas J. Jentsch[1,2,9]

Defects in the astrocytic membrane protein MLC1, the adhesion molecule GlialCAM or the chloride channel ClC-2 underlie human leukoencephalopathies. Whereas GlialCAM binds ClC-2 and MLC1, and modifies ClC-2 currents *in vitro*, no functional connections between MLC1 and ClC-2 are known. Here we investigate this by generating loss-of-function *Glialcam* and *Mlc1* mouse models manifesting myelin vacuolization. We find that ClC-2 is unnecessary for MLC1 and GlialCAM localization in brain, whereas GlialCAM is important for targeting MLC1 and ClC-2 to specialized glial domains *in vivo* and for modifying ClC-2's biophysical properties specifically in oligodendrocytes (OLs), the cells chiefly affected by vacuolization. Unexpectedly, MLC1 is crucial for proper localization of GlialCAM and ClC-2, and for changing ClC-2 currents. Our data unmask an unforeseen functional relationship between MLC1 and ClC-2 *in vivo*, which is probably mediated by GlialCAM, and suggest that ClC-2 participates in the pathogenesis of megalencephalic leukoencephalopathy with subcortical cysts.

[1] Leibniz-Institut für molekulare Pharmakologie (FMP), Department Physiology and Pathology of Ion Transport, D-13125 Berlin, Germany. [2] Max-Delbrück-Centrum für Molekulare Medizin (MDC), D-13125 Berlin, Germany. [3] Physiology Section, Physiological Sciences II, Universitat de Barcelona, E-08907 Barcelona, Spain. [4] Molecular Genetics Laboratory-IDIBELL, E-08908 Barcelona, Spain. [5] Institute of Neuropathology, Pathologic Anatomy Service, IDIBELL-University Hospital Bellvitge, E-08907 L'Hospitalet de Llobregat, Spain. [6] Centro de Investigación en Red de Enfermedades Raras CIBERER, ISCIII U-730, E-08908 Barcelona, Spain. [7] Genetics Section, Physiological Sciences II, Universitat de Barcelona, E-08907 Barcelona, Spain. [8] Centro de Investigación en Red de Enfermedades Raras CIBERER, ISCIII U-750, E-08907 Barcelona, Spain. [9] NeuroCure Cluster of Excellence, Charité Universitätsmedizin Berlin, D-10117 Berlin, Germany. * These authors contributed equally to this work. † Present address: Département de Pharmacologie et Toxicologie, Université de Lausanne, CH-1005 Lausanne, Switzerland (M.A.). Correspondence and requests for materials should be addressed to V.N. (email: vnunes@idibell.cat) or to R.E. (email: restevez@ub.edu) or to T.J.J. (email: Jentsch@fmp-berlin.de).

Several forms of leukodystrophies, degenerative disorders affecting the white matter of the brain, are associated with vacuolization of myelin sheaths that enwrap axons of central neurons. A particular subentity of this disease, megalencephalic leukoencephalopathy with subcortical cysts (in short MLC), can be caused by mutations in either *MLC1* (ref. 1), encoding a protein predicted to span the plasma membrane eight times, or less frequently in *GLIALCAM*[2,3], which encodes the adhesion molecule GlialCAM of the immunoglobulin superfamily[4]. MLC1 and GlialCAM bind each other, and this binding originally suggested *GLIALCAM* as a candidate gene for MLC[2]. GlialCAM was first identified as being downregulated in hepatic cancer (hence, its original name HepaCAM[5]), but is predominantly expressed in glial cells[6]. GlialCAM co-localizes with its binding partner MLC1 at astrocytic endfeet contacting blood vessels and at astrocyte–astrocyte contacts[7]. GlialCAM and MLC1 share this localization with the ClC-2 chloride channel[8]. In addition to other symptoms[9], *Clcn2*$^{-/-}$ mice display leukodystrophy[8], suggesting that ClC-2 deficiency might underlie human leukoencephalopathy. Screens for *CLCN2* mutations in leukodystrophy patients were initially negative[8,10], but a recent study identified *CLCN2* mutations in a distinct form of leukoencephalopathy[11]. Clinical symptoms of either form of the disease include ataxia and sometimes spasticity. On the basis of a limited number of patients, *CLCN2* leukodystrophy differs from MLC in the magnetic resonance imaging pattern of affected brains[11]. By contrast, clinical and magnetic resonance imaging features of patients with the MLC1 disease entity (mutations in *MLC1*) are virtually indistinguishable from those affected by MLC2A (*GLIALCAM* mutations on both alleles). The disease is more benign in patients with heterozygous *GLIALCAM* mutations in dominantly inherited MLC2B[2].

GlialCAM binds not only MLC1 but also ClC-2 (ref. 12), a widely expressed Cl^- channel activated by hyperpolarization and cell swelling[13–15]. ClC-2 is found in both neurons and glia. GlialCAM directs ClC-2 and MLC1 to cell–cell contacts in heterologous expression. This effect is abolished by several point mutations found in MLC2 patients[3,7,12]. GlialCAM drastically changes ClC-2 currents in various expression systems by increasing their amplitudes and almost abolishing their inward rectification[12]. It thus appears possible that GlialCAM mutations cause leukodystrophy by mislocalizing ClC-2 and/or by affecting its currents. By contrast, no effects of MLC1 on ClC-2 function, localization or abundance were found[12,16]. Thus, it remains unclear why patients with *MLC1* mutations have the same symptoms as patients with recessive *GLIALCAM* mutations, who, based on these cell culture data, would be expected to be more severely affected.

Here we investigate the functional network of MLC1, GlialCAM and ClC-2 *in vivo,* and its role in leukodystrophy, by generating mice that lack MLC1 or GlialCAM proteins (*Mlc1*$^{-/-}$ and *Glialcam*$^{-/-}$ mice, respectively) and *Glialcam*$^{dn/dn}$ knockin mice harbouring a dominant point mutation found in patients[2,12]. All three mouse lines develop progressive myelin vacuolization in the cerebellum. Loss of GlialCAM changes the localization and abundance of ClC-2 and MLC1, and surprisingly loss of MLC1 changes the localization of ClC-2 and GlialCAM. The linearization and enhancement of ClC-2 currents by GlialCAM that is known from heterologous expression is observed in OLs, but not in Bergmann glia (BG). Hence, GlialCAM-dependent anchoring of ClC-2 to plasma membrane domains is not necessarily coupled with changes in ClC-2 current characteristics. Crosses between different *Clcn2* and *Glialcam* models indicate that the pathology observed with loss of GlialCAM or MLC1 may be partially attributed to a secondary loss of ClC-2 function, but that the loss of either GlialCAM or MLC1 has additional pathogenic effects.

Results

Mlc1 and Glialcam mouse models. Exons 2 and 3 of the *Mlc1* gene were deleted to generate *Mlc1*$^{-/-}$ mice (Supplementary Fig. 1a,b). Western blots confirmed the absence of the MLC1 protein (Fig. 1a). A point mutation was inserted into the mouse *Glialcam* gene that changes G89 in the first immunoglobulin domain to serine (Supplementary Fig. 1c–e). This mutation (G89S) is found in MLC patients with dominant disease[2]. Exons 2–4 were flanked by loxP sites to generate GlialCAM knockout (*Glialcam*$^{-/-}$) mice by crossing *Glialcam*^{G89S,loxP} (in the following called *Glialcam*^{dn}) mice with deleter mice[17] (Supplementary Fig. 1c,e). *Glialcam*^{dn} messenger RNA was expressed at normal levels in the brain (Fig. 1b). Western blots showed that the G89S mutation did not reduce GlialCAM levels (Fig. 1c,d) and that GlialCAM, although initially called HepaCAM, lacks significant expression in the liver[6] (Fig. 1a). As expected, GlialCAM was absent from *Glialcam*$^{-/-}$ brain.

Mlc1$^{-/-}$, *Glialcam*$^{-/-}$ and *Glialcam*$^{dn/dn}$ mice were viable and fertile. Similar to *Clcn2*$^{-/-}$ mice[8], they lacked overt ataxia or spasticity as might have been expected from MLC patients with mutations in the *MLC1* or *GLIALCAM* (*HEPACAM*) genes[1,2].

Interdependent protein expression of GlialCAM MLC1 and ClC-2. We wondered whether the expression of ClC-2 and MLC1, both of which bind GlialCAM[2,12], might be changed in the *Glialcam* mouse models. As myelin vacuolization is most pronounced in the cerebellum of *Clcn2*$^{-/-}$ mice[8] and in the present *Glialcam* and *Mlc1* models (see below), we separately studied protein expression in the cerebellum and the rest of the brain. ClC-2 was reduced by ~50% in *Glialcam*$^{-/-}$ and *Glialcam*$^{dn/dn}$ cerebella (Fig. 1c) but not in the remaining brain (Fig. 1d). MLC1 was strongly decreased in the whole brain of *Glialcam*$^{-/-}$ mice, whereas in *Glialcam*$^{dn/dn}$ mice, MLC1 was moderately decreased only in the cerebellum (Fig. 1c,d). Although MLC1 reportedly binds GlialCAM, but not ClC-2 (refs 2,12), ClC-2 was reduced in *Mlc1*$^{-/-}$ cerebellum (Fig. 1c), whereas GlialCAM appeared nearly unchanged (Fig. 1c,d). Agreeing with previous work[12], GlialCAM and MLC1 were not reduced in *Clcn2*$^{-/-}$ brain and MLC1 appeared even somewhat increased in *Clcn2*$^{-/-}$ cerebellum (Fig. 1c,d).

Hence, GlialCAM stabilizes MLC1 and the G89S mutant partially retains this stabilizing effect. Both proteins stabilize ClC-2 in the cerebellum. However, ClC-2 is not required for the stability of either GlialCAM or MLC1. These stabilizing effects occur post-transcriptionally as quantitative real-time PCR showed no changes in messenger RNA levels (Fig. 1b).

Mutually dependent localization of GlialCAM MLC1 and ClC-2. Whereas GlialCAM directs ClC-2 and MLC1 to cell–cell junctions, MLC1 co-transfection does not change the localization of either GlialCAM or ClC-2 (refs 7,12). We asked whether these *in vitro* results are relevant *in vivo*. We first focused on cerebellar BG because their long, straight processes showed particularly prominent, overlapping labelling for ClC-2, MLC1 and GlialCAM (Fig. 2a). Moreover, the morphology of BG allows easy visualization of changes in subcellular localization. Whereas ClC-2 disruption had no detectable effect on GlialCAM and MLC1 in BG[12] (Fig. 2a), ablation of GlialCAM strongly reduced the labelling for both ClC-2 and MLC1 and changed their localization (Fig. 2a,b). Rather than being concentrated along BG processes, both proteins showed faint diffuse staining in the molecular layer and in BG somata where a sizeable portion of immunoreactivity appeared intracellular (Fig. 2b).

In *Glialcam*$^{dn/dn}$ mice, in which GlialCAM-binding properties might be altered by the G89S mutation in the first extracellular

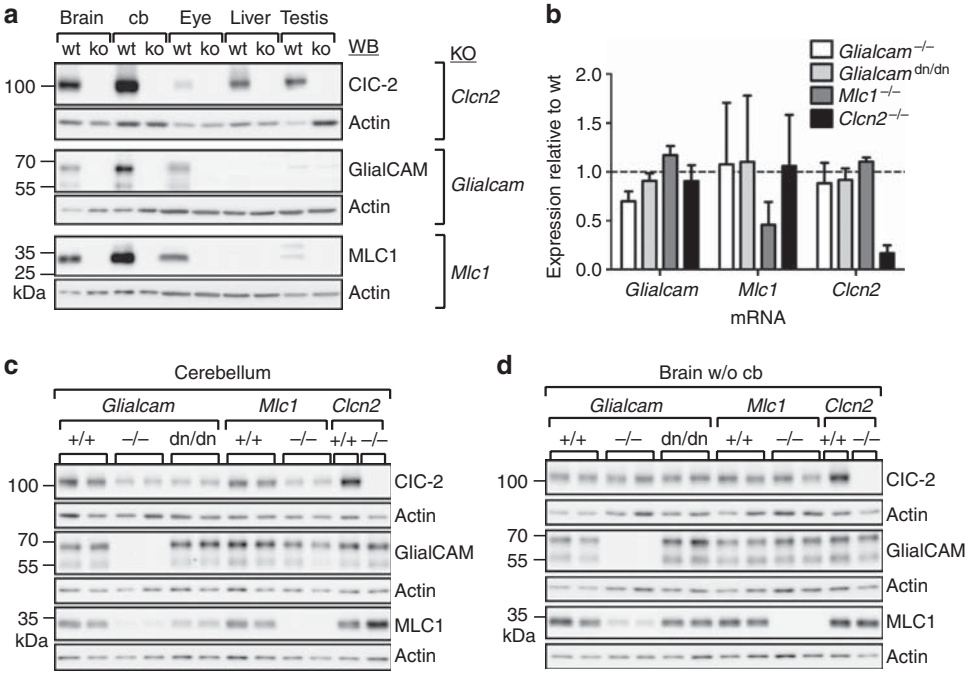

Figure 1 | Expression of ClC-2, GlialCAM and MLC1 in *Glialcam* and *Mlc1* mouse models. (**a**) Western blots for ClC-2 (top), GlialCAM (middle) and MLC1 (bottom) of membrane fractions isolated from organs of WT, and $Clcn2^{-/-}$, $Glialcam^{-/-}$ or $Mlc1^{-/-}$ mice, respectively (age: 10–12 weeks). For ClC-2, equal amounts of protein per organ were loaded, whereas for GlialCAM and MLC1 blots, 10 times more protein was loaded for the eye, liver and testis compared with the brain (without cerebellum) and cerebellum (cb). (**b**) Quantitative real-time PCR to determine levels of *Glialcam*, *Mlc1* and *Clcn2* messenger RNA in the cerebellum of different mouse models. Primers were chosen to amplify regions that were not deleted in corresponding knockout (KO) mice. Bars, relative expression level compared with WT sibling; error bars, s.d. ($n \geq 2$). (**c**) Comparison of ClC-2, GlialCAM and MLC1 protein levels in cerebellum and (**d**) remainder of the brain of WT, $Glialcam^{-/-}$, $Glialcam^{dn/dn}$, $Mlc1^{-/-}$ and $Clcn2^{-/-}$ mice by western blots of membrane fractions from 10-week-old mice. (**c**,**d**) Western blots representative for three independent experiments. Actin served as a loading control. All full size blots can be found in Supplementary Fig. 2.

Ig-domain[2], GlialCAM antibodies did not label the straight BG processes, but still diffusely stained the molecular layer (Fig. 2a). Heterozygous $Glialcam^{+/dn}$ mice showed an intermediate phenotype with MLC1 being diffusely labelled in the molecular layer and only small amounts remaining along BG processes (Fig. 2a). In both homo- and heterozygous $Glialcam^{dn}$ mice, ClC-2 was retained in BG somata with ClC-2 extending further into BG processes in $Glialcam^{+/dn}$ mice (Fig. 2a).

Agreeing with the western blot analysis, overall labelling of ClC-2 was reduced in $Mlc1^{-/-}$ cerebella (Fig. 2a), and ClC-2 was retained in BG somata like in $Glialcam^{-/-}$ mice (Fig. 2a,b). GlialCAM immunolabelling was similarly diffuse in $Mlc1^{-/-}$ as in $Glialcam^{dn/dn}$ cerebellum.

ClC-2, GlialCAM and MLC1 localization at astrocytic endfeet along blood vessels was reduced in $Glialcam^{-/-}$, $Glialcam^{dn/dn}$ and $Mlc1^{-/-}$ mice (Fig. 3a). In contrast, the localization of the water channel aquaporin 4 and the K^+-channel Kir4.1 (KCNJ10), two proteins reported[18] to reside in a complex with MLC1, were not changed in $Mlc1^{-/-}$ and $Glialcam^{-/-}$ mice (Fig. 3b).

In wild-type (WT) OLs, ClC-2, GlialCAM and MLC1 clustered around their somata (Fig. 4), as previously described for ClC-2 and GlialCAM[8,12]. However, unlike ClC-2 and GlialCAM, MLC1 is apparently not expressed in OLs[2,19,20]. As MLC1 was detected in neighbouring *bona fide* astrocytes (Fig. 4), the MLC1 staining at oligodendrocytic somata may stem from contact-forming astrocytic processes.

In $Glialcam^{-/-}$, $Glialcam^{dn/dn}$ and $Mlc1^{-/-}$ mice, ClC-2 no longer formed distinct clusters at the oligodendrocytic plasma membrane but showed faint diffuse, inhomogenous cytoplasmic staining (Fig. 4). Similar changes were seen with G89S-mutant GlialCAM, which was additionally detected in more intense labelling in neighbouring cells. A similar distribution was found with WT GlialCAM in $Mlc1^{-/-}$ mice. In $Glialcam^{-/-}$ and $Glialcam^{dn/dn}$ mice, MLC1 was diffusely distributed throughout the cytoplasm of adjacent astrocytes, but not in oligodendrocytic somata (Fig. 4). Since OLs lack MLC1, its effect on oligodendrocytic GlialCAM and ClC-2 cannot be cell autonomous.

Hence, both GlialCAM and MLC1 were necessary for each other's correct localization and for the correct targeting of ClC-2 in glial cells, whereas ClC-2 disruption had no significant effect on GlialCAM (see also ref. 12) and MLC1 (Table 1). The changed localization of ClC-2 and MLC1 in the *Glialcam* mouse models is compatible with *in vitro* results[7,12]. However, the effect of MLC1 deletion was unexpected because MLC1 is believed not to bind ClC-2 and to have no role in GlialCAM targeting[7,12].

GlialCAM *trans*-interactions localize MLC1 and ClC-2 *in vitro*. Our *in vivo* data agree with the effect of GlialCAM on ClC-2 and MLC1 localization in transfected cells, but contrast with the missing impact of MLC1 on GlialCAM[7,12]. To systematically analyse the localization of all three proteins, we separately transfected HeLa cells with different combinations of ClC-2, GlialCAM and MLC1 and later combined these cells to form contacts on further growth (Fig. 5). Immunofluorescent labelling revealed that GlialCAM expression in both cells was necessary and sufficient to direct ClC-2 or MLC1 to cell–cell contacts (Fig. 5a–c, filled arrows). This targeting did not require ClC-2 or MLC1 to be present in both cells (Fig. 5a,b). Expression of ClC-2

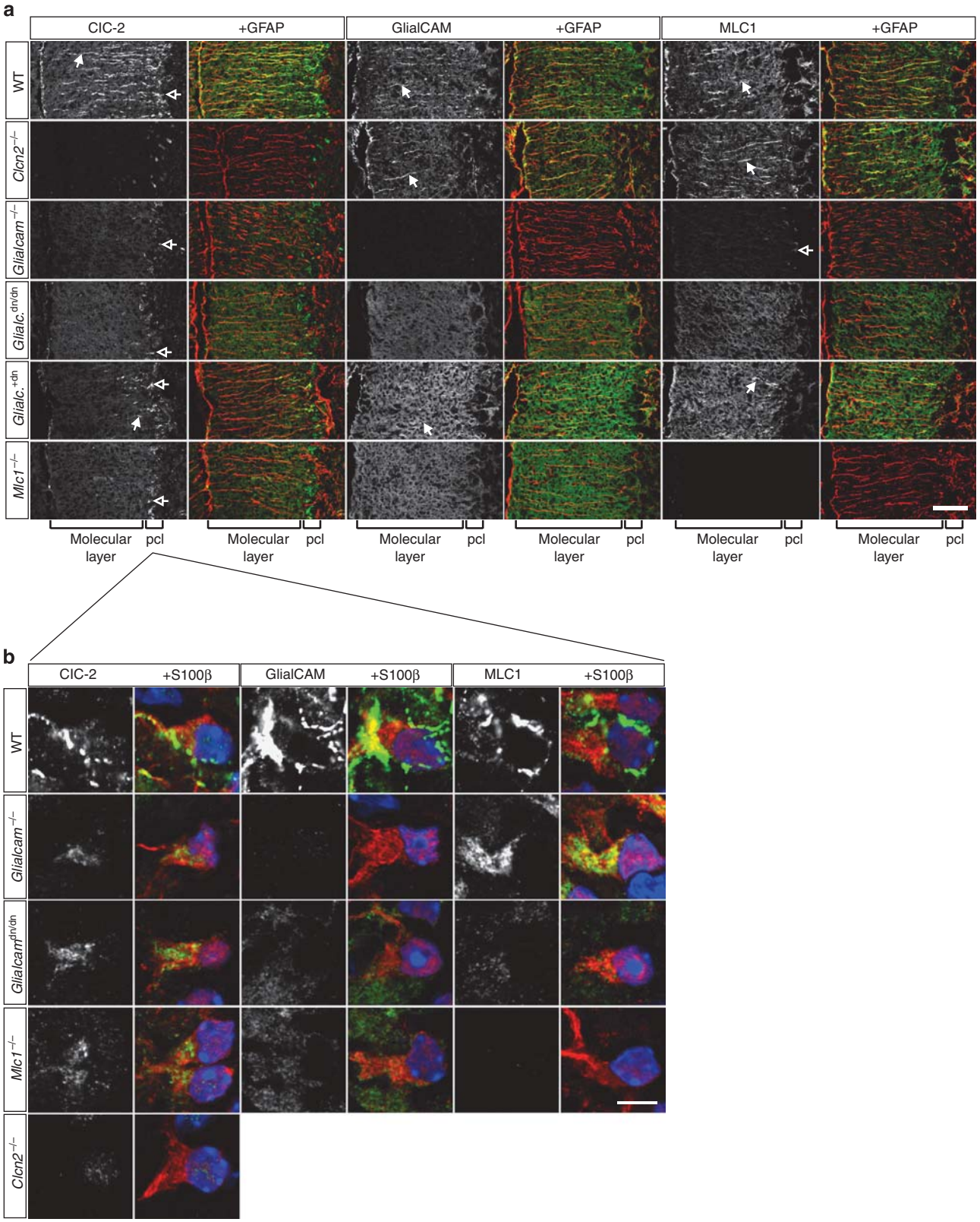

Figure 2 | *Glialcam* and *Mlc1* knockout alters localization of ClC-2, GlialCAM and MLC1 in BG. (**a**) Immunohistochemical (IHC) staining of ClC-2, GlialCAM and MLC1 in the molecular layer of the cerebellum. Co-staining for the astrocytic cytoskeletal protein GFAP (red) visualizes BG processes. Somata of BG are located in the Purkinje cell layer (pcl). Arrows with filled heads point to staining along BG processes, arrows with open heads point to labelled BG somata. Staining respective knockout (KO) sections controls the specificity of antibodies. Note that ClC-2 staining in the Purkinje cell layer of *Clcn2*$^{-/-}$ mice results from non-specific nuclear staining by the ClC-2 antibody. Scale bar, 50 μm. (**b**) IHC staining of ClC-2, GlialCAM and MLC1 in BG somata of the cerebellar Purkinje cell layer. Sections were co-stained for the astrocyte marker protein S100β (red) that localizes to the cytoplasm of BG. Nuclei were stained with 4′,6-diamidino-2-phenylindole. Scale bar, 5 μm. For each genotype/antibody combination, two brain sections each of at least three different mice were analysed.

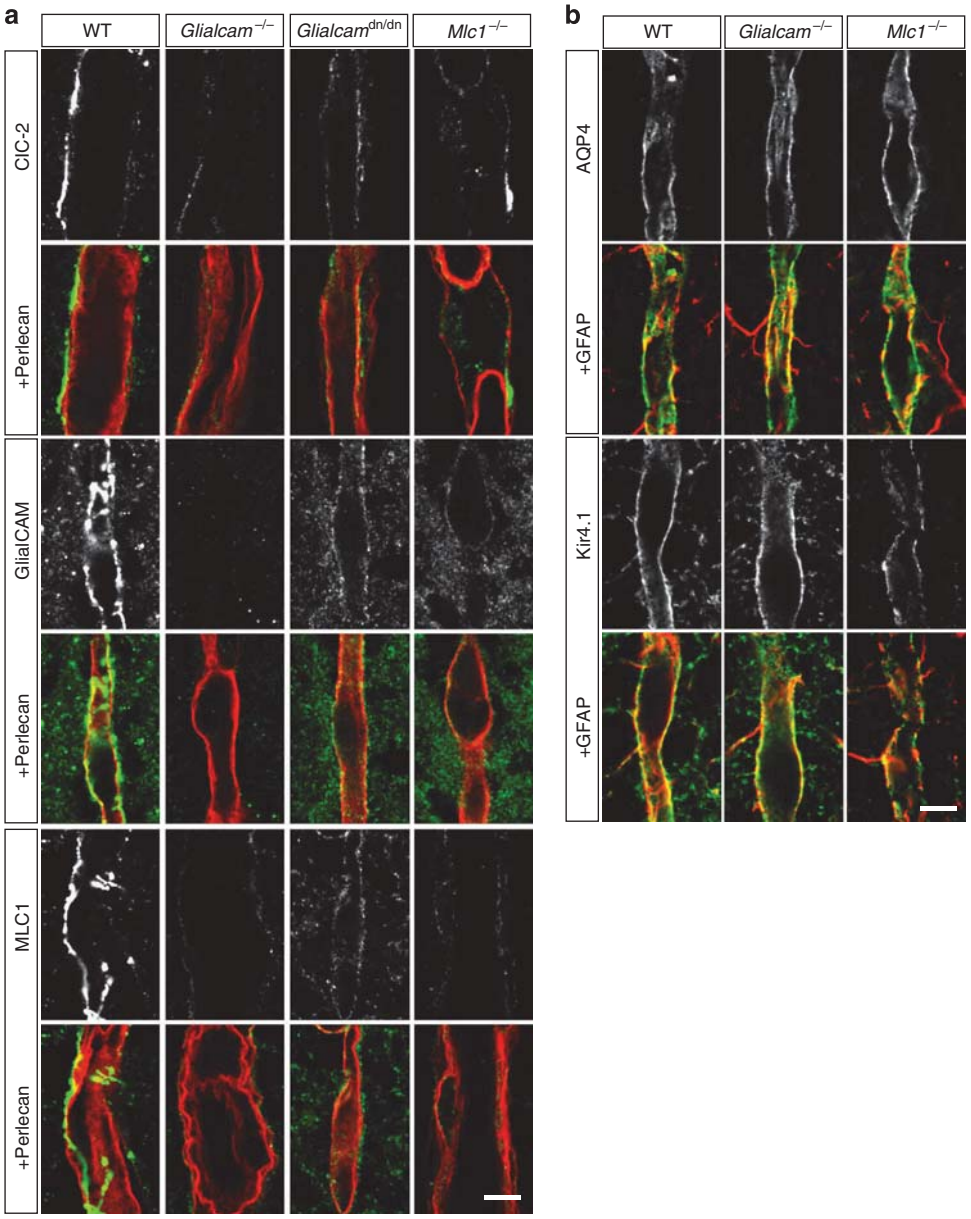

Figure 3 | *Glialcam* and *Mlc1* knockout mislocalizes ClC-2, MLC1 and GlialCAM along blood vessels. (**a**) Immunofluorescent staining of ClC-2, GlialCAM and MLC1 along blood vessels of the hippocampus in mice of different genotypes. Sections were co-stained for perlecan (heparan-sulphate-proteoglycan) a marker for endothelial cells. (**b**) Immunofluorescent staining of aquaporin-4 (AQP4) and Kir4.1 along blood vessels of the hippocampus. Section were co-stained with the astrocyte marker GFAP that labels astrocytic endfeet contacting blood vessels. Scale bar, 5 μm. For each genotype and antibody combination, two brain sections each of at least two different mice were analysed.

or MLC1 alone did not affect the localization of GlialCAM, MLC1 or ClC-2 in neighbouring cells even when they co-expressed two of these proteins (Fig. 5d–g). Hence, homophilic interactions of GlialCAM *in trans* may suffice to anchor and concentrate GlialCAM at cell–cell contacts. Binding in *cis* of GlialCAM to ClC-2 or MLC1 concentrates these latter proteins at the same site without requiring an interaction with ClC-2 or MLC1 on the adjacent cell.

Modification of ClC-2 currents by GlialCAM and MLC1 in glia. When overexpressed in *Xenopus* oocytes, HEK cells or primary astrocytes, GlialCAM increases ClC-2 currents and almost abolishes its inward rectification[12]. To examine whether these changes occur *in vivo*, we performed whole-cell patch clamp experiments in brain slices (Figs 6 and 7). Patch pipette solutions contained CsCl to suppress K^+ currents and the gap junction blocker carbenoxolone to electrically isolate the patched cell from the panglial network[21]. Control experiments with transfected HEK cells confirmed that carbenoxolone did not affect ClC-2 currents (Supplementary Fig. 3a–c). Na^+ currents were suppressed by replacing extracellular Na^+ with N-methyl-D-glucamine ($NMDG^+$) (Supplementary Fig. 3f).

We first measured BG (Fig. 6 and Supplementary Fig. 3g–i) because they prominently express ClC-2, GlialCAM and MLC1 and display strongly changed ClC-2 localization upon disruption of GlialCAM or MLC1 (Fig. 2a). We initially identified BG by fluorescence in mice expressing enhanced green fluorescent protein (eGFP) under the control of the glial fibrillary acidic protein (GFAP) promoter[22] and later by dye filling through the patch pipette (Supplementary Fig. 3d,e). This labelling revealed

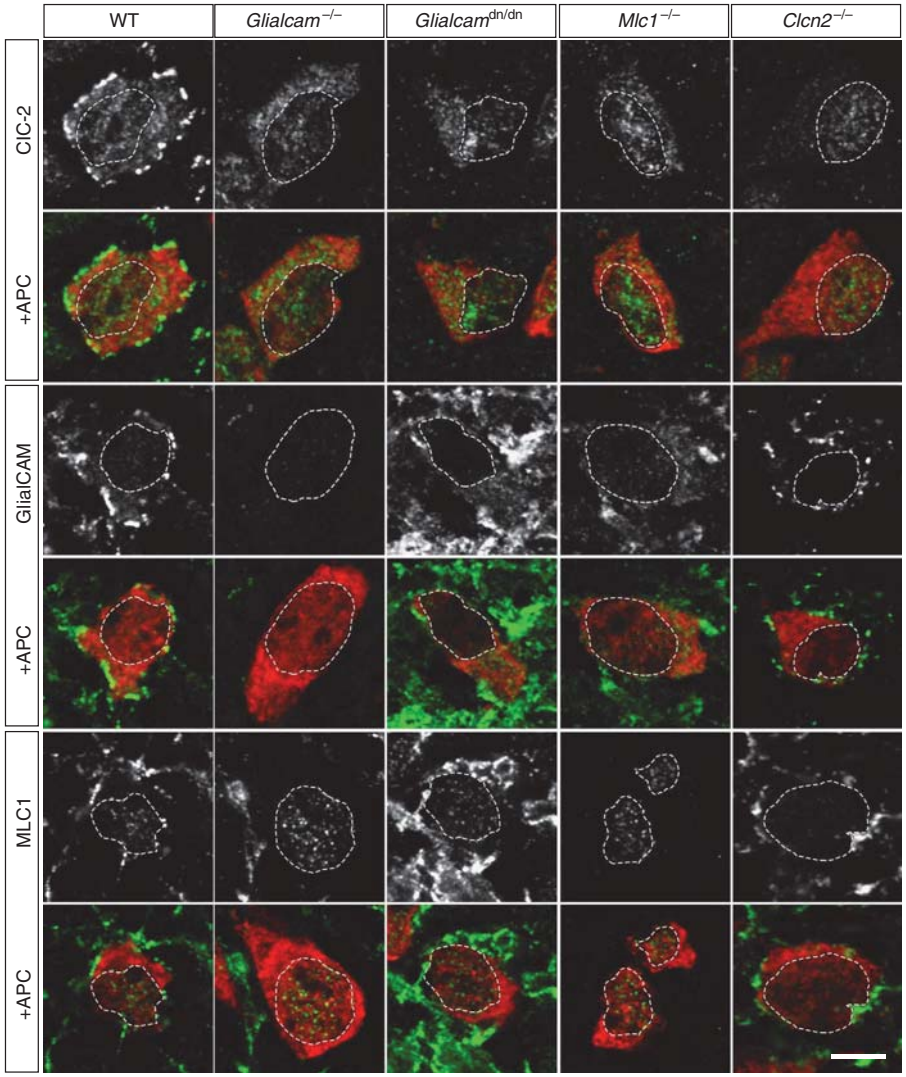

Figure 4 | *Glialcam* and *Mlc1* knockout alters the localization of ClC-2, GlialCAM and MLC1 in OLs. Immunohistochemical staining of OLs in fibre tracts of the cerebellum. The cytoplasm of OLs was stained with an antibody against adenomatous polyposis coli (APC) protein. This co-labelling revealed considerable amounts of GlialCAM and MLC1 in cells adjacent to OLs (*bona fide* astrocytes), as particularly evident in *Glialcam*$^{dn/dn}$ mice. The faint punctate staining of nuclei with the MLC1 and ClC-2 antibodies is unspecific as revealed by *Mlc1*$^{-/-}$ and *Clcn2*$^{-/-}$ sections, respectively. Note that GlialCAM and MLC1 labelling is unchanged in *Clcn2*$^{-/-}$ mice. Dotted lines mark the location of nuclei within OLs. Scale bar, 5 μm. For each genotype/antibody combination, at least two brain sections each of at least three different mice were analysed.

no obvious differences in BG morphology among genotypes (Supplementary Fig. 3e). Surprisingly, BG Cl^- currents did not display the linear current–voltage relationship expected from ClC-2/GlialCAM heteromers[12] (Supplementary Fig. 3a–c) but showed the slow activation by hyperpolarization (Fig. 6a) that is typical for ClC-2 (without GlialCAM)[14]. Later, an unusual apparent inactivation set in which became faster with hyperpolarization and appeared to reach completion after ~4 s (Supplementary Fig. 3f). The absence of these currents from *Clcn2*$^{-/-}$ BG (Fig. 6c), however, identified them as ClC-2 currents.

Whole-cell Cl^- currents obtained from BG somata of *Glialcam*$^{-/-}$ or *Glialcam*$^{dn/dn}$ mice did not display the expected[12] increased rectification but lacked the apparent inactivation observed in WT glia (Fig. 6e,g,m, Supplementary Fig. 4a,c,d,f,h,i). Similar non-inactivating ClC-2 currents were observed with BG from *Mlc1*$^{-/-}$ mice (Fig. 6i,m and Supplementary Fig. 4e,j). Heterozygous *Glialcam*$^{+/-}$ BG showed currents similar to WT (Supplementary Figs 4b,g and 5d). These results might indicate that, rather than abolishing its rectification as *in vitro*[12], *in vivo* GlialCAM causes ClC-2 to inactivate.

However, the cell capacitance of *Glialcam*$^{-/-}$, *Glialcam*$^{dn/dn}$, *Mlc1*$^{-/-}$ and to a lesser extent of *Clcn2*$^{-/-}$ BG was increased and more variable compared with WT (Fig. 6k). The augmented capacitance suggested an increased cell volume that might change whole-cell currents by reducing the dissipation of Cl^- gradients and/or the electrical access to ion channels in distant processes. Indeed, when we superfused BG with hypotonic solution to induce cell swelling (which resulted in the expected increase in cell capacitance (Supplementary Fig. 5a)), the apparent inactivation of WT and *Glialcam*$^{+/-}$ Cl^- currents was attenuated or even abolished, whereas the non-inactivating currents of *Glialcam*$^{-/-}$ BG and background currents of *Clcn2*$^{-/-}$ BG were unchanged (Fig. 6b,d and Supplementary Fig. 5b–e). Conversely, exposure of *Glialcam*$^{-/-}$, *Glialcam*$^{dn/dn}$ or *Mlc1*$^{-/-}$ BG to hypertonic solution partially reproduced the current 'inactivation' observed in WT BG at isoosmolarity (Fig. 6f,h,j and Supplementary Fig. 5f–h). Hence, cell swelling

Table 1 | Summary of major phenotypes in mouse models of leukodystrophy.

	WT	*Clcn2*$^{-/-}$	*Glialcam*$^{-/-}$	*Mlc1*$^{-/-}$	*Glialcam*$^{dn/dn}$
Myelin vacuolization*	−	●●●	●●	●●	●●
Protein expression†					
ClC-2	Ctrl	−	↓	↓	↓
GlialCAM	Ctrl	↔	−	↔	↔
MLC1	Ctrl	↑	↓↓	−	↓
Localization along BG processes‡					
ClC-2	+	−	−	−	−
GlialCAM	+	+	−	−	−
MLC1	+	+	−	−	−
Cl$^-$ *currents of BG*					
Rectification§	+	NA	+	+	+
Current density‖	Ctrl	NA	↓	↓	↓
Apparent inactivation	+	NA	−	−	−
Membrane capacitance¶	Ctrl	↑	↑↑	↑↑	↑↑
Clustering around OL somata#					
ClC-2	+	−	−	−	−
GlialCAM	+	+	−	−	−
MLC1	+	+	−	−	−
Cl$^-$ *currents of OL*					
Rectification§	−	NA	+	+	+
Current density**	Ctrl	NA	↓	↓	↓
Membrane capacitance¶	Ctrl	↑	↑	↑	↑
Localization along blood vessels					
ClC-2	+	−	↓	↓	↓
GlialCAM	+	↔	−	↓	↓
MLC1	+	↔	↓	−	↓

BG, Bergmann glia; Ctrl, control; NA, not applicable; OL, oligodendrocytes; +, present; −, absent; ↔, no change;↑, increase;↓, decrease compared with WT.
*Degree of vacuolization scored in the cerebellum. *Glialcam*$^{+/dn}$ mice displayed weakest vacuolization (●). *Clcn2*$^{-/-}$*Glialcam*$^{-/-}$ mice displayed strongest vacuolization (●●●●).
†Changes in protein expression in the cerebellum of the different mouse models compared with WT.
‡Scored for the presence and absence of protein located along BG processes in different mouse models.
§Activation by hyperpolarization (inward rectifying).
‖Measured at 0.25 s from the start of the voltage pulse. Changes compared with WT.
¶Changes compared with WT.
#Scored for the presence and absence of protein clustered around the somata of OLs in different mouse models.
**Measured at the end of the voltage pulse (1.5 s). Changes compared with WT.

probably contributes to the lack of apparent ClC-2 inactivation in *Glialcam*$^{-/-}$ and *Mlc1*$^{-/-}$ mice. However, cell capacitance and the degree of 'inactivation' did not correlate across cells of different genotypes (Supplementary Fig. 6). As WT and mutant BG cells rather segregated into two distinct groups, additional factors like the changed compartmentalization of ClC-2 in mutant mice (Fig. 2a) or possibly loss of interaction with other proteins may play a role in suppressing the apparent 'inactivation' of ClC-2 currents. The decrease in current amplitudes upon hypertonic shrinkage (Fig. 6f,h,j) may be due to reduced electrical accessibility of ClC-2 in cell processes or due to the intrinsic osmosensitivity of ClC-2 (ref. 13).

From our previous *in vitro* data[12] we had expected a large decrease of ClC-2 current amplitudes with *Glialcam* ablation, but averaged current amplitudes of *Glialcam*$^{-/-}$ BG rather appeared larger than WT (Fig. 6a,e). When normalized to cell capacitance, however, current amplitudes of *Glialcam*$^{-/-}$, *Glialcam*$^{dn/dn}$ and *Mlc1*$^{-/-}$ BG were moderately smaller compared with WT when measured at early time points (Fig. 6l), and nearly unchanged at 1.5 s when WT currents were reduced by the apparent inactivation (Fig. 6m). The mild reduction in ClC-2 current density in *Glialcam*$^{-/-}$ and *Mlc1*$^{-/-}$ BG is consistent with the decreased ClC-2 expression in these cells (Fig. 2).

Whereas overall BG morphology appears normal in our mouse models, myelin vacuolization (shown below) pointed to pathological changes in OLs, which were therefore included in our analysis (Fig. 7 and Supplementary Fig. 3j–m). Their identity was confirmed by dye filling that did not reveal obvious morphological differences among the genotypes (Fig. 7l). Unlike BG, Cl^- currents of OLs lacked time-dependent activation by hyperpolarization (Fig. 7a). About 60% of these currents could be attributed to ClC-2 by comparison with *Clcn2*$^{-/-}$ OLs (Fig. 7a–c and Supplementary Fig. 7a). Consistent with effects of GlialCAM in heterologous expression[12], Cl^- currents of *Glialcam*$^{-/-}$ OLs were smaller and displayed the typical activation by hyperpolarization when corrected for background currents of *Clcn2*$^{-/-}$ mice (Fig. 7d,e). Although currents were small, Cl^- currents of *Mlc1*$^{-/-}$ and *Glialcam*$^{+/-}$ OLs appeared similarly rectifying (Fig. 7f,g,j,k,n and Supplementary Fig. 7b,e). Currents from *Glialcam*$^{dn/dn}$ OLs showed less voltage-dependent activation (Fig. 7h,i and Supplementary Fig. 7d), consistent with the observation that human mutations in GlialCAM Ig domains interfere with its homophilic binding *in trans*, but not with its effect on ClC-2 currents[12]. The membrane capacitance of *Glialcam*$^{-/-}$, *Glialcam*$^{dn/dn}$, *Mlc1*$^{-/-}$ and *Clcn2*$^{-/-}$ OLs was increased, although not quite to the same extent as in BG (Fig. 7m compared with Fig. 6k).

Hence, the effect of GlialCAM on ClC-2 currents known from heterologous expression[12] (Supplementary Fig. 3a–c) can be observed in OLs, but not in BG (Table 1). On the

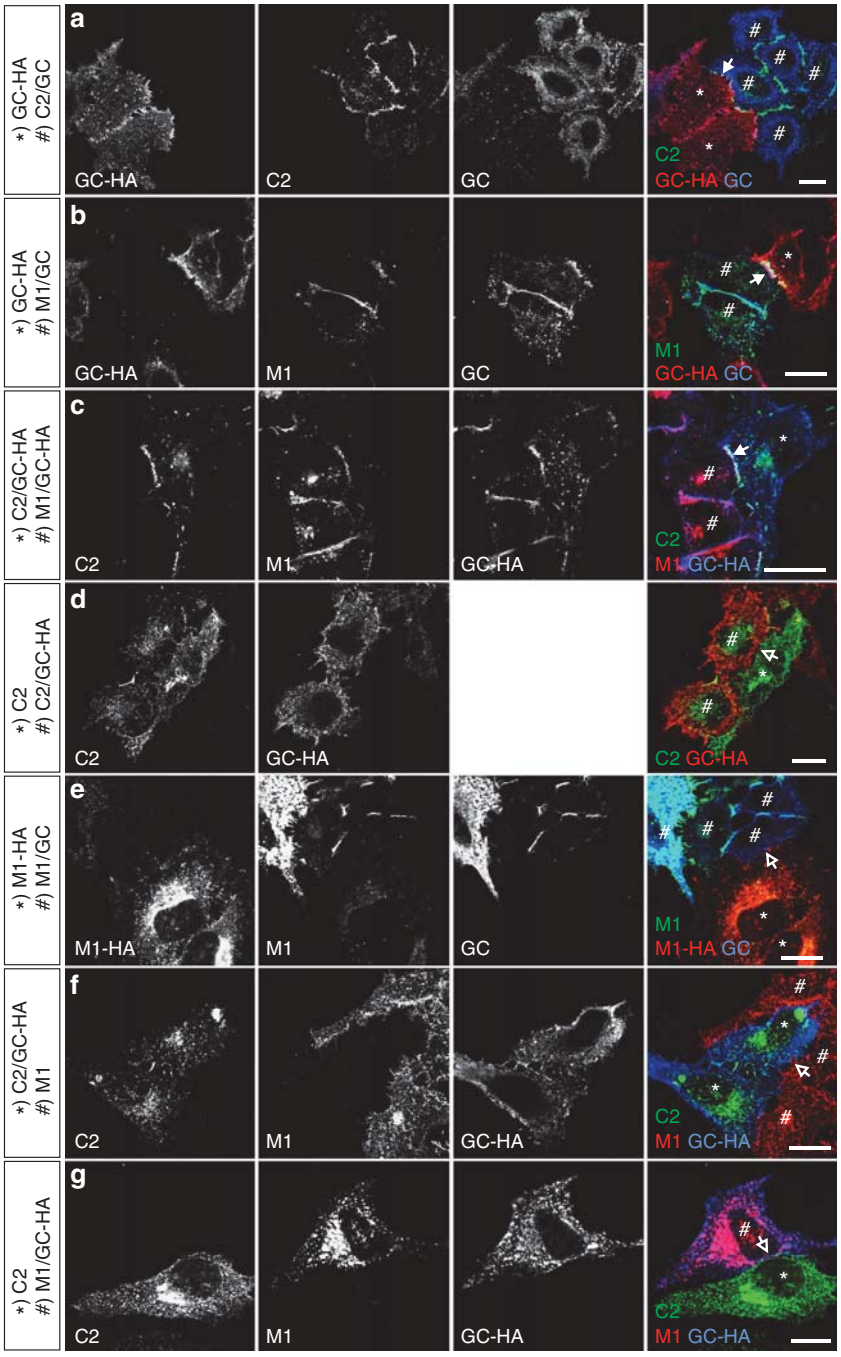

Figure 5 | Enrichment of ClC-2 GlialCAM and MLC1 at cell–cell contacts requires expression of GlialCAM in both neighbouring cells. HeLa cells were transfected with different combinations of *Clcn2*, *Glialcam* and *Mlc1* cDNAs (untagged or haemagglutinin (HA) tagged). Differentially transfected cells were plated onto coverslips and processed for immunofluorescent staining. Individual channel images are displayed in the first three columns, merged images are shown in the fourth column (from left to right). Labels in the lower left corner of each panel indicate the overexpressed protein that was stained with specific antibodies. cDNAs transfected into cells are indicated to the left of each row; in the fourth row cells are labelled with '*' and '#' according to the cDNA combination they were transfected with. Arrows with filled heads point to cell–cell contacts with protein enrichment, arrows with open heads to contacts without protein enrichment. Scale bar, 20 μm; C2 = ClC-2; GC = GlialCAM; M1 = MLC1. Images shown are representative of at least four images from at least two independent experiments.

basis of their increased capacitance, both types of glia appear to be swollen.

Leukodystrophy in *Glialcam* *Mlc1* and *Clcn2* mouse models. Brain sections from *Glialcam*$^{-/-}$, *Glialcam*$^{dn/dn}$ and *Mlc1*$^{-/-}$ mice revealed myelin vacuolization that slowly progressed over several months (Fig. 8a). Vacuolization was most prominent in fibre tracts of the cerebellum, similar to what was found in *Clcn2*$^{-/-}$ mice[8]. While the degree and time course of vacuolization was comparable across *Glialcam*$^{-/-}$, *Glialcam*$^{dn/dn}$ and *Mlc1*$^{-/-}$ mice, they altogether developed vacuolization more slowly and less severely than *Clcn2*$^{-/-}$ mice. Not until around 1 year of age

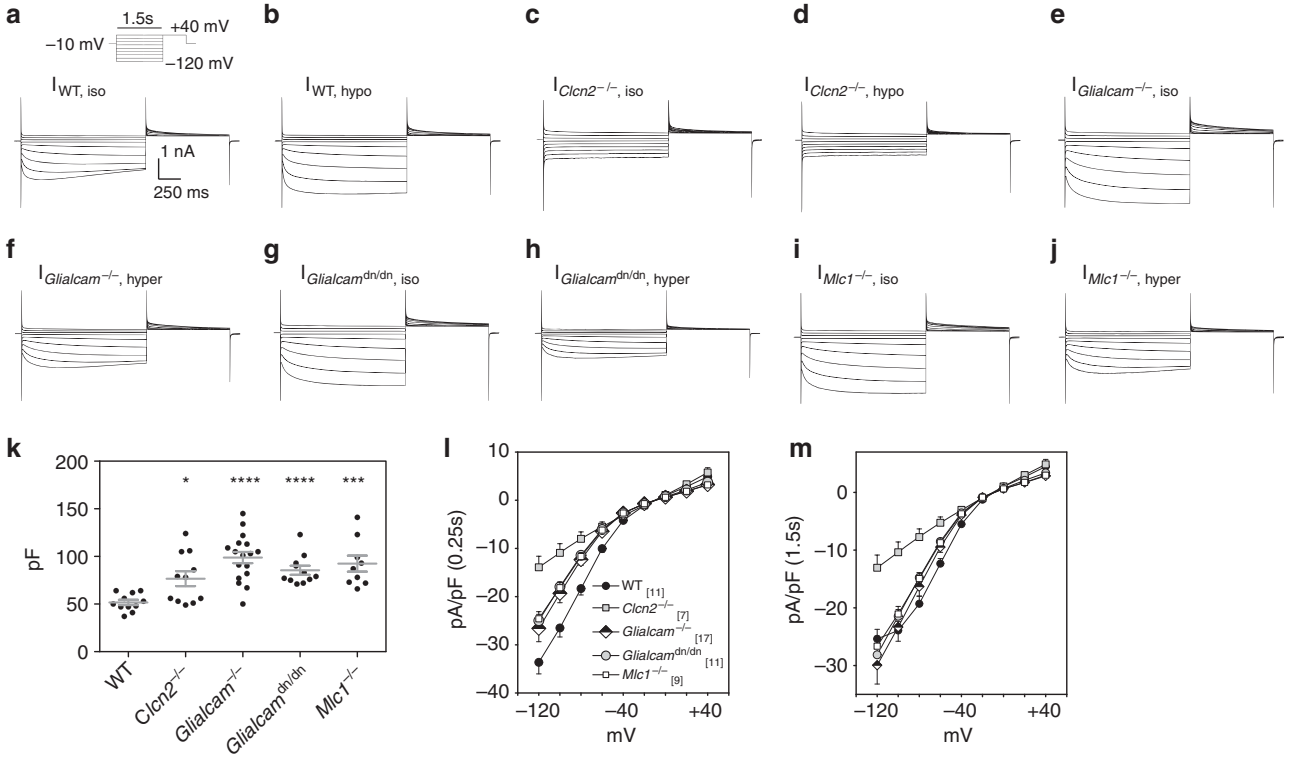

Figure 6 | ClC-2 currents in BG. (**a**–**j**) Current tracings from voltage-clamped BG were averaged for the different mouse models analysed (aged 3–4 weeks). ClC-2 currents were elicited with a voltage pulse protocol. As labelled, measurements were done in either isotonic (iso), hypotonic (hypo) or hypertonic (hyper) bath conditions. Cells were first patched in aCSF and then superfused with an $NMDG^+$-based 'isotonic' solution containing carbenoxolone to measure ClC-2 currents. Sometimes, this was followed by superfusion with either a hypotonic or hypertonic bath solution for additional measurements. The number of cells averaged were the following: WT, iso (9); WT, hypo (3); *Clcn2*$^{-/-}$, iso (7); *Glialcam*$^{-/-}$, iso (15), *Glialcam*$^{-/-}$, hyper (5); *Mlc1*$^{-/-}$, iso (9); *Mlc1*$^{-/-}$, hyper (3), *Glialcam*$^{dn/dn}$, iso (11); *Glialcam*$^{dn/dn}$, hyper (4). Note that some experiments using shorter and longer pulse protocols were not included for averaging traces shown here but were included for statistical analysis. Traces are scaled uniformly. (**k**) Individual membrane capacitance values of BG from different genotypes. Horizontal and vertical bars represent mean and s.e.m., respectively. *P* values between WT and the various mouse models using the Mann–Whitney test: $^*P \leq 0.05$, $^{***}P \leq 0.001$, $^{****}P \leq 0.0001$. (**l**,**m**) Current densities (amplitudes normalized to capacitance) as a function of voltage measured in isotonic bath conditions at 0.25 s (**l**) or 1.5 s (**m**) after the beginning of the voltage pulse. Plotted values are mean ± s.e.m. The total number of cells in (**l**,**m**) is given in panel (**l**). Legend symbols in (**l**) apply also to symbols in (**m**).

was discrete vacuolization apparent in cerebellar fibre tracts of *Glialcam*$^{dn/+}$ mice.

After appearing in the cerebellum, vacuolization extends to several brain regions in *Clcn2*$^{-/-}$ mice[8]. By contrast, myelin vacuolization was largely restricted to the cerebellum of *Glialcam*$^{-/-}$, *Glialcam*$^{dn/dn}$ and *Mlc1*$^{-/-}$ mice even after 1 year (Supplementary Fig. 8a). In contrast to early retinal degeneration of *Clcn2*$^{-/-}$ mice[9], the retinae of *Mlc1* and *Glialcam* mouse models were unaffected up to 1 year of age (Supplementary Fig. 8b). Electron microscopy revealed vacuoles in myelin sheaths of cerebellar axons from *Glialcam*$^{-/-}$, *Glialcam*$^{dn/dn}$ and *Mlc1*$^{-/-}$ mice (Fig. 8b). Modest pathological changes were also seen in somata of astrocytes and OLs. Their cytoplasm appeared less electron dense and occasional vacuoles could be observed in astrocytes (Supplementary Fig. 9).

One may hypothesize that the leukodystrophy observed in *Glialcam*$^{-/-}$ and *Mlc1*$^{-/-}$ mice might be entirely due to the associated changes in ClC-2 and the resulting consequences for ion homoeostasis[8]. In this case, the additional loss of GlialCAM in *Clcn2*$^{-/-}$/*Glialcam*$^{-/-}$ mice should not increase the severity of leukodystrophy over that of *Clcn2*$^{-/-}$ mice. However, in mice lacking both proteins' vacuolization appeared earlier and was more severe (Fig. 8c). We also crossed *Glialcam*$^{-/-}$ with *Clcn2*$^{hyp/hyp}$ mice that express ClC-2 at $<10\%$ of WT levels (Supplementary Fig. 1f–i). *Clcn2*$^{hyp/hyp}$ mice lacked white matter vacuolization at 17 weeks of age (Fig. 8d), demonstrating that a small amount of ClC-2 suffices to maintain myelin integrity as long as ClC-2 is correctly targeted and regulated by GlialCAM. Furthermore, the reduction in ClC-2 protein levels in *Glialcam* and *Mlc1* mouse models is *per se* not responsible for myelin vacuolization, as their ClC-2 levels are considerably higher than in the hypomorphic mouse. Crossing *Clcn2*$^{hyp/hyp}$ with *Glialcam*$^{-/-}$ mice, however, strongly increased their myelin vacuolization (Fig. 8d), suggesting that ClC-2 and GlialCAM operate in the same pathogenic pathway.

Discussion

We have analysed several genetic mouse models for human leukodystrophy to dissect the pathogenic roles of the multipass membrane protein MLC1, the cell adhesion molecule GlialCAM and the Cl^--channel ClC-2. The clustering of these proteins at glial plasma membrane domains depended on the presence of both MLC1 and GlialCAM, but not on ClC-2. The reduction in oligodendrocytic Cl^- currents in *Glialcam* and *Mlc1* mouse models indicated that impaired glial ion homoeostasis contributes to MLC disease. Mice lacking both ClC-2 and GlialCAM, however, showed that MLC leukodystrophy cannot be attributed solely to a loss of ClC-2.

GlialCAM can bind MLC1 (ref. 2) and ClC-2 (ref. 12) within the same cell and this binding might be mutually exclusive[12].

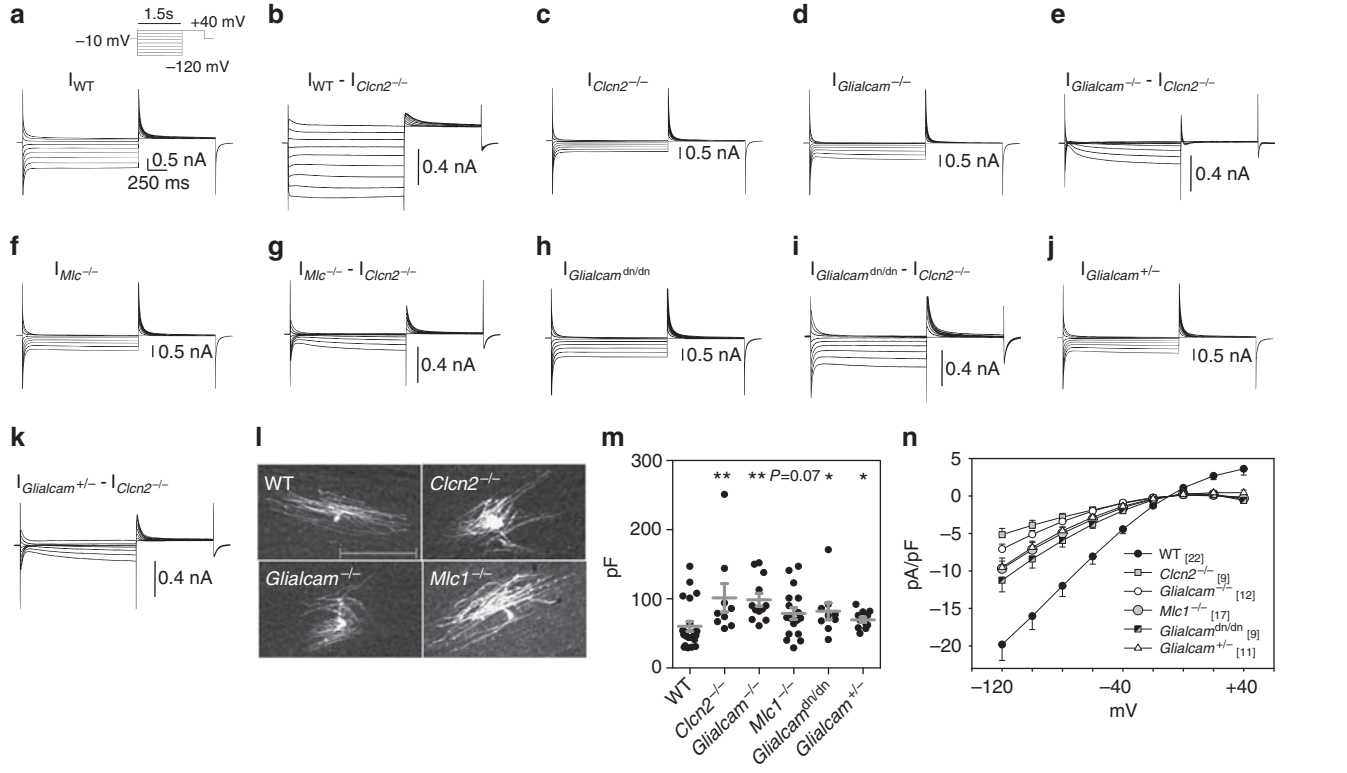

Figure 7 | ClC-2 currents in OLs. (**a**,**c**,**d**,**f**,**h**,**j**) Current tracings from voltage-clamped OLs of the corpus callosum in isotonic bath solutions were averaged for the different mouse models analysed. Currents were elicited in the same way as described in Fig. 5. The number of cells used for averaging traces were WT (22), *Clcn2*$^{-/-}$ (9), *Glialcam*$^{-/-}$ (11), *Mlc1*$^{-/-}$ (17), *Glialcam*$^{dn/dn}$ (9) and *Glialcam*$^{+/-}$ (12). (**b**,**e**,**g**,**i**,**k**) The average current from *Clcn2*$^{-/-}$ cells was subtracted from the average current from respective mouse models to obtain the 'subtracted' current, which is due to ClC-2 expression. (**l**) Confocal scans of tissue sections for selected mouse models where OLs were dialyzed with biocytin through the patch pipette. Scale bar, 100 μm. (**m**) Individual membrane capacitance values of OLs from different genotypes. Horizontal and vertical bars represent mean and s.e.m., respectively. Reported *P* values were calculated between WT and the various mouse models using the Mann–Whitney test. $^{*}P \leq 0.05$, $^{**}P \leq 0.01$. (**n**) Current densities (amplitude normalized to capacitance) measured at the end of a 1.5-s voltage pulse as a function of clamp voltage plotted as mean ± s.e.m.

GlialCAM also forms *cis*-homo-oligomers within the membrane[4,7]. Homo-oligomer formation does not require the cytoplasmic carboxy terminus[4], but the relevant binding sites are not yet known. GlialCAM also interacts with itself *in trans* through its extracellular Ig domains. These domains might interact also with other proteins. Indeed, GlialCAM overexpression increases adhesion to the extracellular matrix and modulates cell migration, and GlialCAM localizes to cell protrusions in spread cells[4,23,24].

By accumulating at cell–cell contacts through homophilic interactions *in trans*, GlialCAM targets ClC-2 and MLC1 to these sites in cultured cells[2,12,25] and stabilizes MLC1 (ref. 25). By contrast, ClC-2 levels do not increase with GlialCAM co-transfection[12], and MLC1 expression lacks discernible effects on either GlialCAM[7] or ClC-2 (refs 12,16). The present systematic analysis of cell pairs revealed that accumulation of ClC-2 or MLC1 at cell–cell junctions only required GlialCAM, but neither ClC-2 nor MLC1, to be present in both cells.

Our work demonstrates that GlialCAM localizes ClC-2 and MLC1 to distinct sites also *in vivo*. Without GlialCAM, MLC1 and ClC-2 accumulated in BG somata. We were surprised that disruption of MLC1 also mislocalized GlialCAM and ClC-2. As MLC1 may not bind ClC-2 (refs 12,16), its effect on ClC-2 might be mediated by the mislocalization of GlialCAM. However, the effect of MLC1 on GlialCAM is equally unexpected since knockdown of MLC1 in astrocytes changed neither the expression nor the localization of GlialCAM[7]. Does MLC1 stabilize the GialCAM–GlialCAM interaction *in vivo*, an effect easily overlooked *in vitro* because of overexpression? Or does MLC1 serve as a co-receptor for GlialCAM, with GlialCAM/MLC1 binding *in trans* not only to GlialCAM but also to other proteins present in the brain but absent in cell culture?

Surprisingly, *Mlc1* disruption also destabilized GlialCAM and ClC-2 in OLs, although they apparently lack MLC1 (refs 2,19,20). MLC1 expression appears to be restricted to astrocytes since *Mlc1*$^{-/-}$ mice now revealed that previously reported axonal labelling for MLC1 (refs 20,26) was unspecific. ClC-2, GlialCAM and MLC1 cluster at oligodendrocytic somata close to Cx47 (refs 8,12), which forms gap junctions with astrocytes[27]. We speculate that astrocytic GlialCAM might be unstable without astrocytic MLC1, which in turn may destabilize the ClC-2/GlialCAM complexes on OLs because they now lack their cognate interaction partner.

The G89S mutation introduced into *Glialcam*^{dn} mice is found in patients with dominantly inherited MLC2B disease[2]. It changes a residue in the extracellular Ig-like domain and probably interferes with binding to ligands. Indeed, when GlialCAM carries disease-causing mutations in Ig domains (for example, G89D that affects the same residue as G89S), neither GlialCAM nor MLC1 or ClC-2 accumulate at cell–cell junctions[2,12]. However, mutants like G89D can still bind MLC1 (ref. 7) or ClC-2 and can modify its Cl^- currents[12]. Similarly, the GlialCAM G89S mutant was mislocalized in *Glialcam*$^{dn/dn}$ mice *in vivo* and consequently failed to correctly localize ClC-2 and MLC1. MLC1 abundance

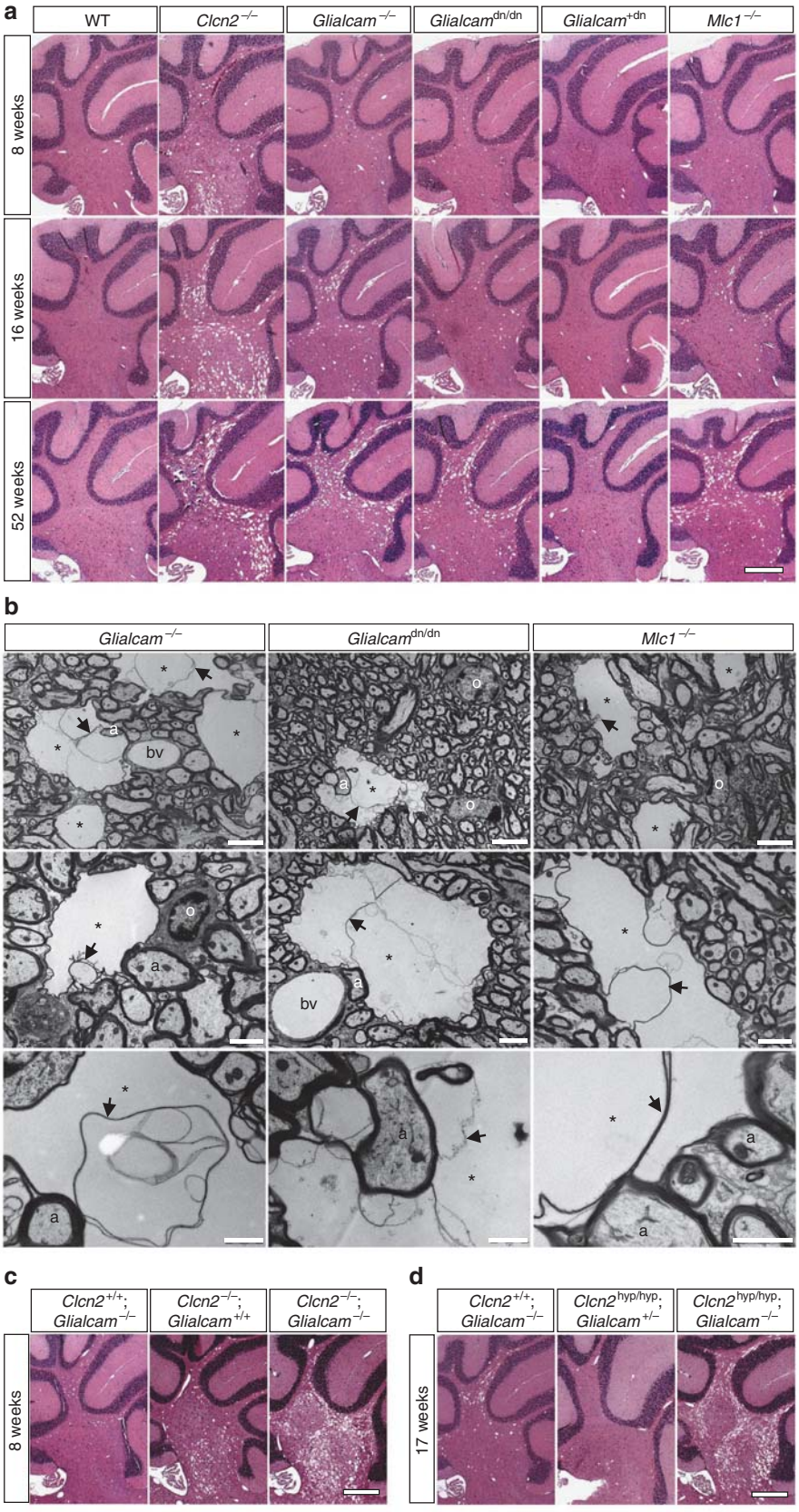

Figure 8 | Myelin vacuolization in *Glialcam* and *Mlc1* mouse models. (**a**) Haematoxylin–eosin (H&E) staining of sagittal paraffin sections of the cerebellum of 8, 16 and 52-week-old mice. (**b**) Ultrastructural analyses of myelin vacuolization. Myelin vacuolization at different magnifications. asterisk, myelin vacuole; arrow, aberrant myelin sheet inside vacuole; a, axon; bv, blood vessel; o, oligodendrocyte. Scale bars, 5 μm (upper row); 2 μm (middle row); 1 μm (bottom row). (**c**) H&E staining of the cerebellum of 8-week-old *Clcn2*$^{-/-}$, *Glialcam*$^{-/-}$ double-mutant mice. (**d**) H&E staining of the cerebellum of 17-week-old *Clcn2*$^{hyp/hyp}$, *Glialcam*$^{-/-}$ double-mutant mice. Scale bar, 400 μm (**a**,**c**,**d**). For each genotype and age, two animals (≥4 sections each) were analysed.

was robustly decreased in *Glialcam*$^{-/-}$ mice, suggesting an increased stability of GlialCAM/MLC1 complexes. The GlialCAM mutant, although mislocalized, partially retained its stabilizing effect on MLC1, in particular outside the cerebellum (Fig. 1c,d). No such stabilization was observed for ClC-2, possibly indicating that mutant GlialCAM binds ClC-2 less strongly than MLC1. Western blots suggested that ClC-2 is more efficiently stabilized by GlialCAM in the cerebellum than in the rest of the brain. However, ClC-2 is also expressed in neurons where its expression should not depend on GlialCAM. Hence, this result may be due to a higher glial versus neuronal ClC-2 expression in the cerebellum.

ClC-2 is a widely expressed plasma membrane Cl^- channel that slowly activates on hyperpolarization, cell swelling and moderately acidic extracellular pH[13,15]. These characteristics were observed in heterologous overexpression and in native cells[9,28] including neurons[29,30] and astrocytes[31–33]. Upon heterologous co-expression, GlialCAM increases ClC-2 currents and drastically changes their properties from inwardly rectifying to a nearly ohmic current–voltage relationship, an effect that does not require GlialCAM–GlialCAM *trans*-interactions[12]. It has remained unclear whether the linearization of ClC-2 currents also occurs *in vivo* or results from non-physiological overexpression. Indeed, other groups have shown that native astrocytes display typical hyperpolarization-activated ClC-2 currents[31–34]. Strikingly, we observed the expected effect of GlialCAM on Cl^- currents only in OLs, although BG also co-expresses ClC-2 and GlialCAM. *Glialcam*$^{-/-}$ OLs displayed typical inwardly rectifying ClC-2 currents, whereas similarly background corrected currents from WT cells were larger and neither showed time dependence nor inward rectification.

In contrast to OLs, BG showed hyperpolarization-activated Cl^- currents with or without GlialCAM. Current amplitudes at *Glialcam*$^{-/-}$ or *Mlc1*$^{-/-}$ BG somata were moderately increased, but when normalized to membrane capacitance they were rather decreased. Cell swelling, as indicated by increased membrane capacitance of *Glialcam*$^{-/-}$ or *Mlc1*$^{-/-}$ BG, may have improved the electrical accessibility of BG processes that retain some ClC-2. Indeed, current amplitudes were reduced when *Glialcam*$^{-/-}$, *Glialcam*$^{dn/dn}$ and *Mlc1*$^{-/-}$ BG were shrunk by exposure to hypertonicity.

Why did GlialCAM change the rectification of ClC-2 in OLs, but neither at BG somata nor in astrocytes[31–34] if all three cell types co-express these two proteins? One may hypothesize that MLC1, which is expressed in BG but not in OLs, may interfere with the biophysical effect of GlialCAM on ClC-2 currents. However, the additional expression of MLC1 did not change the effect of GlialCAM on ClC-2 currents in *Xenopus* oocytes[12]. An easy explanation would be a higher GlialCAM/ClC-2 ratio in OLs, an assumption difficult to verify by immunohistochemistry. Bolstering this notion, overexpression of GlialCAM in native astrocytes increased Cl^- currents and reduced their rectification[12]. However, the strong effect of GlialCAM on ClC-2 localization and abundance in BG suggests that the majority of ClC-2 is normally anchored and stabilized by GlialCAM. This anchoring might require less GlialCAM per ClC-2 than the change in channel rectification. The stoichiometry of ClC-2/GlialCAM binding is currently unknown. One could speculate that binding of one GlialCAM molecule to a homodimeric ClC-2 channel suffices for anchoring, but that two (or more) GlialCAM β-subunits are required to change the gating of the two ClC-2 pores[35].

An increase of up to twofold in membrane capacitance of BG and OLs suggested that their volume was increased when either MLC1, GlialCAM or ClC-2 was lacking. Independent evidence for cell swelling was obtained from the apparent inactivation of ClC-2 currents in WT BG that could be reversed by hypo-osmotic swelling and was abolished in *Glialcam*$^{-/-}$ cells.

A common denominator for the increase in glial cell volume may be a reduction of ClC-2 currents. Loss of ClC-2, which is swelling activated[13,15] and constitutively open when modified by GlialCAM[12] may cause cell swelling because the Cl^- equilibrium potential of glia[36–38] predicts an outwards direction of Cl^- flux and associated water transport. Although ClC-2 currents at BG somata were not reduced in *Glialcam* or *Mlc1* mouse models, ClC-2 was strongly decreased along BG processes. At these sites, which escape our patch clamp analysis, ClC-2 currents might be linearized and enhanced by GlialCAM and might influence cell volume. MLC1 was reported[39] to stimulate the ubiquitous volume-regulated anion channel (VRAC) that is distinct from ClC-2 (ref. 13) and is not known at the molecular level[40]. Short interfering RNA-mediated knockdown of GlialCAM or MLC1 reduced VRAC currents[25]. This effect is probably indirect as AQP4 knockdown also reduced astrocytic VRAC currents[41]. Since both ClC-2 and VRAC mediate Cl^- currents, and because membrane capacitance was also increased in *Clcn2*$^{-/-}$ mice, the simplest explanation for glial swelling remains a lack of ClC-2. Another factor may be the lack or downregulation of GlialCAM-mediated adhesion in *Glialcam* and *Mlc1* mouse models, respectively. The somewhat larger increase in cell capacitance of BG from *Glialcam*$^{-/-}$ and *Mlc1*$^{-/-}$ mice compared with *Clcn2*$^{-/-}$ mice is compatible with this notion.

Disruption of all three genes, that is, *Clcn2*, *Glialcam* and *Mlc1*, entails leukodystrophy in mice and humans. Since GlialCAM binds to both ClC-2 and MLC1 and disruption of either *Glialcam* or *Mlc1* affects the localization and abundance of the two other proteins, this raises the question whether loss-of-function mutations in those genes cause leukodystrophy through a common pathway.

Four observations suggest loss of ClC-2 function as the prime suspect for such a pathway: first, ClC-2 localization was changed upon *Glialcam* or *Mlc1* disruption, whereas lack of ClC-2 had no detectable effect on either GlialCAM or MLC1. Second, OLs, the cells mainly affected by vacuolization, showed decreased ClC-2 Cl^- currents in both *Glialcam*$^{-/-}$ and *Mlc1*$^{-/-}$ mice. As OLs lack MLC1 (refs 2,19,20), the myelin vacuolization in *Mlc1*$^{-/-}$ mice may result from the secondary loss of ClC-2 and/or GlialCAM. Third, leukoencephalopathy was more severe in *Clcn2*$^{-/-}$ mice than in *Glialcam*$^{-/-}$ or *Mlc1*$^{-/-}$ mice, which retain reduced ClC-2 levels in glia. The fact that disruption of *Clcn2*, but not of *Glialcam* or *Mlc1*, additionally causes testicular and retinal degeneration[9] is because of the wider expression pattern of ClC-2 (ref. 14). Fourth, when *Glialcam*$^{-/-}$ mice were crossed with *Clcn2*$^{hyp/hyp}$ mice that express $<10\%$ of WT ClC-2 levels but lack leukodystrophy, myelin vacuolization of resulting *Glialcam*$^{-/-}$/*Clcn2*$^{hyp/hyp}$ mice was more severe than in *Glialcam*$^{-/-}$ mice, suggesting a common pathogenic pathway.

We have previously hypothesized[8] that ClC-2 disruption causes leukodystrophy by disturbing the buffering of extracellular ions analogous to the postulated role of ClC-2 in regulating the *milieu extérieur* of sertoli cells and photoreceptors[9]. Indirect support for this model came from the co-localization at astrocytic endfeet of ClC-2 with the K^+ channel Kir4.1 (refs 42,43), whose inactivation also entails leukodystrophy[42,44] as does ablation of glial connexins 32 and 47 (refs 45–47). These proteins are thought to co-operate in 'K^+ siphoning'[48]. This model states that K^+ released from neurons during action potential repolarization is taken up by Kir4.1 into the connexin-linked astroglial network and is then equilibrated with serum through astrocytic endfeet at blood vessels. Cl^- fluxes through ClC-2 may be needed for an overall electroneutral transport across glial

plasma membranes during K^+ siphoning. The linearization of ClC-2 currents by GlialCAM may be important for K^+ siphoning as a rise of extracellular K^+ upon neuronal activity is expected to depolarize the glial membrane and shut down ClC-2. Dysregulation of Cl^- concentrations in the small extracellular clefts might also change extracellular pH through Cl^-/HCO_3^- exchangers[9]. Cell type-specific disruption of ClC-2 will be needed to clarify whether leukodystrophy results from a loss of ClC-2 currents in OLs, astrocytes or both.

Genetic evidence, however, showed that GlialCAM loss elicits leukodystrophy only in part through ClC-2. Since pathology was more severe in *Clcn2*$^{-/-}$/*Glialcam*$^{-/-}$ than in *Clcn2*$^{-/-}$ mice, GlialCAM ablation has additional, ClC-2-independent pathogenic effects. The lack of GlialCAM-mediated cell adhesion may also come into play, but the low abundance of GlialCAM in myelin sheaths and the prominence of other adhesion molecules[49] makes a direct role in myelin vacuolization unlikely. Moreover, vacuolization developed after apparently normal brain and myelin development, an observation that is important in view of the report[24] that overexpression of GlialCAM in U373-MG glioblastoma cells induces glial differentiation. It seems more likely that the downregulation or mislocalization of other proteins like MLC1 may contribute, together with changes in ClC-2, to MLC pathology. Unfortunately, except for its role in leukodystrophy and its protein interaction partners, not much is known about the function of MLC1.

This work has revealed important functional interactions *in vivo* of ClC-2, GlialCAM and MLC1 (Table 1), three proteins underlying human leukodystrophies. *In vitro* studies had shown that the adhesion molecule GlialCAM directly interacted with either MLC1 or ClC-2, changing their subcellular localization and profoundly altering ClC-2 currents[12]. However, no effect of MLC1 on GlialCAM or ClC-2 had been described. Here we showed that in addition to GlialCAM also MLC1, but not ClC-2, is important for tethering the protein complex to specific plasma membrane domains of both astrocytes and OLs *in vivo*. Although GlialCAM, together with MLC1, anchors ClC-2 in both types of glia, the rectification of ClC-2 Cl^- currents was only abolished in OLs. Hence, the localizing effect of GlialCAM can be dissociated from its impact on ClC-2 channel function. Reduction or change in ClC-2 currents is common to all forms of leukodystrophy studied here. Hence mutations in both *GLIALCAM* and *MLC1* may cause leukencephalopathy in part through impaired brain ion homoeostasis. Crosses between *Clcn2*$^{-/-}$ and *Glialcam*$^{-/-}$ mice, however, show that the loss of GlialCAM or MLC1 has additional pathogenic effects unrelated to ClC-2. The unexpected similar effects of *Mlc1* and *Glialcam* ablation on their protein partners rationalize the undistinguishable symptomatology of the MLC1 and MLC2A forms of human leukodystrophy.

Methods

Mice. All animal experiments were approved and in compliance with LaGeSo, Berlin, Germany, and the Animal Care and Ethics Committee of the IDIBELL and the rules set by the Government of Cataluña, Spain. Experiments were performed with mice at different ages (indicated in figure legends), and both sexes were used interchangeably.

Mlc1$^{-/-}$ mice were generated by Institut Clinique de la Souris (Strasbourg, France). The targeting vector was obtained from amplification of BAC RP 24-467H19 (5′-arm) and from amplification of 129S2/SvPas genomic DNA (3′-arm). Exons 2 and 3 were flanked by loxP sites. Exon 3 contained additionally a neomycin cassette flanked by FRT sites. The targeting vector was introduced into the H129 embryonic stem (ES) cell strain by electroporation and positive clones were selected by PCR. Homologous recombination was confirmed by Southern blotting and chromosomal integrity was checked by karyotyping. Correctly targeted ES cell clones were injected into C57BL/6 blastocysts and chimeric animals were crossed to FLPrecombinase expressing 'deleter' mice (in C57BL/6 background) to remove the neomycin-resistant cassette. To generate *Mlc1*$^{-/-}$ mice, *Mlc1*$^{lox/lox}$ mice were crossed to Cre-deleter mice to remove the floxed exons 2 and 3. PCR genotyping was performed using primer sequences 5′-CTGAATCTAGATGAGTTTGGGTGGC-3′ (P1); 5′-GAAACCCTCTAATTGTAGTAAGTG-3′, 5′-GAAAACCCTCTAATTGTAGTAAGTG-3′ (P2); and 5′-GCACCACAGCACCACAACATGC-3′ (P3).

Mice carrying the dominant-negative mutation G89S in exon 2 of the *Gliacam* (*Hepacam*) gene (*Glialcam*$^{dn/dn}$) and additionally having exons 2–4 flanked by loxP sites were generated by TaconicArtemis (Cologne, Germany) and were kept in a C57Bl/6 genetic background. The targeting vector was generated from BAC clones of the C57BL/6J RPCIB-731 library. Two positive selection markers, a neomycin-resistant cassette flanked by FRT sites and a puromycin-resistant cassette flanked by F3 sites, were inserted into introns 1 and 4, respectively. The targeting vector was introduced into the C57BL/6 NTac ES cell line by electroporation and positive clones were selected by PCR, and homologous recombination was confirmed by Southern blotting. Correctly targeted ES cell clones were injected into C57BL/6 blastocysts and chimeric animals were crossed to FLPe recombinase expressing 'deleter' mice (in C57BL/6 background) to remove neomycin and puromycin-resistant cassettes. To generate *Glialcam*$^{-/-}$ mice, *Glialcam*$^{dn/dn}$ mice were crossed to Cre-deleter mice (in C57BL/6 background) to remove the 'floxed' exons 2–4. PCR genotyping was performed using primer sequences 5′-CTATTTCCTGCCATACTACCTCC-3′ (P1), 5′-TGCCTTTGCTTTCTCAGTCC-3′ (P2) and 5′-TGAGCACAGACGCAACTCC-3′ (P3).

Generation of *Clcn2*$^{-/-}$ mice has been described previously[9]. Mice expressing low levels of ClC-2 (hypomorph *Clcn2*, *Clcn2*$^{hyp/hyp}$) were generated unintentionally by insertion of loxP sites flanking exons 2 and 3 of *Clcn2*. A 10.6-kb fragment of R1 ES cell genomic DNA containing exons 1–21 of *Clcn2* were cloned into pKO Scrambler Plasmid 901 (Lexicon Genetics Inc.). A neomycin-resistant cassette flanked by loxP sites and AscI sites at both ends was inserted into the ClaI site between exons 1 and 2 in a double-blunt manner. A third loxP site and an additional EcoRV site to aid Southern blot analyses were inserted between exons 3 and 4. The targeting construct was introduced into R1 ES cells by electroporation and positive clones were selected by Southern blot analyses. Selected positive clones were then electroporated with a Cre recombinase expression construct for removal of the neomycin-resistant cassette. Clones that had the neomycin-resistant cassette removed were chosen for injection into C57BL/6 blastocysts. PCR genotyping was performed using primers 5′-TTAGGCTGGAATTTGCCCGAGAGG-3′ (P1), 5′-GAGGAGGTGAGCAAGACAAAAGGG-3′ (P2) 5′-GGCAAAGGCTGGCGAGGTAACTTC-3′ (P3) and 5′-AGGGAAGGCAAGGCTAGAGAAGGC-3′ (P4). *Clcn2*$^{-/-}$, *Mlc1*$^{-/-}$ and *Clcn2*$^{hyp/hyp}$ mice were in a C57BL/6-129/Svj mixed genetic background, while *Glialcam*$^{-/-}$ and *Glialcam*$^{dn/dn}$ were in a C57BL/6 background. For some electrophysiological measurements mice were crossed to a transgenic line expressing enhanced green fluorescence protein under the control of the human GFAP promotor[22] (FVB/N background), resulting in enhanced green fluorescence protein expression in astrocytes.

Generation of antibodies. Antibodies against mouse ClC-2 were raised in rabbits against two peptide sequences of different length corresponding to the extreme C terminus: (C)WGPRSRHGLPREGTPSDSDDK***S***Q (used for western blotting) and (C)HGLPREGTPSDSDDK***S***Q (by Biogenes, Berlin, Germany; used for immunofluorescence staining). A cysteine in the native protein sequence was replaced by the highlighted serine to prevent coupling of this residue to the carrier protein.

GlialCAM-specific antibodies used for western blots were raised in rabbits to peptide (C)LKDKDSSEPDENPATEPR, and those used for immunostainings were raised in guinea pigs to peptide (C)AGVQRIREQDESGQVEISA. Both peptide sequences correspond to non-overlapping parts of the intracellular C-terminal region of mouse GlialCAM.

Antibodies recognizing the amino terminus of mouse MLC1 (used for immunostaining) were raised in rabbits and guinea pigs against peptide TREGQFREELGYDRM(C)[20]. Antibodies to the MLC1 C terminus (used for western blotting) were raised in rabbits against peptide CPQERPAGEVVRGPLKEFDK.

Generation of antibodies was performed by Pineda Antibody Services (Berlin, Germany), unless indicated otherwise. '(C)' indicates cysteines not included in native protein sequence that were added to facilitate coupling to carrier protein. Antibodies were affinity purified from serum using the immunizing peptide.

Western blot analyses. For western blot analyses, membrane fractions were isolated from mouse tissue. To this end, tissue homogenate was prepared in 20 mM Tris–HCl pH 7.4, 140 mM NaCl, 2 mm EDTA with protease inhibitors (4 mM Pefabloc and Complete EDTA-free protease inhibitor cocktail, Roche) using a glass Dounce homogenizer and cleared by centrifugation for 10 min at 1,000 *g*. Membrane fractions were pelleted from the cleared homogenate by ultracentrifugation for 30 min at 270,000 *g*, and the pellet was resuspended by sonification in 50 mM Tris pH 6.8, 140 mM NaCl, 2 mM EDTA with protease inhibitors. Equal amounts of protein were separated by SDS–polyacrylamide gel electrophoresis and blotted onto nitrocellulose. Blots were reprobed with mouse anti-β-actin (Clone AC-74, Sigma A2228, 1:5,000) as a loading control.

Immunohistochemistry. Deeply anaesthetized mice were perfused with 1% paraformaldehyde (PFA) in PBS and 6 µm sagittal cryosections were prepared from brains. Sections were postfixed with 1% PFA/PBS for 10 min, permeabilized with 0.2% Triton-X100 in PBS and blocked with 3% BSA in PBS. Antibodies were

diluted in blocking buffer. Incubation with primary antibody (see below for dilution) was performed at 4 °C overnight, incubation with secondary antibodies (1:1,000) coupled to Alexa fluorophores (Molecular Probes) was carried out for 1 h at room temperature. Nuclei were stained with 4′,6-diamidino-2-phenylindole (Sigma). In addition to the self-generated primary antibodies described above, the following commercial antibodies were used: mouse anti-GFAP (clone G-A-5, Sigma G3893, 1:1,000), mouse anti-S100β (clone SH-B1, Sigma S2532, 1:1,000), mouse anti-APC (clone CC1, Merck Millipore OP80, 1:200) and rat anti-heparan-sulphate-proteoglycan (perlecan, clone A7L6, Merck Millipore MAB1948P, 1:2,000) and goat anti-aquaporin-4 (Santa Cruz sc-9888, 1:50). The rabbit anti-Kir4.1 (used here at a dilution of 1:100) was kindly provided by S Takeuchi[50]. Images were acquired using an LSM510 confocal microscope and ZEN software (Zeiss).

Histology. For histological analyses of brains and eyes, mice were perfused with 4% PFA/PBS and organs were postfixed overnight. Haematoxylin–eosin staining was performed on 6 µm paraffin sections of brains and eyes.

Electron microscopy. For ultrastructural studies, deeply anaesthetized mice were transcardially perfused with 4% paraformaldeyhde (PFA) and 2.5% glutaraldehyde in 0.1 M PB (pH 7.4). The brains were removed and cut vertically into two halves. The brain samples were postfixed in the same fixative overnight at 4 °C. Brains were cut into 150 µm sagittal sections of the cerebellum with a Leica vibratome. Cerebellum sections were cut into 1 mm^3 fragments. They were rinsed with 0.1 M PB (pH 7.4) and postfixed with 2% aqueous osmium tetroxide and 1.5% potassium hexacyanoferrate (K3[Fe(CN)6]) for 30 min. After rinsing with 50% ethanol, sections were stained en bloc with 1% uranylacetate for 1 h in 70% ethanol. Fragments were dehydrated in graded ethanol, followed by infiltration of propylene oxide and embedding in Epon (Electron Microscopic Sciences, Hatfield, PA, USA). Ultrathin sections (60 nm) were prepared with a Reichert Ultracut S, stained in 5% uranylacetate and 0.4% lead citrate ((C6H5O7)2Pb3). Stained ultrathin sections were examined with a Zeiss 902 at 80 kV and a Fei Tecnai G F20 at 200 kV. Photographs were taken with a Megaview 3 Camera and a Gatan Ultrascan 1000 Camera. Two mice per genotype were examined, with more than 10 ultrathin sections each and that displayed consistent results.

Molecular biology. For quantitative real-time PCR, total RNA was isolated from the cerebellum of 11–18-week-old mice using the RNeasy lipid tissue mini kit with on-column DNase digestion (Qiagen). Complementary DNA was synthesized from 1 µg of RNA using Superscript II reverse transcriptase (Invitrogen). PCR reactions were prepared using Power Sybr Green PCR Master Mix (Applied Biosciences) and ran in triplicates in a StepOnePlus Real-Time PCR System with StepOne Software (Applied Biosystems) to monitor amplification and melting curves. Relative expression of mutant mice compared with WT siblings was calculated using the ΔΔCT method and *β-actin* as an internal control. The following primers were used: 5′-GACCGCCTAAAATCAGAAGCA-3′ and 5′-TGGCTCTGTAGCAGGG TTTT-3′ for *Glialcam*; 5′-TCAGTGCGATTCCCAACTTTCA-3′ and 5′-GGACC GGGCCGAAATGAT-3′ for *Mlc1*. Primer sequences for *Clcn2*: 5′-CAGTGACTG CAAAATCGACCC-3′ and 5′-CATAAGCATGGTCCACTCCCA-3′ and for β-actin: 5′-TGTGATGGTGGGAATGGGTCAGAA-3′ and 5′-TGTGGTGCCAGA TCTTCTCCATGT-3′ as described previously[8,51]. Missplicing in $Clcn2^{hyp/hyp}$ was detected by semiquantitative reverse transcription–PCR. Total RNA was isolated from brain using Trizol reagent (Invitrogen) and cDNA synthesis was performed as described above. Subsequently, PCR was performed using the following primer sequences: 5′-ATGGCGGCTGCAACGGCTG-3′ and 5′-AGGTTAGCCCAATG ACCTTAGC-3′. Expression constructs for mouse *Glialcam* and *Mlc1* were generated by PCR using full-length cDNA clones (SourceBioScience) as templates. Where applicable, C-terminal haemagglutinin (HA) tags were added by PCR and constructs were cloned into the pcDNA3.1 mammalian expression vector (Invitrogen). The cDNAs for rat *Clcn2* and human *Glialcam* were cloned in the pFROG vector for expression with the mammalian CMV promoter.

Cell culture/transfection. HeLa cells (DSMZ, Germany, ACC 57, lot 17) were transfected with *Clcn2*, *Glialcam* or *Mlc1* expression constructs using polyethylenimine. One day post transfection, cells were split and seeded onto coverslips. Three days after transfection, cells were fixed with 4% PFA/PBS, permeabilized with 0.2% Triton-X100/PBS and subjected to antibody staining as described for immunohistochemistry on tissue sections.

Electrophysiological analysis of glial cells in brain slices. Unless specified, concentrations are in mM and all solutions for incubating slices were constantly oxygenated with carbogen (5% CO_2 in O_2). Mice (3–4 weeks old of both gender) were deeply anaesthetized and either 200 µm sagittal sections for BG or 150 µm coronal sections for corpus callosum OLs were prepared using a vibrating microtome (Leica VT1200S, Germany) in 'low Ca^{2+}' artificial cerebrospinal fluid (aCSF) containing: 134 NaCl, 2.5 KCl, 10 glucose, 26 $NaHCO_3$, 1.25 K_2HPO_4, 1.3 $MgCl_2$, and 0.2 $CaCl_2$ and adjusted to pH 7.4 with NaOH and to 325 ± 5 mOsm kg^{-1}. Sagittal slices were allowed to recover in standard aCSF (2 $CaCl_2$) for at least 45 min at room temperature. Coronal slices, following sectioning, were first heated at 37 °C for 30 min in standard aCSF before transferring to room temperature. Measurements were performed at room temperature. Slices were adhered to poly-L-lysine-coated coverslips and transferred to a recording chamber (Luigs & Neumann, Germany) with constant perfusion of aCSF (1–2 ml min^{-1}) and mounted to an upright microscope equipped with a × 60 water immersion objective and both differential interference contrast and fluorescence optics (Olympus BX51WI). Patch pipettes were fabricated from glass capillaries (World Precision Instruments PG52151-4, USA; DMZ Universal Puller, Germany) and filled with an intracellular solution containing: 140 CsCl, 1 $MgCl_2$, 10 HEPES, 5 EGTA, 0.2 disodium carbenoxolone (Sigma-Aldrich) and adjusted to pH 7.3 with CsOH and to 290 mOsm kg^{-1}. Either 0.5 mg ml^{-1} Alexa Fluor 488 (Life Technologies A10436) or 2 mg ml^{-1} biocytin (Sigma B4261) was added to the patch pipette to confirm cell identity during the recording or following slice fixation for *post hoc* analysis, respectively. Ag-AgCl wires were used for recording and reference electrodes. Using a computer-controlled microelectrode amplifier (Multiclamp 700B) and acquisition software (Clampex 10.3, Molecular Devices, USA), patch pipettes typically registered resistances of 5–7 MΩ with a small voltage pulse. For patch clamping of BG and OLs in the tight seal configuration (> 1 GΩ), small somata adjacent to the larger Purkinje cells were selected, and small somata typically grouped in a row parallel to fibres in white matter tracts were selected, respectively. On acquisition of the conventional whole-cell configuration, large voltage-independent currents were seen in both BG and OLs on short voltage pulses from + 40 to − 100 mV from a holding potential of − 10 mV. Morphologically, BG typically had two or three thin processes radiating across the molecular layer and terminating in the pia. OLs typically had processes that were sparsely branched and were orientated in parallel with myelinated fibres. To isolate ClC-2 currents, slices were perfused with a Na^+- and K^+-free extracellular solution containing: 117 NMDG-Cl, 23 NMDG-HCO_3, 5 CsCl, 1.3 $MgCl_2$, 9 glucose, 2 $CaCl_2$, 0.2 Na_2-carbenoxolone and adjusted to pH 7.3 with CsOH and 295 ± 5 mOsm kg^{-1}. Typically, at least 10–15 min were needed before the membrane conductance stabilized on perfusion with the NMDG-Cl bath solution. To elicit ClC-2 currents, voltage steps from + 40 to up to − 120 mV from a holding potential of − 10 mV were used. A final 1 s voltage step at + 40 mV was applied before returning to the holding potential. Signals were digitized at 10 KHz, filtered at 2 kHz and stored for off-line analysis. Using the standard membrane test function in Clampex software, membrane capacitance and resistances were obtained online at the end of the experiment using a small 5 mV pulse from a holding potential of − 10 mV. In some experiments, slices were perfused with either a hypotonic diluted NMDG-Cl solution (80%) to 235 ± 5 mOsm kg^{-1}, or a hypertonic NMDG-Cl with sucrose added to 325 ± 5 mOsm kg^{-1}. Averaging, normalizing and subtracting trace profiles were done off-line using ClampFit 10.3 (Molecular Devices). Current profiles were acquired using the same voltage pulse protocol (1.5 s steps from + 40 to − 120 mV including a 1-s tail current at + 40 mV before returning back to the holding potential of − 10 mV). Currents from each cell were averaged by genotype to obtain an average current (I) profile. In other analyses, the average I profile from each genotype was divided ('Arithmetic tool') by its average capacitance (C) to obtain the average current density (I/C) profile. For trace subtraction, either I or I/C trace profiles from $Clcn2^{-/-}$ mice were subtracted ('Arithmetic tool') from the respective I or I/C trace profiles from WT, $Glialcam^{-/-}$, $Mlc1^{-/-}$, $Glialcam^{dn/dn}$ or $Glialcam^{+/-}$ animals to examine the ClC-2-specific I or I/C trace profiles in the different mouse models.

Processing of biocytin-filled cells in brain slices. Following patch clamp experiments, slices were fixed in 4% PFA (in 1 × PBS) overnight at 4 °C. Slices were washed in wash buffer containing 0.1 M PB pH 7.4 and 0.25% Triton-X100. Slices were blocked in wash buffer containing 5% normal goat serum for 2 h at room temperature. For secondary detection, Alexa Fluor 555 Streptavidin (Life Technologies) was added to the slices at a 1:500 dilution for overnight incubation at 4 °C. Slices were washed and mounted on gelatinized slides with Fluoromount G (SouthernBiotech). Images were acquired with a confocal microscope (Zeiss LSM 510).

Patch clamp measurements in HEK cells. HEK293 cells were transfected in 12-well plates at ~50% confluency with either 0.5 µg of plasmid encoding rat ClC-2 or 0.25 µg of plasmid encoding rat ClC-2 and 0.25 µg of plasmid encoding human Glialcam. All cells were co-transfected with a reporter plasmid expressing GFP. Using a microelectrode amplifier (Multiclamp 700B) with acquisition software (Clampex 10.3; Molecular Devices, USA), whole-cell currents were measured by patch clamp analysis 2 days after transfection. When filled with an intracellular solution containing (in mM): 140 CsCl, 1 $MgCl_2$, 10 HEPES and 5 EGTA adjusted to pH 7.3 and to 290 ± mOsm kg^{-1}, patch pipettes registered resistances of 4–5 MΩ. The bath solution was composed of (in mM): 140 NaCl, 2 $MgSO_4$, 2 $CaCl_2$, 10 HEPES, 22 sucrose and adjusted to pH 7.4 with NaOH and to 325 ± 5 mOsm kg^{-1} with sucrose. ClC-2 currents were elicited with 1 s voltage pulses from + 40 to − 120 mV and a final voltage pulse at + 40 mV before returning back to the holding potential of − 10 mV. Individual cells were first measured in normal bath solution and again following superfusion of bath solution containing 200 µM disodium carbenoxolone. Signals were digitized at 10 KHz, filtered at 2 kHz and stored for off-line analysis using ClampFit software.

Statistics. Statistical significance was assessed between two groups using the non-parametric Mann–Whitney test (Prism, GraphPad Software, USA).

References

1. Leegwater, P. A. *et al.* Mutations of *MLC1* (KIAA0027), encoding a putative membrane protein, cause megalencephalic leukoencephalopathy with subcortical cysts. *Am. J. Hum. Genet.* **68,** 831–838 (2001).
2. López-Hernández, T. *et al.* Mutant GlialCAM causes megalencephalic leukoencephalopathy with subcortical cysts, benign familial macrocephaly, and macrocephaly with retardation and autism. *Am. J. Hum. Genet.* **88,** 422–432 (2011).
3. Arnedo, T. *et al.* Expanding the spectrum of megalencephalic leukoencephalopathy with subcortical cysts in two patients with *GLIALCAM* mutations. *Neurogenetics*. PMID: 24202401 (2013).
4. Moh, M. C., Zhang, C., Luo, C., Lee, L. H. & Shen, S. Structural and functional analyses of a novel ig-like cell adhesion molecule, hepaCAM, in the human breast carcinoma MCF7 cells. *J. Biol. Chem.* **280,** 27366–27374 (2005).
5. Chung Moh, M., Hoon Lee, L. & Shen, S. Cloning and characterization of hepaCAM, a novel Ig-like cell adhesion molecule suppressed in human hepatocellular carcinoma. *J. Hepatol.* **42,** 833–841 (2005).
6. Favre-Kontula, L. *et al.* GlialCAM, an immunoglobulin-like cell adhesion molecule is expressed in glial cells of the central nervous system. *Glia* **56,** 633–645 (2008).
7. López-Hernández, T. *et al.* Molecular mechanisms of MLC1 and GLIALCAM mutations in megalencephalic leukoencephalopathy with subcortical cysts. *Hum. Mol. Genet.* **20,** 3266–3277 (2011).
8. Blanz, J. *et al.* Leukoencephalopathy upon disruption of the chloride channel ClC-2. *J. Neurosci.* **27,** 6581–6589 (2007).
9. Bösl, M. R. *et al.* Male germ cells and photoreceptors, both depending on close cell-cell interactions, degenerate upon ClC-2 Cl^--channel disruption. *EMBO J.* **20,** 1289–1299 (2001).
10. Scheper, G. C. *et al.* Analysis of *CLCN2* as candidate gene for megalencephalic leukoencephalopathy with subcortical cysts. *Genet. Test. Mol. Biomarkers* **14,** 255–257 (2010).
11. Depienne, C. *et al.* Brain white matter oedema due to ClC-2 chloride channel deficiency: an observational analytical study. *Lancet. Neurol.* **12,** 659–668 (2013).
12. Jeworutzki, E. *et al.* GlialCAM, a protein defective in a leukodystrophy, serves as a ClC-2 Cl^- channel auxiliary subunit. *Neuron* **73,** 951–961 (2012).
13. Gründer, S., Thiemann, A., Pusch, M. & Jentsch, T. J. Regions involved in the opening of CIC-2 chloride channel by voltage and cell volume. *Nature* **360,** 759–762 (1992).
14. Thiemann, A., Gründer, S., Pusch, M. & Jentsch, T. J. A chloride channel widely expressed in epithelial and non-epithelial cells. *Nature* **356,** 57–60 (1992).
15. Jordt, S. E. & Jentsch, T. J. Molecular dissection of gating in the ClC-2 chloride channel. *EMBO J.* **16,** 1582–1592 (1997).
16. Duarri, A. *et al.* Knockdown of MLC1 in primary astrocytes causes cell vacuolation: a MLC disease cell model. *Neurobiol. Dis.* **43,** 228–238 (2011).
17. Schwenk, F., Baron, U. & Rajewsky, K. A cre-transgenic mouse strain for the ubiquitous deletion of *loxP*-flanked gene segments including deletion in germ cells. *Nucleic Acids Res.* **23,** 5080–5081 (1995).
18. Boor, I. *et al.* MLC1 is associated with the dystrophin-glycoprotein complex at astrocytic endfeet. *Acta Neuropathol.* **114,** 403–410 (2007).
19. Schmitt, A. *et al.* The brain-specific protein MLC1 implicated in megalencephalic leukoencephalopathy with subcortical cysts is expressed in glial cells in the murine brain. *Glia* **44,** 283–295 (2003).
20. Teijido, O. *et al.* Localization and functional analyses of the MLC1 protein involved in megalencephalic leukoencephalopathy with subcortical cysts. *Hum. Mol. Genet.* **13,** 2581–2594 (2004).
21. Tress, O. *et al.* Panglial gap junctional communication is essential for maintenance of myelin in the CNS. *J. Neurosci.* **32,** 7499–7518 (2012).
22. Nolte, C. *et al.* GFAP promoter-controlled EGFP-expressing transgenic mice: a tool to visualize astrocytes and astrogliosis in living brain tissue. *Glia* **33,** 72–86 (2001).
23. Moh, M. C., Tian, Q., Zhang, T., Lee, L. H. & Shen, S. The immunoglobulin-like cell adhesion molecule hepaCAM modulates cell adhesion and motility through direct interaction with the actin cytoskeleton. *J. Cell. Physiol.* **219,** 382–391 (2009).
24. Lee, L. H., Moh, M. C., Zhang, T. & Shen, S. The immunoglobulin-like cell adhesion molecule hepaCAM induces differentiation of human glioblastoma U373-MG cells. *J. Cell. Biochem.* **107,** 1129–1138 (2009).
25. Capdevila-Nortes, X. *et al.* Insights into MLC pathogenesis: GlialCAM is an MLC1 chaperone required for proper activation of volume-regulated anion currents. *Hum. Mol. Genet.* **22,** 4405–4416 (2013).
26. Teijido, O. *et al.* Expression patterns of MLC1 protein in the central and peripheral nervous systems. *Neurobiol. Dis.* **26,** 532–545 (2007).
27. Maglione, M. *et al.* Oligodendrocytes in mouse corpus callosum are coupled via gap junction channels formed by connexin47 and connexin32. *Glia* **58,** 1104–1117 (2010).
28. Nehrke, K. *et al.* Loss of hyperpolarization-activated Cl^- current in salivary acinar cells from *Clcn2* knockout mice. *J. Biol. Chem.* **26,** 23604–23611 (2002).
29. Rinke, I., Artmann, J. & Stein, V. ClC-2 voltage-gated channels constitute part of the background conductance and assist chloride extrusion. *J. Neurosci.* **30,** 4776–4786 (2010).
30. Clark, S., Jordt, S. E., Jentsch, T. J. & Mathie, A. Characterization of the hyperpolarization-activated chloride current in dissociated rat sympathetic neurons. *J. Physiol.* **506,** 665–678 (1998).
31. Makara, J. K. *et al.* Astrocytes from mouse brain slices express ClC-2-mediated Cl^- currents regulated during development and after injury. *Mol. Cell. Neurosci.* **23,** 521–530 (2003).
32. Ferroni, S., Marchini, C., Nobile, M. & Rapisarda, C. Characterization of an inwardly rectifying chloride conductance expressed by cultured rat cortical astrocytes. *Glia* **21,** 217–227 (1997).
33. Fava, M., Ferroni, S. & Nobile, M. Osmosensitivity of an inwardly rectifying chloride current revealed by whole-cell and perforated-patch recordings in cultured rat cortical astrocytes. *FEBS Lett.* **492,** 78–83 (2001).
34. Makara, J. K., Petheö, G. L., Tóth, A. & Spät, A. pH-sensitive inwardly rectifying chloride current in cultured rat cortical astrocytes. *Glia* **34,** 52–58 (2001).
35. Weinreich, F. & Jentsch, T. J. Pores formed by single subunits in mixed dimers of different CLC chloride channels. *J. Biol. Chem.* **276,** 2347–2353 (2001).
36. Hoppe, D. & Kettenmann, H. Carrier-mediated Cl^- transport in cultured mouse oligodendrocytes. *J. Neurosci. Res.* **23,** 467–475 (1989).
37. Wang, H., Yan, Y., Kintner, D. B., Lytle, C. & Sun, D. GABA-mediated trophic effect on oligodendrocytes requires Na-K-2Cl cotransport activity. *J. Neurophysiol.* **90,** 1257–1265 (2003).
38. MacVicar, B. A., Tse, F. W., Crichton, S. A. & Kettenmann, H. GABA-activated Cl^- channels in astrocytes of hippocampal slices. *J. Neurosci.* **9,** 3577–3583 (1989).
39. Ridder, M. C. *et al.* Megalencephalic leucoencephalopathy with cysts: defect in chloride currents and cell volume regulation. *Brain* **134,** 3342–3354 (2011).
40. Okada, Y., Sato, K. & Numata, T. Pathophysiology and puzzles of the volume-sensitive outwardly rectifying anion channel. *J. Physiol.* **587,** 2141–2149 (2009).
41. Benfenati, V. *et al.* Functional down-regulation of volume-regulated anion channels in AQP4 knockdown cultured rat cortical astrocytes. *J. Neurochem.* **100,** 87–104 (2007).
42. Neusch, C., Rozengurt, N., Jacobs, R. E., Lester, H. A. & Kofuji, P. Kir4.1 potassium channel subunit is crucial for oligodendrocyte development and in vivo myelination. *J. Neurosci.* **21,** 5429–5438 (2001).
43. Butt, A. M. & Kalsi, A. Inwardly rectifying potassium channels (Kir) in central nervous system glia: a special role for Kir4.1 in glial functions. *J. Cell. Mol. Med.* **10,** 33–44 (2006).
44. Djukic, B., Casper, K. B., Philpot, B. D., Chin, L. S. & McCarthy, K. D. Conditional knock-out of Kir4.1 leads to glial membrane depolarization, inhibition of potassium and glutamate uptake, and enhanced short-term synaptic potentiation. *J. Neurosci.* **27,** 11354–11365 (2007).
45. Menichella, D. M., Goodenough, D. A., Sirkowski, E., Scherer, S. S. & Paul, D. L. Connexins are critical for normal myelination in the CNS. *J. Neurosci.* **23,** 5963–5973 (2003).
46. Menichella, D. M. *et al.* Genetic and physiological evidence that oligodendrocyte gap junctions contribute to spatial buffering of potassium released during neuronal activity. *J. Neurosci.* **26,** 10984–10991 (2006).
47. Uhlenberg, B. *et al.* Mutations in the gene encoding gap junction protein alpha 12 (connexin 46.6) cause Pelizaeus-Merzbacher-like disease. *Am. J. Hum. Genet.* **75,** 251–260 (2004).
48. Rash, J. E. Molecular disruptions of the panglial syncytium block potassium siphoning and axonal saltatory conduction: pertinence to neuromyelitis optica and other demyelinating diseases of the central nervous system. *Neuroscience* **168,** 982–1008 (2010).
49. Laursen, L. S. & Ffrench-Constant, C. Adhesion molecules in the regulation of CNS myelination. *Neuron Glia Biol.* **3,** 367–375 (2007).
50. Ando, M. & Takeuchi, S. Immunological identification of an inward rectifier K^+ channel (Kir4.1) in the intermediate cell (melanocyte) of the cochlear stria vascularis of gerbils and rats. *Cell Tissue Res.* **298,** 179–183 (1999).
51. Billig, G. M., Pál, B., Fidzinski, P. & Jentsch, T. J. Ca^{2+}-activated Cl^- currents are dispensable for olfaction. *Nat. Neurosci.* **14,** 763–769 (2011).

Acknowledgements

We thank L. Leisle for detecting aberrant splicing in *Clcn2*$^{hyp/hyp}$ mice, N. Richter and H. Kettenmann for advice on patching OLs, A. Duarri and M. Font-Llitjòs for starting work with *Mlc1*$^{-/-}$ constructs, S. Takeuchi for the Kir4.1 antibody, and A. Weidlich, J. Jedamzick, P. Seidler, R. Silluè, S. Alcántara, L. Gónzalez and E. Prat for technical assistance. K.G. was supported by the Boehringer Ingelheim Fonds and is a student of the Freie Universität Berlin. This study was supported by ELA Research Foundation,

ELA2009-017C4, ELA2012-014C2B to R.E. and V.N., MINECCO SAF2009-12606-CO2-02 to V.N., SAF 2009-07014, SAF 2012-31486, PS09/02672-ERARE and Icrea Academia prize to R.E., Catalonian Government SGR2009-1490 to V.N. and SGR2009-719 to R.E., and DFG (Exc 257) and Prix Louis-Jeantet de Médecine to T.J.J.

Author contributions

The *Glialcam* mouse models were generated from the lab of T.J.J. and the *Mlc1* mouse model was generated from the labs of R.E. and V.N.. M.B.H.-B. generated antibodies and analysed all mouse models (histology, IHC, immunoblots) and transfected cells. S.S. generated antibodies and analysed the *Mlc1* mouse model (histology, IHC, immunoblots). I.J.O. analysed all mouse models by electrophysiology. I.F. and S.H. performed EM analysis. M.A. generated the *Clcn2*$^{hyp/hyp}$ mouse model. K.G. developed the method for recording glial chloride currents. C.V. and M.L.d.H. performed histology and biochemical analysis on the *Mlc1* mouse model. All authors planned and analysed experiments. T.J.J., R.E. and V.N. supervised experiments. T.J.J. was the primary writer and managed producing the manuscript with critical input from R.E., V.N. for design, content and style. All authors read and provided feedback on the manuscript.

Additional information

Supplementary Information accompanies this paper at http://www.nature.com/naturecommunications

Competing financial interests: The authors declare no competing financial interests.

Reprints and permission information is available online at http://npg.nature.com/reprintsandpermissions/

How to cite this article: Hoegg-Beiler, M. B. *et al.* Disrupting MLC1 and GlialCAM and ClC-2 interactions in leukodystrophy entails glial chloride channel dysfunction. *Nat. Commun.* 5:3475 doi: 10.1038/ncomms4475 (2014).

Megalencephalic leukoencephalopathy with subcortical cysts protein 1 regulates glial surface localization of GLIALCAM from fish to humans

(Human Molecular Genetics, 2014)

Contribució:

- Preparació del teixit per als estudis de ME (Figura 1)
- Generació dels constructes zGlialCAMa, zGlialG89S, zGlialG89D, zGlialD128N
- Estudis de localització de zMLC1 i rClC-2 en presència de zGlialCAMa (Figura 2 C,D,E,F,G,H)
- Anàlisis de les imatges de MRI i càlcul del volum cerebral (Figura 6 A,B,G)
- Estudis de localització realitzats en el teixit de la pacient (Figura 7)
- Posta a punt del cultiu primari d'astròcits del ratolí *knock-out* de *Mlc1*
- Anàlisis de MLC1 i GlialCAM en els astròcits del *knock-out* (Figura 8 A,B,C,D,E)
- Preparació dels cultius per als anàlisis electrofisiològics
- Estudi del fenotip vacuolitzant en els astròcits del *knock-out* (Figura 8 H,I,J)
- Estudi de localització de GlialCAM en condicions d'alt contingut de K^+ (Figura 9)
- Estudi de l'expressió i la localització de les mutacions de zGlialCAMa (Figura Suplementària 3)

HMG Advance Access published May 27, 2014

Human Molecular Genetics, 2014 ***1–18***
doi:10.1093/hmg/ddu231

Megalencephalic leukoencephalopathy with subcortical cysts protein 1 regulates glial surface localization of GLIALCAM from fish to humans

Sònia Sirisi[1,4,†], Mónica Folgueira[5,†], Tania López-Hernández[1], Laura Minieri[6], Carla Pérez-Rius[1], Héctor Gaitán-Peñas[1], Jingjing Zang[7], Albert Martínez[2], Xavier Capdevila-Nortes[1], Pedro De La Villa[8], Upasana Roy[9,10], A. Alia[9,10], Stephan Neuhauss[7], Stefano Ferroni[6], Virginia Nunes[3,4,11], Raúl Estévez[1,12,‡,*] and Alejandro Barrallo-Gimeno[1,12,‡,*]

[1]Sección de Fisiología, Departamento de Ciencias Fisiológicas II, [2]Department of Cell Biology and [3]Sección de Genética, Departamento de Ciencias Fisiológicas II, Universidad de Barcelona, Barcelona, Spain [4]Laboratorio de Genética Molecular-IDIBELL, L'Hospitalet de Llobregat, Spain [5]Department of Cell & Molecular Biology, University of A Coruña, A Coruña, Spain [6]Department of Pharmacy and Biotecnology, University of Bologna, Bologna, Italy [7]Institute of Molecular Life Sciences, University of Zurich, Zurich, Switzerland [8]Department of Systems Biology, University of Alcalá, Alcalá de Henares, Madrid, Spain [9]Leiden Institute of Chemistry, Leiden University, Leiden, The Netherlands [10]Institute of Medical Physics and Biophysics, University of Leipzig, Leipzig, Germany [11]U-730 and [12]U-750, Centro de Investigación en red de Enfermedades Raras (CIBERER), ISCIII, Barcelona, Spain

Received March 19, 2014; Revised and Accepted May 8, 2014

Megalencephalic leukoencephalopathy with subcortical cysts (MLC) is a leukodystrophy characterized by myelin vacuolization and caused by mutations in *MLC1* or *GLIALCAM*. Patients with recessive mutations in either *MLC1* or *GLIALCAM* show the same clinical phenotype. It has been shown that GLIALCAM is necessary for the correct targeting of MLC1 to the membrane at cell junctions, but its own localization was independent of MLC1 *in vitro*. However, recent studies in *Mlc1*$^{-/-}$ mice have shown that GlialCAM is mislocalized in glial cells. In order to investigate whether the relationship between Mlc1 and GlialCAM is species-specific, we first identified MLC-related genes in zebrafish and generated an *mlc1*$^{-/-}$ zebrafish. We have characterized *mlc1*$^{-/-}$ zebrafish both functionally and histologically and compared the phenotype with that of the *Mlc1*$^{-/-}$ mice. In *mlc1*$^{-/-}$ zebrafish, as in *Mlc1*$^{-/-}$ mice, Glialcam is mislocalized. Re-examination of a brain biopsy from an MLC patient indicates that GLIALCAM is also mislocalized in Bergmann glia in the cerebellum. *In vitro*, impaired localization of GlialCAM was observed in astrocyte cultures from *Mlc1*$^{-/-}$ mouse only in the presence of elevated potassium levels, which mimics neuronal activity. In summary, here we demonstrate an evolutionary conserved role for MLC1 in regulating glial surface levels of GLIALCAM, and this interrelationship explains why patients with mutations in either gene (*MLC1* or *GLIALCAM*) share the same clinical phenotype.

INTRODUCTION

Megalencephalic leukoencephalopathy with subcortical cysts (MLC) is a rare type of congenital leukodystrophy characterized mainly by myelin vacuolization and early onset of macrocephaly (1). Magnetic resonance imaging (MRI) of patient's brains shows diffuse signal abnormality, and this method is used for diagnosis during childhood (2). MLC is caused by mutations

*To whom correspondence should be addressed at: Facultat de Medicina, Departament de Ciències Fisiològiques II, Universitat de Barcelona, C/Feixa Llarga s/n 08907 L'Hospitalet de Llobregat, Barcelona, Spain. Tel: +34 934039781; Fax: +34 934024268; Email: restévez@ub.edu (R.E.); abarrallo@ub.edu (A.B.-G.)
†These authors contributed equally.
‡These authors share last authorship.

in either *MLC1* (MIM #605908) or *GLIALCAM* (MIM #611642) genes (3,4).

MLC1 encodes for a membrane protein, which is expressed in several brain barriers, mainly in ependymal cells, astrocytes surrounding blood vessels and Bergmann radial glia in the cerebellum. In all cells, MLC1 is localized at cell junctions (5–7). Surprisingly, MLC1 is not expressed in oligodendrocytes, the site of the primary pathology of MLC (8). Mutations have been found across the whole coding sequence (3,9–11), which cause protein folding defects that lead to degradation of MLC1 (12,13). The function of MLC1 is still unknown, although it has been related to the activation of volume-regulated anion currents (VRAC) (14,15), involved in cellular osmotic response. It has been indicated that a reduced VRAC activity may lead to intracellular water accumulation and to the vacuolization observed in patients (15,16). In addition, other studies have suggested that MLC1 cooperates with the Na^+/K^+-ATPase and the TRPV4 channel (17,18), although the exact mechanism is still unknown.

GlialCAM (also called HEPACAM due to its original discovery in hepatic cancer cells) is a cell adhesion molecule of the immunoglobulin family (19) that is mostly expressed in glial cells (20) and co-localizes with MLC1 at astrocyte–astrocyte junctions (4). MLC patients with recessive mutations in *GLIALCAM* (known as MLC2A type of MLC, MIM #613925) present the same phenotype as patients carrying recessive mutations in *MLC1* (MLC1 type of MLC, MIM #604004) (4,21). Some MLC patients have dominant mutations in the *GLIALCAM* gene (MLC2B type of MLC, MIM #613926), and these are associated to various degrees of phenotypic expression, ranging from a transient benign form of MLC, to macrocephaly and mental retardation with or without autism (4,21).

Both data obtained from *in vitro* and from *GlialCAM*$^{-/-}$ mice have demonstrated that GlialCAM is necessary for MLC1 to exit the endoplasmatic reticulum and target cell junctions (13,15,22). Furthermore, a mistargeting of both GlialCAM and MLC1 to cell junctions has been shown by *in vitro* studies with most missense *GLIALCAM* mutations (either recessive or dominant) and with *GlialCAM*$^{dn/dn}$ knock-in mice harbouring a dominant mutation (4,13,22,23). In contrast, GlialCAM seems to be able to traffic to cell junctions by itself (13,19). Thus, the overlapping phenotype of MLC1 and MLC2A patients can be understood because of the cardinal role of MLC1 in the pathogenesis of MLC.

However, GlialCAM, but not MLC1, is detected in oligodendrocytes (4,20); it was also found that GlialCAM functions as an auxiliary glial-specific subunit of the broadly expressed ClC-2 chloride channel (24). Furthermore, MLC-related *GLIALCAM* mutations impair the trafficking of ClC-2 to cell junctions (23,24). Analyses of *GlialCAM*$^{-/-}$ and *GlialCAM*$^{dn/dn}$ knock-in mice have shown that localization of ClC-2 in glial junctions is dependent on GlialCAM (22). Thus, based on these *in vitro* and *in vivo* data, patients carrying recessive *GLIALCAM* mutations should be more severely affected than patients carrying recessive *MLC1* mutations, as ClC-2 channel may also be affected in those carrying *GLIALCAM* mutations. However, there are no clinical differences between these two types of patients.

Recent studies with *Mlc1*$^{-/-}$ mice have shown that, contrary to what was expected based on the lack of direct interaction between MLC1 and ClC-2, GlialCAM and ClC-2 are mislocalized in astrocytes and oligodendrocytes when MLC1 is absent (22). Based on cell culture data, it was indicated that MLC1 and ClC-2 could indirectly interact through homotypic extracellular GlialCAM-mediated interactions (22), as previously suggested (25). These results indicate that lack of function of ClC-2 may be involved in the pathogenesis of MLC (22). Lack of ClC-2 function has also been associated with a distinct form of leukoencephalopathy (26).

The mislocalization of GlialCAM found in *Mlc1*$^{-/-}$ mice contradicts previous results obtained using RNA interference of *Mlc1* in rat astrocytes and localization studies of GLIALCAM around blood vessels in a sample from an MLC1 patient (13). Although RNA interference may not completely reproduce the gene knockout phenotype, we have previously shown that Mlc1 RNAi induces a significant decrease in Mlc1 protein levels (12,13). Thus, it is unclear if GlialCAM is unstable without MLC1 only in mice, or whether this is a general mechanism.

To solve this controversy, we decided to examine the relationship between Mlc1 and GlialCAM in other animal species. We generated a zebrafish model for MLC based on the lack of mlc1. As in mice, characterization of the zebrafish model revealed that loss of mlc1 impairs the correct localization of glialcam. Re-examination of the brain biopsy from a MLC1 patient that had been previously studied revealed that GlialCAM was mislocalized in Bergmann glia. These results confirm that the MLC1-dependent localization of GlialCAM is a general mechanism, as data from *Mlc1*$^{-/-}$ mouse had shown. As in the RNA interference experiments, cultured astrocytes from *Mlc1*$^{-/-}$ mice show normal GlialCAM localization, but slightly reduced VRAC activity. However, we observed that mimicking neuronal activity in *Mlc1*$^{-/-}$ astrocyte cultures causes GlialCAM mislocalization. Hence, data presented here explain previous discrepancies and reveal a conserved activity-regulated role of MLC1 in determining the localization of GLIALCAM.

RESULTS

GlialCAM is also mislocalized in Mlc1$^{-/-}$ astrocytes close to ependymal cells

In situ hybridization and immunohistochemistry studies have demonstrated that MLC1 and GLIALCAM co-localize in astrocytes close to brain barriers, Bergmann glia and ependymal cells, and that GLIALCAM is additionally expressed in oligodendrocytes (4,6,7,20). In *Mlc1*$^{-/-}$ mice, GlialCAM is mislocalized in astrocytes, Bergmann glia and oligodendrocytes (22). We examined whether GlialCAM was also mislocalized in ependymal cells by means of electron microscopy. To our surprise, gold particle-labelled antibodies showed that Mlc1 is not present in ependymal cells, but rather in astrocyte–astrocyte contacts below ependymal cells (Fig. 1A and C). Control experiments in *Mlc1*$^{-/-}$ mice confirmed the specificity of the signal (Fig. 1B and D). GlialCAM co-localized with Mlc1 in subependymal astrocyte–astrocyte contacts (Fig. 1E and G), and, as observed previously in astrocytes and oligodendrocytes, GlialCAM was also mislocalized in astrocytes near ependymal cells in *Mlc1*$^{-/-}$ mice (Fig. 1F and H). Thus, we conclude that the absence of *Mlc1* in mice causes mistargeting of GlialCAM in all types of glial cells.

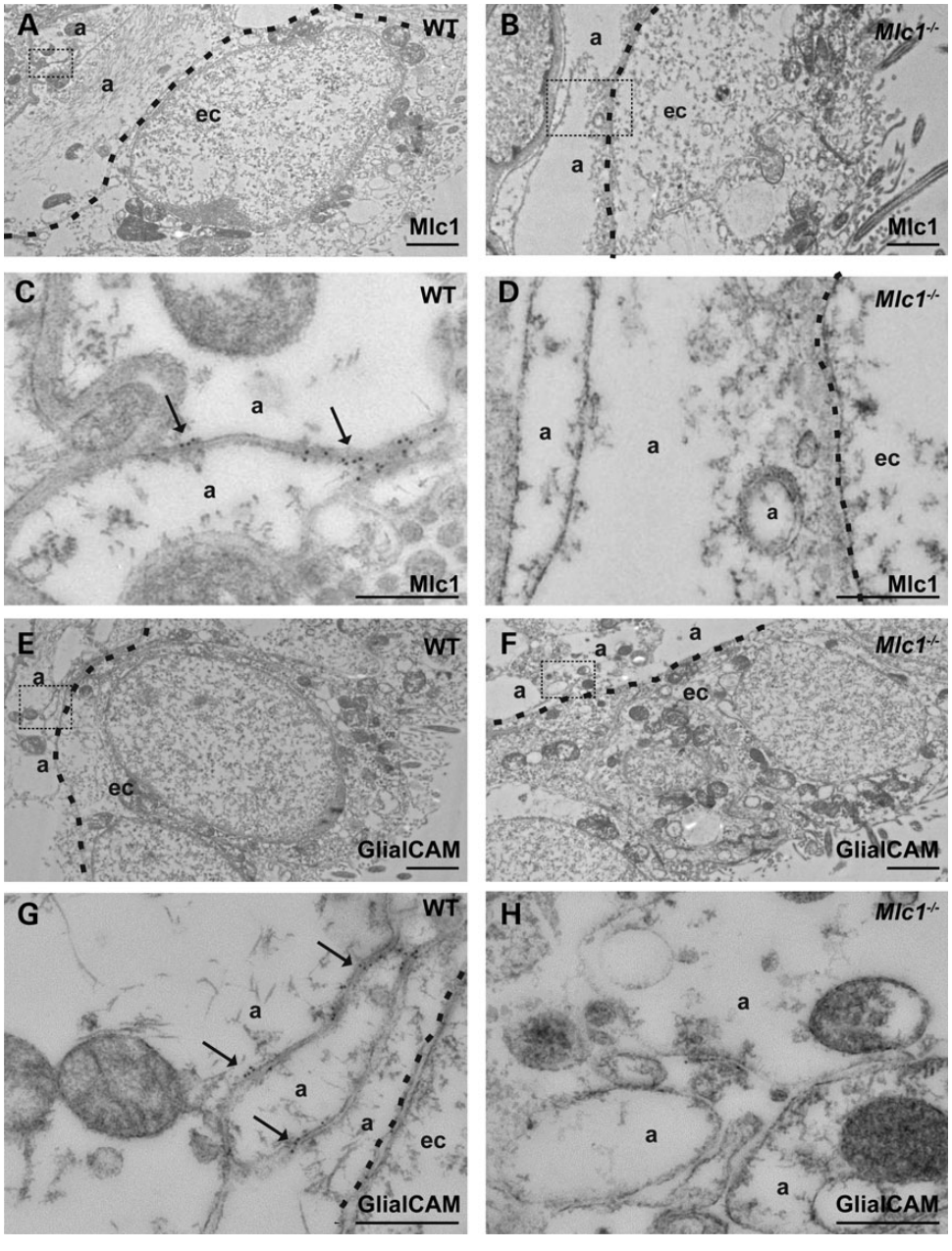

Figure 1. GlialCAM does not localize to astrocyte junctions in subependymal astrocytes in *Mlc1*$^{-/-}$ mice. (**A**–**D**) EM immunolabelling of ependymal cells shows localization of Mlc1 in astrocyte–astrocyte junctions (arrows) near ependymal cells (A and C). Dotted lines highlight boundaries between ependymal cells (ec) and inner astrocytic processes (a). The signal was specific as it was absent in Mlc1$^{-/-}$ mice (B and D). The insets in (A) and (B) are shown amplified in (C) and (D). Scale bars: (A, B): 2 μm; (C, D): 500 nm. (**E**–**H**) EM immunolabelling images of GlialCAM in astrocyte junctions below ependymal cells (arrows) (E, G). GlialCAM protein could not be observed in astrocyte–astrocyte junctions in *Mlc1*$^{-/-}$ mice (F, H). The insets in (E) and (F) are shown amplified in (G) and (H). Scale bars: (E and F): 2 μm; (G and H): 500 nm.

Identification of MLC-related genes in zebrafish

To address whether this Mlc1-dependent mislocalization of GlialCAM was a conserved feature, we decided to generate an *Mlc1*-deficient animal model in another species. By means of sequence database inspection, we found that genes encoding the orthologue of human *MLC1* are present in all vertebrates, including zebrafish (*Danio rerio*), that has a single orthologue (Supplementary Material, Fig. S1A). In contrast, metazoan model organisms, such as *Drosophila melanogaster* and *Caenorhabditis elegans*, which lack myelin, do not possess *MLC1* orthologues (3). For *GLIALCAM*, we observed that the teleost-specific genome duplication yielded two *glialcam* paralogues: *glialcama* and *glialcamb* (Supplementary Material, Fig. S2A).

Sequence comparison between zebrafish *mlc1* and its human ortholog showed an overall 53% identity that was higher (63%) at the putative transmembrane domains and the terminal part of the C-terminus (Supplementary Material, Fig. S1B). Both *glialcam* paralogues showed a 76% identity with human

GLIALCAM across the two extracellular Ig-domains and the putative transmembrane domain, but the conservation of the C-terminal intracellular domain was very low, saved for a stretch of residues in the central part (Supplementary Material, Fig. S2B).

We cloned zebrafish *mlc1* and both *glialcam* paralogues, fused to an intracellular FLAG tag, and expressed them transiently in HeLa cells. Importantly, glialcama could be predominantly detected in cell junctions (Fig. 2A), while glialcamb was found in a diffuse manner (Fig. 2B). Like its human counterpart (13), glialcama was able to target zebrafish mlc1 (Fig. 2C–E) and rat chloride channel ClC-2 (24) (Fig. 2F–H) to cell junctions. Furthermore, glialcama and not glialcamb was able to modify the functional properties of rat ClC-2-mediated currents in *Xenopus* oocytes. Glialcama, as with the human ortholog (24), not only increased ClC-2-mediated currents, but also changed rectification and activation properties (Fig. 2I–L). To additionally verify that glialcama behaves as human GLIALCAM, we analysed glialcama variants containing MLC-related mutations in conserved residues (Supplementary Material, Fig. S2B) that have previously shown trafficking defects (13). As happened in human *GLIALCAM* (4), we observed that the introduction of MLC-related mutations in glialcama negatively affected its junctional localization without substantially interfering with its expression levels (Supplementary Material, Fig. S3A–C).

These results suggest that zebrafish glialcama, and not glialcamb, could perform the same physiological functions as human GLIALCAM. Therefore, we decided to focus our studies on this zebrafish paralogue.

Generation of a mutant mlc1 zebrafish line

We generated a zebrafish *mlc1* knockout line by sequencing the first exons of the *mlc1* gene on the ENU-based TILLING library at the laboratory of Dr C. Moens at the FHCRC (Seattle, USA). Unfortunately, we did not detect any stop, frameshift or splice site mutations that would potentially abolish normal protein expression. However, we detected a missense mutation (c.241T>G) in one allele (*mlc1*^{fh328}), resulting in the substitution of a conserved hydrophobic residue (isoleucine) for a charged one (arginine; p.81I>R) on the predicted first transmembrane domain of the protein. We hypothesized that the introduction of a positive charge in the transmembrane domain could be deleterious for its protein expression. In order to test this, we introduced the equivalent mutation (V64R, Supplementary Material, Fig. S1B) in human MLC1 carrying *HA* epitope tags (one at the *N*-terminus and the other extracellular) and assayed surface expression by an ELISA-based luminescence assay in *Xenopus* oocytes (Fig. 3A). We used oocytes because their incubation temperature (18°C) would reveal whether the mutation causes folding defects (27). No surface expression could be detected, confirming our hypothesis that the mutation was deleterious.

Therefore, the heterozygous founder zebrafish were pair-wise mated and out-crossed for several generations to eliminate any other background mutations from the original ENU mutagenesis (see Materials and Methods). As the mutation results in a novel *Dde*I restriction site, it was possible to perform RFLP genotyping, and gene sequencing confirmed the presence of the mutation (Fig. 3B and C). As our previous antibodies against human or mouse Mlc1 proteins did not recognize the zebrafish orthologue (data not shown), we developed a new rabbit polyclonal antibody that was able to detect zebrafish mlc1 (Fig. 3D and E). We assayed mlc1 expression in brain extracts from wild-type, heterozygous and homozygous *mlc1*^{fh328} adult fish siblings. No mlc1 protein expression could be detected in homozygotes, validating the allele *mlc1*^{fh328} as an *mlc1* knockout line, which we will refer to as *mlc1*$^{-/-}$ zebrafish from now on (Fig. 3F). As with the *Mlc1*$^{-/-}$ mouse (22), the homozygous *mlc1*$^{-/-}$ zebrafish turned out to be viable and fertile, with the expected mendelian ratio among adult descendants.

Expression pattern of mlc1 in the adult zebrafish brain and retina

We determined the expression pattern of *mlc1* in adult tissues by RT-qPCR (Fig. 4A) and western blot (Fig. 4B). This showed that *mlc1* is mainly expressed in the brain and at reduced levels in the eye. We performed immunofluorescence experiments to determine which cell types express mlc1 in the adult brain, using the *mlc1*$^{-/-}$ zebrafish as a control. Prominent immunoreactivity was observed at the ventricular and pial surface of the brain, and around some blood vessels (Fig. 4C, D, F). Additionally, mlc1 immunoreactivity was observed in radial processes within the brain parenchyma (Fig. 4D). Lack of staining in the *mlc1*$^{-/-}$ zebrafish brain confirmed the specificity of our results (Fig. 4E). Staining of mlc1 in the transgenic line *fli1a:GFP*, which expresses GFP in the vascular endothelium (28), confirmed that the mlc1 protein is present at astrocytic perivascular processes (Fig. 4F). mlc1 staining around brain ventricles and radial-like structures was also positive for glial fibrillary acid protein (gfap) antibody (Fig. 4G and H), indicating that these are astroglial-like cells (29). Thus, expression of mlc1 in the zebrafish brain is very similar to that found in humans.

We also analysed the localization of mlc1 in the retina. High expression of mlc1 was detected at the inner limiting membrane of the retina. Specificity of the antibody was confirmed by lack of staining in *mlc1*$^{-/-}$ zebrafish retina (Fig. 4I and J). Double immunostaining with gfap demonstrated that mlc1 was strongly expressed in Müller glia end-feet in the inner limiting membrane (Fig. 4K). Furthermore, we also observed weak mlc1 and gfap co-expression at fine radial glial processes away from the vitreal surface of the retina (Fig. 4K).

Glialcama localization in the adult brain and retina is affected in mlc1$^{-/-}$ zebrafish

As with *mlc1*, we determined the pattern of expression of *glialcama* using RT-qPCR in adult tissues. mRNA for *glialcama* was more broadly expressed compared with *mlc1*, but showed the highest expression levels in the brain. Detection of glialcama protein in tissue extracts by western blot using a newly developed glialcama antibody (Supplementary Material, Fig. S3D) confirmed its higher expression in the brain (Fig. 5B), and its presence in the eye.

We next addressed the localization of glialcama in brain and retina from wild-type and *mlc1*$^{-/-}$ zebrafish (Fig. 5C and D). Similar to mlc1, we detected strong immunoreactivity to glialcama in radial glial cell bodies and their processes (Fig. 5C and D), which were also positive for gfap (Fig. 5E). In contrast,

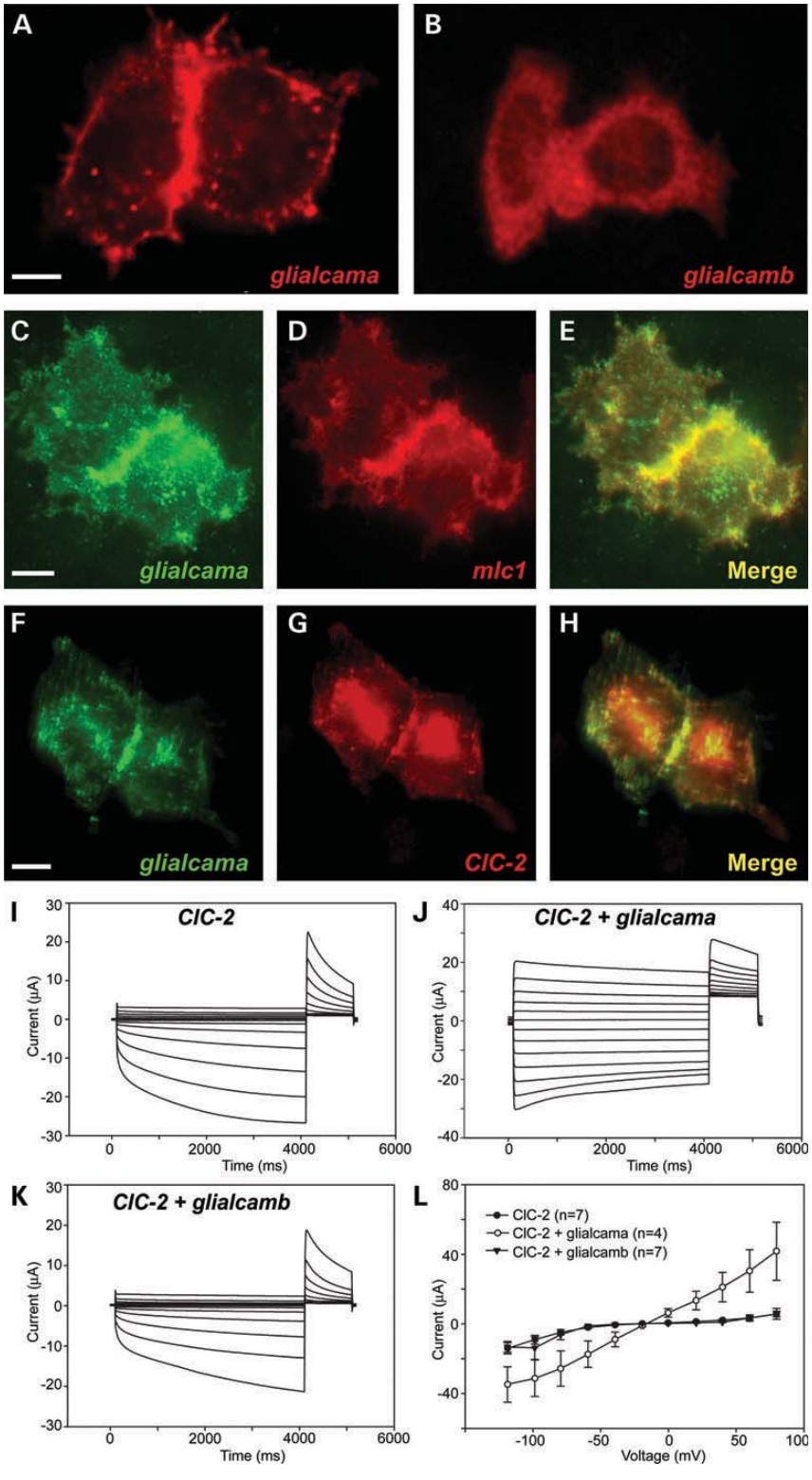

Figure 2. Characterization of the zebrafish orthologues of *Mlc1* and *Glialcam.* (**A** and **B**) *glialcama* and *glialcamb* were transfected separately in HeLa cells and detected through the FLAG epitope with immunofluorescence. While glialcama is specifically located in cell–cell junctions, glialcamb protein presented a diffuse location. Scale bar: 10 μm. (**C**–**E**) Co-transfection of *glialcama* and *mlc1* in HeLa cells reveals their co-localization at cell junctions. Scale bar: 10 μm. (**F**–**H**) Co-transfection of *glialcama* and rat *ClC-2* in HeLa cells reveals their co-localization at cell junctions. Scale bar: 10 μm. (**I**–**L**) A typical current trace mediated by rat ClC2 (I) expressed in oocytes and after co-expression with glialcama (J) or glialcamb (K). Only glialcama is able to modify the functional properties of ClC-2. The apparent inactivation observed sometimes at very negative voltages is an artefact caused by chloride depletion inside the oocytes (J). (L) Average steady-state current–voltage relationship of ClC-2 (black circles) and ClC-2 co-expressed with glialcama (white circles) or with glialcamb (triangles). Glialcama increased ClC-2-mediated conductance and changed its rectification properties.

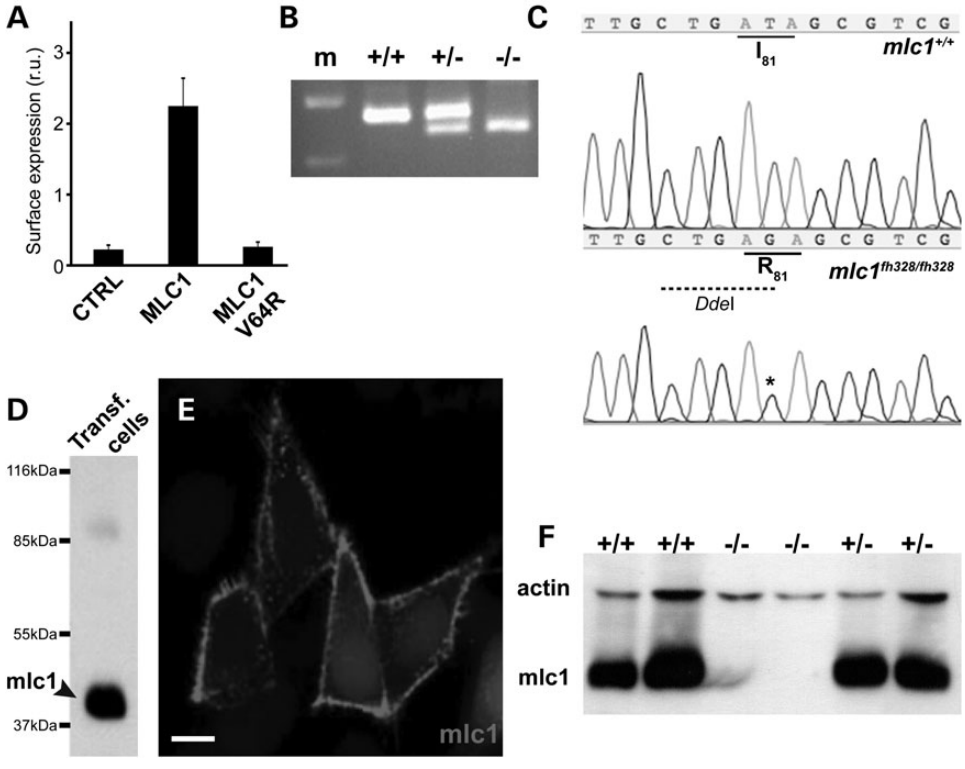

Figure 3. Generation of a zebrafish model for MLC based on the inactivation of mlc1. (**A**) Expression in *Xenopus* oocytes of human MLC1 carrying the V64R mutation abolishes its surface expression, as assayed by detection by an ELISA-based assay. (**B**) Restriction analysis with *Dde*I allows for the identification of wild-type (+/+), heterozygous (+/−) or homozygous mutant (−/−) fish of the *mlc1*^{fh328} allele. m: molecular weight marker. (**C**) Zebrafish *mlc1*^{fh328} allele originates the I81R mutation, and generates a *Dde*I restriction site. (**D** and **E**) Custom-generated antibody against mlc1 detects a protein of the expected molecular weight (around 42 kDa, arrowhead) and its localization in the membrane on *mlc1*-transfected HeLa cells. The band observed at about 85 kDa corresponds to mlc1 dimers. Scale bar (E): 10 μm. (**F**) Western blot of brain extracts from adult wild-type (+/+), heterozygous (+/−) or homozygous mutant (−/−) fish for the *mlc1*^{fh328} allele demonstrates the absence of the mlc1 protein in the homozygous zebrafish.

a more diffuse glialcama staining was observed in the same brain regions in *mlc1*$^{-/-}$ zebrafish (Fig. 5F). We addressed if lack of detection was due to reduced protein expression by western blot using brain extracts, but no changes in protein expression levels were observed (Fig. 5G). We also studied glialcama localization in the retina, as its laminar arrangement could allow easier visualization of subcellular mislocalization. As observed for mlc1, glialcama was highly expressed at Müller glia end-feet at the inner limiting membrane (Fig. 5H and I). This expression was absent in *mlc1*$^{-/-}$ zebrafish. Thus, as we observed in the brain, glialcama was mislocalized in the retina of *mlc1*$^{-/-}$ zebrafish (Fig. 5J).

We can conclude that lack of mlc1 in zebrafish causes glialcama mislocalization in glial cells in the brain and retina, in a similar manner to that found in *Mlc1*$^{-/-}$ mice (22).

Comparison of mouse and zebrafish Mlc1 knockout phenotypes

The phenotypes of Mlc1 mouse and zebrafish knockouts were compared. Histopathology of brain sections from *Mlc1*$^{-/-}$ mice revealed largely restricted myelin vacuolization in fibre tracts of the cerebellum (22). In agreement with these histology results, T_2-weighted MRI of the brain of *Mlc1*$^{-/-}$ mice showed lesions in white matter tracts of the cerebellum from about 6 months of age that increased with age (Fig. 6A and B). Measurement of brain volume revealed that the whole brain is bigger in *Mlc1*$^{-/-}$ than in wild-type mice at the same age (Fig. 6G).

In zebrafish, we analysed the brain of four adult (14 months old) *mlc1*$^{-/-}$ zebrafish by MRI. We only observed very minor lesions in the telencephalon and mesencephalon (Fig. 6C–F) which showed similar relaxation times as cerebrospinal fluid, thus suggesting that they were due to increased fluid. As in mice, measurements of different brain areas revealed that the telencephalon seems larger in comparison with the whole brain in mutant than in wild-type zebrafish (Fig. 6H).

Thus, both animal models showed two typical MLC features: megalencephaly and increased fluid accumulation. However, we failed to observe the presence of vacuoles in any region of the zebrafish brain by general histological procedures (eight different animals; Supplementary Material, Fig. S4A and B) or electron transmission microscopy (four different animals; Supplementary Material, Fig. S4E and F). We conclude that the *mlc1*$^{-/-}$ zebrafish develops less severe lesions than the *Mlc1*$^{-/-}$ mice in the brain, which in turn also develops a less severe phenotype than humans.

As glialcama and mlc1 are co-expressed in Müller cells in the retina, we also studied and compared retina morphology between mice and zebrafish. As in *Mlc1*$^{-/-}$ mice (22), the retina of *mlc1*$^{-/-}$ zebrafish did not show lesions after histological staining (Supplementary Material, Fig. S4C and D). We also

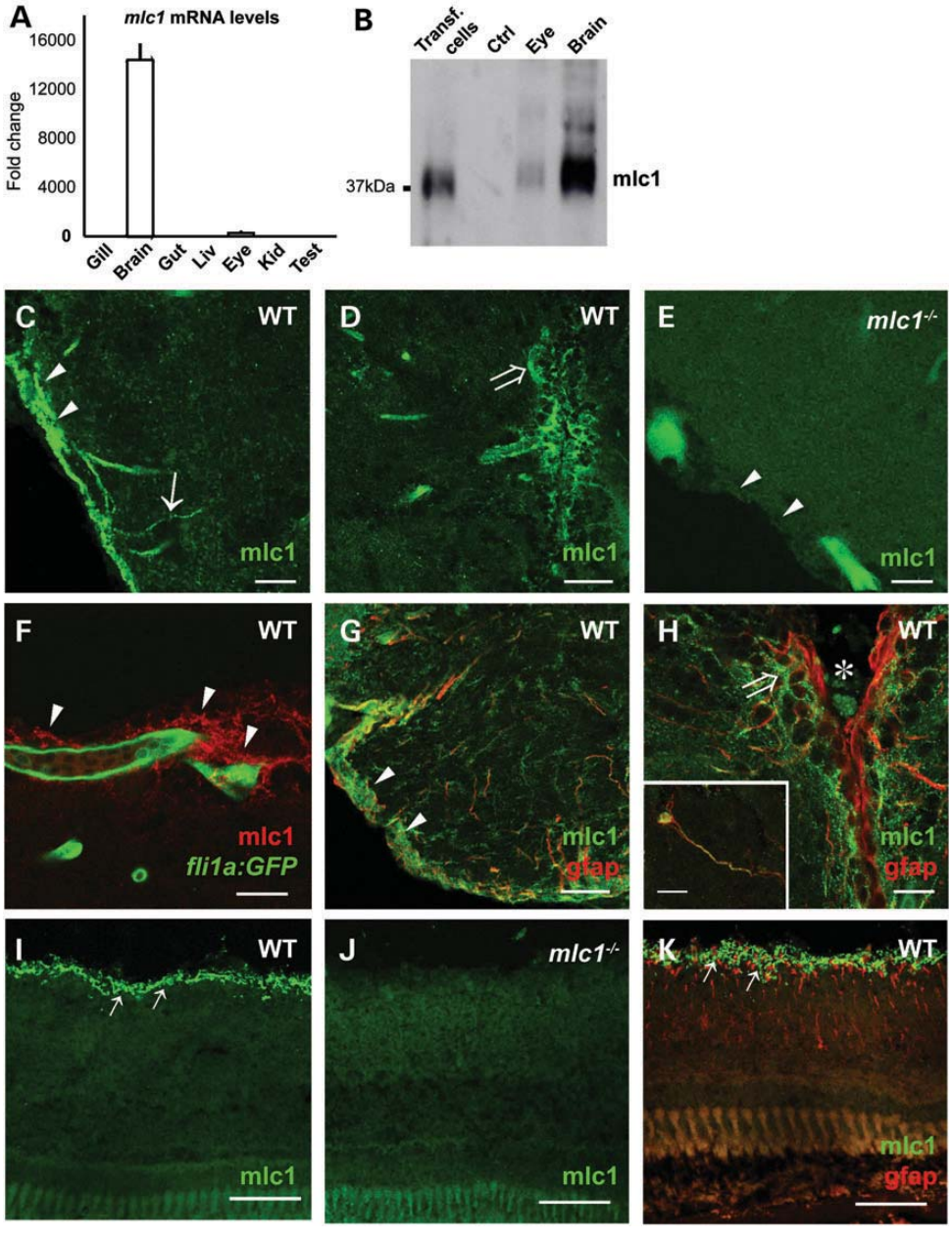

Figure 4. *mlc1* expression and localization pattern in adult zebrafish. (**A**) qPCR with RNA from adult tissues shows the expression of *mlc1* almost exclusively in the brain, and at a lesser level in the eye. (**B**) Western blot with the custom mlc1 antibody shows its expression on the brain and eye. As controls, we used extracts from mlc1-transfected and untransfected HeLa cells. (**C**–**F**) Immunofluorescence detection of mlc1 in the zebrafish adult brain. (C) mlc1 is expressed in radial glia processes (arrow) and pial end-feet (arrowheads). (D) mlc1 expression surrounds the ventricle of the brain (open arrow). (E) No immunoreactivity is observed in *mlc1*$^{-/-}$. Arrowheads point to the pial surface of the brain. Scale bars: 20 μm. (F) Localization of mlc1 (red) in glial perivascular processes (arrowheads) around blood vessels (green) in the brain of a *fli1a::GFP* transgenic zebrafish. Scale bar: 10 μm. (**G** and **H**) mlc1 co-localizes with the astrocytic protein gfap in the zebrafish adult brain at the pial (arrowhead in G) and ventricular surfaces of the brain (open arrow in H). Asterisk labels the ventricle. Scale bars: 15 μm. Inset: gfap and mlc1 co-expression at the cell body and radial processes of an astrocyte located in a subependymal zone. Scale bar: 15 μm. (**I**–**K**) Localization of mlc1 on the retina. (I) mlc1 is expressed in the inner limiting membrane (arrows) of the retina. (J) No immunoreactivity against mlc1 is observed in *mlc1*$^{-/-}$ zebrafish retina. (K) Double immunofluorescence with gfap (red) confirms mlc1 expression (green) in radial glia processes and Müller glia end-feet (arrow) at inner limiting membrane. Scale bars: 100 μm.

evaluated the visual function by recording electro-retinograms (ERG) in *Mlc1*$^{-/-}$ mice and *mlc1*$^{-/-}$ zebrafish (Supplementary Material, Fig. S5). No significant differences of the means of b-wave amplitude between wild-type and *mlc1*$^{-/-}$ fish at any light condition were observed (Supplementary Material, Fig. S5A). The relation of normalized b-wave amplitude and the light intensity (inset in Supplementary Material, Fig. S5A) showed complete overlaps between the two groups, suggesting that the sensitivity in *mlc1*$^{-/-}$ fish does not differ from wild-types. Similar observations have been found in 2-month-old adults (Supplementary Material, Fig. S5B). Similar tests were performed on 1-year-old adult *Mlc1*$^{-/-}$ mice. Analysis of the

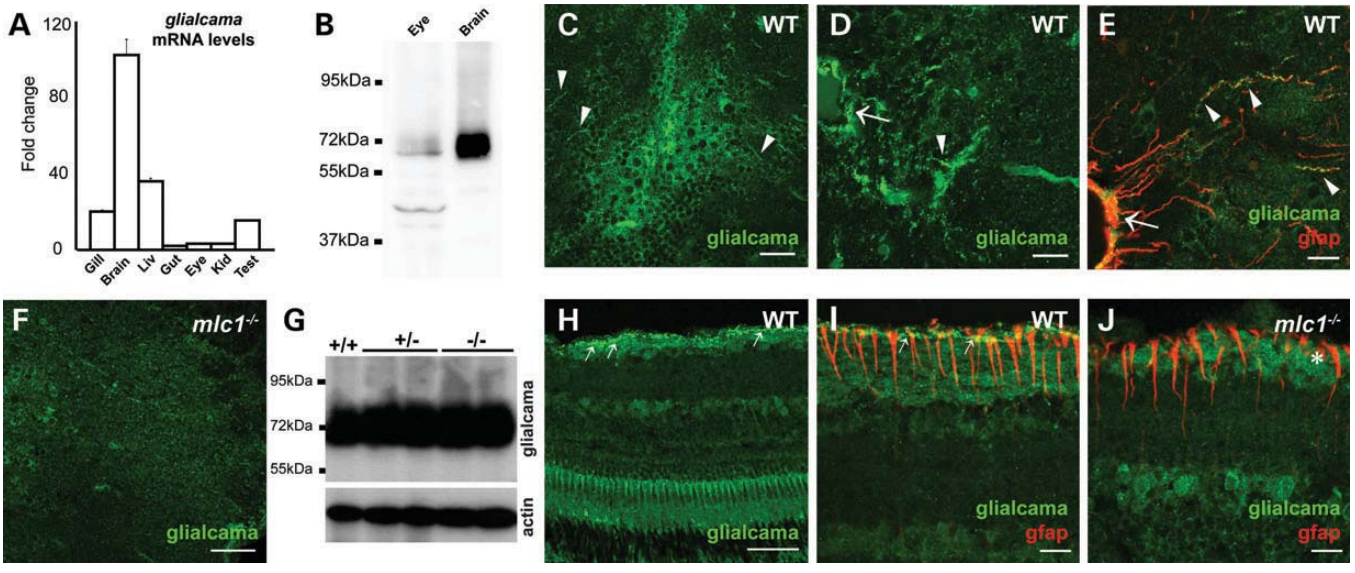

Figure 5. Glialcama is mislocalized in *mlc1*$^{-/-}$ zebrafish. (**A**) qPCR with RNA from adult tissues shows the highest expression of *glialcama* in the brain, but also in other tissues. (**B**) Western blot with the custom antibody shows glialcama expression on the brain and eye. (**C** and **D**) Immunofluorescence detection of glialcama in the zebrafish adult brain. We observed glialcam expression both in radial processes (arrowheads in C and D) and end-feet (arrow in D). Scale bars: 50 μm in (C), 20 μm in (D). (**E**) Co-localization of glialcama (green) and the astrocytic protein gfap (red) at radial glia processes (arrowheads) and end-feet (arrow). Scale bar: 20 μm. (**F**) glialcama signal is more diffuse in the brain of *mlc1*$^{-/-}$ zebrafish. Scale bar: 50 μm. (**G**) Expression levels of glialcama in the brain are not different between wild-type (+/+), heterozygous (+/−) and *mlc1*$^{-/-}$ zebrafish. Actin level was used as a loading control. (**H**–**J**) Localization of glialcama on the retina. (H) Strong expression is observed at the inner limiting membrane (arrows) of the retina in wild-type zebrafish. (**I**) Double immunofluorescence with gfap confirms glialcama expression in Müller glia end-feet (arrows). Note the funnel-like form of Müller glia end-feet. (J) In *mlc1*$^{-/-}$ zebrafish, only a diffuse labelling is observed with no strong expression in the inner limiting membrane (asterisk). Scale bars: 100 μm in (H), 20 μm in (I) and (J).

amplitudes of the different components of the ERG showed no significant differences between wild-type and *Mlc1*$^{-/-}$ mice (Supplementary Material, Fig. S5C).

Human GLIALCAM is also mislocalized in the Bergmann glia of a MLC1 patient

Our studies with *Mlc1*$^{-/-}$ mice and *mlc1*$^{-/-}$ zebrafish have revealed mislocalization of GlialCAM in astrocytes and oligodendrocytes. However, previous studies from a biopsy of a MLC patient indicated that GLIALCAM was not mislocalized around blood vessels in the cortex (13).

We re-examined the localization of GLIALCAM in the cerebellum of this same human brain biopsy. We focused on the cerebellum, as it is more severely affected in *Mlc1*$^{-/-}$ mice (22). As previously shown (13), we could not detect MLC1 in Bergmann glia from the MLC patient (Fig. 7A–F). In addition, staining with GLIALCAM antibodies revealed that it was in fact mislocalized in Bergmann glia in the MLC patient (Fig. 7G–L). Control staining with GFAP revealed that these changes were not due to defects in the integrity of the tissue. Thus, we can conclude that the mislocalization of GLIALCAM caused by the absence of MLC1 is a conserved feature from fish to humans, even though the phenotype is more severe as we climb the evolutionary ladder.

VRAC activity in cultured astrocytes from Mlc1$^{-/-}$ mice is still present

We cultured astrocytes from *Mlc1*$^{-/-}$ mice and analysed GlialCAM localization. Unexpectedly, lack of Mlc1 did not change GlialCAM localization (Fig. 8A–D) and expression (Fig. 8E) in *Mlc1*$^{-/-}$ astrocyte cultures. This result agreed with previous experiments that showed that knocking down Mlc1 in rat astrocytes changed neither the expression nor the localization of GlialCAM in cell junctions (13).

As MLC1 have been related with the activity of VRAC (14,15), we analysed chloride currents in Mlc1$^{-/-}$ astrocyte cultures. In wild-type and *Mlc1*$^{-/-}$ astrocytes, replacing intra- and extracellular Na^+ and K^+ ions with Cs^+ (to block sodium and potassium currents) and with symmetric Cl^-, the whole-cell background conductance was very low (Fig. 8F). In both type of astrocytes, hypotonicity challenge promoted a large, reversible increase in ramp current in the whole range of membrane potentials (Fig. 8F and Supplementary Material, Fig. S6A and C). These hypotonicity-activated currents reversed at ∼0 mV, were blocked by the specific VRAC inhibitor 4-(2-butyl-6,7-dichlor-2-cyclopentylindan-1-on-5-yl) oxobutyric acid (DCPIB) (30), and showed instantaneous activation and time-dependent inactivation at more positive potentials (Fig. 8F and Supplementary Material, Fig. S6A–D). These data indicated that hypotonicity-activated VRAC channels in wild-type and *Mlc1*$^{-/-}$ mouse astrocytes which are functionally identical to those described in rat astrocytes (31,32). The observation that the putative ClC-2 inhibitor cadmium (33) did not affect the hypotonicity-activated currents (Supplementary Material, Fig. S6E and F) strongly indicated that these Cl^- currents were not mediated by ClC-2, which is also present in mouse astrocytes (34). Comparison of VRAC amplitudes between wild-type and *Mlc1*$^{-/-}$ astrocytes indicated that VRAC was slightly reduced in astrocytes obtained from *Mlc1*$^{-/-}$ mouse (Fig. 8G). These results support the view that Mlc1 does not mediate directly

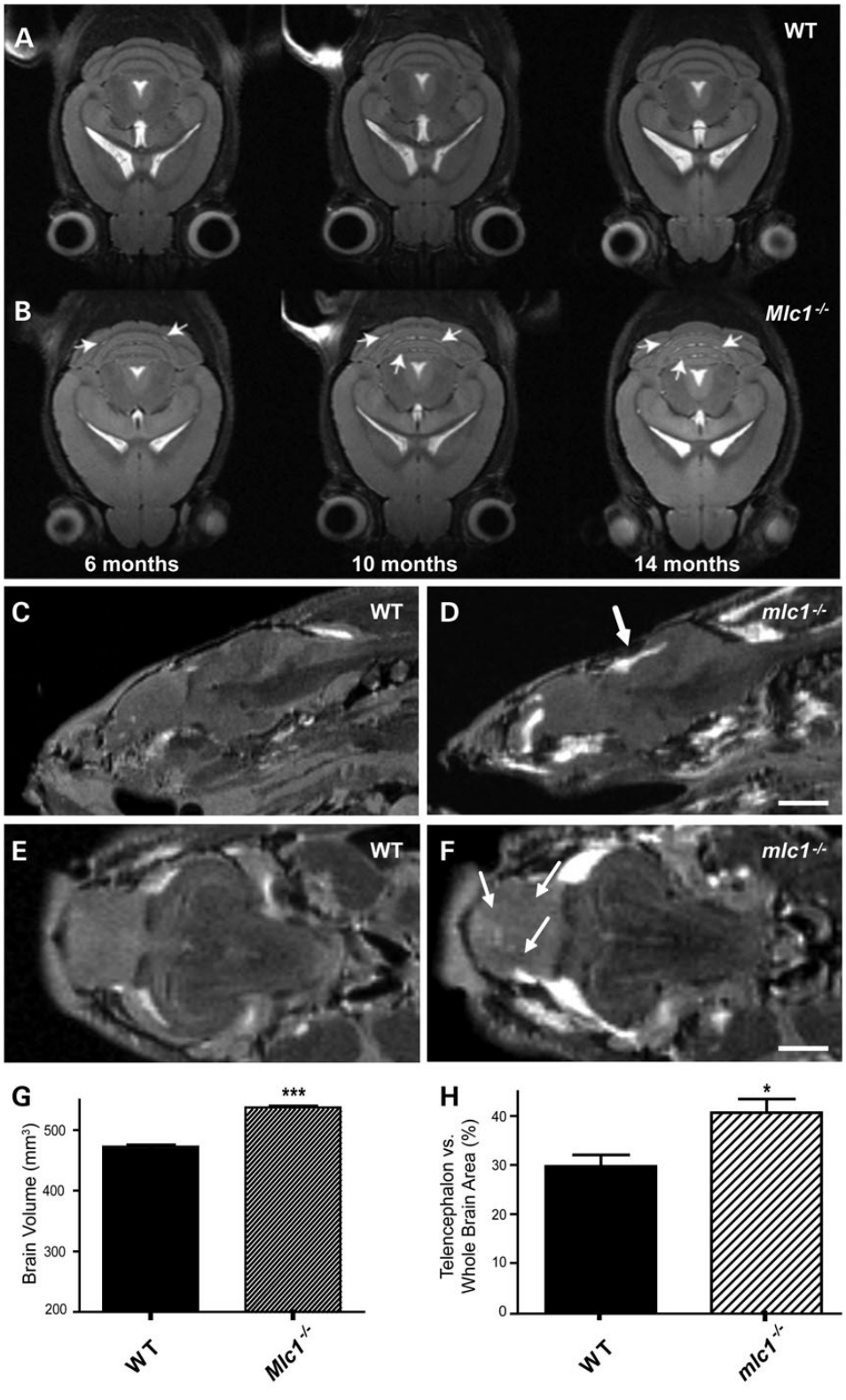

Figure 6. MRI of *Mlc1*$^{-/-}$ mice and *mlc1*$^{-/-}$ zebrafish. (**A** and **B**) MRI of mice from different ages show progressive presence of white matter lesions (arrows) in the cerebellum of *Mlc1*$^{-/-}$ animals (B), but not in wild-type mice (A). (**C**–**F**) MRI of adult zebrafish reveals the presence of small lesions in the mesencephalon (thick arrow in D) and telencephalon (arrows in F) in *mlc1*$^{-/-}$ zebrafish. Hyperintense signals in (D) and (F) may correspond to fat containing tissue in or around the brain. (C) and (E) correspond to images from wild-type zebrafish. Scale bars: 1 mm in (C) and (D), 500 μm in (E) and (F). (**G**) Brain volume is higher in *Mlc1*$^{-/-}$ mice. Brain volume was estimated by quantifying the area of consecutive MRI images using ImageJ. Data correspond to seven wild-type and seven *Mlc1*$^{-/-}$ mice ($P < 0.0001$). (**H**) Telencephalon appears bigger relative to the whole brain in *mlc1*$^{-/-}$ zebrafish ($P < 0.05$).

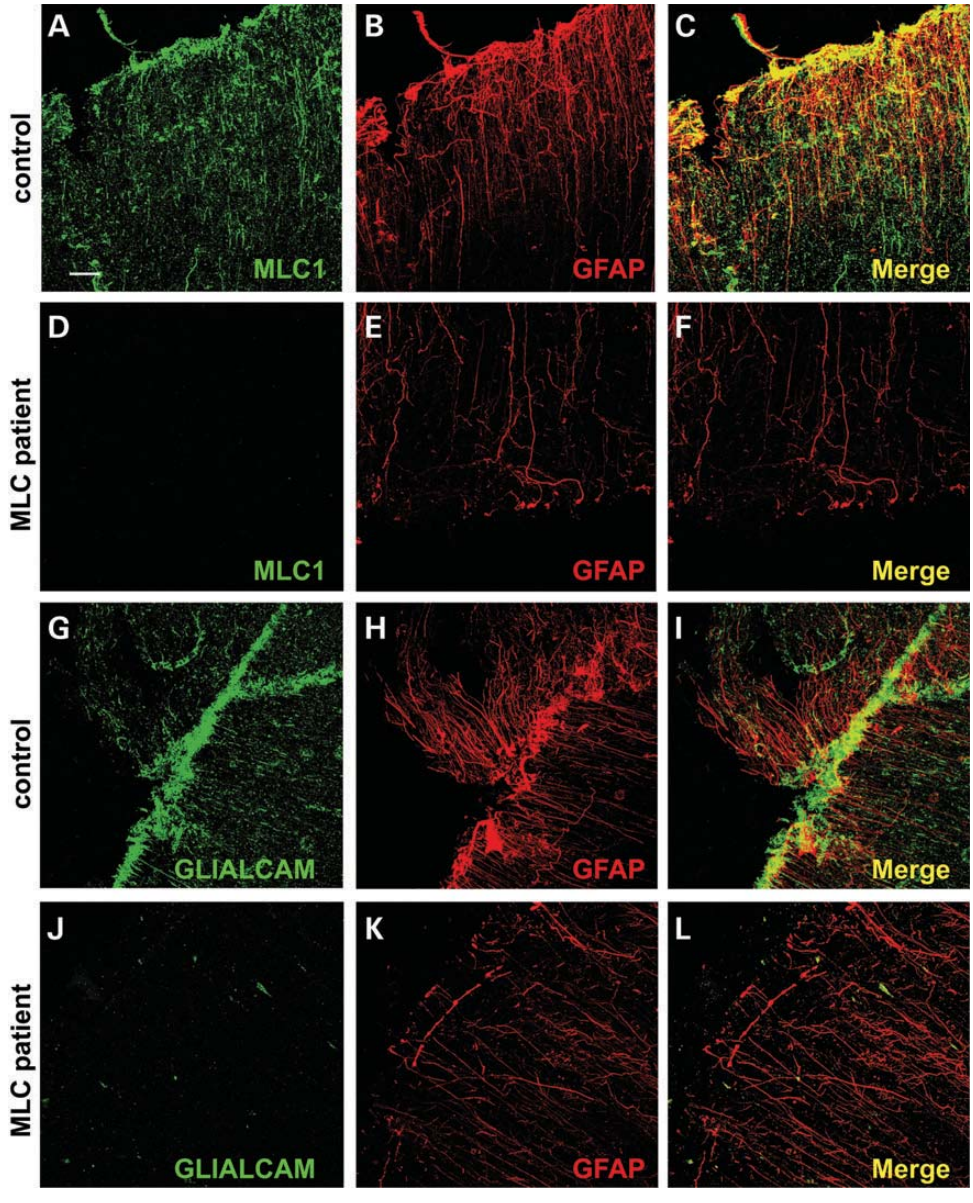

Figure 7. GLIALCAM is mislocalized in the cerebellum of a patient with a missense mutation in *MLC1*. (**A**–**F**) Immunofluorescence detection of MLC1 and GFAP proteins in the cerebellum of a control subject (A–C) and an MLC patient (D-F) carrying a homozygous mutation in *MLC1* shows the absence of the MLC1 protein in the patient. Scale bar: 40 μm. (**G**–**L**) Immunofluorescence detection of GLIALCAM and GFAP proteins in the cerebellum of a control subject (G–I) and an MLC patient (J–L) carrying a homozygous mutation in *MLC1* shows the diffuse signal for GLIALCAM in the absence of MLC1.

VRAC current. To detect whether the non-statistically significant VRAC reduction may lead to astrocyte vacuolation, we stained wild-type (Fig. 8H) and *Mlc1*$^{-/-}$ astrocytes (Fig. 8I) with the freely diffusible fluorescent reagent calcein. Vacuoles were more frequently observed in *Mlc1*$^{-/-}$ astrocytes (Fig. 8J).

Glialcam localization is dependent on Mlc1 with high extracellular potassium concentration

Why is GlialCAM mislocalized in *Mlc1*$^{-/-}$ astrocytes in tissue and not in culture? Mislocalization of GlialCAM in humans was better observed in Bergmann glia, which are bathed in a high extracellular potassium concentration due to cerebellar neuronal activity (35). Thus, we treated cultured astrocytes obtained from wild-type and *Mlc1*$^{-/-}$ mice with physiological medium or with an isosmotic solution with higher potassium concentration, mimicking neuronal activity. In wild-type astrocytes under high potassium concentration, there was no change on the localization of Mlc1 (Fig. 9A–D), but there was a slight increase of GlialCAM in cell junctions. When similar experiments were repeated in astrocytes from *Mlc1*$^{-/-}$, GlialCAM was detected intracellularly after high-potassium treatment (Fig. 9E–H). This effect was even more evident when astrocytes were infected with adenoviruses expressing human Flag-tagged GLIALCAM (Fig. 9I–L). Control staining with the junctional marker β-catenin revealed that these distribution changes caused by increasing extracellular potassium were specific to GlialCAM (Fig. 9M–P).

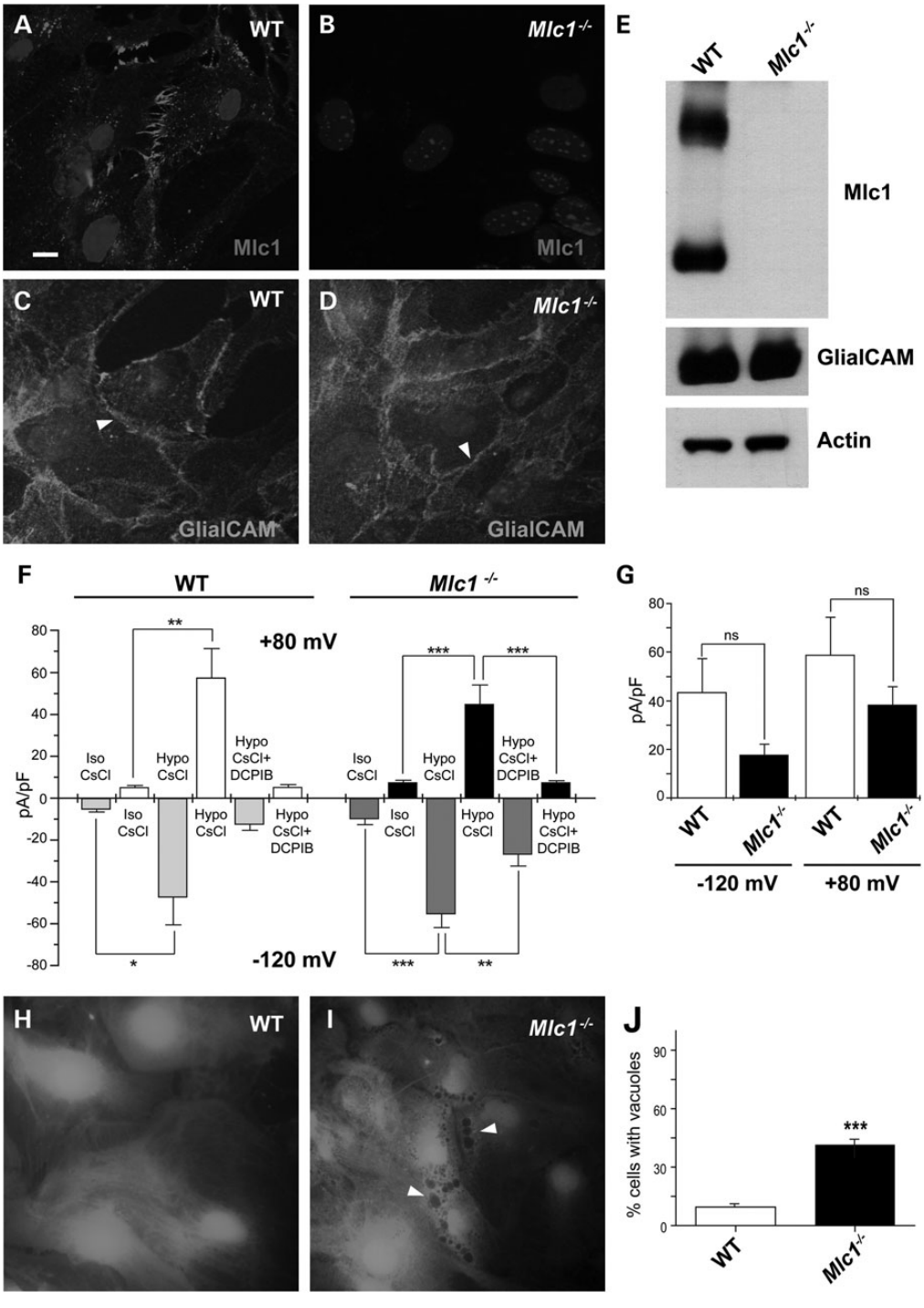

Figure 8. Cultured *Mlc1*$^{-/-}$ astrocytes do not show mislocalization of Glialcam and still present a VRAC response. (**A** and **B**) Immunofluorescence detection of Mlc1 in cultured astrocytes from newborn pups confirms the absence of the Mlc1 protein in *Mlc1*$^{-/-}$ mice. (**C** and **D**) Immunofluorescence detection of Glialcam in cultured astrocytes from newborn pups shows that Glialcam protein is present in cell junctions in *Mlc1*$^{-/-}$ mice, unlike it is seen *in vivo*. Scale bar: 10 μm. (**E**) Western blot of brain extracts show no difference in Glialcam protein levels between wild-type and *Mlc1*$^{-/-}$ mice. (**F** and **G**) Depression of the hypotonicity-evoked chloride current with the Volume Regulated Anion Channel (VRAC) inhibitor DCPIB in wild-type (WT) and *Mlc1*$^{-/-}$ mouse cultured astrocytes. (F) Bar graph of membrane current densities (mean ± SEM) at +80 mV (upper bars) and −120 mV (lower bars) measured in isotonic (Iso CsCl) and hypotonic conditions (Hypo CsCl) and after addition of DCPIB (10 μM) to the hypotonic solution (Hypo CsCl + DCPIB) in wild-type ($n = 9$) and *Mlc1*$^{-/-}$ ($n = 17$) astrocytes. Statistical significance was calculated using paired two-tailed Student's *t*-test; $^{*}P < 0.05$, $^{**}P < 0.01$, $^{***}P < 0.001$. (G) Bar graph of DCPIB-sensitive currents (mean ± SEM) induced by hypotonic challenge at −120 and +80 mV in wild-type ($n = 7$) and *Mlc1*$^{-/-}$ ($n = 7$) mouse astrocytes. Differences in current densities were not significant (ns). (**H** and **I**) Typical pictures of astrocytes obtained from wild-type (H) and *Mlc1*$^{-/-}$ (I) mice. Arrowheads point to vacuoles observed mostly in *Mlc1*$^{-/-}$ astrocytes. (**J**) Quantification of the number of cells containing vacuoles. A cell was positive for vacuolation if have at least three vacuoles of a size bigger than 0.5 μm. Scale bar: 10 μm.

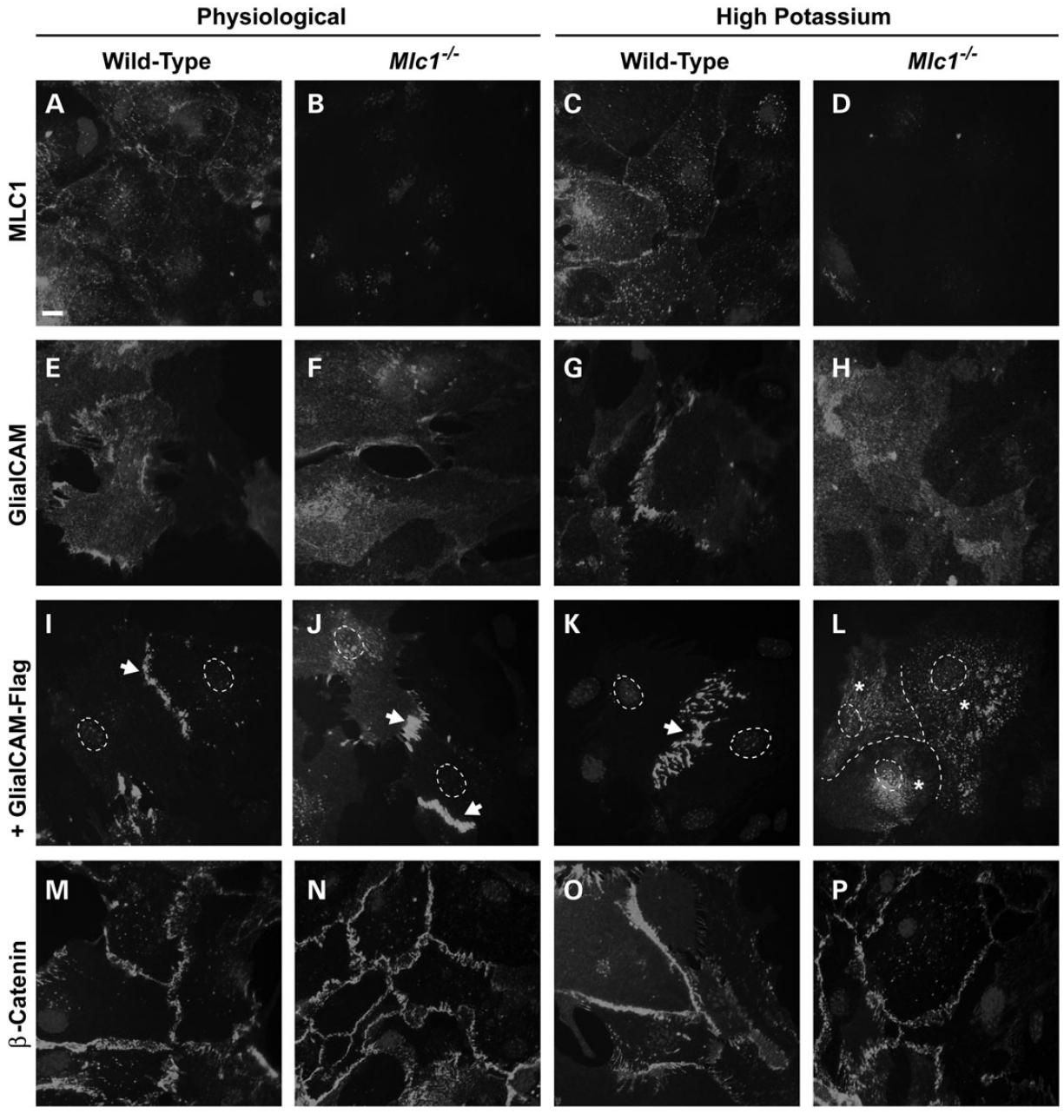

Figure 9. Glialcam localization to astrocyte junctions depends on Mlc1 and the presence of high extracellular potassium concentration. (**A**–**D**) Mlc1 localization in cell junctions in cultured mouse astrocytes do not change between physiological conditions or high extracellular potassium exposure. Scale bar: 10 μm. (**E**–**H**) Glialcam localization in cell junctions in cultured mouse astrocytes is lost when *Mlc1*$^{-/-}$ astrocytes are subjected to 6 h treatment with high extracellular potassium. Four independent experiments gave similar results. (**I**–**L**) Adenoviral-mediated expression of human Flag-tagged GLIALCAM in wild-type and *Mlc1*$^{-/-}$ cultured mouse astrocytes confirms the effect of the high extracellular potassium concentration on GlialCAM localization in cell junctions (arrows) in the absence of Mlc1, when it is found almost exclusively in the cytoplasm (asterisks). Dotted line in (L) labels the junctions between three adjacent astrocytes. Four independent experiments gave similar results. (**M**–**P**) High extracellular potassium concentration does not alter of the localization of a control junctional protein (β-catenin) in cultured mouse astrocytes.

DISCUSSION

We have analysed two animal models (zebrafish, mice) lacking MLC1 protein and compared them with a brain biopsy from an MLC patient. In all cases, localization of GlialCAM at cell junctions is abolished by lack of MLC1. In cultured mouse astrocytes from *Mlc1*$^{-/-}$, this effect is only observed when mimicking neuronal activity.

Despite the fact that *Mlc1* is one of the most astrocyte-specific genes (36,37) and its mutation leads to MLC (3), its precise function is still unknown. As MLC1 is a membrane protein with low homology to ion channels, a possible role as a channel or transporter has been suggested (6). However, no such function has been found so far. RNA interference experiments of *Mlc1* in cultured astrocytes indicated that it may be a component or regulator of VRAC (14,15). Here, we demonstrate that VRAC activity is

still present in the absence of Mlc1. We conclude that MLC1 may affect VRAC activity in an indirect manner and is not a molecular component of VRAC. In agreement with this hypothesis, very recently it has been demonstrated that VRAC activity is mediated by LRRC8 heteromers (38,39). Further work will be needed to define the biochemical relationship between MLC1/GlialCAM and LRRC8 proteins.

Further insight into MLC1 biology came from the finding that another MLC-causing gene, which encodes the cell adhesion molecule GLIALCAM (4), is necessary for stabilizing and targeting MLC1 to astrocyte junctions (4,15). In contrast, GLIALCAM targeting *in vitro* was independent of MLC1 (19,13). However, recent work performed with *Mlc1*$^{-/-}$ and *GlialCAM*$^{-/-}$ mice demonstrated that both mutants reproduce MLC symptoms and that Mlc1 is necessary for GlialCAM localization (22).

We decided to expand the repertoire of MLC animal models to solve this contradiction. We have characterized the orthologues of *MLC1* and *GLIALCAM* in zebrafish. The zebrafish (and other teleost fishes) genome contains two *glialcam* paralogues of which only *glialcama* behaves as mammalian *Glialcam* in terms of subcellular localization and modulation of the chloride channel ClC-2 (24). Both mlc1 and glialcama show a similar expression pattern in the brain as murine Mlc1 and Glialcam (4). mlc1 and glialcama are localized to glial cells especially around brain barriers, radial glia processes and end-feet, and also in Müller glia of the retina.

We have generated a zebrafish line carrying a mutation in *mlc1* that abrogates its protein expression. However, the conservation of *mlc1* in zebrafish does not translate into a severe MLC-like phenotype. We could only detect minor lesions and megalencephaly in the brain of *mlc1*$^{-/-}$ zebrafish by MRI, but not myelin vacuolization even in fish older than 1 year. Although in humans MLC is evident during the first year of life (1), mouse knockout models of both *Glialcam* and *Mlc1* did not present vacuolization during their firsts months of life (22). This difference could reflect their heterochrony of myelination, and that MLC manifests when myelination is at its highest level (1). Zebrafish show regular compact myelin (40), but protein composition differs: P_0 is the major component of CNS myelin, rather than PLP, like in mammals (41). In the transition from an aquatic to a terrestrial environment, there was a switch from P_0 to PLP as the major CNS myelin protein, which provided more neuroprotection (42). Myelination in zebrafish larvae starts at 3 days post-fertilization (dpf), and *myelin basic protein* expression increases at least till 29 dpf (43), but new myelin deposition has been reported in trout even older than 1 year (44). Another significant difference with mammalian brains is the capacity of the adult zebrafish brain for neurogenesis (45) and even repair after injury (46). This is linked to the capacity for re-myelination (47,48). Therefore, it is possible to speculate that zebrafish are able to repair myelin sheath damage produced by the lack of mlc1 protein, so vacuolization never reaches a detectable stage by means of histological methods.

Absence of mlc1 in zebrafish brain leads to the misslocalization of glialcama, as we observed in *Mlc1*$^{-/-}$ mice. This prompted us to re-examine a human MLC biopsy. We found similar results in the cerebellum of the MLC patient. Thus, the reciprocal relationship between MLC1 and GlialCAM for their correct membrane localization has been conserved throughout evolution. This relationship also explains the fact that mutations in either *MLC1* or *GLIALCAM* cause a similar phenotype in MLC1 and MLC2A patients (21).

It has been well described that MLC1 depends on GLIAL CAM for exiting the endoplasmatic reticulum and reaching its junctional localization (15). However, a question remains: why does GLIALCAM mislocalize in the absence of MLC1 *in vivo*? We believe that MLC1 is not working as a chaperone of GLIALCAM, as GLIALCAM *in vitro* is able to traffic to cell junctions in the absence of MLC1. In agreement with this hypothesis, GlialCAM mislocalization in *Mlc1*$^{-/-}$ astrocytes in culture only appeared when mimicking neuronal activity by an increase in extracellular potassium. Thus, differences between *in vivo* and *in vitro* effects of MLC1 on GlialCAM localization may be due to the presence of interacting molecules *in vivo* that are not present in culture.

We also suggest that GlialCAM/MLC1 may have a role in the process of potassium siphoning by glial cells. As a result of neuronal electrical activity, potassium is released in order to repolarize the membrane potential, and this excess of potassium needs to be disposed of in a process known as 'potassium siphoning' (49). Glial cells surrounding neurons take up potassium by Kir4.1 channels and then transfer it through Connexin junctions to the astrocytic end-feet surrounding blood vessels, where it is eliminated. Ablation of Kir4.1 (50) or Connexins 32 and 47 (51) results in leukodystrophy characterized by water accumulation in myelin. Work with *Mlc1*$^{-/-}$, *GlialCAM*$^{-/-}$ and *Clcn2*$^{-/-}$ mice models (22,60) and the identification of mutations in *CLCN2* in human patients with leukodystrophy (26) have suggested that the chloride channel ClC-2 may also have a role in potassium-coupled chloride influx. In this sense, GlialCAM changes the rectification of the ClC-2 channel (24), allowing chloride influx at depolarized voltages. Interestingly, new studies with ClC-2 from *C. elegans* have also shown that the primary role of ClC-2 is to mediate chloride influx but not efflux (52). Unfortunately, the precise role of MLC1 in this process is still not known. However, based on these studies, we can speculate that it may have a regulatory role controlling the surface expression of GLIALCAM, which may be needed to regulate in turn the activity of CLC-2. Possibly, the severity of the phenotype caused by the depletion of Mlc1 from fish to mouse and human could be explained based on differences in neuronal activity between species, making Mlc1 or Glialcam more necessary to keep ionic homeostasis in the possibly more active human CNS.

In summary, our work show that the functional relationship between the two proteins causing MLC in vertebrates is evolutionary conserved. We have also increased the diversity of vertebrate animal models for this disease that can offer further insights into the molecular interactions between these two proteins. Our work also explains the similarity of phenotypes caused by mutations in either gene. More importantly, we uncovered a role for MLC1 in GlialCAM localization at astrocyte junctions in the presence of neuronal activity, offering new mechanistic insights into the pathophysiology of MLC.

MATERIALS AND METHODS

Zebrafish maintenance

AB or AB/TL strains were used in all the experiments. Adult fish were maintained in the animal facility at the University of

Barcelona, School of Medicine in Bellvitge Campus, under the standard culture conditions: 28°C, 14 h/10 h light/dark period (53). All experimental procedures conformed to the European Community Guidelines on Animal Care and Experimentation and were approved by animal care and use committees.

The *mlc1*^{fh328} allele was obtained from the laboratory of Dr Cecilia Moens, as a result of an ENU-based TILLING screening (62). The mutant line was generated in an *islet1::GFP* background, which was eliminated by out-crossing to AB wild-type fish. Similarly, two other embryonic recessive lethal phenotypes that were not linked to *mlc1*^{fh328} were eliminated by pair-wise mating and out-crossing. The *mlc1*^{fh328} mutation is a T/G transversion in *mlc1* exon 3 that generates a novel *Dde*I restriction site (CTNAG), which was used for genotyping after amplifying the corresponding fragment of genomic DNA by PCR. The following oligonucleotides were used: TAAATGTGTCTATCTG TATCTGACCGTCAG (underlined is a mutation introduced to eliminate an endogenous *Dde*I restriction site, 16 nucleotides upstream from the *Dde*I restriction site generated by the mutation) and TACTCTGCAAGCCAAAAGCA. Genomic DNA was obtained from tail clipping and extraction by Nucleo Spin Tissue kit (Macherey-Nagel).

Mlc1 knockout mice

Mlc1$^{-/-}$ mice were generated by ICS (Institut Clinique de la Souris, Strasbourg, France) as described previously (22).

Human samples

The MLC patient sample analysed here was already reported (13). Briefly, she carried a homozygous mutation in the *MLC1* gene, resulting in an amino acid change (p.S69L) that leads to the reduced stability of the MLC1 protein and its practical absence.

Molecular biology

Plasmids used were constructed using standard molecular biology techniques employing recombinant PCR and the Multisite Gateway system (Invitrogen). The integrity of all cloned constructs was confirmed by DNA sequencing. For localization studies in HeLa cells, proteins were C-terminally fused to the FLAG epitope or HA-tagged and cloned into the pcDNA3 vector (Invitrogen).

RT-PCR

Adult zebrafish were euthanized using an overdose of tricaine (MS222, Sigma), and tissues were quickly dissected and flash-frozen in liquid nitrogen. Total RNA was isolated with TRIZOL (Life Technologies) and retro-transcribed (RT-PCR) using random hexamers with SuperScript III system (Life Technologies). The following oligonucleotides pairs were used for qPCR: GCACGTTCAGTGGACAACTG and CACAATCATT GGGCCTTCAG (*mlc1*), CCCACCCACCAAGACTAAGC and CATCCTCAGTCGTGCTCATCTG (*glialcama*), and as internal controls (54): CTGGAGGCCAGCTCAAACAT and ATCAAGAAGAGTAGTACCGCTACCATTAC (*ef1a*), TCT GGAGGACTGTAAGAGGTATGC and AGACGCACAATC TTGAGAGCAG (*rpl13a*). qPCR was performed with SYBR Select reagent (Life Technologies) in a StepOne apparatus (Life Technologies). The expression levels were calculated using the comparative C_t method normalized to the internal control genes. The final results were expressed as the relative RNA levels as indicated in the corresponding figures, taking into account the efficiency of each primer pair with the Pfaffl method (55).

Generation of custom antibodies against zebrafish proteins

Immune sera against synthetic peptides from zebrafish mlc1 (QREEASAQEVFSYAQMST, corresponding to amino acids 2–19, in green in Supplementary Material, Fig. S1B) and zebrafish glialcama (EDPPTDGENTMHHHSLPR, corresponding to amino acids 405–422, in green in Supplementary Material, Fig. S2B) were raised in rabbits using the services provided by Eurogentec. The peptide was coupled to keyhole limpet haemocyanin via a cysteine residue that has been added to the N-terminal end of the peptide for mlc1 and to the C-terminal of the peptide for glialcama. After four boosts of immunization, the antisera were affinity purified using the peptide covalently coupled to Sulpholink (Pierce). The polyclonal antibodies were tested by immunoblotting and immunofluorescence on HeLa cells expressing mlc1 or glialcama and on zebrafish brain tissue.

Cell culture and immunofluorescence microscopy

HeLa cells were grown on DMEM containing 10% (v/v) fetal bovine serum (Sigma) and 1% penicillin/streptomycin at 37°C in a humidity controlled incubator with 10% CO_2. Cells were cultured and transfected with the Transfectin reagent (BioRad). Twenty-four hours after transfection, the cells were splitted and transferred into glass-covered petri dishes in which experiments were performed after further 24–48 h. To detect expressed proteins, immunofluorescence staining of cells was performed. They were fixed with phosphate-buffered saline (PBS) containing 3% paraformaldehyde for 15 min, blocked and permeabilized with 10% FBS and 0.1% Triton X-100 in PBS for 2 h at room temperature (RT). Primary antibodies were diluted in the same solution and incubated overnight at 4°C. Cells were washed and incubated for 2 h at RT with secondary antibodies. Cover slips were mounted in Vectashield medium (Vector Laboratories) with 1.5 μg/ml DAPI (Sigma) and visualized using an Olympus DSU spinning disk confocal.

Images were analysed using ImageJ. Pairs of cells were analysed manually and quantified as being in junctions or not being in junctions (around the plasma membrane or intracellular). Intensity profile analysis was used to discern the localization.

Histological staining methods

For immunofluorescence in zebrafish, individuals were deeply anaesthetized in 0.1% tricaine (MS222, Sigma) in fresh water, and then transcardiacally perfused with 4% paraformaldehyde. Fish heads were post-fixed for 24 h at RT. Then brains and eyes were dissected out, cryoprotected and frozen with liquid

nitrogen-cooled methylbutane. Transverse sections (12 μm thick) were cut on a cryostat and mounted onto gelatinized slides.

Sections were rinsed in PBS and pre-incubated with normal goat serum (Sigma, 1:100) for 1 h. Next, they were incubated with a primary antibody or a cocktail of primary antibodies overnight at room temperature. Antibody dilutions used were: rabbit anti-zebrafish mlc1, 1:100; rabbit anti-zebrafish glialcama, 1:100; mouse anti-gfap (ZIRC), 1:500; rat anti-GFP (Nacalai Tesque), 1:1000. After PBS washes, sections were incubated with secondary fluorescent antibodies (Alexa Fluor 488 or 568, 1:500, Invitrogen) for 1 h. After additional PBS washes, sections were mounted using the glycerol-based mounting medium.

For haematoxylin–eosin staining, we used paraffin sections from tissue fixed in Bouin's fixative. Sections were de-waxed and stained using Meyer's haematoxylin followed by eosin. Sections were dehydrated and mounted for imaging.

Zebrafish sections were observed and photographed either under a laser scanning confocal microscope (Nikon A1R) or a bright-field microscope (Nikon E100). Images were adjusted for brightness and contrast with Adobe Photoshop or Corel Photopaint, and they were assembled with Adobe Illustrator.

Human samples were processed and analysed as described previously (13).

Electron microscopy

For electron immunogold experiments, small samples of brain mice tissue were obtained and fixed in 4% paraformaldehyde and 0.1% glutaraldehyde in 0.12 M phosphate buffer, and processed. They were cryoprotected gradually in sucrose and cryofixed by immersion in liquid propane. Freeze substitution was performed at −90°C during 3 days in an Automatic Freeze Substitution System (AFS, Leica); methanol containing 0.5% uranylacetate was used as a substitution medium. Infiltration was carried out in Lowicryl HM20 at −50°C and then polymerized with UV light. Ultrathin sections were collected, and when needed, processed for post embedding immunostaining. For immunostaining, grids were incubated with rabbit anti-Mlc1 (1:10) or mouse anti-GlialCAM (1:10) antisera. The binding of the primary antibody was visualized by incubating with a secondary antibody conjugated to 18 nm gold particles (British BioCell, International). Ependymal cells were recognized by their epithelial location, presence of microvilli and cilia, and high density of organelles in the cytoplasm. Astrocytic processes showed a cytoplasm light appearance with the presence of some fibrils and a very few number of organelles (56).

For electron microscopy of zebrafish myelin sheaths, zebrafish were anaesthetized and transcardially perfused using 4% paraformaldehyde and 0.1% glutaraldehyde in 0.1 M cacodylate buffer with 0.5% calcium chloride. Small pieces of tissue were post-fixed in the same fixative (2 h) and then in 1% osmium tetroxide—with 1.5% potassic ferrocyanide (2 h). Tissue was then dehydrated and included in an epoxy resin. Semithin and thin sections were obtained using an ultramicrotome, mounted and imaged in an electron transmission microscope.

Astrocyte cultures from wild-type and Mlc1$^{-/-}$ mice

Mouse astrocyte cultures were performed as previously described from P0 to P2 mouse pups of the corresponding genotype (16). Calcein stainings were performed by treating the astrocytes with Calcein-AM 2 μM (Life Technologies) for 10 min and then with physiological solution (122 mM NaCl, 3.3 mM KCl, 0,4 mM $MgSO_2$, 1.3 mM $CaCl_2$, 1.2 mM KH_2PO_4, 25 mM Hepes, 10 mM glucose, pH 7.2, 300 mOsm/kg). In some experiments, astrocytes were treated for 6 h with physiological solution or high potassium medium (60 mM NaCl, 60 mM KCl, 0.4 mM $MgSO_2$, 1.3 mM $CaCl_2$, 1.2 mM KH_2PO_4, 25 mM Hepes, 10 mM glucose, pH 7.2, 300 mOsm/kg), to mimic neuronal activity. Then, they were fixed in 4% PFA and processed for immunofluorescence as described above.

Mouse magnetic resonance imaging

Mouse MRI experiments were conducted on a 7.0T BioSpec 70/30 horizontal animal scanner (Bruker BioSpin), equipped with a 12 cm inner diameter actively shielded gradient system (400 mT/m) in at least seven animals of the same age. Receiver coil was a phased array surface coil for mouse brain. Animals were placed in a supine position in a Plexiglas holder with a nose cone for administering anaesthetic gases (isofluorane in a mixture of 30% O_2 and 70% CO_2), fixed using a tooth bar, ear bars and adhesive tape. Tripilot scans were used for accurate positioning of the animal's head in the isocentre of the magnet.

High-resolution T_2-weighted images were acquired by using TurboRARE (rapid acquisition with rapid enhancement) sequence applying repetition time of 2969 ms, echo time of 36 ms, RARE factor = 8, 10 averages, slice thickness = 0.3 mm, number of slices = 25 for horizontal view, 25 coronal slices, field of view = 25 × 25 mm, matrix size = 240 × 240 pixels, resulting in a spatial resolution of 0.104 × 0.104 mm in 0.3 mm slice thickness.

T_2 relaxometry maps were acquired with multislice-multiecho (MSME) sequence by applying 16 different TEs, from 11 to 176 ms, TR = 4764 ms, slice thickness = 0.5 mm, number of coronal slices = 18, FOV = 20 × 20 mm and matrix size = 256 × 256 pixels, resulting in a spatial resolution of 0.078 × 0.078 mm in 0.5.00 mm slice thickness.

Zebrafish magnetic resonance imaging

Magnetic resonance microimaging (μMRI) of zebrafish was performed on a vertical wide-bore 9.4T Bruker Avance 400WB spectrometer, with a 1000 mT/m actively shielded imaging gradient insert (Bruker Biospin GmbH). A birdcage RF coil with an inner diameter 1 cm was used for excitation and detection. The system was interfaced to a Linux PC running Topspin 2.0 and Paravision 5.0 software (Bruker Biospin GmbH). For μMRI, adult zebrafish were euthanized and fixed in 4% buffered paraformaldehyde (Zinc Formal-Fixx, ThermoShandon) for 3 days and subsequently embedded in Fomblin. Before each μMRI measurement, the magnetic field homogeneity was optimized by shimming. Each session of measurements began with a multislice orthogonal gradient-echo sequence for position determination and selection of the desired region for subsequent experiments. High-resolution T_2-weighted imaging was acquired by using TurboRARE (rapid acquisition with rapid enhancement) sequences with echo time (TE) = 10.5 ms; repetition time (TR) = 5000 ms; RARE factor = 4; slice thickness 0.2 mm; number of slices 15; field

of view 12 × 12 mm; image matrix of 256 × 256 pixels, resulting in an in-plane resolution of 47 μm.

T_2 relaxation time measurement in zebrafish brain was performed with MSME sequence by applying eight different TEs (8.5, 17.0, 25.5, 34.0, 42.5, 51.0, 59.5 and 68.0 ms); TR = 1.5 s; slice thickness 0.5 mm; number of slices 6, FOV 12 × 12 mm^2 and matrix size 256 × 256 pixels, resulting in an in-plane resolution of 47 μm. For calculation of T_2 relaxation time, regions of interest (ROIs) were drawn at various locations within the zebrafish brain. Another ROI in the muscle was used as an internal control. Means and standard deviation for T_2 relaxation times for each ROI were calculated.

Two-electrode voltage clamp, western and surface expression in Xenopus oocytes

Xenopus oocytes were injected and maintained as described (57). For rat ClC-2, 10 ng cRNA were injected. When co-expressing, 5 ng cRNA of *glialcama* or *glialcamb* were coinjected with rat ClC-2. Oocytes were perfused with ND96 (in mM): 96 NaCl, 2 KCl, 1.8 $CaCl_2$, 1 $MgCl_2$ and 5 HEPES/TRIS (pH 7.4). To estimate the specific ClC-2-mediated chloride currents, iodide (80 mM NaI replacing the NaCl), which blocks ClC-2-mediated outward currents (58), was applied in every experiment. Oocytes that did not exhibit a significant block were discarded. Currents were measured using a TEC-05X voltage amplifier and the CellWorks program (npi).

Western blot experiments and surface expression in oocytes were performed similarly as previously described (6).

Zebrafish electroretinogram recordings

ERGs were performed at 1-month and 2-month-old young adults (at least five animals). The young adults were anaesthetized by fish system water containing 0.75 mM 3-aminobenzoic acid methyl ester (MESAB, Sigma-Aldrich) and 4.6 mM $NaHCO_3$ before recording. All the experiments were performed at room temperature (20°C).

Fish were dark adapted for at least 30 min and then were placed on the filter paper in the middle of a plastic recording chamber which was filled by 1% agarose. The reference electrode was inserted into the agarose. After the fish was moisturized by a drop of Ringeŕs solution (111 mM NaCl, 2.5 mM KCl, 1 mM $CaCl_2$, 1.6 mM $MgCl_2$, 10 μm EDTA, 10 mM glucose and 3 mM HEPES buffer, adjusted to pH 7.7–7.8 with NaOH), the eye was removed by a loop made of tungsten wire. The loop was placed behind the eye and was pressed down to cut the optic nerve. Meanwhile forceps were used to pull the body and discard it. The isolated eye was then positioned to face the light source (ZEISS XBO 75 W). The recording electrode, filled with Ringer's solution, was placed against the centre of the cornea. All these pre-recording steps were done under dim red illumination. Stimulation light intensity was 6000 lux and attenuated by neutral density filters. Stimulus duration was 100 ms and delivered 50 ms after the recording began. Electronic signals were amplified 1000 times by a pre-amplifier (P55 A.C. Preamplifier, Astro-Med. Inc, Grass Technology) with a band pass between 0.1 and 100 Hz, digitized by DAQ Board NI PCI-6035E (National Instruments) via NI BNC-2090 accessories and displayed via self-developed NI Labview program (59). All the figures were prepared by Origin (Microcal Software).

Mouse electroretinogram recording

The mice were dark-adapted overnight before ERG recording. Under dim red light (λ > 600 nm), the mice were anaesthetized with an i.p. injection of a solution of ketamine (70 mg/kg, Ketolar®, Parke-Davies, S.L.) and xylazine (10 mg/kg, Rompún®) and kept on a heating pad to maintain normal body temperature at 37°C. A topical drop of 1% tropicamide (Colicursí Tropicamida 1%®; Alcon-Cusí, S.A.) were applied to the eyes of the experimental animals before ERG testing. Electrical responses were obtained with Burian-Allen electrodes (Hansen Labs) positioned on the cornea. A drop of methylcellulose (Methocel 2%®; Novartis Laboratories CIBA Vision) was positioned on the cornea to improve electrical conductivity. The reference electrode was placed in the mouth, and the ground electrode at the base of the tail. After positioning the electrodes, the mice were placed in a Ganzfeld stimulator. Stimulation flashes were provided by a Ganzfeld dome light source, which ensured a uniform illumination of the retina and provided a wide range of light intensities. Electrical signals generated in the retina were amplified (×1000) and band filtered between 0.3 and 1000 Hz, using a Grass amplifier (CP511 AC amplifier, Grass Instruments). Electrical signals were digitized at 20 kHz, using a Power Lab data acquisition board (AD Instruments) and displayed on a PC computer monitor. The ERG responses were elicited by stimulation of the retina with light intensities ranging between 10^{-4} and 10^2 cd/s/m^{-2}. A series of ERG responses were averaged (≈20 ERG traces) for each light intensity, after adjusting the time interval between flashes to ensure complete recovery of the response. Standard ERG waves were recorded according to the method recommended by the International Society for Clinical Electrophysiology of Vision (ISCEV).

Electrophysiological measurements on mouse astrocytes

Electrophysiological measurements were performed with the whole-cell configuration of the patch-clamp technique as previously described (60). Briefly, pipette had a resistance of 2–4 MΩ when filled with the intracellular solution. Membrane currents were amplified (amplifier List EPC-7) filtered at 2 kHz (−3 dB) and acquired at a sample rate of 5 kHz on a microcomputer for off-line analyses (pClamp 6, Axon Instruments and Origin 6.0, MicroCal). The access resistance (below 10 MΩ) was corrected for 60–80%. Current densities were calculated by dividing the current values measured at each membrane potential by the cell capacitance estimated from the capacitive transients of the recorded cells corrected by means of the analogical circuit of the patch-clamp amplifier. For the isolation of the Cl^- conductance, the external perfusing saline, called isotonic (Iso CsCl), was (mM): 122 CsCl, 2 $MgCl_2$, 2 $CaCl_2$, 10 TES, 5 glucose, pH 7.4 with CsOH and osmolality ~320 mOsm with mannitol. The intracellular (pipette) solution was composed of (mM): 126 CsCl, 2 $MgCl_2$, 1 EGTA, 10 TES, pH 7.2 and osmolality ~300 mOsm with mannitol. Hypotonic extracellular solution (Hypo CsCl) ~260 mOsm was obtained by omitting mannitol. Osmolality was measured with a vapour–pressure osmometer (Wescor 5500, Delcon). All salts and various

molecules were from Sigma. The DCPIB was prepared in DMSO at a concentration 1000-fold higher than that used in the perfusing saline.

SUPPLEMENTARY MATERIAL

Supplementary Material is available at *HMG* online.

ACKNOWLEDGEMENTS

We thank Marisol Montolio and Hernan López-Schier for their help in the initial stages of the project, Esther Prat and Laura González for the management of the *Mlc1* colony, Lara Sedó and Beatriz Gamarra for excellent fish care, Verónica López-Guillín and Catalina Sueiro for assistance with electron microscopy and histology and Lupe Soria for mice MRI. We also thank Thomas J Jentsch and Ian Orozco for critical reading of the article. We also thank IDIBELL and Alvaro Gimeno (Estabulari Bellvitge) for their help to setup the zebrafish facility.

Conflict of Interest statement. None declared.

FUNDING

This work was supported in by SAF 2009-07014 (R.E.) and SAF2012-31486 (R.E.), PS09/02672-ERARE to R.E., ELA Foundation 2009-017C4 and 2012-014C2B project (R.E. and V.N.), 2009 SGR 719 (R.E.), SAF 2009-12606-C02-02 (V.N.), 2009 SGR01490 (V.N.). R.E. is a recipient of an ICREA Academia prize.

REFERENCES

1. Van der Knaap, M.S., Boor, I. and Estevez, R. (2012) Megalencephalic leukoencephalopathy with subcortical cysts: chronic white matter oedema due to a defect in brain ion and water homoeostasis. *Lancet Neurol.*, **11**, 973–985.
2. Van der Knaap, M.S., Valk, J., Barth, P.G., Smit, L.M., van Engelen, B.G. and Tortori Donati, P. (1995) Leukoencephalopathy with swelling in children and adolescents: MRI patterns and differential diagnosis. *Neuroradiology*, **37**, 679–686.
3. Leegwater, P.A., Yuan, B.Q., van der Steen, J., Mulders, J., Konst, A.A., Boor, P.K., Mejaski-Bosnjak, V., van der Maarel, S.M., Frants, R.R., Oudejans, C.B. *et al.* (2001) Mutations of MLC1 (KIAA0027), encoding a putative membrane protein, cause megalencephalic leukoencephalopathy with subcortical cysts. *Am. J. Hum. Genet.*, **68**, 831–838.
4. Lopez-Hernandez, T., Ridder, M.C., Montolio, M., Capdevila-Nortes, X., Polder, E., Sirisi, S., Duarri, A., Schulte, U., Fakler, B., Nunes, V. *et al.* (2011a) Mutant GlialCAM causes megalencephalic leukoencephalopathy with subcortical cysts, benign familial macrocephaly, and macrocephaly with retardation and autism. *Am. J. Hum. Genet.*, **88**, 422–432.
5. Boor, P.K., de Groot, K., Waisfisz, Q., Kamphorst, W., Oudejans, C.B., Powers, J.M., Pronk, J.C., Scheper, G.C. and van der Knaap, M.S. (2005) MLC1: a novel protein in distal astroglial processes. *J. Neuropathol. Exp. Neurol.*, **64**, 412–419.
6. Teijido, O., Martinez, A., Pusch, M., Zorzano, A., Soriano, E., Del Rio, J.A., Palacin, M. and Estevez, R. (2004) Localization and functional analyses of the MLC1 protein involved in megalencephalic leukoencephalopathy with subcortical cysts. *Hum. Mol. Genet.*, **13**, 2581–2594.
7. Teijido, O., Casaroli-Marano, R., Kharkovets, T., Aguado, F., Zorzano, A., Palacin, M., Soriano, E., Martinez, A. and Estevez, R. (2007) Expression patterns of MLC1 protein in the central and peripheral nervous systems. *Neurobiol. Dis.*, **26**, 532–545.
8. Van der Knaap, M.S., Barth, P.G., Vrensen, G.F. and Valk, J. (1996) Histopathology of an infantile-onset spongiform leukoencephalopathy with a discrepantly mild clinical course. *Acta Neuropathol.*, **92**, 206–212.
9. Leegwater, P.A., Boor, P.K., Yuan, B.Q., van der Steen, J., Visser, A., Konst, A.A., Oudejans, C.B., Schutgens, R.B., Pronk, J.C. and van der Knaap, M.S. (2002) Identification of novel mutations in MLC1 responsible for megalencephalic leukoencephalopathy with subcortical cysts. *Hum. Genet.*, **110**, 279–283.
10. Montagna, G., Teijido, O., Eymard-Pierre, E., Muraki, K., Cohen, B., Loizzo, A., Grosso, P., Tedeschi, G., Palacin, M., Boespflug-Tanguy, O. *et al.* (2006) Vacuolating megalencephalic leukoencephalopathy with subcortical cysts: functional studies of novel variants in MLC1. *Hum. Mutat.*, **27**, 292.
11. Wang, J., Shang, J., Wu, Y., Gu, Q., Xiong, H., Ding, C., Wang, L., Gao, Z., Wu, X. and Jiang, Y. (2011) Identification of novel MLC1 mutations in Chinese patients with megalencephalic leukoencephalopathy with subcortical cysts (MLC). *J. Hum. Genet.*, **56**, 138–142.
12. Duarri, A., Teijido, O., Lopez-Hernandez, T., Scheper, G.C., Barriere, H., Boor, I., Aguado, F., Zorzano, A., Palacin, M., Martinez, A. *et al.* (2008) Molecular pathogenesis of megalencephalic leukoencephalopathy with subcortical cysts: mutations in MLC1 cause folding defects. *Hum. Mol. Genet.*, **17**, 3728–3739.
13. Lopez-Hernandez, T., Sirisi, S., Capdevila-Nortes, X., Montolio, M., Fernandez-Duenas, V., Scheper, G.C., van der Knaap, M.S., Casquero, P., Ciruela, F., Ferrer, I. *et al.* (2011b) Molecular mechanisms of MLC1 and GLIALCAM mutations in megalencephalic leukoencephalopathy with subcortical cysts. *Hum. Mol. Genet.*, **20**, 3266–3277.
14. Ridder, M.C., Boor, I., Lodder, J.C., Postma, N.L., Capdevila-Nortes, X., Duarri, A., Brussaard, A.B., Estevez, R., Scheper, G.C., Mansvelder, H.D. *et al.* (2011) Megalencephalic leucoencephalopathy with cysts: defect in chloride currents and cell volume regulation. *Brain*, **134**, 3342–3354.
15. Capdevila-Nortes, X., López-Hernández, T., Apaja, P.M., López de Heredia, M., Sirisi, S., Callejo, G., Arnedo, T., Nunes, V., Lukacs, G.L., Gasull, X. *et al.* (2013) Insights into MLC pathogenesis: GlialCAM is an MLC1 chaperone required for proper activation of volume-regulated anion currents. *Hum. Mol. Genet.*, **22**, 4405–4216.
16. Duarri, A., Lopez de Heredia, M., Capdevila-Nortes, X., Ridder, M.C., Montolio, M., Lopez-Hernandez, T., Boor, I., Lien, C.F., Hagemann, T., Messing, A. *et al.* (2011) Knockdown of MLC1 in primary astrocytes causes cell vacuolation: a MLC disease cell model. *Neurobiol. Dis.*, **43**, 228–238.
17. Brignone, M.S., Lanciotti, A., Macioce, P., Macchia, G., Gaetani, M., Aloisi, F., Petrucci, T.C. and Ambrosini, E. (2011) The beta1 subunit of the Na,K-ATPase pump interacts with megalencephalic leucoencephalopathy with subcortical cysts protein 1 (MLC1) in brain astrocytes: new insights into MLC pathogenesis. *Hum. Mol. Genet.*, **20**, 90–103.
18. Lanciotti, A., Brignone, M.S., Molinari, P., Visentin, S., De Nuccio, C., Macchia, G., Aiello, C., Bertini, E., Aloisi, F., Petrucci, T.C. *et al.* (2012) Megalencephalic leukoencephalopathy with subcortical cysts protein 1 functionally cooperates with the TRPV4 cation channel to activate the response of astrocytes to osmotic stress: dysregulation by pathological mutations. *Hum. Mol. Genet.*, **21**, 2166–2180.
19. Chung Moh, M., Hoon Lee, L. and Shen, S. (2005) Cloning and characterization of hepaCAM, a novel Ig-like cell adhesion molecule suppressed in human hepatocellular carcinoma. *J. Hepatol.*, **42**, 833–841.
20. Favre-Kontula, L., Rolland, A., Bernasconi, L., Karmirantzou, M., Power, C., Antonsson, B. and Boschert, U. (2008) GlialCAM, an immunoglobulin-like cell adhesion molecule is expressed in glial cells of the central nervous system. *Glia*, **56**, 633–645.
21. Van der Knaap, M.S., Lai, V., Kohler, W., Salih, M.A., Fonseca, M.J., Benke, T.A., Wilson, C., Jayakar, P., Aine, M.R., Dom, L. *et al.* (2010) Megalencephalic leukoencephalopathy with cysts without MLC1 defect. *Ann. Neurol.*, **67**, 834–837.
22. Hoegg-Beiler, M.B., Sirisi, S., Orozco, I., Ferrer, I., Hohensee, S., Auberson, M., Gödde, K., Vilches, C., López de Heredia, M., Nunes, V., Estévez, R. and Jentsch, T. (2014) Disrupting MLC1 GlialCAM and ClC-2 interactions in leukodystrophy entails glial Cl- channel dysfunction. *Nat. Commun*, **5**, 3475.
23. Arnedo, T., Aiello, C., Jeworutzki, E., Dentici, M.L., Uziel, G., Simonati, A., Pusch, M., Bertini, E. and Estévez, R. (2013) Expanding the spectrum of megalencephalic leukoencephalopathy with subcortical cysts in two patients with GLIALCAM mutations. *Neurogenetics*. doi:10.1007/s10048-013-0381-x.
24. Jeworutzki, E., Lopez-Hernandez, T., Capdevila-Nortes, X., Sirisi, S., Bengtsson, L., Montolio, M., Zifarelli, G., Arnedo, T., Muller, C.S., Schulte,

U. *et al.* (2012) GlialCAM, a protein defective in a leukodystrophy, serves as a ClC-2 Cl(−) channel auxiliary subunit. *Neuron*, **73**, 951–961.
25. Maduke, M.C. and Reimer, R.J. (2012) Biochemistry to the rescue: a ClC-2 auxiliary subunit provides a tangible link to leukodystrophy. *Neuron*, **73**, 855–857.
26. Depienne, C., Bugiani, M., Dupuits, C., Galanaud, D., Touitou, V., Postma, N., van Berkel, C., Polder, E., Tollard, E., Darios, F. *et al.* (2013) Brain white matter oedema due to ClC-2 chloride channel deficiency: an observational analytical study. *Lancet Neurol.*, **12**, 659–668.
27. Drumm, M.L., Wilkinson, D.J., Smit, L.S., Worrell, R.T., Strong, T.V., Frizzell, R.A., Dawson, D.C. and Collins, F.S. (1991) Chloride conductance expressed by delta F508 and other mutant CFTRs in Xenopus oocytes. *Science*, **254**, 1797–1799.
28. Lawson, N.D. and Weinstein, B.M. (2002) In vivo imaging of embryonic vascular development using transgenic zebrafish. *Dev. Biol.*, **248**, 307–318.
29. Cuoghi, B. and Mola, L. (2009) Macroglial cells of the teleost central nervous system: a survey of the main types. *Cell Tissue Res.*, **338**, 319–332.
30. Decher, N., Lang, H.J., Nilius, B., Bruggemann, A., Busch, A.E. and Steinmeyer, K. (2001) DCPIB is a novel selective blocker of I(Cl,swell) and prevents swelling-induced shortening of guinea-pig atrial action potential duration. *Br. J. Pharmacol.*, **134**, 1467–1479.
31. Benfenati, V., Nicchia, G.P., Svelto, M., Rapisarda, C., Frigeri, A. and Ferroni, S. (2007) Functional down-regulation of volume-regulated anion channels in AQP4 knockdown cultured rat cortical astrocytes. *J. Neurochem.*, **100**, 87–104.
32. Parkerson, K.A. and Sontheimer, H. (2004) Biophysical and pharmacological characterization of hypotonically activated chloride currents in cortical astrocytes. *Glia*, **46**, 419–436.
33. Clark, S., Jordt, S.E., Jentsch, T.J. and Mathie, A. (1998) Characterization of the hyperpolarization-activated chloride current in dissociated rat sympathetic neurons. *J. Physiol.*, **506**(Pt 3), 665–678.
34. Makara, J.K., Rappert, A., Matthias, K., Steinhauser, C., Spat, A. and Kettenmann, H. (2003) Astrocytes from mouse brain slices express ClC-2-mediated Cl- currents regulated during development and after injury. *Mol. Cell Neurosci.*, **23**, 521–530.
35. Wang, F., Xu, Q., Wang, W., Takano, T. and Nedergaard, M. (2012) Bergmann glia modulate cerebellar Purkinje cell bistability via Ca2+-dependent K+ uptake. *Proc. Natl Acad. Sci. USA*, **109**, 7911–7916.
36. Cahoy, J.D., Emery, B., Kaushal, A., Foo, L.C., Zamanian, J.L., Christopherson, K.S., Xing, Y., Lubischer, J.L., Krieg, P.A., Krupenko, S.A. *et al.* (2008) A transcriptome database for astrocytes, neurons, and oligodendrocytes: a new resource for understanding brain development and function. *J. Neurosci.*, **28**, 264–278.
37. Lovatt, D., Sonnewald, U., Waagepetersen, H.S., Schousboe, A., He, W., Lin, J.H.-C., Han, X., Takano, T., Wang, S., Sim, F.J. *et al.* (2007) The transcriptome and metabolic gene signature of protoplasmic astrocytes in the adult murine cortex. *J. Neurosci.*, **27**, 12255–12266.
38. Voss, F.K., Ullrich, F., Münch, J., Lazarow, K., Lutter, D., Mah, N., Andrade-Navarro, M.A., von Kries, J.P., Stauber, T. and Jentsch, T.J. (2014) Identification of LRRC8 heteromers as an essential component of the volume-regulated anion channel VRAC. *Science*. doi:10.1126/science.1252826.
39. Qiu, Z., Dubin, A.E., Mathur, J., Tu, B., Reddy, K., Miraglia, L.J., Reinhardt, J., Orth, A.P. and Patapoutian, A. (2014) SWELL1, a plasma membrane protein, is an essential component of volume-regulated anion channel. *Cell*, **157**, 447–458.
40. Brosamle, C. and Halpern, M. (2002) Characterization of myelination in the developing zebrafish. *Glia*, **39**, 47–57.
41. Jeserich, G., Klempahn, K. and Pfeiffer, M. (2008) Features and functions of oligodendrocytes an myelin proteins of lower vertebrate species. *J. Mol. Neurosci.*, **35**, 117–126.
42. Yin, X., Baek, R.C., Kirschner, D.A., Peterson, A., Fujii, Y., Nave, K.-A., Macklin, W.B. and Trapp, B.D. (2006) Evolution of a neuroprotective function of central nervous system myelin. *J. Cell Biol.*, **172**, 469–478.
43. Buckley, C.E., Marguerie, A., Alderton, W.K. and Franklin, R.J.M. (2010) Temporal dynamics of myelination in the zebrafish spinal cord. *Glia*, **58**, 802–812.
44. Jeserich, G. (1981) A morphological and biochemical study of myelin of myelinogenesis in fish brain. *Dev. Neurosci.*, **4**, 373–381.
45. Chapouton, P., Jagasia, R. and Bally-Cuif, L. (2007) Adult neurogenesis in non-mammalian vertebrates. *BioEssays*, **29**, 745–757.
46. Kyritsis, N., Kizil, C., Zocher, S., Kroehne, V., Kaslin, J., Freudenreich, D., Iltzsche, A. and Brand, M. (2012) Acute inflammation initiates the regenerative response in the adult zebrafish brain. *Science*, **338**, 1353–1356.
47. Buckley, C.E., Goldsmith, P. and Franklin, R.J.M. (2008) Zebrafish myelination: a transparent model for remyelination?. *Dis. Model. Mech.*, **1**, 221–228.
48. Dubois-Dalcq, M., Williams, A., Stadelmann, C., Stankoff, B., Zalc, B. and Lubetzki, C. (2008) From fish to man: understanding endogenous remyelination in central nervous system demyelinating diseases. *Brain*, **131**, 1686–1700.
49. Rash, J.E. (2010) Molecular disruptions of the panglial syncytium block potassium siphoning and axonal saltatory conduction: pertinence to neuromyelitis optica and other demyelinating diseases of the central nervous system. *Neuroscience*, **168**, 982–1008.
50. Neusch, C., Rozengurt, N., Jacobs, R.E., Lester, H.A. and Kofuji, P. (2001) Kir4.1 potassium channel subunit is crucial for oligodendrocyte development and in vivo myelination. *J. Neurosci.*, **21**, 5429–5438.
51. Menichella, D.M., Majdan, M., Awatramani, R., Goodenough, D.A., Sirkowski, E., Scherer, S.S. and Paul, D.L. (2006) Genetic and physiological evidence that oligodendrocyte gap junctions contribute to spatial buffering of potassium released during neuronal activity. *J. Neurosci.*, **26**, 10984–10991.
52. Branicky, R., Miyazaki, H., Strange, K. and Schafer, W.R. (2014) The voltage-gated anion channels encoded by clh-3 regulate egg laying in *C. elegans* by modulating motor neuron excitability. *J. Neurosci.*, **34**, 764–775.
53. Westerfield, M. (2000) *The Zebrafish Book. A Guide for the Laboratory use of Zebrafish (Danio Rerio)*, University of Oregon Presss, Eugene.
54. Tang, R., Dodd, A., Lai, D., McNabb, W.C. and Love, D.R. (2007) Validation of zebrafish (Danio rerio) reference genes for quantitative real-time RT-PCR normalization. *Acta Biochim. Biophys. Sin. (Shanghai)*, **39**, 384–390.
55. Pfaffl, M.W. (2001) A new mathematical model for relative quantification in real-time RT-PCR. *Nucleic Acids Res.*, **29**, e45.
56. Peters, A., Palay, S.L. and de Webster, H.F. (1991) *The Fine Structure of the Nervous System: The Neurons and Their Supporting Cells*. Saunders Company, Philadelphia, USA.
57. Estevez, R., Schroeder, B.C., Accardi, A., Jentsch, T.J. and Pusch, M. (2003) Conservation of chloride channel structure revealed by an inhibitor binding site in ClC-1. *Neuron*, **38**, 47–59.
58. Thiemann, A., Grunder, S., Pusch, M. and Jentsch, T.J. (1992) A chloride channel widely expressed in epithelial and non-epithelial cells. *Nature*, **356**, 57–60.
59. Rinner, O., Rick, J.M. and Neuhauss, S.C.F. (2005) Contrast sensitivity, spatial and temporal tuning of the larval zebrafish optokinetic response. *Invest. Ophthalmol. Vis. Sci.*, **46**, 137–142.
60. Ferroni, S., Marchini, C., Nobile, M. and Rapisarda, C. (1997) Characterization of an inwardly rectifying chloride conductance expressed by cultured rat cortical astrocytes. *Glia*, **21**, 217–227.
61. Blanz, J., Schweizer, M., Auberson, M., Maier, H., Muenscher, A., Hubner, C.A. and Jentsch, T.J. (2007) Leukoencephalopathy upon disruption of the chloride channel ClC-2. *J. Neurosci.*, **27**, 6581–6589.
62. Wienholds, E., van Eeden, F., Kosters, M., Mudde, J., Plasterk, R.H. and Cuppen, E. (2003) Efficient target-selected mutagenesis in zebrafish. *Genome Res*, **13**, 2700–2707.